



UCL

**GAS-LIQUID TWO-PHASE
FLOW AND REACTION IN
MICROSTRUCTURED REACTORS**

by

Nan Shao

Department of Chemical Engineering

University College London

2010

A thesis submitted for the degree of

Doctor of Philosophy

I, Nan Shao confirm that the work presented in this thesis is my own. Where information has been derived from other sources, I confirm that this has been indicated in the thesis.

Abstract

The thesis presents investigations on two-phase gas-liquid microstructured reactors operating in Taylor flow and the dependence of reactor performance on design parameters. Literature review revealed that flow patterns in microchannels are affected not only by channel dimension, fluids flowrates and surface tension, but also by wall wettability and gas inlet size. A universal flow regime map does not seem to exist. The hydrodynamic parameters of Taylor flow were investigated both by Computational Fluid Dynamics simulations and experiments in microstructures with sizes 0.3mm – 1mm and various inlet configurations such as T- and Y- junctions fabricated in-house. The same parameters that influence flow patterns and their transitions were also found to affect Taylor bubble sizes. To account for the effect of inlet conditions, correlations were developed for predicting bubble/slug size in the T- and Y- inlet geometries that were used subsequently. Mass transfer with and without chemical reaction was investigated numerically in Taylor flow microreactors using CO₂ physical absorption into water or chemical absorption into NaOH aqueous solution. Chemical absorption was enhanced by a factor of 3-18 over physical absorption. With reaction present, the reactor performance depended mainly on the gas-liquid interfacial area, while mixing within the phases was only important in physical absorption. This agreed with the experimental results of a similar reaction system, which showed that bifurcating main channels, where new interfaces are generated, significantly improved reaction conversion while meandering channels that enhance liquid mixing had little impact. Finally, the performance of a Taylor flow microreactor was evaluated for an industrial fast gas-liquid reaction of CO₂ absorption from fuel gas into amine solutions. The Taylor flow microreactor offered the largest specific area and the smallest reactor volume compared to other microreactor types. However, in order to meet absorption specifications for the case considered multistage absorption would have been necessary.

Acknowledgments

This thesis would not have been possible without the support of many people.

I would like to thank my principal supervisor Dr Panagiota Angeli and my second supervisor Prof. Asterios Gavriilidis. Their excellent supervision, contribution and guidance throughout my PhD studies are more than appreciated.

Financial support from the Overseas Research Students (ORS) Award Scheme, University College London Graduate School Research Scholarships and The Old Students Association Trust Scholarships is also gratefully acknowledged.

Many thanks to EPSRC for providing the high speed camera systems that make the research more fruitful and interesting. I'm also grateful to people in the workshop, who turned many design ideas into reality and also offered many useful advices for microchannel fabrications.

Dr Wael Salman, who introduced me to the work of Taylor flow and numerical modelling, deserves a special acknowledgment for his advice and friendship. Dr Enhong Cao also deserves a special acknowledgment for sharing his expertise in lab work.

I am grateful to all the past and present PhD students in Department of Chemical Engineering at UCL for their sharing, companion and support. In particular, many thanks to Jia Sun and Dr Baodong Wang, who have been colleagues and friends of mine since university.

Great thanks go to my husband, Dr Gang Xu, whose support and encouragement escort me through the darkest days. Your many love, patience and contributions to the housework are very appreciated.

Finally, I would like to thank my parents Mr. Peigang Shao and Mrs. Jingyun Su and my sister Mrs. Fei Shao. Without your endless and unconditional love and support for all these years, I will not be this far today.

Table of Contents

ABSTRACT	3
ACKNOWLEDGMENTS	4
TABLE OF CONTENTS	5
LIST OF FIGURES	10
LIST OF TABLES	20
1 THESIS INTRODUCTION	22
1.1 PROCESS INTENSIFICATION – INNOVATION FOR CHEMICAL INDUSTRY	23
1.2 MICROSTRUCTURED REACTORS – OPPORTUNITIES AND CHALLENGES	25
1.3 THESIS MOTIVATION AND OBJECTIVES.....	26
1.4 THESIS OUTLINE	26
2 LITERATURE SURVEY	28
2.1 GAS-LIQUID TWO-PHASE FLOW IN MICROCHANNELS.....	31
2.2 FLOW PATTERNS FORMED IN MICROCHANNELS.....	31
2.3 SURFACE TENSION AND MARANGONI EFFECT	45
2.4 CONTACT ANGLE AND WETTABILITY	45
2.5 TAYLOR FLOW	47
2.5.1 <i>Geometric characteristics of Taylor flow</i>	48
2.5.2 <i>Taylor flow formation and bubble size</i>	49
2.5.3 <i>Bubble velocity</i>	53
2.5.4 <i>Film thickness</i>	55
2.5.5 <i>Flow patterns in liquid slugs</i>	58
2.5.6 <i>Mass transfer</i>	60
2.6 MICROSTRUCTURED REACTORS	62
2.6.1 <i>Contact principles for gas-liquid microreactors</i>	63
2.6.1.1 Continuous-phase microreactors.....	63
2.6.1.2 Dispersed-phase microreactors	65
2.6.2 <i>Structure design of microstructured reactors</i>	67
2.6.2.1 Inlet design	67
2.6.2.2 Main channel design	73
2.6.2.3 Outlet design.....	75
2.7 CONCLUDING REMARKS.....	77

3 REVIEW ON GAS-LIQUID TWO-PHASE FLOW TRANSITIONS IN MICROCHANNELS ...	79
3.1 INTRODUCTION	82
3.2 PARAMETERS INFLUENCING FLOW REGIMES AND THEIR TRANSITIONS.....	82
3.2.1 <i>Flow orientation</i>	82
3.2.2 <i>Channel size</i>	83
3.2.3 <i>Channel geometry</i>	86
3.2.4 <i>Wall wetting conditions</i>	87
3.2.5 <i>Fluid properties</i>	89
3.2.6 <i>Inlet conditions</i>	91
3.3 FLOW REGIME PREDICTION	91
3.4 CONCLUSIONS	95
4 EFFECT OF INLET CONDITIONS ON GAS-LIQUID FLOW REGIMES IN MICROCHANNELS	97
4.1 INTRODUCTION	99
4.2 EXPERIMENTAL SETUP.....	99
4.3 RESULTS AND DISCUSSIONS	100
4.3.1 <i>Flow patterns</i>	100
4.3.2 <i>Effect of inlet size</i>	101
4.3.3 <i>Effect of inlet configuration</i>	103
4.3.4 <i>Effect of capillary size</i>	104
4.3.5 <i>Comparison with literature</i>	105
4.4 CONCLUSIONS	107
5 CFD SIMULATIONS OF THE EFFECT OF INLET CONDITIONS ON TAYLOR FLOW FORMATION.....	108
5.1 INTRODUCTION	111
5.2 FLOW SYSTEM AND MODEL FORMULATION	112
5.3 RESULTS AND DISCUSSIONS	115
5.3.1 <i>Bubble formation mechanism</i>	115
5.3.2 <i>Effect of inlet conditions on bubble size</i>	118
5.3.2.1 Effect of gas and liquid velocity	118
5.3.2.2 Effect of liquid property	118
5.3.2.3 Effect of nozzle size and its wall thickness.....	120
5.3.2.4 Effect of wall wetting condition.....	121
5.3.3 <i>Bubble size comparison with literature</i>	122
5.4 CONCLUSIONS	125
6 MICROREACTOR DESIGN AND TAYLOR BUBBLE LENGTH PREDICTION	126
6.1 INTRODUCTION	128

Table of Contents

6.2	MICROREACTOR FABRICATION	128
6.3	MICROREACTOR INLET DESIGN	133
6.4	EXPERIMENTAL SETUP	134
6.5	RESULTS AND DISCUSSIONS	135
6.5.1	<i>Inlet design</i>	135
6.5.2	<i>Effect on bubble length of inlet conditions</i>	136
6.5.2.1	Effect of channel orientation.....	137
6.5.2.2	Effect of gas and liquid flowrate.....	138
6.5.2.3	Effect of surface tension	139
6.5.2.4	Effect of gas inlet size.....	141
6.5.2.5	Effect of main channel size.....	142
6.5.2.6	Effect of inlet configuration.....	144
6.5.3	<i>Prediction of bubble length</i>	148
6.6	CONCLUSIONS	151
7	MASS TRANSFER AND REACTION IN TAYLOR FLOW MICROREACTOR	152
7.1	INTRODUCTION	156
7.2	REACTION SYSTEM	156
7.3	REACTOR DESIGN	158
7.4	EXPERIMENTAL SET UP	161
7.5	MODEL FORMULATION	162
7.6	RESULTS AND DISCUSSIONS	164
7.6.1	<i>Series I reactors</i>	165
7.6.2	<i>Series II reactors</i>	170
7.7	CONCLUSIONS	178
8	NUMERICAL PARAMETRIC STUDY ON TAYLOR FLOW MICROREACTOR	180
8.1	INTRODUCTION	183
8.2	MODEL FORMULATION	183
8.3	RESULTS AND DISCUSSIONS	186
8.3.1	<i>Effect of fluid flow and chemical reaction</i>	186
8.3.2	<i>Effect of bubble length</i>	190
8.3.3	<i>Effect of slug length</i>	191
8.3.4	<i>Effect of film thickness</i>	191
8.3.5	<i>Effect of unit cell length</i>	194
8.3.6	<i>Effect of channel dimension</i>	195
8.3.7	<i>Mass transfer coefficient and enhancement factor</i>	196
8.4	CONCLUSIONS	198
9	MICROREACTOR APPLICATION STUDY ON FUEL GAS ABSORPTION IN AMINE SOLUTIONS	200

Table of Contents

9.1	INTRODUCTION	203
9.2	SYSTEM CHARACTERIZATION	205
9.2.1	<i>Operating conditions</i>	205
9.2.2	<i>Reaction system</i>	207
9.2.3	<i>Physical properties</i>	209
9.2.3.1	Gas phase	209
9.2.3.2	Liquid phase	210
9.3	FALLING FILM REACTOR	211
9.3.1	<i>Model formulation</i>	211
9.3.2	<i>Model validation</i>	214
9.3.3	<i>Preliminary results and discussions</i>	215
9.3.3.1	Base case characterization	215
9.3.3.2	Effect of liquid film thickness	218
9.3.3.3	Effect of gas film thickness	219
9.3.3.4	Effect of MDEA concentration	220
9.3.3.5	Effect of reaction rate constant	221
9.3.4	<i>Results and discussions – With elevated reaction rate</i>	223
9.3.4.1	Base case characterization	223
9.3.4.2	Effect of liquid viscosity	226
9.4	TAYLOR FLOW REACTOR	227
9.4.1	<i>Model formulation</i>	228
9.4.2	<i>Results and discussions</i>	231
9.4.2.1	Base case characterization	231
9.4.2.2	Multistage absorption	233
9.4.2.3	Effect of bubble length	234
9.4.2.4	Effect of liquid flowrate	235
9.4.2.5	Effect of channel size	238
9.5	ANNULAR FLOW REACTOR	239
9.5.1	<i>Model formulation</i>	239
9.5.2	<i>Results and discussions</i>	240
9.5.2.1	Base case characterization	240
9.5.2.2	Multistage absorption	243
9.5.2.3	Effect of film thickness	244
9.5.2.4	Effect of channel size	245
9.6	REACTOR PERFORMANCE COMPARISON	246
9.7	CONCLUSIONS	249
9.7.1	<i>Falling film reactor</i>	249
9.7.2	<i>Taylor flow reactor</i>	249
9.7.3	<i>Annular flow reactor</i>	250
10	CONCLUSIONS & RECOMMENDATIONS FOR FUTURE STUDY	252

Table of Contents

10.1	THESIS SUMMARY	253
10.2	RECOMMENDATION FOR MICROREACTOR DESIGN	257
10.3	RECOMMENDATIONS FOR FUTURE STUDY	258
	BIBLIOGRAPHY	261
	APPENDIX	276
	APPENDIX A CALCULATING BUBBLE/SLUG LENGTH FROM BUBBLE FREQUENCY	279
	APPENDIX B COMPARISON OF METHODS TO UPDATE THE GAS-LIQUID INTERFACIAL CONCENTRATION 281	
	APPENDIX C SENSITIVITY STUDY ON SIMULATION TIME STEPS	283
	APPENDIX D NUMERICAL MODEL VERIFICATION	284
	APPENDIX E CALCULATION OF REACTION CONVERSION FOR CO ₂ ABSORPTION EXPERIMENTS	287
	APPENDIX F TAYLOR BUBBLE SPLITTING IN BIFURCATING CHANNELS	288
	APPENDIX G NUMERICAL MODEL CODE FOR TAYLOR FLOW FORMATION	290
	APPENDIX H NUMERICAL MODEL REPORT FOR TAYLOR FLOW MASS TRANSFER	295
	REFEREED RESEARCH PAPERS FROM THIS THESIS	316

List of Figures

FIGURE 1.1 PROCESS INTENSIFICATION AND ITS COMPONENTS. STANKIEWICZ AND MOULIJN (2000).	24
FIGURE 2.1 GENERAL CLASSIFICATION OF GAS-LIQUID TWO-PHASE FLOW PATTERNS.	32
FIGURE 2.2 BUBBLY FLOW. (A), (B) BUBBLY FLOW (TRIPLETT ET AL., 1999, AIR/WATER, $D = 1.097\text{MM}$); (C) CAPILLARY BUBBLY FLOW (ZHAO AND BI, 2001, AIR/WATER, EQUILATERAL TRIANGULAR CHANNEL, $D_H = 0.866\text{MM}$).	33
FIGURE 2.3 TAYLOR FLOW. (A) TAYLOR FLOW (TRIPLETT ET AL., 1999, AIR/WATER, $D = 1.097\text{MM}$, PYREX CAPILLARY); (B) DRY PLUG FLOW (LEE AND LEE, 2008, AIR/WATER, $D = 1.59\text{MM}$, TEFLON TUBE WITH $\theta = 110^\circ$); (C) BUBBLE-TRAIN SLUG (CHEN ET AL., 2002, NITROGEN/WATER, $D = 1\text{MM}$).	34
FIGURE 2.4 TAYLOR-ANNULAR FLOW. (A) TAYLOR-ANNULAR FLOW (TRIPLETT ET AL., 1999, AIR/WATER, SEMI-TRIANGULAR CHANNEL OF $D_H = 1.09\text{MM}$); (B) LIQUID RING FLOW (SERIZAWA ET AL., 2002, AIR/WATER, $D = 50\text{MM}$).	35
FIGURE 2.5 (A), (B) CHURN FLOW (TRIPLETT ET AL., 1999, AIR/WATER, $D = 1.097\text{MM}$).	36
FIGURE 2.6 ANNULAR FLOW: (A) ANNULAR FLOW (TRIPLETT ET AL., 1999, AIR/WATER, $D = 1.097\text{MM}$); (B) RIVULET FLOW (BARAJAS AND PANTON, 1993, AIR/WATER); (C) DRY FLOW (CUBAUD AND HO, 2004, AIR/WATER).	36
FIGURE 2.7 DISPERSED FLOW: (A) BARAJAS AND PANTON (1993), AIR/WATER; (B) YANG AND SHIEH (2001), AIR/WATER, $D = 3\text{MM}$.	37
FIGURE 2.8 THREE PHASES AT THE CONTACT INTERFACE.	45
FIGURE 2.9 SCHEMATIC PROGRESS IN THE WETTING BEHAVIOUR OF BUBBLES AT INCREASING Ca (JENSEN, 2002).	46
FIGURE 2.10 TAYLOR FLOW UNIT CELL, REPRESENTED AS ONE BUBBLE AND ONE LIQUID SLUG.	47
FIGURE 2.11 3-D VIEW OF TAYLOR BUBBLE SHAPE IN A SQUARE CAPILLARY WITH SIDE LENGTH OF 2MM. (A) $Ca = 0.009$; (B) $Ca = 1.45$; (C) $Ca = 3.04$; (D) CROSS SECTIONAL VIEW OF THE BUBBLE PROFILE, (\blacktriangle) $Ca = 0.005$; (\blacksquare) $Ca = 0.009$; (\bullet) $Ca = 0.026$; (Δ) $Ca = 0.054$; (\square) $Ca = 0.21$; (\circ) $Ca = 0.4$; (\times) $Ca = 1.35$; ($-$) $Ca = 3.04$. TAHA AND CUI (2006A).	48
FIGURE 2.12 TAYLOR BUBBLE RISE VELOCITY IN STAGNANT WATER AND DILUTE AQUEOUS SOLUTIONS CONTAINED IN VERTICAL TUBES (TAHA AND CUI, 2006B).	54
FIGURE 2.13 LIQUID FILM SHAPE IN SQUARE MICROCHANNEL WITH NON-AXISYMMETRIC BUBBLE ($Ca < 0.04$, YUE ET AL. 2008).	55
FIGURE 2.14 FILM THICKNESS AS A FUNCTION OF THE CAPILLARY NUMBER Ca . BRETHERTON USED ANILINE AND BENZENE, WHILE TAYLOR USED A SYRUP-WATER MIXTURE, GLYCERINE AND LUBRICATING OIL. KREUTZER ET AL., (2005B).	56
FIGURE 2.15 DIMENSIONLESS FILM THICKNESS VERSUS Ca IN SQUARE CAPILLARIES. ON THE TOP AXIS, THE VELOCITY OF THE BUBBLE IS PLOTTED, ASSUMING WATER-LIKE PROPERTIES $\mu_L = 10^{-3}\text{Pa s}$ AND $\Sigma = 0.073\text{ N/M}$ (KREUTZER ET AL., 2005B).	57

List of Figures

FIGURE 2.16 SKETCH OF LIQUID STREAMLINES FOR THE FLOW OF ELONGATED BUBBLES IN CAPILLARIES. (A) $M > 0.5$, TOTAL BYPASS; (B),(C) $M < 0.5$, FORMATION OF STAGNATION RING. THE QUANTITY M IS DEFINED AS $\frac{U_B - U_{TP}}{U_B}$ (TAYLOR, 1961). 58

FIGURE 2.17 VELOCITY FIELD IN TAYLOR FLOW INSIDE CIRCULAR CAPILLARIES ($D = 2\text{MM}$) WITH A REFERENCE FRAME MOVING WITH THE BUBBLE (TAHA AND CUI, 2006B). $Ca = 0.032$ FOR THE TOP PATTERN, AND THE STREAMLINES BOW SHARPLY TO COMPLETE THE VORTEX PATH SIMILAR TO FIGURE 2.16 (B); IN THE BOTTOM ONE, $Ca = 0.924$ AND THE VORTEX IS HARDLY SEEN TO FORM A BYPASS PATTERN SIMILAR TO FIGURE 2.16 (A). 59

FIGURE 2.18 MASS TRANSFER IN A TAYLOR FLOW UNIT CELL. THE HORIZONTAL ARROWS: GAS TO LIQUID MASS TRANSFER OCCURRING INTO THE LIQUID SLUG FROM THE BUBBLE CAPS; THE VERTICAL ARROWS: GAS TO LIQUID MASS TRANSFER OCCURRING INTO THE LIQUID FILM FROM THE BUBBLE. ... 60

FIGURE 2.19 (A) FALLING-FILM MICROREACTOR AND SCHEMATIC SHOWING THE GAS-LIQUID CONTACTING (AL-RAWASHDEH ET AL., 2008); (B) FLOW PATTERNS OBSERVED IN FALLING-FILM MICROREACTOR (ZHANG ET AL., 2009). A: CORNER RIVULET FLOW; B: FALLING FILM FLOW WITH DRY PATCHES; C: COMPLETE FALLING LIQUID FILM FLOW. 64

FIGURE 2.20 ASSEMBLED MESH MICROREACTOR AND A SCANNING ELECTRON MICROGRAPH OF THE MESH PORES (WENN ET AL., 2003). 65

FIGURE 2.21 VARIOUS INLETS DEVELOPED FROM THE T- JUNCTION. G: GAS INLET; L: LIQUID INLET; M: MAIN CHANNEL. (A) T-JUNCTION WITH THE GAS AND LIQUID INLET CHANNEL PERPENDICULAR TO THE MAIN CHANNEL; (B) T-JUNCTION WITH EITHER THE GAS OR LIQUID INLET CHANNEL IN THE DIRECTION OF THE MAIN CHANNEL; (C) Y-JUNCTION INLET; (D) CROSS-JUNCTION INLET; (E) FLOW-FOCUSING INLET. 68

FIGURE 2.22 T- AND Y-JUNCTION INLET WITH DIFFERENT ANGLES (TAN ET AL., 2009). 69

FIGURE 2.23 EFFECT OF INLET CHANNEL SIZE ON BUBBLE LENGTH (AMADOR ET AL., 2004). 70

FIGURE 2.24 EFFECT OF T-JUNCTION ORIENTATION ON GAS AND LIQUID SLUG LENGTH (QIAN AND LAWAL, 2006). THE RED AND BLUE STAND FOR THE GAS AND LIQUID PHASE RESPECTIVELY. 70

FIGURE 2.25 EFFECT OF INLET MIXING ON GAS AND LIQUID SLUG LENGTH (QIAN AND LAWAL, 2006). 70

FIGURE 2.26 INLET DESIGN EXAMPLES FOR FLOW EVEN DISTRIBUTION DURING SCALE-OUT. (A) INLET PRESSURE-DROP CHANNELS TO PREVENT CROSS TALK BETWEEN MAIN CHANNELS (DE MAS ET AL., 2003B); (B) GAS DISTRIBUTION CHANNELS OF DIFFERENT LENGTH AND SIZE AND LIQUID DISTRIBUTOR THAT ALSO SERVE AS PRESSURE-DROP CHANNELS (LOSEY ET AL., 2002). IN B, GAS INLET IS SPLIT INTO 4 STREAMS AND THEN INTERLEAVED WITH 5 LIQUID INLET STREAMS; (C) GAS DISTRIBUTION CHANNEL WITH MULTI-STAGE EQUAL-ARMED BIFURCATING CHANNELS (WADA ET AL., 2006). 72

FIGURE 2.27 INLET DESIGN EXAMPLE TO IMPROVE THE REACTIVE PHASE MIXING BY FORMING TAYLOR FLOW USING AN INERT GAS AND INITIATING CHAOTIC MIXING BY TRAVELLING THE FLOW IN A MEANDERING CHANNEL (YEN ET AL., 2005). 73

FIGURE 2.28 EXAMPLES OF CURVED MAIN CHANNELS. (A) INERT OIL PHASE SUSPENDS THE REACTIVE PHASE IN MEANDERING MICROCHANNELS. CHANNELS WERE 45MM DEEP; INLET CHANNELS WERE 50MM AND MEANDERING CHANNELS WERE 28MM WIDE; $Re \sim 5.3$ (WATER), $Re \sim 2.0$ (OIL) (SONG ET AL., 2003); (B)

List of Figures

CHANNELS WITH PERIODICALLY PINCHED, OBTUSE ZIGZAG, AND ACUTE ZIGZAG STRUCTURES AND THE REACTION CONVERSION ACHIEVED (LIDA ET AL., 2009). THE CHANNELS ARE RECTANGULAR WITH CROSS SECTION OF 790 MM WIDE AND 500 MM DEEP, AND 2 M LENGTH. 74

FIGURE 2.29 MICROCHANNEL FABRICATED WITH CATALYST POSTS TO IMPROVE GAS-LIQUID CONTACT. THE POSTS ARE 50MM IN DIAMETER AND 300MM HIGH, ARRANGED IN STAGGERED ARRAYS IN CHANNELS 300MM DEEP, 625MM WIDE AND 20 MM LONG. (A) MICROSTRUCTURED CATALYST SUPPORTS PRIOR TO POROUS SILICON FORMATION; (B) VIEW OF MICRON SCALE STRIATIONS ON THE POSTS. LOSEY ET AL. (2002). 75

FIGURE 2.30 DISENGAGEMENT CHAMBER DESIGN AT THE CAPILLARY OUTLET TO REDUCE PRESSURE FLUCTUATIONS (AMADOR ET AL., 2004)..... 76

FIGURE 2.31 GAS-LIQUID SEPARATOR DESIGN BY APPLYING A NEGATIVE DIFFERENTIAL PRESSURE. (A) SEPARATOR WITH A MICROCAPILLARY ARRAY (SEVERAL THOUSANDS OF 20MM CAPILLARIES ON A 3MM DIAMETER ARRAY). GÜNTHER ET AL. (2003); (B) SINGLE-STAGE AND TWO-STAGE SEPARATOR, PROVIDING AN INTEGRATED DESIGN FOR LIQUID MIXING (THROUGH FIRST-STAGE SEPARATOR) AND THE SUBSEQUENT REACTION (THROUGH SECOND-STAGE SEPARATOR). THE LIQUID IS DRAWN THROUGH 16 CAPILLARIES OF 20MM WIDE. GÜNTHER ET AL. (2005)..... 77

FIGURE 3.1 COMPARISON OF FLOW PATTERN TRANSITIONS IN HORIZONTAL AND VERTICAL CHANNELS (HASSAN ET AL., 2005). REGIMES IN CAPITAL ARE FOR HORIZONTAL FLOW MAP, AND ONES IN LOWER CASE ARE FOR VERTICAL FLOW MAP. 83

FIGURE 3.2 COMPARISON OF FLOW PATTERN TRANSITIONS IN CIRCULAR CHANNELS WITH DIFFERENT INTERNAL DIAMETERS (COLEMAN AND GARIMELLA, 1999). 84

FIGURE 3.3 COMPARISON OF FLOW PATTERN TRANSITIONS FOR UPWARD FLOW IN TRIANGULAR MINI CHANNELS WITH DIFFERENT HYDRAULIC DIAMETERS (ZHAO AND BI, 2001). REGIME NAMES IN BOLD FONT REFER TO THE 2.886 AND 1.443MM CHANNELS, WHILE NAMES IN NORMAL FONT REFER TO THE 0.886MM CHANNEL. 85

FIGURE 3.4 COMPARISON OF FLOW PATTERN TRANSITIONS IN CIRCULAR ($D = 1.097\text{MM}$) AND SEMI-TRIANGULAR CHANNELS ($D_H = 1.09\text{MM}$) (TRIPLETT ET AL., 1999)..... 86

FIGURE 3.5 EFFECT OF CONTACT ANGLE ON FLOW PATTERN TRANSITIONS FOR AIR-WATER FLOWS (BARAJAS AND PANTON, 1993). $D = 1.6\text{MM}$ 87

FIGURE 3.6 TWO-PHASE FLOW PATTERNS IN A $100\mu\text{M}$ QUARTZ TUBE. IN THE LEFT COLUMN, THE TUBE IS FAIRLY TREATED BY DRAWING ETHANOL THROUGH THE TEST SECTION. IN THE RIGHT COLUMN, THE TUBE IS CAREFULLY TREATED WITH THE COMBINATION OF MECHANICAL CLEANING WITH A SOFT BRUSH AND ULTRASONIC VIBRATION IN A POOL OF HIGH PURITY DISTILLED WATER, ETHANOL AND DILUTE HYDROCHLORIC ACID (SERIZAWA ET AL., 2002). 88

FIGURE 3.7 EFFECT OF WALL WETTABILITY ON FLOW PATTERN MORPHOLOGIES FOR AIR/WATER FLOWS IN A SQUARE CHANNEL WITH $D_H = 525\mu\text{M}$ (CUBAUD ET AL., 2006). THE HYDROPHILIC FLOWS WERE REALISED IN A SILICON CHANNEL WITH GLASS TOP ($\theta \approx 9^\circ$ FOR SILICON AND $\theta \approx 25^\circ$ FOR GLASS); THE HYDROPHOBIC FLOWS WERE REALISED IN THE SAME CHANNEL WITH TEFLON COATING ($\theta \approx 120^\circ$). 89

List of Figures

FIGURE 3.8 EFFECT OF LIQUID SURFACE TENSION AND VISCOSITY ON FLOW PATTERN TRANSITIONS IN A RECTANGULAR MICROCHANNEL WITH HYDRAULIC DIAMETER $D_H = 187.5\mu\text{m}$. THE LINES HAVE BEEN FITTED TO DATA PRESENTED BY WAELCHLI AND VON ROHR (2006). THE TRANSITION BOUNDARIES FOR BUBBLY AND ANNULAR FLOWS HAVE BEEN DRAWN IN THE FIGURE WHILE THE PATTERNS BETWEEN THESE TWO LINES ARE TAYLOR AND TAYLOR-ANNULAR FLOWS. 90

FIGURE 3.9 COMPARISON WITH THE UNIVERSAL FLOW REGIME MAP BY HASSAN ET AL. (2005). LETTERS IN NORMAL, ITALIC AND UNDERSCORE FONTS STAND FOR DATA BY HASSAN ET AL. (2005), YANG AND SHIEH (2001), AND CHUNG AND KAWAJI (2004) RESPECTIVELY. 93

FIGURE 3.10 COMPARISON WITH THE UNIVERSAL FLOW REGIME MAP BY CUBAUD AND HO (2004). LETTERS IN NORMAL, ITALIC AND UNDERSCORE FONTS STAND FOR DATA BY CUBAUD AND HO (2004), YANG AND SHIEH (2001), AND CHUNG AND KAWAJI (2004) RESPECTIVELY. 93

FIGURE 3.11 COMPARISON WITH THE UNIVERSAL FLOW REGIME MAP BY AKBAR ET AL. (2003). LETTERS IN NORMAL, ITALIC AND UNDERSCORE FONTS STAND FOR DATA BY AKBAR ET AL. (2003), YANG AND SHIEH (2001), AND CHUNG AND KAWAJI (2004) RESPECTIVELY. 94

FIGURE 3.12 COMPARISON WITH THE UNIVERSAL FLOW REGIME MAP BY WAELCHLI AND VON ROHR (2006). LETTERS IN NORMAL, ITALIC AND UNDERSCORE FONTS STAND FOR DATA BY WAELCHLI AND VON ROHR (2006), YANG AND SHIEH (2001), AND CHUNG AND KAWAJI (2004) RESPECTIVELY. 94

FIGURE 4.1 INLET CONFIGURATIONS. (A) T; (B) Y; (C) CGP; (D) CLP. G: GAS INLET; L: LIQUID INLET; M: MAIN CHANNEL. 99

FIGURE 4.2 FLOW PATTERNS OBSERVED IN VARIOUS CAPILLARIES AND GAS-LIQUID FLOWRATES. FLOW IS FROM RIGHT TO LEFT. 100

FIGURE 4.3 EFFECT OF INLET SIZE ON FLOW PATTERN TRANSITIONS. $D_C = 0.5\text{MM}$, T INLET CONFIGURATION. COLORED SYMBOLS REPRESENT THE FLOW PATTERNS FOR $D_I = 0.5\text{MM}$. BLACK SOLID LINES REPRESENT THE FLOW PATTERN TRANSITION LINES FOR $D_I = 1.25\text{MM}$ 102

FIGURE 4.4 TAYLOR BUBBLE VOLUME FOR DIFFERENT INLET SIZES. $D_C = 0.5\text{MM}$, $U_{GS} = 0.761\text{M/S}$, T INLET CONFIGURATION. 102

FIGURE 4.5 EFFECT OF INLET SIZE ON FLOW PATTERN TRANSITIONS. $D_C = 0.75\text{MM}$, T INLET CONFIGURATION. SYMBOLS REPRESENT THE FLOW PATTERNS FOR $D_I = 0.5\text{MM}$. BLACK SOLID LINES REPRESENT THE FLOW PATTERN TRANSITION LINES FOR $D_I = 1.25\text{MM}$ 103

FIGURE 4.6 TAYLOR BUBBLE VOLUME FOR DIFFERENT INLET CONFIGURATIONS SHOWN IN FIGURE 4.1. $D_C = 0.5\text{MM}$, $D_I = 0.5\text{MM}$, $U_{GS} = 0.761\text{M/S}$ 103

FIGURE 4.7 EFFECT OF CAPILLARY SIZE ON FLOW PATTERN TRANSITIONS. $D_I = 0.5\text{MM}$, T INLET CONFIGURATION. SYMBOLS REPRESENT FLOW PATTERNS FOR $D_C = 0.5\text{MM}$. BLACK SOLID LINES REPRESENT THE TRANSITION LINES FOR $D_C = 0.75\text{MM}$ 104

FIGURE 4.8 TAYLOR BUBBLE VOLUME FOR DIFFERENT CAPILLARY SIZES. $D_I = 0.5\text{MM}$, $Q_G = 8.96\text{M/S}$, T INLET CONFIGURATION. 105

FIGURE 4.9 COMPARISON OF FLOW PATTERN TRANSITIONS WITH THE LITERATURE UNIVERSAL FLOW REGIME MAPS BY (A) AKBAR ET AL. (2003), (B) CUBAUD AND HO (2004) AND (C) HASSAN ET AL. (2005). $D_I = 0.5\text{MM}$, T INLET CONFIGURATION. SYMBOLS IN PLAIN, ITALIC AND UNDERLINED ARE FOR

List of Figures

THE LITERATURE, FLOWS IN 0.5MM CAPILLARY AND FLOWS IN 0.75MM CAPILLARY RESPECTIVELY.
 107

FIGURE 5.1 THE SOLUTION DOMAIN WITH ITS BOUNDARY CONDITIONS. 113

FIGURE 5.2 BUBBLE FORMATION IN AIR-WATER SYSTEM WITH $\theta = 0^\circ$. $D_C = 1\text{MM}$, $D_N = 0.11\text{MM}$, $U_{GS} = 0.0155\text{M/S}$, $U_{LS} = 0.02\text{M/S}$, AT TIMES A: 0.0014S, B: 0.007S, C: 0.014S, D: 0.028S, E: 0.0322S, F: 0.0378S, G: 0.0392S. 116

FIGURE 5.3 BUBBLE FORMATION IN AIR-WATER SYSTEM WITH $\theta = 180^\circ$. $D_C = 1\text{MM}$, $D_N = 0.11\text{MM}$, $U_{GS} = 0.0155\text{M/S}$, $U_{LS} = 0.02\text{M/S}$, AT TIMES A: 0.0014S, B: 0.007S, C: 0.021S, D: 0.035S, E: 0.0406S, F: 0.0434S AND G: 0.0462S. 116

FIGURE 5.4 THE MOVEMENT OF THE THREE PHASE CONTACT LINE ON THE TOP WALL OF THE NOZZLE DURING BUBBLE FORMATION AT VERY LOW GAS FLOWRATES. 117

FIGURE 5.5 EFFECT OF GAS VELOCITY ON BUBBLE VOLUME. $D_C = 1\text{MM}$, $D_N = 0.11\text{MM}$, $U_{LS} = 0.02\text{M/S}$, $\theta = 0^\circ$, AIR-WATER SYSTEM. 119

FIGURE 5.6 EFFECT OF LIQUID VELOCITY ON BUBBLE VOLUME. $D_C = 1\text{MM}$, $D_N = 0.11\text{MM}$, $U_{GS} = 0.0294\text{M/S}$, $\theta = 0^\circ$, AIR-WATER SYSTEM. 119

FIGURE 5.7 EFFECT OF FLUID PROPERTY ON BUBBLE VOLUME. $D_C = 1\text{MM}$, $D_N = 0.34\text{MM}$, $U_{LS} = 0.02\text{M/S}$, $\theta = 0^\circ$ 120

FIGURE 5.8 EFFECT OF GAS NOZZLE SIZE ON BUBBLE VOLUME. $D_C = 1\text{MM}$, $U_{LS} = 0.02\text{M/S}$, $\theta = 0^\circ$, AIR-WATER SYSTEM. 120

FIGURE 5.9 EFFECT OF WALL THICKNESS ON BUBBLE VOLUME. CASE 1: $U_{GS} = 0.0329\text{M/S}$, $U_{LS} = 0.02\text{M/S}$; CASE 2: $U_{GS} = 0.0294\text{M/S}$, $U_{LS} = 0.01\text{M/S}$. $D_C = 1\text{MM}$, $D_N = 0.11\text{MM}$, $\theta = 0^\circ$, AIR-WATER SYSTEM. 121

FIGURE 5.10 EFFECT OF CONTACT ANGLE ON BUBBLE VOLUME: (A) $\theta = 0^\circ$, $V_B = 0.773 \times 10^{-9}\text{M}^3$; (B) $\theta = 60^\circ$, $V_B = 0.829 \times 10^{-9}\text{M}^3$; (C) $\theta = 180^\circ$. $D_C = 1\text{MM}$, $D_N = 0.11\text{MM}$, $U_{GS} = 0.0155\text{M/S}$, $U_{LS} = 0.02\text{M/S}$, $T = 0.03\text{S}$, AIR-WATER SYSTEM. 122

FIGURE 5.11 COMPARISON OF SIMULATED DIMENSIONLESS BUBBLE LENGTHS WITH THOSE PREDICTED BY LITERATURE CORRELATIONS. 124

FIGURE 6.1 LAYOUT OF A REACTOR CHIP AND THE BONDING JIG FOR DIFFUSION BONDING. 129

FIGURE 6.2 PHOTOGRAPHS OF CHANNEL BOTTOM UNDER DIFFERENT ENGRAVING CONDITIONS. CUTTER TIP SIZE: 0.1MM, CHANNEL DEPTH: 0.5MM. 130

FIGURE 6.3 AVERAGE TOP AND BOTTOM WIDTH AND THE DETERMINED CHANNEL DEPTH FOR CHANNELS ENGRAVED UNDER THE SAME CONDITIONS. CUTTER TIP: 0.5MM, CHANNEL DEPTH: 0.5MM. 131

FIGURE 6.4 (A) CUTTER SHAPE (MASTERGRAVE LTD, THE SUPPLIER) AND (B) THE PRODUCED CHANNEL CROSS SECTION PROFILE. W AND H ARE CHANNEL BOTTOM WIDTH AND CHANNEL DEPTH RESPECTIVELY. 132

FIGURE 6.5 INLET CONFIGURATIONS USED IN THE INLET DESIGN STUDY. 133

FIGURE 6.6 EXPERIMENTAL SCHEMATIC FOR THE INVESTIGATION OF MICROREACTOR INLET DESIGN. 134

FIGURE 6.7 DIMENSIONLESS BUBBLE LENGTH OBTAINED UNDER DIFFERENT TESTING SCENARIA. (A) AIR/WATER SYSTEM; (B) AIR/OCTANE SYSTEM. $Q_G = 0.932\text{ML/MIN}$ 135

FIGURE 6.8 BUBBLE SIZE STANDARD DEVIATION UNDER DIFFERENT TESTING SCENARIA. $Q_G = 0.932\text{ML/MIN}$ 136

List of Figures

FIGURE 6.9 INLET CONFIGURATIONS USED IN THE PARAMETRIC STUDY ON BUBBLE SIZES. (A) T-JUNCTION;
 (B) Y-JUNCTION; (C) M-JUNCTION. 137

FIGURE 6.10 EFFECT OF INLET ORIENTATION ON BUBBLE LENGTH. $Q_G = 3.26\text{ML}/\text{MIN}$, $D_H = 0.577\text{MM}$, $D_{H,GIN} = 0.577\text{MM}$, $D_{H,LIN} = 0.577\text{MM}$, LIQUID PHASE: WATER, INLET CONFIGURATION: T-JUNCTION. V: VERTICAL; H_G_UPPER: HORIZONTAL WITH GAS PHASE IN THE UPPER INLET; H_L_UPPER: HORIZONTAL WITH LIQUID PHASE IN THE UPPER INLET. 138

FIGURE 6.11 EFFECT OF GAS AND LIQUID FLOWRATE ON (A) BUBBLE LENGTH AND (B) UNIT CELL FREQUENCY. $D_H = 0.577\text{MM}$, $D_{H,GIN} = 0.577\text{MM}$, $D_{H,LIN} = 0.577\text{MM}$, LIQUID PHASE: WATER, INLET CONFIGURATION: Y-JUNCTION, ORIENTATION: VERTICAL UPFLOW..... 139

FIGURE 6.12 EFFECT OF LIQUID PHASE SURFACE TENSION ON BUBBLE LENGTH. (A) $D_H = 0.345\text{MM}$; (B) $D_H = 0.577\text{MM}$; (C) $D_H = 0.816\text{MM}$. $Q_G = 1.56\text{ML}/\text{MIN}$, $D_{H,GIN} = 0.577\text{MM}$, $D_{H,LIN} = 0.577\text{MM}$, INLET CONFIGURATION: T-JUNCTION, ORIENTATION: HORIZONTAL. 141

FIGURE 6.13 EFFECT OF GAS INLET SIZE ON BUBBLE LENGTH. $Q_G: 1.56\text{ML}/\text{MIN}$, $D_H = 0.577\text{MM}$, $D_{H,LIN} = 0.577\text{MM}$, LIQUID: OCTANE, INLET CONFIGURATION: T-JUNCTION, ORIENTATION: HORIZONTAL. 141

FIGURE 6.14 EFFECT OF MAIN CHANNEL SIZE ON BUBBLE LENGTH (A) AND UNIT CELL FREQUENCY (B). $Q_G: 1.56\text{ML}/\text{MIN}$, $D_{H,GIN} = 0.577\text{MM}$, $D_{H,LIN} = 0.577\text{MM}$, LIQUID: WATER, INLET CONFIGURATION: T-JUNCTION, ORIENTATION: HORIZONTAL. 143

FIGURE 6.15 BUBBLE LENGTHS UNDER DIFFERENT INLET CONFIGURATIONS. $Q_G: 1.56\text{ML}/\text{MIN}$, $D_H = 0.577\text{MM}$, $D_{H,LIN} = 0.577\text{MM}$, ORIENTATION: HORIZONTAL FOR THE MAIN CHANNEL..... 147

FIGURE 6.16 COMPARISON OF BUBBLE LENGTHS CALCULATED FROM LITERATURE CORRELATIONS AND EXPERIMENTAL RECORDED UNIT CELL FREQUENCY. $Q_G: 0.62\sim 3.26\text{ML}/\text{MIN}$, $Q_L: 2\sim 18\mu\text{L}/\text{S}$, $D_H: 0.345\sim 0.816\text{MM}$, $D_{H,GIN}: 0.345\sim 0.816\text{MM}$, LIQUID: WATER AND OCTANE, INLET CONFIGURATION: T-JUNCTION, ORIENTATION: HORIZONTAL. 149

FIGURE 6.17 COMPARISON BETWEEN EXPERIMENTALLY RECORDED UNIT CELL FREQUENCIES AND PREDICTED ONES USING EQ. 6.1 AND EQ. 6.2..... 149

FIGURE 6.18 COMPARISON OF BUBBLE LENGTHS MEASURED FROM EXPERIMENTAL IMAGES WITH THOSE CALCULATED FROM EQ. 6.1 AND EQ. 6.2. $Q_G: 0.62\sim 3.26\text{ML}/\text{MIN}$, $Q_L: 2\sim 18\mu\text{L}/\text{S}$, $D_H: 0.345\sim 0.816\text{MM}$, $D_{H,GIN}: 0.345\sim 0.816\text{MM}$, LIQUID: WATER AND OCTANE, ORIENTATION: HORIZONTAL. 150

FIGURE 6.19 COMPARISON BETWEEN SIMULATED BUBBLE LENGTHS (QIAN AND LAWAL, 2006) WITH THOSE CALCULATED FROM EQ. 6.1 AND EQ. 6.2. $U_{GS}: 0.05\sim 0.1\text{M}/\text{S}$, $U_{LS}: 0.02\sim 0.2\text{M}/\text{S}$, $D: 3\text{MM}$, $D_{GIN}: 3\text{MM}$, LIQUID: WATER, ORIENTATION: VERTICAL, INLET: T-JUNCTION. 150

FIGURE 7.1 SERIES I REACTOR DESIGN – WITHOUT REACTION QUENCHING CHANNEL. (A) STRAIGHT CHANNEL; (B) MEANDERING CHANNEL; (C) BIFURCATING CHANNEL. 158

FIGURE 7.2 SERIES II REACTOR DESIGN – WITH REACTION QUENCHING CHANNEL. 160

FIGURE 7.3 SCHEMATIC EXPERIMENTAL SET UP FOR THE INVESTIGATION OF MASS TRANSFER AND REACTION IN TAYLOR FLOW MICROREACTORS. 161

FIGURE 7.4 GEOMETRY AND BOUNDARIES OF THE COMPUTATIONAL DOMAIN 163

FIGURE 7.5 CO₂ CONVERSION COMPARISON BETWEEN EXPERIMENTAL AND NUMERICAL RESULTS IN SERIES I STRAIGHT CHANNEL REACTORS. 168

List of Figures

FIGURE 7.6 EXPERIMENTAL CO₂ CONVERSIONS IN SERIES I STRUCTURED REACTORS. $D_H = 0.331\text{MM}$, $Q_L = 0.12\text{ML/MIN}$, $Q_G = 0.37\text{-}1.12\text{ML/MIN}$ 169

FIGURE 7.7 EXPERIMENTAL AND SIMULATION RESULTS FOR SERIES II STRAIGHT CHANNEL REACTORS. $D_H = 0.577\text{MM}$; $Q_G = 1.407\text{ML/MIN}$ 174

FIGURE 7.8 POINT NAOH CONCENTRATION IN THE UPPER AND LOWER PART OF THE BUBBLE SIDE FILM IN A SERIES II STRAIGHT CHANNEL REACTOR. $(x-0.5D_B)/A = 0.33$, $D_H = 0.577\text{MM}$, $Q_G = 1.407\text{ML/MIN}$, $Q_L = 5\text{ML/S}$ 174

FIGURE 7.9 SIMULATION RESULTS FOR A SERIES II STRAIGHT CHANNEL REACTOR. $D_H = 0.577\text{MM}$, $Q_G = 1.407\text{ML/MIN}$, $Q_L = 20\text{ML/S}$. (A) AVERAGE CONCENTRATIONS CHANGE WITH TIME; (B) CO₂ CONCENTRATION PROFILE IN THE GAS BUBBLE. 175

FIGURE 7.10 EFFECT OF RESIDENCE TIME ON REACTION CONVERSION IN SERIES II STRAIGHT CHANNEL REACTORS WITH VARIOUS CHARACTERISTIC DIMENSIONS. $Q_G = 1.407\text{ML/MIN}$, $Q_L = 20\text{ML/MIN}$ 176

FIGURE 7.11 EXPERIMENTAL CONVERSIONS IN SERIES II STRAIGHT AND CIRCULAR MEANDERING CHANNEL REACTORS. $Q_G = 1.407\text{ML/MIN}$, $Q_L = 5, 10, 15, 20\text{ML/MIN}$, $L = 20\text{MM}$ 177

FIGURE 7.12 EXPERIMENTAL CONVERSIONS IN SERIES II STRAIGHT AND ELLIPTICAL MEANDERING CHANNEL REACTORS. $Q_G = 1.407\text{ML/MIN}$, $Q_L = 5, 10, 15, 20\text{ML/MIN}$, $L = 50\text{MM}$, $A = 1.4\text{MM}$ 177

FIGURE 7.13 BUBBLE FORMATION TIME t_B IN SERIES II CIRCULAR MEANDERING CHANNEL REACTORS. $Q_G = 1.407\text{ML/MIN}$, $Q_L = 5, 10, 15, 20\text{ML/MIN}$, $L = 20\text{MM}$ 178

FIGURE 8.1 EFFECT OF BUBBLE VELOCITY ON LIQUID UTILISATION INDEX AND CO₂ ABSORPTION FRACTION. $D = 0.5\text{MM}$, $L_S = 0.26\text{MM}$, $L_B = 0.25\text{MM}$, $L_{UC} = 1\text{MM}$, $A = 5\text{MM}$, $T = 0.05\text{S}$. CASE NO. 1-4. 187

FIGURE 8.2 EFFECT OF BUBBLE LENGTH ON LIQUID UTILIZATION INDEX AND CO₂ ABSORPTION FRACTION. $D = 0.5\text{MM}$, $U_B = 0.05\text{M/S}$, $L_S = 0.26\text{MM}$, $A = 5\text{MM}$, $T = 0.05\text{S}$. CASE NO. 3, 5 AND 6. 190

FIGURE 8.3 EFFECT OF SLUG LENGTH ON LIQUID UTILIZATION INDEX AND CO₂ ABSORPTION FRACTION. $D = 0.5\text{MM}$, $U_B = 0.05\text{M/S}$, $L_B = 0.25\text{MM}$, $A = 5\text{MM}$, $T = 0.05\text{S}$. CASE NO. 3, 7 AND 8. 191

FIGURE 8.4 EFFECT OF FILM THICKNESS ON LIQUID UTILIZATION INDEX AND CO₂ ABSORPTION FRACTION. $D = 0.5\text{MM}$, $U_B = 0.05\text{M/S}$, $L_S = 0.26\text{MM}$, $L_B = 2\text{MM}$, $T = 0.05\text{S}$. CASE NO. 5, 9 AND 10. 192

FIGURE 8.5 STREAMLINE PLOT IN LIQUID SLUG FOR CASES WITH DIFFERENT FILM THICKNESS. $A = 1\text{MM}$ (A), 5MM (B) AND 50MM (C). $D = 0.5\text{MM}$, $U_B = 0.05\text{M/S}$, $L_S = 0.26\text{MM}$, $L_B = 2\text{MM}$, $T = 0.05\text{S}$. CASE NO. 5, 9 AND 10. 193

FIGURE 8.6 TRANSVERSAL CO₂ CONCENTRATION PROFILE FOR CASES WITH DIFFERENT FILM THICKNESS. $D = 0.5\text{MM}$, $U_B = 0.05\text{M/S}$, $L_S = 0.26\text{MM}$, $L_B = 2\text{MM}$, $T = 0.05\text{S}$. CASE NO. 5, 9 AND 10. 194

FIGURE 8.7 EFFECT OF UNIT CELL LENGTH ON LIQUID UTILIZATION INDEX AND CO₂ ABSORPTION FRACTION. $D = 0.5\text{MM}$, $U_B = 0.05\text{M/S}$, $E_B = 0.55$, $A = 5\text{MM}$, $T = 0.05\text{S}$. CASE NO. 3, 11 AND 12. 195

FIGURE 8.8 EFFECT OF CHANNEL DIMENSION ON LIQUID UTILIZATION INDEX AND CO₂ ABSORPTION FRACTION. $U_B = 0.05\text{M/S}$, $E_B = 0.55$, $V_{UC} = 0.196\text{ML}$, $T = 0.05\text{S}$. CASE NO. 3 AND 13. 196

FIGURE 8.9 THE COMPARISON OF K_{LA} BETWEEN SIMULATION RESULTS (TABLE 8.2) AND PREDICTIONS BY LITERATURE CORRELATIONS (EQ. 2.23-EQ. 2.26). $T = 0.05\text{S}$ 197

FIGURE 9.1 CONVENTIONAL PROCESS FLOW DIAGRAM OF CO₂ REMOVAL AND RECOVERY. 204

FIGURE 9.2. POSSIBLE FLOW PATTERNS FOR THE SYSTEM UNDER INVESTIGATION. BASED ON THE FLOW MAP OF TRIPLETT ET AL. (1999). 206

List of Figures

FIGURE 9.3. REPRESENTATIVE TAYLOR BUBBLE CAPTURED IN A SYSTEM WITH SIMILAR OPERATING FLOWRATES. $D = 1\text{MM}$, $20\text{VOL}\% \text{CO}_2$, 0.2M NAOH , $U_{GS} = 0.17\text{M/S}$, $U_{LS}/U_{GS} = 0.052$ 207

FIGURE 9.4. 3D VIEW OF A FALLING FILM MICROREACTOR THAT CONSISTS OF A NUMBER OF PLATES OF 4M WIDTH, ZERO THICKNESS AND ADJUSTABLE HEIGHT, WHICH ARE PACKED IN PARALLEL..... 212

FIGURE 9.5. SIMULATION DOMAINS AND BOUNDARIES FOR THE FALLING FILM MICROREACTOR. THE SCALE HAS BEEN ADJUSTED FOR BETTER VISUALIZATION..... 212

FIGURE 9.6 MODEL VALIDATION USING THE EXPERIMENTAL AND ANALYTICAL MODELLING RESULTS FROM ZANFIR ET AL. (2005)..... 214

FIGURE 9.7 CO_2 CONVERSION AT DIFFERENT GAS RESIDENCE TIME IN BOTH CO- AND COUNTER-CURRENTLY OPERATED FALLING FILM REACTOR. $\Delta_G = 1\text{MM}$, $\Delta_L = 218\mu\text{M}$, $K_I = 18.1\text{M}^3/(\text{KMOL S})$, $C_{\text{MDEA},0} = 4.578\text{KMOL/M}^3$, $Q_L = 0.194\text{M}^3/\text{S}$, $Q_G = 3.954\text{M}^3/\text{S}$ 215

FIGURE 9.8 TRANSVERSAL CONCENTRATION PROFILES IN COUNTERCURRENT FALLING FILM REACTOR AT DIFFERENT REACTOR HEIGHT. (A) $C_{\text{CO}_2(\text{G})}$; (B) $C_{\text{CO}_2(\text{L})}$; (C) C_{MDEA} . $\Delta_G = 1\text{MM}$, $\Delta_L = 218\mu\text{M}$, $H = 10\text{M}$, $K_I = 18.1\text{M}^3/(\text{KMOL S})$, $C_{\text{MDEA},0} = 4.578\text{KMOL/M}^3$, $Q_L = 0.194\text{M}^3/\text{S}$, $Q_G = 3.954\text{M}^3/\text{S}$ 217

FIGURE 9.9 TRANSVERSE CO_2 PROFILES AT REACTOR OUTLET FOR VARIOUS FILM THICKNESSES. $\Delta_G = 1\text{MM}$, $H = 1\text{M}$, $K_I = 18.1\text{M}^3/(\text{KMOL S})$, $C_{\text{MDEA},0} = 4.578\text{KMOL/M}^3$, $Q_L = 0.194\text{M}^3/\text{S}$, $Q_G = 3.954\text{M}^3/\text{S}$ 219

FIGURE 9.10 EFFECT OF GAS CHAMBER SIZE ON CO_2 CONVERSION IN FALLING FILM REACTOR. $H = 1\text{M}$, $K_I = 18.1\text{M}^3/(\text{KMOL S})$, $C_{\text{MDEA},0} = 4.578\text{KMOL/M}^3$, $Q_L = 0.194\text{M}^3/\text{S}$, $Q_G = 3.954\text{M}^3/\text{S}$ 220

FIGURE 9.11. EFFECT OF MDEA CONCENTRATION ON CO_2 CONVERSION. $\Delta_G = 1\text{MM}$, $\Delta_L = 218\mu\text{M}$, $H = 1\text{M}$, $K_I = 18.1\text{M}^3/(\text{KMOL S})$, $Q_L = 0.194\text{M}^3/\text{S}$, $Q_G = 3.954\text{M}^3/\text{S}$, $P = 67.46\text{ATM}$, $T = 320.4\text{K}$ 220

FIGURE 9.12 TRANSVERSE DIMENSIONLESS CO_2 PROFILES AT LIQUID PHASE OUTLET FOR VARIOUS INLET MDEA CONCENTRATIONS. $\Delta_G = 1\text{MM}$, $\Delta_L = 218\mu\text{M}$, $H = 1\text{M}$, $K_I = 18\text{M}^3/(\text{KMOL S})$, $Q_L = 0.194\text{M}^3/\text{S}$, $Q_G = 3.954\text{M}^3/\text{S}$, $P = 67.46\text{ATM}$, $T = 320.4\text{K}$ 221

FIGURE 9.13 EFFECT OF REACTION RATE CONSTANT ON CO_2 CONVERSION. $\Delta_G = 1\text{MM}$, $\Delta_L = 218\mu\text{M}$, $H = 1\text{M}$, $C_{\text{MDEA}} = 4.578\text{KMOL/M}^3$, $Q_L = 0.194\text{M}^3/\text{S}$, $Q_G = 3.954\text{M}^3/\text{S}$ 222

FIGURE 9.14 CO_2 CONVERSION AS A FUNCTION OF GAS PHASE RESIDENCE TIME FOR VARIOUS REACTION RATE CONSTANT. $\Delta_G = 1\text{MM}$, $\Delta_L = 218\mu\text{M}$, $C_{\text{MDEA},0} = 4.578\text{KMOL/M}^3$, $Q_L = 0.194\text{M}^3/\text{S}$, $Q_G = 3.954\text{M}^3/\text{S}$ 222

FIGURE 9.15 BASE CASE CONVERSIONS IN THE FALLING FILM REACTOR FOR BOTH CO- AND COUNTER-CURRENT OPERATIONS. $D = 1\text{MM}$, $\Delta_L = 173\mu\text{M}$, $C_{\text{MDEA},0} = 4.578\text{KMOL/M}^3$, $K_I = 180\text{M}^3/(\text{KMOL S})$, $Q_L = 0.194\text{M}^3/\text{S}$, $Q_G = 3.954\text{M}^3/\text{S}$ 224

FIGURE 9.16 PLOT OF TRANSVERSAL AND AXIAL CONCENTRATION PROFILES IN THE BASE CASE OF THE FALLING FILM REACTOR FOR COUNTERCURRENT OPERATION. (A) TRANSVERSAL $C_{\text{CO}_2(\text{G})}$; (B) TRANSVERSAL $C_{\text{CO}_2(\text{L})}$; (C) TRANSVERSAL C_{MDEA} ; (D) AXIAL $C_{\text{CO}_2(\text{G})}$, $C_{\text{CO}_2(\text{L})}$, AND C_{MDEA} . $D = 1\text{MM}$, $H = 1.4\text{M}$, $C_{\text{MDEA},0} = 4.578\text{KMOL/M}^3$, $K_I = 180\text{M}^3/(\text{KMOL S})$, $Q_L = 0.194\text{M}^3/\text{S}$, $Q_G = 3.954\text{M}^3/\text{S}$ 226

FIGURE 9.17 CONVERSIONS IN COUNTERCURRENT FALLING FILM REACTORS OPERATED UNDER DIFFERENT LIQUID VISCOSITY. $D = 1\text{MM}$, $C_{\text{MDEA},0} = 4.578\text{KMOL/M}^3$, $K_I = 180\text{M}^3/(\text{KMOL S})$, $Q_L = 0.194\text{M}^3/\text{S}$, $Q_G = 3.954\text{M}^3/\text{S}$ 227

FIGURE 9.18 3D VIEW OF A TAYLOR FLOW MICROREACTOR, CONSISTING OF BUNDLES OF CIRCULAR MICROCHANNELS..... 228

List of Figures

FIGURE 9.19 2D SOLUTION DOMAIN FOR TAYLOR FLOW MICROREACTORS. THE SCALE HAS BEEN MODIFIED TO PROVIDE CLEARER VISUALIZATION. THE DOTTED LINE SHOWS THE LOCATION THAT CONCENTRATION PROFILES ARE PLOTTED IN LATER STUDY.	229
FIGURE 9.20 REACTION CONVERSION CHANGES WITH REACTOR HEIGHT FOR THE BASE CASE OF TAYLOR FLOW REACTOR. $D = 1\text{MM}$, $C_{MDEA,0} = 4.578\text{KMOL}/\text{M}^3$, $K_I = 180\text{M}^3/(\text{KMOL S})$	231
FIGURE 9.21 TRANSVERSAL CONCENTRATION PROFILES ALONG THE MIDDLE CROSS SECTION OF THE UNIT CELL FOR THE BASE CASE OF TAYLOR FLOW REACTOR. (A) $C_{CO_2(G)}$; (B) $C_{CO_2(L)}$; (C) C_{MDEA} . $D = 1\text{MM}$, $C_{MDEA,0} = 4.578\text{KMOL}/\text{M}^3$, $K_I = 180\text{M}^3/(\text{KMOL S})$	233
FIGURE 9.22 SCHEMATIC OF TWO STAGE ABSORPTION WITH REACTORS ARRANGED IN A VIRTUALLY COUNTERCURRENT WAY.	234
FIGURE 9.23 CONVERSION CHANGES WITH REACTOR HEIGHT FOR A TWO-STAGE CO_2 ABSORPTION IN TAYLOR FLOW REACTORS.	234
FIGURE 9.24 TIME TO ACHIEVE 95% \bar{X}_E AS A FUNCTION OF THE SPECIFIC AREA FOR VARIOUS BUBBLE LENGTHS IN TAYLOR FLOW REACTORS.	235
FIGURE 9.25 CONCENTRATION PROFILE OF CO_2 IN LIQUID PHASE AND VELOCITY PLOT. (A) BASE CASE WITH COLOUR SCALE RANGES FROM 2.349 (BLUE) TO 2.386 (RED); (B) $Q_G/Q_L = 1$ WITH COLOUR SCALE RANGES FROM 4.613E-3 (BLUE) TO 5.78E-3 (RED).	237
FIGURE 9.26 CONVERSION CHANGES WITH REACTOR HEIGHT WHEN LIQUID CONVECTION IS OR IS NOT SOLVED. (A) BASE CASE; (B) $Q_G/Q_L = 1$	238
FIGURE 9.27 CONVERSION CHANGES WITH REACTOR HEIGHT FOR VARIOUS Q_G/Q_L IN TAYLOR FLOW REACTOR. $D = 1\text{MM}$, $C_{MDEA,0} = 4.578\text{KMOL}/\text{M}^3$, $K_I = 180\text{M}^3/(\text{KMOL S})$	238
FIGURE 9.28 CONVERSION CHANGES WITH REACTOR HEIGHT FOR TAYLOR FLOW REACTOR OF DIFFERENT CHANNEL SIZE. $C_{MDEA,0} = 4.578\text{KMOL}/\text{M}^3$, $K_I = 180\text{M}^3/(\text{KMOL S})$	239
FIGURE 9.29 SIMULATION DOMAINS FOR AN ANNULAR FLOW REACTOR. THE SCALE HAS BEEN ADJUSTED FOR BETTER VISUALIZATION.	240
FIGURE 9.30 BASE CASE CONVERSION CHANGES WITH ANNULAR FLOW REACTOR HEIGHT. $D = 1\text{MM}$, $C_{MDEA,0} = 4.578\text{KMOL}/\text{M}^3$, $K_I = 180\text{M}^3/(\text{KMOL S})$, $Q_G = 3.954\text{M}^3/\text{S}$, $Q_L = 0.19\text{M}^3/\text{S}$	241
FIGURE 9.31 TRANSVERSAL AND AXIAL REACTANTS CONCENTRATION FOR THE BASE CASE IN ANNULAR FLOW REACTOR. (A) $C_{CO_2(G)}$; (B) $C_{CO_2(L)}$; (C) C_{MDEA} ; (D) $C_{CO_2(G)}$, $C_{CO_2(L)}$, AND C_{MDEA} . $D = 1\text{MM}$, $C_{MDEA,0} = 4.578\text{KMOL}/\text{M}^3$, $K_I = 180\text{M}^3/(\text{KMOL S})$	243
FIGURE 9.32 CONVERSION CHANGES WITH REACTOR HEIGHT FOR A TWO-STAGE ABSORPTION PROCESS IN ANNULAR FLOW REACTOR. WITH $D = 1\text{MM}$, $C_{MDEA,0} = 4.578\text{KMOL}/\text{M}^3$, $K_I = 180\text{M}^3/(\text{KMOL S})$	243
FIGURE 9.33 CONVERSIONS IN ANNULAR FLOW REACTOR WITH VARIOUS FILM THICKNESSES. $D = 1\text{MM}$, $C_{MDEA,0} = 4.578\text{KMOL}/\text{M}^3$, $K_I = 180\text{M}^3/(\text{KMOL S})$, $Q_L = 0.194\text{M}^3/\text{S}$, $Q_G = 3.954\text{M}^3/\text{S}$. (A) CONVERSION CHANGES WITH REACTOR HEIGHT; (B) TRANSVERSAL CO_2 CONCENTRATION IN LIQUID PHASE AT A REACTOR HEIGHT OF 0.2M.	245
FIGURE 9.34 CONVERSION CHANGES WITH REACTOR HEIGHT FOR THE ANNULAR FLOW REACTOR WITH VARIOUS CHANNEL DIMENSIONS. $C_{MDEA,0} = 4.578\text{KMOL}/\text{M}^3$, $K_I = 180\text{M}^3/(\text{KMOL S})$, $Q_L = 0.194\text{M}^3/\text{S}$, $Q_G = 3.954\text{M}^3/\text{S}$	245

List of Figures

FIGURE 9.35 A PLOT OF REACTOR VOLUME CHANGES WITH SPECIFIC INTERFACIAL AREA. THE DATA ARE FROM THE BASE CASE FOR EACH REACTOR TYPE. $D = 1\text{MM}$, $C_{MDEA,0} = 4.578\text{KMOL}/\text{M}^3$, $K_1 = 180\text{M}^3/(\text{KMOL S})$, $Q_L = 0.194\text{M}^3/\text{s}$, $Q_G = 3.954\text{M}^3/\text{s}$ 247

List of Tables

TABLE 2.1 LITERATURE ON GAS-LIQUID TWO-PHASE FLOWS IN MINI- AND MICROCHANNELS.	38
TABLE 2.2 WETTABILITY AT DIFFERENT θ VALUES.....	46
TABLE 2.3 LITERATURE CORRELATIONS ON BUBBLE/SLUG LENGTHS IN TAYLOR FLOW.....	52
TABLE 5.1 SIMULATION PARAMETERS USED FOR THE INVESTIGATION OF TAYLOR FLOW FORMATION	112
TABLE 5.2 FLUID PROPERTIES USED IN THE SIMULATIONS OF TAYLOR FLOW FORMATION	112
TABLE 5.3 CONDITIONS USED IN LITERATURE AND THIS WORK FOR DETERMINING BUBBLE LENGTH	123
TABLE 6.1 TESTING SCENARIOS IN THE INLET DESIGN STUDY.	133
TABLE 7.1 VALUES OF H_I IN CALCULATING AT 298K	157
TABLE 7.2 DIMENSIONS OF SINGLE CHANNEL MICROREACTORS IN DESIGN SERIES I AND II.....	160
TABLE 7.3 OPERATING CONDITIONS USED IN THE CO ₂ ABSORPTION EXPERIMENT	161
TABLE 7.4 2D DIMENSIONAL MODEL DETAILS IN GAS DOMAIN FOR THE TAYLOR FLOW REACTOR.....	163
TABLE 7.5 EXPERIMENTAL CONDITIONS AND RESULTS FOR SERIES I REACTORS OF DIFFERENT STRUCTURES. $Q_L = 2\text{ML/S}$, $D_H = 0.331\text{MM}$, $Y_{\text{CO}_2,\text{IN}}\% = 21.75\%$	166
TABLE 7.6 FLOW GEOMETRIC VALUES USED IN THE SIMULATIONS OF SERIES I STRAIGHT CHANNELS, $Y_{\text{CO}_2,\text{IN}}\%$ $= 21.75\%$	167
TABLE 7.7 EXPERIMENTAL CONDITIONS AND RESULTS FOR SERIES II CHANNELS OF DIFFERENT STRUCTURES. $Q_G = 1.4067\text{ML/MIN}$, $D_H = 0.577\text{MM}$, $Y_{\text{CO}_2,\text{IN}}\% = 23\%$	171
TABLE 7.8 FLOW GEOMETRIC VALUES USED IN THE SIMULATIONS OF SERIES II STRAIGHT CHANNELS. $Y_{\text{CO}_2,\text{IN}}\%$ $= 23\%$	172
TABLE 8.1 REACTION CONDITIONS FOR THE NUMERICAL PARAMETRIC STUDY OF TAYLOR FLOW MICROREACTOR.....	183
TABLE 8.2 SIMULATION PARAMETERS, MASS TRANSFER COEFFICIENT AND THE ENHANCEMENT FACTOR FOR VARIOUS CASES. $Y_{\text{CO}_2,\text{IN}} = 5\%$, $C_{\text{NaOH},\text{IN}} = 0.2\text{M}$, $T = 0.05\text{S}$	185
TABLE 8.3 EXAMPLE CO ₂ CONCENTRATION PROFILES. CASE NO. 3.....	188
TABLE 9.1 ADVANTAGES AND DISADVANTAGES FOR VARIOUS AMINES USED IN CO ₂ ABSORPTION.....	203
TABLE 9.2 GAS AND LIQUID FLOW CONDITIONS THAT FEED TO THE CO ₂ ABSORBER.....	206
TABLE 9.3. COEFFICIENTS IN EQ. 9.5 USED TO CALCULATE K_f FOR MDEA KINETICS.....	208
TABLE 9.4. OPERATING CONDITIONS FOR THE REACTION SYSTEM	210
TABLE 9.5 2D MODEL DETAILS IN LIQUID DOMAIN FOR THE FALLING FILM MICROREACTOR.....	213
TABLE 9.6. 2D MODEL DETAILS IN GAS DOMAIN FOR THE FALLING FILM REACTOR.....	214
TABLE 9.7 SENSITIVITY STUDY CASES AND THEIR PARAMETERS FOR THE COUNTERCURRENT FALLING FILM REACTOR. $K_f = 18.1\text{M}^3/(\text{KMOL S})$	218
TABLE 9.8 BASE CASE PARAMETERS FOR COUNTERCURRENT FALLING FILM REACTOR AT ELEVATED REACTION RATE. $K_f = 180\text{M}^3/(\text{KMOL S})$	223

List of Tables

TABLE 9.9 PARAMETERS FOR COUNTERCURRENT FALLING FILM REACTOR AT ENHANCED LIQUID VISCOSITY AND ELEVATED REACTION RATE. $K_I = 180\text{M}^3/(\text{KMOL S})$	227
TABLE 9.10 2D MODEL DETAILS IN LIQUID DOMAIN FOR TAYLOR FLOW REACTORS.	230
TABLE 9.11 2D MODEL DETAILS IN GAS DOMAIN FOR TAYLOR FLOW REACTORS.	230
TABLE 9.12 BASE CASE PARAMETERS FOR TAYLOR FLOW REACTOR AT ELEVATED REACTION RATE. $D = 1\text{MM}$, $C_{MDEA,0} = 4.578\text{KMOL}/\text{M}^3$, $K_I = 180\text{M}^3/(\text{KMOL S})$	231
TABLE 9.13 SIMULATION PARAMETERS FOR CASES WITH DIFFERENT L_B/D_C IN TAYLOR FLOW REACTORS. $D = 1\text{MM}$, $C_{MDEA,0} = 4.578\text{KMOL}/\text{M}^3$, $K_I = 180\text{M}^3/(\text{KMOL S})$, $Q_G = 3.954\text{M}^3/\text{S}$	235
TABLE 9.14 SIMULATION PARAMETERS FOR DIFFERENT Q_G/Q_L SCENARIO IN TAYLOR FLOW REACTORS. $D = 1\text{MM}$, $C_{MDEA,0} = 4.578\text{KMOL}/\text{M}^3$, $K_I = 180\text{M}^3/(\text{KMOL S})$, $Q_G = 3.954\text{M}^3/\text{S}$	236
TABLE 9.15 SIMULATION PARAMETERS IN ANNULAR FLOW REACTOR. $D = 1\text{MM}$, $C_{MDEA,0} = 4.578\text{KMOL}/\text{M}^3$, $K_I = 180\text{M}^3/(\text{KMOL S})$, $Q_G = 3.954\text{M}^3/\text{S}$, $Q_L = 0.19\text{M}^3/\text{S}$	240
TABLE 9.16 PERFORMANCE COMPARISONS FOR THE BASE CASE SCENARIO FOR THE THREE TYPES OF REACTORS. $D = 1\text{MM}$, $C_{MDEA,0} = 4.578\text{KMOL}/\text{M}^3$, $K_I = 180\text{M}^3/(\text{KMOL S})$, $Q_L = 0.194\text{M}^3/\text{S}$, $Q_G = 3.954\text{M}^3/\text{S}$	248

Chapter 1

Thesis Introduction

1.1 Process intensification – Innovation for chemical industry

The main objective of the chemical industry is to deliver products at various scales with high yield, good process control and cost effective. In the current fast changing world, there are increasing demands in new products and applications, which require the chemical industry, the main supplier to other industry sectors, to rely more than ever on the ability to innovate in response to the worldwide changes in market demand and the challenges in maintaining competitiveness. The concept of process intensification is currently re-emerging in academia as well as in industry due to the current trends towards sustainable development but also due to developments in related fields, such as materials science and micro-electro-mechanical systems (MEMS) engineering. A number of definitions of process intensification have been used in literature ([Ramshaw, 1995](#); [Commenge et al., 2005](#); [Becht et al., 2009](#)). The one that can best represent the ideas within this thesis is by [Stankiewicz and Moulijn \(2000\)](#): “Process intensification consists of the development of novel apparatuses and techniques that, compared to those commonly used today, are expected to bring dramatic improvements in manufacturing and processing, substantially decreasing equipment-size/production-capacity ratio, energy consumption, or waste production, and ultimately resulting in cheaper, sustainable technologies”. Their concept is illustrated in Figure 1.1, where the various equipment and methodologies that have been used to achieve process intensification are summarised.

1. Thesis Introduction

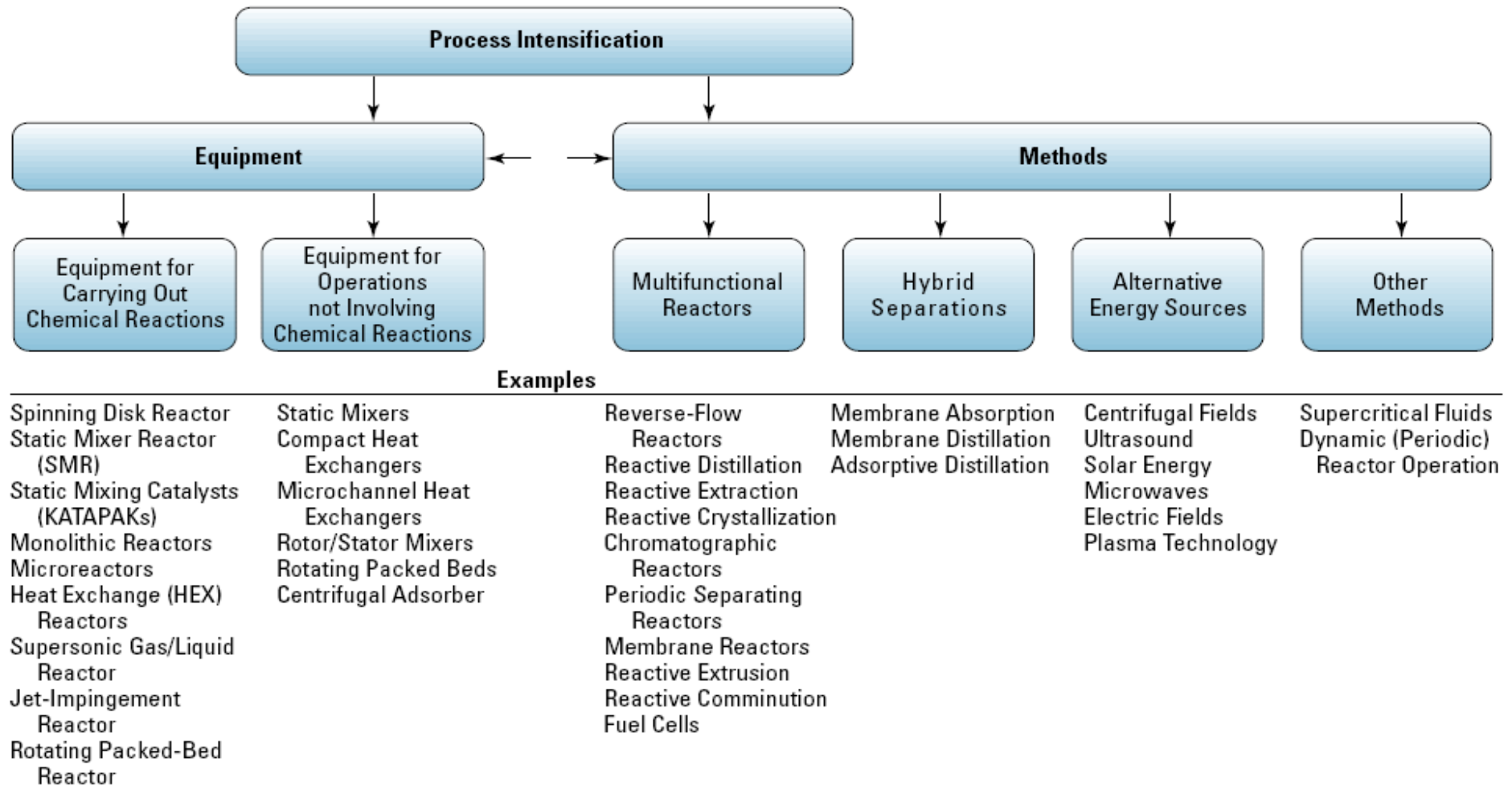


Figure 1.1 Process intensification and its components. Stankiewicz and Moulijn (2000).

1.2 Microstructured reactors – Opportunities and challenges

One way to achieve process intensification is to reduce the size of the units. This is the concept of microstructured reactors that are fabricated using microtechnology and precision engineering and have channels or chambers with internal characteristic dimensions less than 1mm and often in the range of a few hundred microns (Comyns, 2007). The fabrication techniques used as well as the small sizes of these units allow integration of a number of processes such as reactors, gas-liquid separators, and heat exchangers, which makes them suitable for process intensification via the “Methods” shown in Figure 1.1.

In the small spaces of microreactors thin fluid layers form and the surface to volume ratio is large. These key features significantly enhance the heat and mass transfer rates, improve process control and accelerate the contacting and mixing of fluids or reactants (Losey et al., 2002; Günther et al., 2005; Vandu et al., 2005a). The direct advantages from the process engineering point of view would be: embedded and/or portable reactors, improved reaction selectivity and yields, narrow residence time distribution, more reliable utilization of catalysts with reduced quantity and extended life (Losey et al., 2002; Yen et al., 2005; Hessel et al., 2005). Consequently, microstructured reactors can be beneficial in a series of important applications:

- Reactions of explosive, flammable or highly toxic components.
- Generation of uniform and long-time stable emulsions, dispersions or foams.
- Reactions in unusual process or under isothermal conditions.
- Reactions that need fast and homogeneous mixing of the reactants.
- Exploring new reaction pathways and finding economical and environmentally benign solutions to chemical manufacturing.
- New approaches for energy management, catalyst incorporation and integration of functions and unit operations.

With the current trend to integrate other components, such as sensors and actuators, the microengineered structures can have functionalities for measurement and control. In addition, when merged with μ TAS (micro-total-analysis-systems) techniques, the micro-engineered structures can be well extended to many chemical and biological applications, e.g. combinatorial chemistry, high throughput screening and portable analysis measurement devices. Despite of all these advantages, there are still many challenges and uncertainties in the application of microreactors. It is not always clear if “small must be better” (Jensen, 2001). Commenge et al. (2005) demonstrated that

miniaturization was not necessarily beneficial to reactor performance. For example, for homogeneous reactions they proved that the characteristic transfer time is independent of channel radius. The scale dependence of the various phenomena involved will define whether the net performance remains unchanged or even deteriorates. In addition, because of the increased importance of surface forces interfacial phenomena, wall roughness and wettability and confinement effects, that are not usually taken into account in large scale systems, need to be fully characterised. One more challenge is the microreactor scale-out (replication of many units), because reactor monitoring and control become increasingly complex as the number of replicated units grows (Kreutzer et al., 2005c; Hessel et al., 2005). These challenges and uncertainties as well as some business issues, such as the cost position of existing dominant technology, and the alignment between the innovative technology and marketing and sales, prevent the wide adoption of microstructured reactors in industry.

1.3 Thesis motivation and objectives

There is a very large number of industrially important gas-liquid reactions, e.g. chlorinations, hydrogenations, oxidations and sulfonations. In conventional systems problems often occur with poor heat/mass transfer, poor phase contacting – homogeneous phase distribution and control (Hessel et al., 2005). These reactions can benefit by operating in small scale units. The main aim of this thesis is to investigate gas-liquid microstructured reactors and the dependence of the reactor performance on design parameters. Single channel microstructured reactors for non-catalytic and fast gas-liquid reactions that can suffer from mass transfer limitations are considered. The main aim is realized through the objectives below:

- Characterize phenomena that affect process efficiency, such as hydrodynamics, mass transfer and chemical reactions.
- Understand how these phenomena interact at very different space and time scales and how they are affected by reactor dimensions and geometry.
- Investigate reactor design to achieve improved process efficiency.
- Develop numerical models that can be used as investigation tools.

1.4 Thesis outline

The thesis consists of ten chapters. In Chapter 2, literature relevant to the thesis is reviewed. Topics include gas-liquid two-phase flow patterns in microchannels, important phenomena in microscale such as surface tension and contact angle, Taylor

flow hydrodynamics and mass transfer and microstructured reactors and their designs. The first part of the thesis focuses on the adiabatic gas-liquid two-phase flow in microchannels. Chapter 3 critically reviews the literature on major parameters influencing flow pattern transitions and investigates the existence of a universal flow regime map. In Chapter 4 the effects of inlet conditions on gas-liquid flow regimes in microchannels are studied.

The second part of the thesis deals with a particular type of gas-liquid microreactor that operates in Taylor bubble flow. Taylor flow microreactors have been found to be particularly beneficial for carrying out two and three phase reactions and for combinatorial applications (Salman et al., 2007). Taylor flow formation and the effect on bubble size of inlet conditions, i.e. operating conditions, fluid properties and inlet size, are studied in Chapter 5 through Computational Fluid Dynamics (CFD) modelling. In Chapter 6 the hydrodynamic parameters of Taylor flow such as bubble size and distribution are investigated experimentally using microchannels developed in-house with various inlet configurations. The correlations on bubble size developed in Chapter 6 are then used in Chapter 7, where the main reaction channel is studied experimentally. A fast reaction system of CO₂ absorption into NaOH solution in a Taylor flow microreactor is used and the effects of main channel size and structure are investigated. In Chapter 8, the individual effect of Taylor flow geometric parameters such as bubble length, slug length and film thickness on the reactor performance are investigated. Numerical simulations are used for the studies to isolate the effects of these parameters because experimentally any changes in operational conditions or channel geometry usually change more than one of the flow geometry parameters.

In Chapter 9, the performance of a Taylor flow microreactor for an industrial fast gas-liquid reaction is investigated and compared against two other types of microreactors, namely film and annular flow ones. The numerical model formulated in Chapter 8 is modified in this chapter to accommodate flows encountered in the film and annular microreactors.

Finally in Chapter 10 the conclusions are summarized and recommendations for future work are given.

Chapter 2

Literature Survey

Nomenclature

a	Interfacial area, m^{-1}
a'	Coefficient, -
b'	Coefficient, -
C	Coefficient, -
d	Characteristic dimension, m
F	Force, N
k	Roughness, m
k_L	Liquid side mass transfer coefficient, m/s
l	Length, m
m	Relative bubble velocity as defined $\frac{U_B - U_{TP}}{U_B}$
P	Pressure, Pa
Q	Volumetric flowrate, m^3/s
R	Radius of curvature, m
U	Velocity, m/s
r	Channel radius, m
r^0	Centre of toroidal vortex in liquid slug, m
r^l	Radial position of streamline that separates the circulating Vortex in the slug from the liquid film attached to the wall, m
w	Width, m

Greek Symbols

α	Coefficient, -
λ	Coefficient, -
μ	Dynamic viscosity, Pa·s
ρ	Density, kg/m^3
σ	Surface tension, N/m
ε	Volume fraction, -
κ	Surface curvature, m^{-1}
θ	Contact angle between the liquid and the solid surface, °
ω	Contact angle between the gas and liquid inlets, °
Ψ	Ratio of bubble to mean flow velocity, -

2. Literature Survey

Dimensionless Numbers

Ca	Capillary number, $\mu_L(U_{GS}+U_{LS})/\sigma$
$Eö$	Eötvös number, $(\rho_L-\rho_G)d_C^2g/\sigma$
Fr	Froude number, $U_B/[gd(\rho_L-\rho_G)/\rho_L]^{0.5}$
Mo	Morton number, $g\mu_L^4(\rho_L-\rho_G)/\rho_L^2\sigma^3$
N_f	Fluid property number, $(Eö^3/Mo)^{1/4}$
Re	Reynolds number, $\rho Ud/\mu$
Su	Suratman number, $Re_{LS}^2/Ca = \rho_L\sigma d/\mu_L^2$
Sc_L	Liquid Schmidt number, $Sc_L = \frac{\mu_L}{\rho_L D_{CO_2(L)}}$
Sh_L	Liquid Sherwood number, $Sh_L = \frac{k_L d_H}{D_{CO_2(L)}}$
We	Gas Weber number, $\rho U^2 d/\sigma$
We'	Gas Weber number based on density difference, $(\rho_L-\rho_G)U^2 d/\sigma$

Subscripts

A	Advancing
app	Apparent
B	Bubble
$film$	Liquid film
G	Gas
GS	Gas phase superficial
H	Hydraulic
L	Liquid
LS	Liquid phase superficial
R	Receding
$Slug$	slug
TP	Two-phase average

2.1 Gas-liquid two-phase flow in microchannels

Gas-liquid two-phase flow in microchannels has been the subject of increased research interest in the past few years. It is encountered in many important applications, such as miniature heat exchangers, microscale process units, research nuclear reactors, materials processing and thin film deposition technology, biotechnology systems and potentially in space applications. Compared to macro-systems, there are three major differences in flows in microchannels. Firstly, the relative importance of surface over volume forces increases. Secondly, Reynolds number is usually small and laminar flow is established, where viscous forces dominate over inertial ones. Thirdly, effects of wall roughness, wettability and flow confinement become important. There already exists a significant amount of work that attempts to characterize gas-liquid flows in microchannels (e.g. see review papers by [Ghiaasiaan and Abdel-Khalik, 2001](#); [Akbar et al., 2003](#)). In this thesis, adiabatic two-phase flows are considered.

For the transition from gravity to surface tension dominated regimes, which also signifies the transition from macro- to micro-channel flow, different values of the $E\ddot{o}$ have been proposed in the literature. In the work by [Bretherton \(1961\)](#), $E\ddot{o} < 0.84$ was suggested as a criterion for transition to microchannel flow, because below this value a Taylor bubble would no longer rise spontaneously in a water filled vertical capillary under the effect of gravity. [Suo and Griffith \(1964\)](#) proposed $E\ddot{o} < 0.88$ as the criterion for negligible buoyancy effects on a Taylor bubble moving through a liquid in a horizontal tube. [Brauner and Moalem-Maron \(1992\)](#) used the limit of stability and well posedness of the unidirectional continuity and momentum equations during stratified flow in pipes to suggest that surface tension would dominate for $E\ddot{o} < (2\pi)^2$. Substituting the properties of an air-water system, the above criteria give channel dimension, d , of 2.96mm, 2.6mm, and 17.1mm, respectively, for transition to microchannel flow. [Triplett et al. \(1999\)](#) studied air-water flow patterns in circular channels and indicated transition to surface tension dominated regimes for $1\text{mm} < d < 2\text{mm}$. [Chen et al. \(2006\)](#) found experimentally from liquid-vapour R134a flow in vertical, circular test sections that the transition from small to normal pipe flow characteristics occurred in 2mm diameter tube. Characteristics for small tube flow were fully exhibited in tube diameter of 1.1mm.

2.2 Flow patterns formed in microchannels

Visual observations have revealed that flow patterns during two-phase flows in small channels are morphologically similar to those observed in large ones and terminology

from large scale systems is often adopted. However, the major problem in studying and reporting two-phase flow patterns is the lack of uniformity in the terminology; for example slug flow (Galbiati and Andreini, 1994), Taylor flow (Amador et al., 2004) and bubble train flow (Thulasidas et al., 1997) refer to the same pattern. Reversely, it is not uncommon for the same name to be used to describe different patterns. For example, slug flow (Damianides and Westwater, 1988; Barajas and Panton, 1993) has been used to describe Taylor flow (Galbiati and Andreini, 1994; Triplett et al., 1999), as well as wavy-annular flow (Yang and Shieh, 2001). A reason for this lack of uniformity is the difficulty in categorising and analysing transitional flows. In addition, local velocities can significantly change with axial length in microchannels due to high pressure drop, which can cause morphological and flow pattern changes and thus disagreement on the flow patterns reported under identical flow conditions depending on axial location. To overcome this problem flow patterns and their characteristics are summarized below, and names are assigned that will be applied throughout the thesis. Based on the relative importance of the surface tension over inertial forces, three overall flow regimes are identified, namely *surface tension dominated*, *inertia dominated* and *transitional* regimes. These three regimes consist of six main flow patterns, namely bubbly and Taylor flow (surface tension dominated), churn and Taylor-annular (transitional), dispersed and annular (inertia dominated). The flow patterns are presented in Figure 2.1 in a map with gas (U_{GS}) and liquid (U_{LS}) superficial velocities as coordinates.

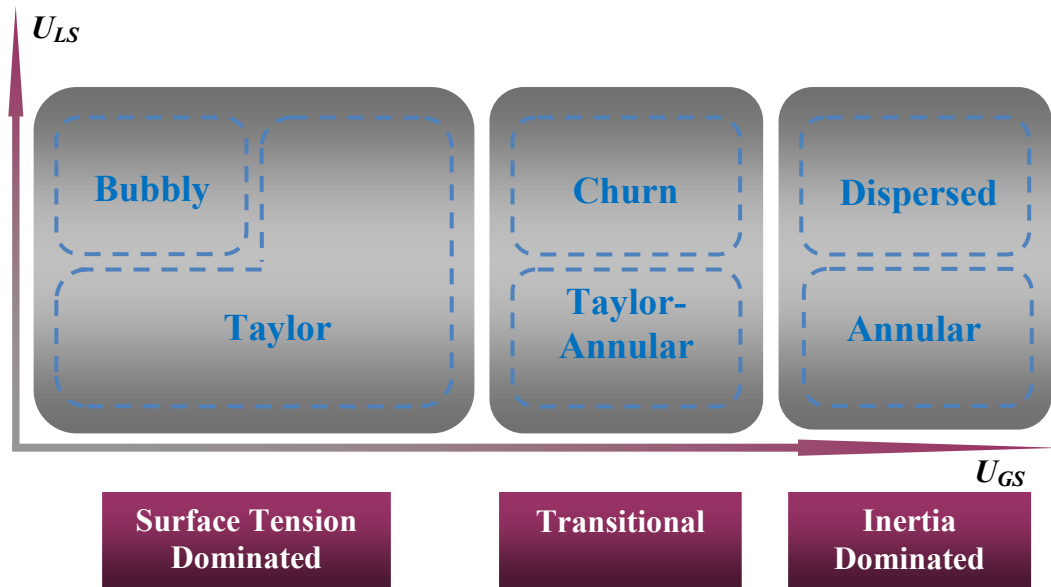
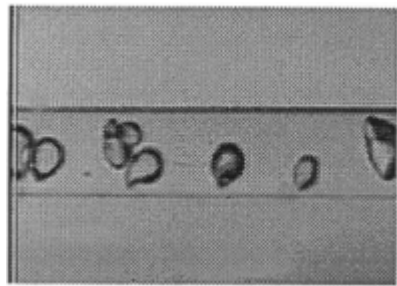


Figure 2.1 General classification of gas-liquid two-phase flow patterns.

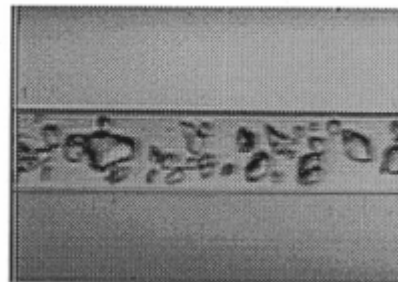
2. Literature Survey

According to Figure 2.1 Taylor flow occurs at low gas and liquid velocities. Increasing the liquid flowrate eventually leads to the disruption of the Taylor bubbles and the pattern changes to bubbly flow. At medium gas velocities, churn and Taylor-annular flow are developed from Taylor flow at high and low U_{LS} respectively. In these transitional regimes, inertial forces start to become influential but surface/interfacial forces are still strong. Although they are transitional flows, churn and Taylor-annular flows are considered as main flow patterns because they occupy a range of operating conditions comparable to the other main flow patterns. A further increase in U_{GS} eventually leads to the inertial dominated dispersed and annular flows. Dispersed flow is not frequently reported in the literature because the high U_{GS} and U_{LS} required are not commonly used in small channels. Even when it is observed it is often included within churn or annular flows (e.g. [Bousman et al., 1996](#)).

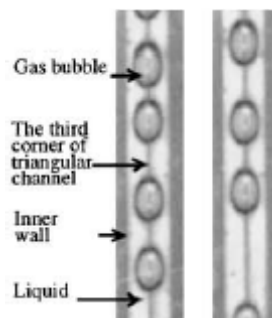
Bubbly flow. Bubbly flow (Figure 2.2) is characterized by distinct and sometimes distorted (non-spherical) bubbles generally considerably smaller than the channel diameter. [Zhao and Bi \(2001\)](#) in their equilateral triangular channel ($d_H = 0.886\text{mm}$) observed bubbles with size close to the tube diameter that line up to form a train which they named capillary bubble flow (Figure 2.2c).



(a) $U_{LS} = 3.021\text{m/s}$, $U_{GS} = 0.083\text{m/s}$;



(b) $U_{LS} = 5.997\text{m/s}$, $U_{GS} = 0.396\text{m/s}$;

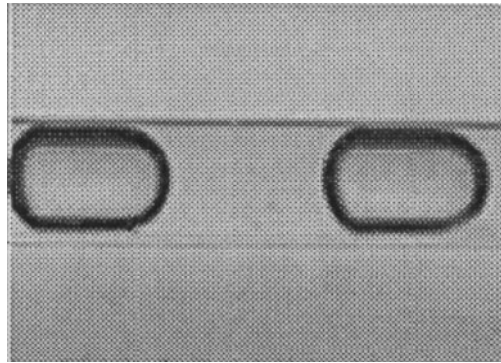


(c) $U_{LS} = 0.1\text{m/s}$, $U_{GS} = 0.2\text{m/s}$;

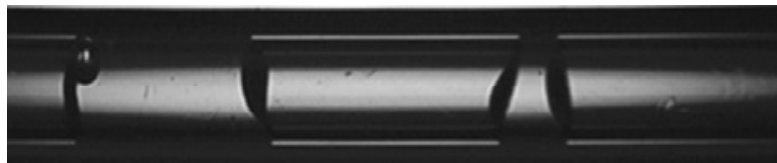
Figure 2.2 Bubbly flow. (a), (b) Bubbly flow ([Triplett et al., 1999](#), air/water, $d = 1.097\text{mm}$); (c) Capillary bubbly flow ([Zhao and Bi, 2001](#), air/water, equilateral triangular channel, $d_H = 0.866\text{mm}$).

2. Literature Survey

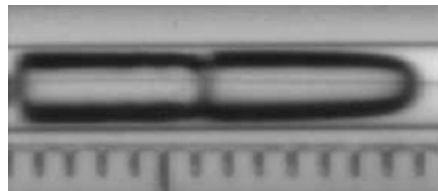
Taylor flow. Taylor flow (also known as segmented, slug, plug, elongated bubble or intermittent flow) is characterized by elongated bubbles with an equivalent diameter larger than that of the channel (Figure 2.3). Liquid slugs separate the gas bubbles while, depending on the channel wettability, a liquid film may form that separates the bubbles from the wall. Serizawa et al. (2002) observed the absence of liquid film in microchannels with contaminated walls. The liquid slug may also contain small gas bubbles. Under certain conditions, bubbles may touch each other with only a thin film separating them to form a bubble-train slug flow (Figure 2.3c, Chen et al., 2002). The pattern is believed to form when the inertia force of the second bubble is large enough to overcome surface tension and break through the liquid slug to join the bubble downstream, but is not sufficient to rupture the interface and properly coalesce with the bubble in front. $We_{GS} = 1$ is used as a criterion for the formation of this pattern (Zhao and Rezkallah, 1993).



(a) $U_{LS} = 0.213\text{m/s}$, $U_{GS} = 0.154\text{m/s}$;



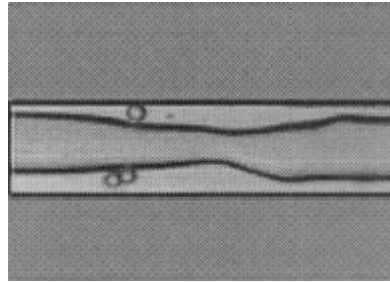
(b) $U_{LS} = 0.05\text{m/s}$, $U_{GS} = 0.5\text{m/s}$;



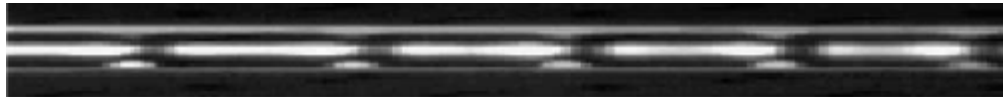
(c) $U_{LS} = 1.11\text{m/s}$, $U_{GS} = 1.57\text{m/s}$;

Figure 2.3 Taylor flow. (a) Taylor flow (Triplett et al., 1999, air/water, $d = 1.097\text{mm}$, Pyrex capillary); (b) dry plug flow (Lee and Lee, 2008, air/water, $d = 1.59\text{mm}$, Teflon tube with $\theta = 110^\circ$); (c) Bubble-train slug (Chen et al., 2002, nitrogen/water, $d = 1\text{mm}$).

Taylor-annular flow. With increasing U_{GS} in Taylor flow at relatively low U_{LS} , the increased gas void fraction leads to the merging of Taylor bubbles to form the Taylor-annular pattern (Figure 2.4), also known as slug-annular flow (Triplett et al., 1999). In this pattern, a gas core is surrounded by a liquid film where large-amplitude solitary waves appear and small bubbles are sometimes present in the liquid. Serizawa et al. (2002) in very small capillaries of $25\mu\text{m} - 100\mu\text{m}$ diameter observed a particular realisation of this pattern (liquid ring, or “Yakitori”, flow in their study, Figure 2.4b) with evenly distributed waves and no bubble entrainment in the liquid film which appeared when the gas flow rate increased to such an extent that the liquid slug is too short to support a stable liquid bridge between two consecutive Taylor bubbles. In mini-channels, e.g. with sizes of the order of millimeters, Taylor-annular flow appears often as slug flow on flow regime maps, in which gas and liquid travel at approximately the same velocity and the waves of the liquid grow to touch the top of the wall and form intermittent liquid slugs (Damianides and Westwater, 1988; Barajas and Panton, 1993).



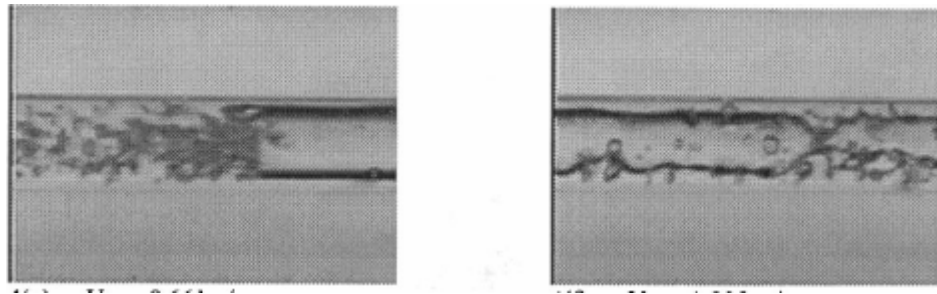
(a) $U_{LS} = 0.057\text{m/s}$, $U_{GS} = 3.308\text{m/s}$;



(b)

Figure 2.4 Taylor-annular flow. (a) Taylor-annular flow (Triplett et al., 1999, air/water, semi-triangular channel of $d_H = 1.09\text{mm}$); (b) Liquid ring flow (Serizawa et al., 2002, air/water, $d = 50\mu\text{m}$).

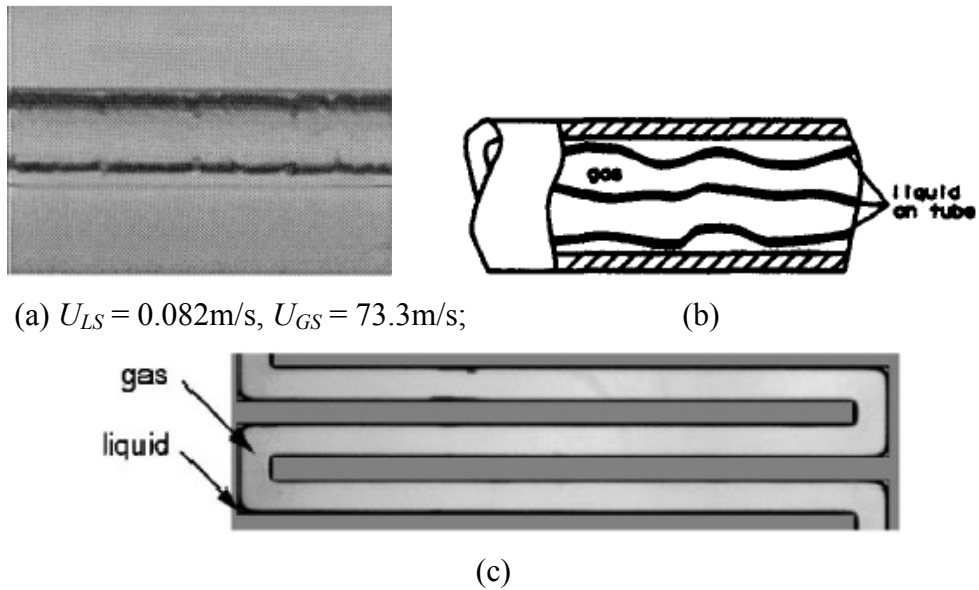
Churn flow. This is a transitional pattern between Taylor and inertia dominated dispersed flow at relatively high liquid velocities. It forms as a result of two processes. In some cases, the elongated Taylor bubbles become unstable near their trailing ends, leading to disruption and entrainment of gas into the liquid (Figure 2.5a). In other cases, at higher gas flow rates, the liquid film that flows on the tube wall becomes very disturbed by the high inertia of the gas core and frothy slugs and drops appear within the gas (Figure 2.5b).



(a) $U_{LS} = 0.661\text{m/s}$, $U_{GS} = 6.183\text{m/s}$; (b) $U_{LS} = 1.205\text{m/s}$, $U_{GS} = 4.631\text{m/s}$;

Figure 2.5 (a), (b) Churn flow (Triplett et al., 1999, air/water, $d = 1.097\text{mm}$).

Annular flow. With increasing U_{GS} in Taylor-annular flow, the long waves disappear and the annular pattern is established (Figure 2.6a). Depending on tube wetting properties, contamination or amount of liquid present, instead of a constant thickness film, streams of liquid may form that twist their way along the tube length much like a river (rivulet flow, Figure 2.6b, Barajas and Panton, 1993). When the liquid film thickness decreases below a certain limit dry flow occurs (Figure 2.6c, Cubaud and Ho, 2004) in which dry patches develop on the wall. The liquid can then appear as droplets on the wall or, in non-circular channels, it is concentrated in the corners.



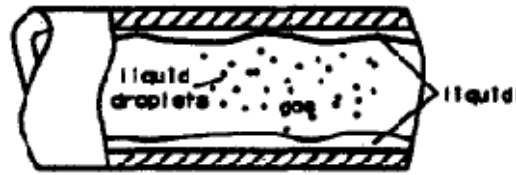
(a) $U_{LS} = 0.082\text{m/s}$, $U_{GS} = 73.3\text{m/s}$;

(b)

(c)

Figure 2.6 Annular flow: (a) annular flow (Triplett et al., 1999, air/water, $d = 1.097\text{mm}$); (b) rivulet flow (Barajas and Panton, 1993, air/water); (c) dry flow (Cubaud and Ho, 2004, air/water).

Dispersed flow. From annular flow, with further increase of U_{LS} , small liquid droplets are entrained in the gas core to form the dispersed pattern (Figure 2.7) and in most cases a liquid film is left in contact with the wall. As mentioned before because of the very high U_{LS} and U_{GS} required, this pattern is not commonly observed in microchannels.



(a)



(b) $U_{LS} = 1.52\text{m/s}$, $U_{GS} = 19.0\text{m/s}$;

Figure 2.7 Dispersed flow: (a) Barajas and Panton (1993), air/water; (b) Yang and Shieh (2001), air/water, $d = 3\text{mm}$.

Literature studies on gas-liquid two-phase flows in microchannels are summarized in Table 2.1. Adiabatic flows are considered in channels with at least one dimension $\leq 1\text{mm}$, where microchannel flow is established (see Section 1.1). The table includes information on channel geometry and material, operating conditions, flow patterns identified, flow transition criteria when given and other key aspects such as channel inlet design.

2. Literature Survey

Table 2.1 Literature on gas-liquid two-phase flows in mini- and microchannels.

Authors	Gas-liquid	Test section	Flow patterns	Flow pattern transitions	Key notes
Suo and Griffith (1964)	Air/water N ₂ /water He/heptane N ₂ /heptane	H ¹ , circular, $d = 1\text{mm}$ and 1.4mm	Taylor (capillary slug) ² , annular	Annular to Taylor at constant liquid fraction ε_L .	Taylor flow characterization and the transition boundary to other regimes.
Galbiati and Andreini (1992)	Air/water	V ³ , downward, $d = 0.5, 1.1, \text{ and } 2\text{mm}$	Taylor (slug), annular		Inlet mixing has a significant effect on flow patterns and their transitions.
Barajas and Panton (1993)	Air/water	H, $d = 1.5875\text{mm}$, four materials with different contact angles: $34^\circ, 61^\circ, 74^\circ, \text{ and } 106^\circ$; $U_{GS} = 0.1\text{-}100\text{m/s}$; $U_{LS} = 0.003\text{-}2\text{m/s}$; the viewing section was 160 diameters downstream of the test section entrance	Wavy, Taylor (plug), Taylor-annular (slug), annular, dispersed bubbly (bubble), rivulet	Little effects of contact angle for transitions in partially wetting systems ($\theta < 90^\circ$). For $\theta > 90^\circ$, most transition boundaries were substantially changed.	Effect of contact angle and tube diameter on flow patterns.

¹ H: horizontal

² Patterns in brackets are names given by the authors

³ V: vertical

2. Literature Survey

Authors	Gas-liquid	Test section	Flow patterns	Flow pattern transitions	Key notes
Fukano and Kariyasaki (1993)	Air/water	H/V (upward and downward), circular, Pyrex, $d = 1, 2.4, 4.9, 9,$ and 26mm; $U_{GS} = 0.1-30\text{m/s}$; $U_{LS} = 0.02-2\text{m/s}$; air injected through air-water mixer	Bubbly (bubble), intermittent, annular	Comparison with Barnea et al. (1983) good only for small pipe size, 4mm; poor agreement with Mandhane et al. (1974) .	No significant effect of channel orientation on the flow patterns for $d < 4.9\text{mm}$. Also investigated time varying void fraction and pressure losses, bubble velocity and film thickness.
Mishima and Hibiki, (1996)	Air/water	V, Pyrex glass and aluminium, circular, $d = 1-4\text{mm}$; $U_{GS} = 0.1-50\text{m/s}$; $U_{LS} = 0.02-2\text{m/s}$; air was injected to the test section	Bubbly, Taylor, churn, annular and dispersed (annular mist)	Transitions were predicted well by Mishima and Ishii's model (Mishima and Ishii, 1984).	Measurement of void fraction, bubble velocity and frictional pressure loss. The void fraction was correlated well by modifying drift flux model with added inner diameter effect.
Coleman and Garimella (1999)	Air/water	H, co-current, Pyrex glass, circular and rectangular $d_H = 1.3, 1.75, 2.6, 5.5\text{mm}$; $U_{GS} = 0.1-100\text{m/s}$; $U_{LS} = 0.01-10\text{ m/s}$	Bubbly, dispersed, Taylor (elongated bubble /plug flow and slug flow), Taylor-annular (wavy-annular), churn (slug), wavy, annular	Good agreement with Damianides and Westwater (1988) ; both show an increase in size of Taylor flow in the map, but disagree with the transition to dispersed flow.	Effect of tube diameter and shape on flow regime transitions. The slug flow reported should cover both Taylor and churn flow according to topology analysis.

2. Literature Survey

Authors	Gas-liquid	Test section	Flow patterns	Flow pattern transitions	Key notes
Triplett et al. (1999)	Air/water	H, circular $d = 1.1$ and 1.45mm (Pyrex); semi-triangular $d_H=1.09$ (acrylic) and 1.49mm (polycarbonated rod); $U_{GS} = 0.02\text{-}80\text{m/s}$; $U_{LS} = 0.02\text{-}8\text{ m/s}$; Inlet with water and air mixer	Similar for all the test sections. Bubbly, churn, Taylor (slug), Taylor-annular (slug-annular), annular	Compared with regime transition correlations of Suo and Griffith (1964) with significant disagreement.	Effects of channel dimension and shape. Very similar results for semi-triangular and circular channels. Overall agreement with similar data by Suo and Griffith (1964), Damianides and Westwater (1988), and Fukano and Kariyasaki (1993).
Yang and Shieh (2001)	Air/water R-134a	H, Pyrex glass, circular $d = 1\text{-}3\text{ mm}$; $U_{GS} = 0.016\text{-}91.5\text{m/s}$; $U_{LS} = 0.006\text{-}2.1\text{m/s}$	Bubbly, Taylor (plug), wavy stratified, wavy-annular (slug), dispersed, annular	Poor agreement with Taitel and Dukler (1976).	Effects of channel diameter and fluid properties. Pattern transitions in air-water could not be clearly distinguished, especially the Taylor to annular flow. In contrast, transition for R-134a is very sharp and clear.
Zhao and Bi (2001)	Air/water	V upward, Lucite equilateral triangular channel, $d_H = 0.866, 1.443$ and 2.886mm ; $U_{GS} = 0.1\text{-}100\text{m/s}$; $U_{LS} = 0.08\text{-}10\text{ m/s}$; fine-plastic-packed porous mixer inlet	Bubbly (capillary bubbly flow for 0.866mm), Taylor (slug), churn, annular	Taitel et al. (1980) and Mishima and Ishii (1984)'s models deviate from experimental data significantly.	Measured water, air flow rate, absolute pressure and pressure drop. Channel size reduction and the sharp corners of the noncircular channels have significant impact on flow patterns and transition boundaries.

2. Literature Survey

Authors	Gas-liquid	Test section	Flow patterns	Flow pattern transitions	Key notes
Chen et al. (2002)	Nitrogen-water	H and V, glass circular, $d = 1$ and 1.5mm ; $U_{GS} = 0.502\text{-}1.1\text{m/s}$; $U_{LS} = 0.399\text{-}3.53\text{m/s}$; Needle injection for gas	Bubbly, Taylor (slug and bubble-train slug), churn, annular		Flow pattern, bubble speed and void fraction were observed and analyzed. Correlations given to predict bubble velocity and modified the drift flux model for void fraction.
Kawahara et al. (2002)	Nitrogen/water	H, fused silica circular, $d = 100\mu\text{m}$; $U_{GS} = 0.1\text{-}60\text{m/s}$; $U_{LS} = 0.02\text{-}4\text{m/s}$; T-junction inlet design	Taylor and Taylor-annular flow (gas core flows with a smooth or ring-shaped film and a serpentine-like gas core surrounded by a deformed liquid film)		The time-averaged void fraction and two-phase frictional pressure drop were analyzed.
Serizawa et al. (2002)	Air/water Steam/water	H, Silica or quartz capillary, circular, $d = 20, 25$ and $100\mu\text{m}$ for air and $50\mu\text{m}$ for steam; $U_{GS} = 0.0022\text{-}295.3\text{m/s}$; $U_{LS} = 0.0032\text{-}17.5\text{m/s}$; two designs of inlet mixing zone	Bubbly, Taylor (slug), Taylor-annular (liquid ring, frothy annular), churn (liquid lump), annular (liquid droplet flow or annular-mist, rivulet)	Pattern transitions generally follow the lines given by Mandhane et al. (1974) but without wavy and stratified flows. Does not agree with Fukano and Kariyasaki (1993).	Effects of surface tension and wettability. Void fraction was calculated. Suggested the existence of dry area underneath a gas slug, possibly because of scale effects and surface wettability.

2. Literature Survey

Authors	Gas-liquid	Test section	Flow patterns	Flow pattern transitions	Key notes
Chung and Kawaji (2004)	N ₂ /water	H, circular, $d = 530, 250, 100$ and $50\mu\text{m}$; $U_{GS} = 0.02\text{-}20\text{m/s}$; $U_{LS} = 0.01\text{-}7\text{m/s}$; gas-liquid mixer as inlet	For 530 and $250\mu\text{m}$, bubbly, Taylor (slug), churn, Taylor-annular (slug-annular) and annular		Study the effect of channel diameter on two-phase flow characteristics. For 530 and $250\mu\text{m}$, flow characteristics were similar to microchannels of $\sim 1\text{mm}$; in the 100 and $50\mu\text{m}$, behaviour is different.
Cubaud and Ho (2004)	Air/water	H, square, glass and silicon, $d_H = 200$ and $525\mu\text{m}$; $U_{GS} = 0.003\text{-}20\text{m/s}$; $U_{LS} = 0.001\text{-}0.2\text{m/s}$; a mixing zone at the inlet	Bubbly, Taylor (wedging), Taylor-annular (slug), annular (annular and dry)	Bubbly to Taylor: $\varepsilon_L \approx 0.75$; Taylor to Taylor-annular: $\varepsilon_L \approx 0.2$; Taylor-annular to annular: 0.04 .	Flow map does not depend on the microchannel size, contrary to large channels. Taylor bubble velocity is found to be equal to the average mixture velocity. Wettability plays an important role in small channels.
Hassan et al. (2005)	Air/water	H, circular borosilicate glass $800\mu\text{m}$, $d = 1$ and 3mm ; $U_{GS} = 10\text{-}100\text{m/s}$; $U_{LS} = 0.02\text{-}3.82\text{m/s}$	Surface tension dominated: bubbly, Taylor (intermittent); inertia dominated: churn and annular		Review paper as well as experimental study. The flow regime transition lines are affected by channel orientation.
Waelchli and von Rohr (2006)	N ₂ /water, ethanol, glycerol (10%) and glycerol (20%)	H, rectangular, silicon, $d = 187.5\text{-}218\mu\text{m}$; $U_{GS} = 0.027\text{-}8.9\text{m/s}$; $U_{LS} = 0.014\text{-}1.4\text{m/s}$; a mixing zone at the inlet	Taylor flow and Taylor-annular (intermittent), annular flow, bubbly flow regime	Use $10^7 Re_{LS}^{0.2} We_{LS}^{0.4} (k/d)^5$ and $Re_{GS}^{0.2} We_{GS}^{0.4}$ as coordinates in the flow map, where k/d is the relative channel roughness.	The ability to predict the correct flow regime is mainly dependent on the similarity of the cross-sectional channel shape and not on a similarity in hydraulic diameters.

2. Literature Survey

Authors	Gas-liquid	Test section	Flow patterns	Flow pattern transitions	Key notes
Haverkamp et al. (2006)	Air/water, isopropanol	H, rectangular, stainless steel ($d_H = 150\mu\text{m}$ and $294.5\mu\text{m}$; $U_{GS} = 0.001\text{-}22\text{m/s}$; $U_{LS} = 0.001\text{-}0.074\text{m/s}$), borosilicate glass ($d_H = 66.67\mu\text{m}$; $U_{GS} = 0.5\text{-}190\text{m/s}$; $U_{LS} = 0.03\text{-}2\text{m/s}$); T-type and Smooth-type mixer for $66.67\mu\text{m}$ channel	$d_H = 150\mu\text{m}$ and $294.5\mu\text{m}$ channels: bubbly, Taylor (slug), Taylor-annular (slug-annular), and annular; $d_H = 66.67\mu\text{m}$ channels: Taylor, churn, annular, Taylor-annular (ring)	By decreasing surface tension, the transition from Taylor to Taylor-annular/annular shifted to higher U_{GS} ; compared with T-type mixer, the transition from Taylor to churn with Smooth-type mixer shifted to higher U_{GS} .	The gas-liquid mixer design was found to be decisive on bubble size, bubble size distribution and flow patterns in microchannels. Using the Smooth-type mixer, bubble sizes and their distribution were improved, i.e. smaller and more regular bubbles were generated. Taylor-annular (ring) flow in $66.67\mu\text{m}$ microchannel was reported to occur at even higher U_{GS} instead of annular flow, which has not been reported in other studies.
Cubaud et al. (2006)	Air/water, water with surfactant	H, square, glass and silicon, $d_H = 525\mu\text{m}$; on-chip cross-shaped mixing chamber as inlet	Hydrophilic flows: bubbly, Taylor (wedging), Taylor-annular (slug), annular (annular and dry); hydrophobic flows: isolated asymmetric bubble flow, wavy bubble flow, scattered droplet flow		Highlight the importance of surface treatment at the microscale. Tube wall hydrophobicity and sharp wedges in square channel, affect flow morphology dramatically.

2. Literature Survey

Authors	Gas-liquid	Test section	Flow patterns	Flow pattern transitions	Key notes
Yue et al. (2008)	CO ₂ /water	H, rectangular polyethylene terephthalate channel modified by glycol; $d_H = 200\mu\text{m}$, $400\mu\text{m}$ and $667\mu\text{m}$; $U_{GS} = 0.04\text{-}70\text{m/s}$; $U_{LS} = 0.02\text{-}2\text{m/s}$; Y-junction inlet with an angle of 60°	Bubbly, Taylor (slug), Taylor-annular (slug-annular), churn, annular	Transition from Taylor to Taylor-annular shifted to higher U_{GS} in smaller channel; transition from Taylor to bubbly and from Taylor-annular to annular did not follow a trend with channel size.	The separated flow model was applied and the two-phase frictional multiplier was modified to include the effect of U_{LS} .
Pohorecki et al. (2008)	N ₂ /water, ethanol	H, rectangular and square PMMA; $d_H = 843\mu\text{m}$; $U_{GS} = 0.01\text{-}50\text{m/s}$; $U_{LS} = 0.02\text{-}1.2\text{m/s}$; Y-junction inlet	Bubbly (bubble), Taylor (slug), Taylor-annular (slug/annular), annular	Taylor to Taylor-annular transition shifted to lower U_{GS} in higher surface tension system.	A criterion for effectiveness of interfacial area in gas-liquid microreactors is proposed.
Lee and Lee (2008)	Air/water, methanol	H, circular, glass ($d = 1.46\text{mm}$ and 1.8mm ; $U_{GS} = 0.5\text{-}50\text{m/s}$; $U_{LS} = 0.004\text{-}0.4\text{m/s}$), Teflon ($d = 1.59\text{mm}$; $U_{GS} = 0.4\text{-}47\text{m/s}$; $U_{LS} = 0.02\text{-}0.8\text{m/s}$); polyurethane ($d = 2\text{mm}$; $U_{GS} = 0.3\text{-}53\text{m/s}$; $U_{LS} = 0.007\text{-}0.4\text{m/s}$); gas-liquid mixer before the testing channel	Taylor (plug), Taylor-annular (slug), annular (annular for wet condition and rivulet for dry condition), stratified (wavy)	Wet flow to dry flow transition given by normalized superficial liquid velocity: $\bar{U}_{LS} = \frac{U_{LS}}{a' + b'\theta}$ where a' and b' are determined experimentally under different wetting conditions.	$\bar{U}_{LS} = 1$ defines the lower boundary for wet flow when $\theta < 50^\circ$, the upper boundary for dry flow when $\theta > 90^\circ$, and transition line from dry to wet flows in $50^\circ < \theta < 90^\circ$. The wet to dry transition depends on contact angle as well as U_{LS} .

2.3 Surface tension and Marangoni effect

Surface tension σ is defined as the force (F) per unit length (l) tending to decrease the surface area (Eq. 2.1):

$$\sigma = \frac{F}{l} \quad \text{Eq. 2.1}$$

Because of the existence of surface tension, an interface will have a tendency to curve. This curvature results in a pressure difference across the interface ΔP (the highest pressure on the concave side). The difference is presented by the Young-Laplace equation:

$$\Delta P = \sigma \left(\frac{1}{R_1} + \frac{1}{R_2} \right) = \sigma (\kappa_1 + \kappa_2) \quad \text{Eq. 2.2}$$

where ΔP is the pressure difference across the curved interface, R_1 and R_2 are the radii of curvature, κ is the surface curvature. The surface tension at a gas-liquid interface is not constant in systems in which gradients in temperature or solute concentration are present. Thereby, gradients in surface tension are developed when there is a component of the gradient of temperature or concentration tangent to an interface, which in turn induce or influence viscous flows in the liquid through the tangential stress at the interface. The secondary flows arising from these surface tension gradients are referred to as Marangoni effects. They can be particularly strong in small channels where surface tension forces dominate and can account for deviations from the flow behaviour seen in large channels. In some cases Marangoni effects have been used to control fluid flow in small channels (Tseng et al., 2004).

2.4 Contact angle and wettability

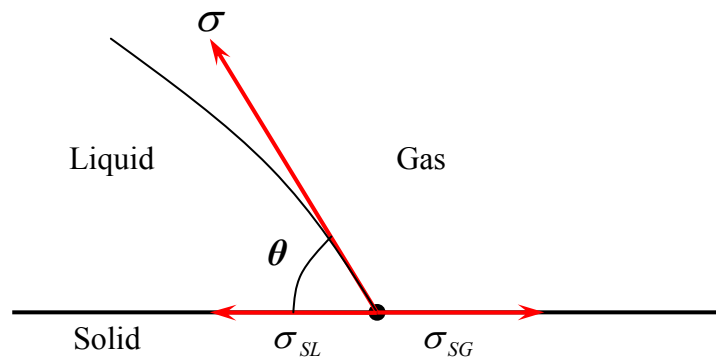


Figure 2.8 Three phases at the contact interface.

In view of the significance of surface tension forces, surface wettability can affect the two-phase flow hydrodynamics in microchannels. Channel walls can influence viscous flow through molecular interactions, and eventually influence the interface shape. At the line of contact of two phases with a solid surface, the angle between a liquid and a solid is named the contact angle θ (Figure 2.8). When θ takes different values, wettability changes accordingly as seen in Table 2.2.

Table 2.2 Wettability at different θ values.

θ	Wettability	Note
0°	Completely wetting	Liquid spreads completely over the solid
$(0^\circ, 90^\circ)$	Wetting	Liquid spreads partially over the solid
$(90^\circ, 180^\circ)$	Non-wetting	Liquid spreads partially over the solid
180°	Completely non-wetting	Not physical

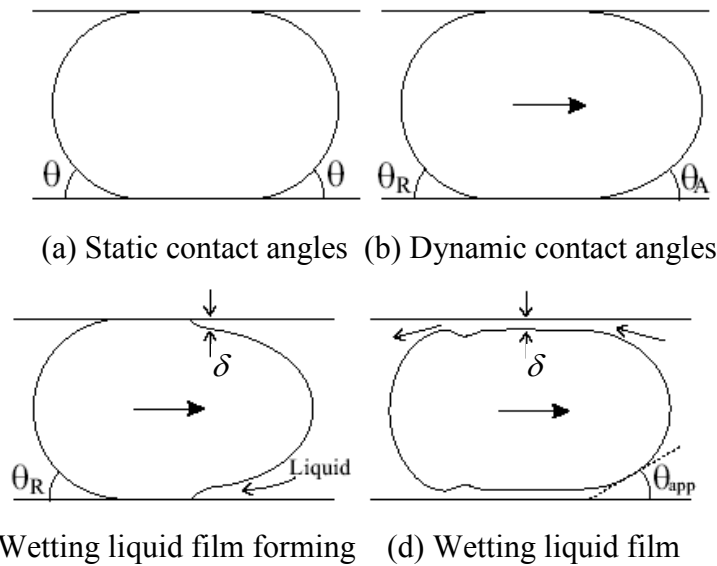


Figure 2.9 Schematic progress in the wetting behaviour of bubbles at increasing Ca (Jensen, 2002).

Experimental observations find that for most material systems, the real contact angle can acquire a range of values within θ_R and θ_A while the contact line remains fixed for angle variations within this range, a phenomenon typically referred to as contact angle hysteresis. The influence of Ca on the contact angles is shown in Figure 2.9 for a bubble in a small channel. Initially at zero velocity, the interface has a given static contact angle θ with the walls (Figure 2.9a). When an external pressure drives the bubble to move the contact angles at the front and back of the bubble will change as a function of

Ca . There will be an advancing angle θ_A and a receding angle θ_R (Figure 2.9b). At still increasing Ca the viscous forces become larger and a film is forming at the bubble front (Figure 2.9c) until finally it separates the gas phase from the wall (Figure 2.9d). The separating liquid film is very thin and it can be difficult in some cases to establish whether it exists or not. For that reason, an apparent contact angle is introduced as seen in Figure 2.9d.

2.5 Taylor flow

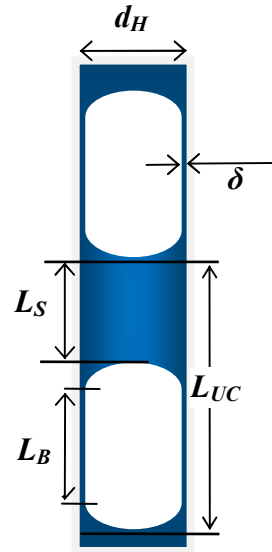


Figure 2.10 Taylor flow unit cell, represented as one bubble and one liquid slug.

As one of the dominant two-phase flow patterns in microchannels, Taylor flow is characterised by periodic occurrence of elongated capsular bubbles with an equivalent diameter several times that of the channel (Figure 2.3). The bubbles are separated by liquid slugs while only a thin liquid film (usually a very small percentage of the channel diameter) exists between them and the channel wall. Because the liquid phase is interrupted by the bubbles the flow pattern in the liquid slugs is modified to form toroidal vortices, which affect hydrodynamics and mass and heat transfer within the liquid significantly. The primary advantages offered by Taylor flow are the greatly reduced axial (Thulasidas et al., 1999; Salman et al., 2004) and improved radial mixing (Irandoust and Andersson, 1992; van Baten and Krishna, 2004, 2005), which can augment two- or three-phase reactions (Vandu et al., 2005) or enhance liquid-liquid mixing (Günther et al., 2005). A unit cell, which consists of a bubble and a liquid slug (Figure 2.10) or a liquid slug and two-half bubbles, is normally used for Taylor flow analysis (Thulasidas et al., 1999; van Baten and Krishna, 2004). For reactive systems,

the hydrodynamics of Taylor flow, e.g. the bubble shape, length and velocity and the film thickness need to be known.

2.5.1 Geometric characteristics of Taylor flow

The geometry of the Taylor bubbles results from a balance of viscosity, surface tension and pressure forces. Bretherton (1961) studied the shape of the front bubble meniscus theoretically and concluded that at small to intermediate Ca , it can be approximated as a hemisphere. Giavedoni and Saita (1999) confirmed the result for $Ca < 0.01$. While for $Ca > 0.1$ the caps of the bubble can no longer be regarded as spherical as reported by Fairbrother and Stubbs (1935). Giavedoni and Saita (1999) studied bubble rear shape and reported constant undulations at the transition region between the constant film and the back cap for $Ca < 0.5$. Increase of Ca leads to flow convex to flat shape at a Ca close to 0.75 and then to concave shape when $1 < Ca < 1.8$. The same trend was also reported in Taha and Cui (2006a) in their numerical study of Taylor bubble shape in square capillaries (Figure 2.11). At low Ca , the bubbles have spherical ends and with increasing Ca , a small indentation appears at the rear until the final development of a concave shape.

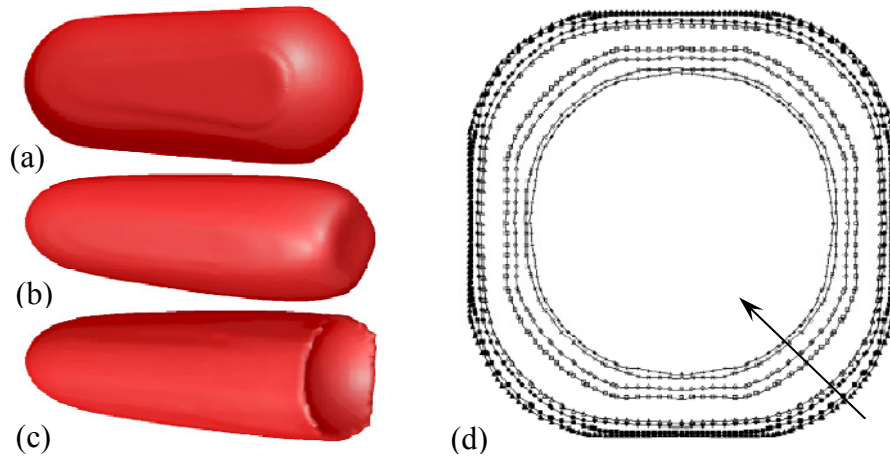


Figure 2.11 3-D view of Taylor bubble shape in a square capillary with side length of 2mm. (a) $Ca = 0.009$; (b) $Ca = 1.45$; (c) $Ca = 3.04$; (d) cross sectional view of the bubble profile, (▲) $Ca = 0.005$; (■) $Ca = 0.009$; (●) $Ca = 0.026$; (Δ) $Ca = 0.054$; (□) $Ca = 0.21$; (○) $Ca = 0.4$; (×) $Ca = 1.35$; (–) $Ca = 3.04$. Taha and Cui (2006a).

In summary, for flows in circular channels with small $Ca (< 10^{-3})$, the shape of Taylor bubbles appear to depart only slightly from that of a capsule with hemispherical caps and a cylindrical body. This geometry has been used for the numerical study of Taylor flow (Salman, 2005; van Baten and Krishna, 2004, 2005). However, in non-circular channels the bubble body is no longer cylindrical because the channel corners are

affected by viscous forces to a greater extent than the regions near the walls. As shown in Figure 2.11d (Taha and Cui, 2006a) a Taylor bubble in a square channel, at low Ca the bubbles tend to flatten against the side walls. With increasing Ca , the liquid film becomes thicker and the bubble radius in the side plane gradually approaches that in the diagonal direction until the bubble acquires an axisymmetric shape as in a circular channel. This took place at $Ca = 3.04$ in Figure 2.11d. It is worth noting that the leaky corners of noncircular channels are much more common in real system, such as porous media, monolith froth reactors and microelectromechanical systems. Also the symmetric flow shape can be lost in channels with nonuniform coating, when minor surface roughness is present or when there is compressibility of the gas phase.

2.5.2 Taylor flow formation and bubble size

Single bubble formation from a nozzle or orifice in a Newtonian fluid has been studied by many investigators (for example see Kumar and Kuloor 1967; Kim et al., 1994; Bhunia et al., 1998; Nahral and Kamotani, 2003; Gnyloskurenko et al., 2003). A force balance analysis during the formation process characterised most of these works and two sets of forces, namely detaching and attaching forces, were identified. Factors affecting bubble formation and corresponding forces as proposed by the literature include gas-flux, buoyancy, bubble inertia, liquid inertia, shear-lift, pressure, surface tension and liquid drag (Kim et al., 1994; Bhunia et al., 1998; Nahral and Kamotani, 2000). Their relevant importance is determined by the scale of the system and the flow regime. For example, the attaching effect of surface tension could be predominant at small scales or reduced gravity, while the effect of liquid drag force could be significantly different in a fast flowing compared to a quiescent liquid. Accordingly, various bubble formation models have been developed and the bubble volume was defined. In the single-stage model of Walters and Davidson (1963), the detaching force was considered to be in a continuous balance with the attaching force. Kumar and Kuloor (1967) disagreed with this static model and proposed a dynamic two-stage model, in which a force balance was only achieved at the end of the first stage. The two stages defined were bubble expansion and detachment. During the expansion stage, bubbles reside on the nozzle while during the detachment stage they “lift off” and form a neck connecting them to the nozzle tip. The two-stage model is frequently adopted for the investigation of bubble formation (Kim et al., 1994; Bhunia et al., 1998; Nahral and Kamotani, 2000). Gnyloskurenko et al., (2003) investigated bubble formation from a 1mm diameter orifice at very low gas flowrates of 2ml/min ($U_G = 0.042\text{m/s}$) and

presented a multi-stage model, in which the stages of bubble nucleation, under critical growth, critical growth and necking, were identified.

By equating the detaching and attaching forces, bubble volume can be calculated. At intermediate and low gas flowrates ($<10^4$ ml/s), the effect of the inertia force diminishes (Kumar and Kuloor, 1967), while the effect of surface tension has to be included to balance the buoyancy force. The fact that the discrepancy between model predictions and experimental data increased with decreasing gas flow rate (Gnyloskurenko et al., 2003) suggests that other parameters, apart from surface tension, play a role. In the study of Byakova et al. (2003), bubble volume at low gas velocity was found to depend on wettability. By increasing the equilibrium contact angle, i.e. worsening the liquid wettability on the gas nozzle wall, the bubble volume was found to increase by more than 50%.

Taylor bubble sizes in microchannels, however, cannot be predicted accurately by models based on force balance. On one hand, Taylor bubbles deform significantly as they grow and approach the channel wall, deviating from the spherical shape assumed by most force balance models. On the other hand, at the low Reynolds numbers encountered in microchannels viscous forces are important and have to be taken into account. Some correlations based on both experimental data and numerical simulations have been suggested in the literature (Table 2.3). Laborie et al. (1999) correlated experimentally bubble and slug lengths in 1-4mm capillaries to Reynolds and Eötvös numbers as given by Eq. 2.3 and Eq. 2.4 respectively. A porous membrane was used to form the dispersed phase. Based on the experimental data by Heiszwolf et al. (2001) in a 200cpsi monolith reactor, where a distributor was used for the liquid phase, Kreutzer (2003) suggested Eq. 2.5 for slug length in square channels. Liu et al. (2005) used the dependence of mass transfer coefficient on slug length (Berčić and Pintar, 1997) to derive an empirical correlation (Eq. 2.6) from their experiments in capillaries ranging from 0.9 to 3mm ID and with a T- inlet. The predictions seemed to be good (Figure 10 in their study), but the comparison with Eq. 2.4 and Eq. 2.5 was poor. Eq. 2.6 was further modified by Akbar and Ghiaasiaan (2006) to include gas holdup (Eq. 2.7) by fitting their numerical results and the experimental data by Liu et al. (2005) and Laborie et al. (1999). The comparison had a standard deviation of 19.5%. In another numerical study of Taylor bubble and slug lengths, Qian and Lawal (2006) correlated their 148 set of data obtained by Computational Fluid Dynamics 2D simulations in a microchannel with 1 mm width and T-inlet with different dimensions to derive the length of a unit cell

(one bubble and one slug) (Eq. 2.8). Bubble and slug lengths can be obtained by multiplying the equation with the respective phase holdup. The correlation showed that the bubble and slug lengths depend mainly on the phase holdup and slightly on Reynolds and Capillary numbers. [Garstecki et al. \(2006\)](#) suggested a scaling law (Eq. 2.9) to determine bubble size formed via a T-junction in a rectangular microchannel of width w . The value of α is of the order of 1, depending on the geometry of the T-junction, but is independent of the fluid properties (flow rates and two-phase superficial velocities are between 0.01 to 1 $\mu\text{l/s}$, and 0.1 to 1.1 m/s respectively). In contrast to [Garstecki et al. \(2006\)](#), [Xiong et al. \(2007\)](#) reported for a cross flow inlet that viscosity and surface tension affected bubble size and proposed to replace the channel width w in Eq. 2.9 by bubble width w_B . In their study α was equal to 1. [Cubaud et al. \(2005\)](#), using a cross-flow inlet, also found a correlation similar to Eq. 2.9 where ε_L^{-1} was used instead of $1+Q_G/Q_L$ but without the coefficient α . Another similar correlation using Q_G/Q_L was reported by [Tan et al. \(2009\)](#), who incorporated the angle ω at which the gas and liquid inlets contact (Eq. 2.10). In contrast with [Garstecki et al. \(2006\)](#), they found that viscosity and interfacial tension affected the bubble length and they were taken into account through Ca . This disagreement could probably be because of the higher flowrates used by [Tan et al. \(2009\)](#), which exceed the values as suggested in [Garstecki et al. \(2006\)](#) (0.7-5 $\mu\text{l/s}$ vs. 0.01-1 $\mu\text{l/s}$). In Eq. 2.10, λ is coefficient determined from experimental data. In particular, λ_3 and λ_4 , were regarded to characterize the shape of the interface and the equilibrium between the shear force of the continuous flow and the interfacial tension, and were given as functions of the geometry of the inlet of the main channel respectively ([Tan et al., 2009](#)).

The above correlations show the dependence of bubble and slug sizes on operating conditions and fluid properties. The lack of agreement between the correlations suggests that other parameters also affect the sizes. [Qian and Lawal \(2006\)](#) found significant dependence of bubble and slug lengths on the inlet geometry. By varying T-junction orientation and size of inlet channels as well as the degree of premixing of the two fluids in their numerical simulations, the slug length was found to vary up to 300% under the same operating conditions. In general, small mixing zones and good premixing at the inlet favoured short bubble and slug lengths. Bubble size distributions within the main channel at constant operating conditions have also been observed, e.g. experimentally by [Mantle et al. \(2002\)](#) and theoretically by [Qian and Lawal \(2006\)](#), who attributed them to the toroidal vortices that are generated at the inlet and propagate

throughout the channel length. [Kreutzer et al. \(2005a\)](#) limited the occurrence of uniform slug and bubble sizes to $0.25 < U_{LS}/U_{GS} < 2$.

Table 2.3 Literature correlations on bubble/slug lengths in Taylor flow

	$\frac{L_B}{d_C} = 0.0878 \frac{\text{Re}_B^{0.63}}{Eo^{1.26}}, \text{Re}_B = \frac{\rho_L U_B d_C}{\mu_L},$	Eq. 2.3
Laborie et al. (1999)	$Eo = \frac{(\rho_L - \rho_G) d_C^2 g}{\sigma}$	
	$\frac{L_S}{d_C} = 3451 \left(\frac{1}{\text{Re}'_{GS} Eo} \right)^{1.27}, \text{Re}'_{GS} = \frac{\rho_L U_{GS} d_C}{\mu_L}$	Eq. 2.4
Kreutzer (2003)	$\frac{L_S}{d_C} = \frac{\varepsilon_L}{-0.00141 - 1.556 \varepsilon_L^2 \ln(\varepsilon_L)}, \varepsilon_L \approx \frac{U_{LS}}{U_{GS} + U_{LS}}$	Eq. 2.5
Liu et al. (2005)	$\frac{U_{TP}}{\sqrt{L_S}} = 0.088 \text{Re}_{GS}^{0.72} \text{Re}_{LS}^{0.19*}, \text{Re}_{GS} = \frac{\rho_G U_{GS} d_C}{\mu_G},$ $\text{Re}_{LS} = \frac{\rho_L U_{LS} d_C}{\mu_L}$	Eq. 2.6
Akbar and Ghiaasiaan (2006)	$\frac{U_{TP}^{-0.33}}{\sqrt{L_S}} = 142.6 \varepsilon_G^{0.56} \left(\frac{d_C}{L_{UC}} \right)^{0.42} \text{Re}_{GS}^{-0.252*}, \varepsilon_G = \frac{U_{GS}}{U_B}$	Eq. 2.7
Qian and Lawal (2006)	$\frac{L_B + L_S}{d_C} = 1.637 \varepsilon_G^{-0.893} (1 - \varepsilon_G)^{-1.05} \text{Re}_B^{-0.075} Ca^{-0.0687},$ $\varepsilon_G \approx \frac{U_{GS}}{U_{GS} + U_{LS}}, Ca = \frac{\mu_L U_B}{\sigma}$	Eq. 2.8
Garstecki et al. (2006)	$\frac{L_B}{w} = 1 + \alpha \frac{Q_G}{Q_L}, Q < 0.06 \text{ml/min}, Ca < 10^{-2}$	Eq. 2.9
Tan et al. (2009)	$\frac{L_B}{w} = \lambda_1 \left(\frac{Q_G}{Q_L \sin \omega} + \lambda_2 \cot \omega \right)^{\lambda_3} Ca^{\lambda_4}$ $Q < 0.24 \text{ml/min}, Ca < 10^{-2}$	Eq. 2.10

* Equation is not dimensionless and units are in SI

Systematic experimental investigations on the effect of inlet conditions on Taylor flow were carried out by [Amador et al. \(2004\)](#) and [Salman et al. \(2006\)](#). Taylor bubble formation from a nozzle in a channel was found to follow three mechanisms: formation of a gas chamber at the top of the gas nozzle with the bubble detaching from the end of

it; formation of a meniscus at the nozzle that leads to pressure built up behind it until the gas finally erupts to form a bubble; the third mechanism is similar to the two-stage model known in the literature. Bubble lengths, formed at T- and Y- junction and co-flow configurations with various gas/liquid inlet dimensions, were found to depend significantly on the ratio of gas to liquid superficial velocities and gas inlet diameter for any given geometry. According to [Garstecki et al. \(2006\)](#) under typical conditions in microchannels (widths and heights of the order of 10 to 100 μ m, flow rates of the order of 0.01 to 1 μ l/s and $Ca < 10^{-2}$), where interfacial forces dominate shear stresses, bubble break-up is controlled by the pressure drop across the bubble. A “squeezing mechanism” was suggested to describe the process: the expansion of gas phase to the entire cross section of the main channel confines the liquid phase to the film region, and builds up pressure upstream the liquid that leads to the “squeezing” of the bubble neck until complete bubble breakage. However, the model is only appropriate when the width to the height ratio of the main channel is larger than 1 and the gas inlet to the main channel width ratio is larger than 0.5. Bubble size was found to be dependent on the ratio of the volumetric flowrates of the two phases and the T-junction geometry (see Eq. 2.9), which agreed with [Amador et al. \(2004\)](#). [Haverkamp et al. \(2006\)](#) characterized gas-liquid flow in single and multiple rectangular microchannels by using two inlet mixing geometries. For both of them the gas-feed was flanked by two equal liquid inlets, but the channel connecting to the main channel had different designs. In the T-mixer, the width of the connecting channel followed a two-stage reduction while in the smooth mixer the width of the channel was smoothly reduced. The mixer design was reported to affect the flow pattern map and the bubble formation mechanism. In the smooth mixer bubble sizes were reduced and the bubble size distribution was narrower compared to the T-mixer.

2.5.3 Bubble velocity

The shape and the velocity of a bubble ascending through a stagnant liquid have been found to be influenced by the forces acting on it, namely the viscous, inertial and interfacial forces. Three dimensionless numbers can sufficiently characterize the motion of single Taylor bubbles, namely Eötvös number $E\ddot{o} = g(\rho_L - \rho_G)d^2/\sigma$, Morton number $Mo = g\mu_L^4(\rho_L - \rho_G)/\rho_L^2\sigma^3$ and Froude number $Fr = U_B/[gd(\rho_L - \rho_G)/\rho_L]^{0.5}$. The Eötvös number represents the relative significance of buoyancy over surface tension forces. The Morton number is referred to as the property group. The Froude number represents the ratio of inertial to gravitational forces. [Taha and Cui \(2006b\)](#) summarized data from

experiments and correlations as well as their numerical simulations in one $Fr \sim E\ddot{o}$ map and found good agreement for Taylor bubble rising velocity in stagnant low viscosity liquids in vertical channels (Figure 2.12).

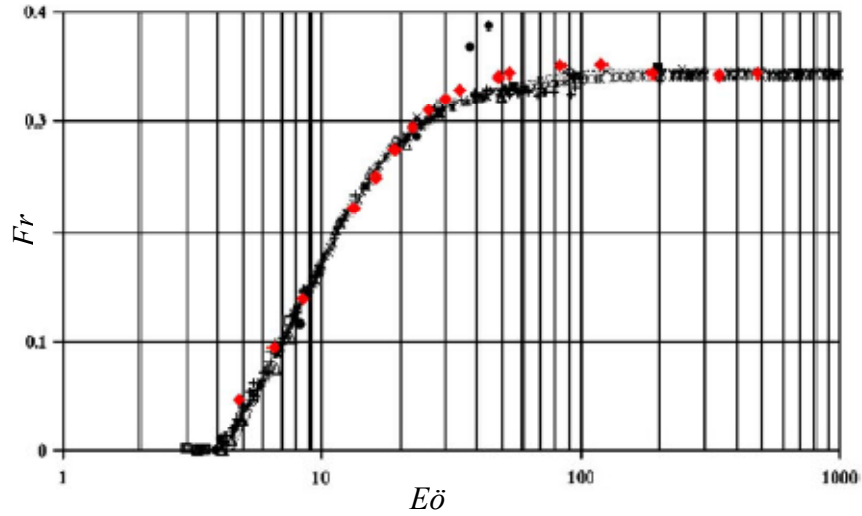


Figure 2.12 Taylor bubble rise velocity in stagnant water and dilute aqueous solutions contained in vertical tubes (Taha and Cui, 2006b).

The pioneering work of Nicklin et al. (1962) initiated the investigation of bubble motion in flowing liquids by recognising that the bubble velocity consists of two components:

$$U_B = U_0 + C_I U_{TP} \quad \text{Eq. 2.11}$$

where U_0 represents the bubble velocity in a stagnant liquid, while the second term refers to the transport of the bubble by the liquid slug average velocity. C_I is an experimentally determined coefficient depending on the velocity profile ahead of the bubble and is taken $C_I \approx 1.2$ for turbulent flow and $C_I \approx 2$ for laminar flow (Collins et al., 1978). In small capillaries, the bubble drift velocity is very small compared with the average slug velocity due to the enlarged surface tension force and Eq. 2.12 is used. Laborie et al. (1999) found that C_I is a function of $E\ddot{o}$. When $E\ddot{o} \rightarrow 0$, C_I tends to a value of 1.7, while when $E\ddot{o} > 0$, C_I was found to depend on the fluid property number $N_f ((E\ddot{o}^3/Mo)^{1/4})$. A modified model was introduced by Fukano and Kariyasaki (1993) and Mashima and Hibiki (1996) given as Eq. 2.13 where C_I and C_2 depend on tube diameter and liquid properties. Liu et al. (2005) proposed a correlation (Eq. 2.14) which fitted well to their experimental results carried out in both circular and square channels with various working liquids. The Ca ranges from 0.0002 to 0.39. Akbar and Ghiaasiaan (2006) found that Eq. 2.14 predicted well their numerical Taylor bubble velocity results in a 1mm capacity within Ca range of 0.005 to 0.05. Eq. 2.14 will be used throughout this thesis for bubble velocity prediction.

$$U_B = C_1 U_{TP} \quad \text{Eq. 2.12}$$

$$U_B = C_1 U_{TP}^{C_2} \quad \text{Eq. 2.13}$$

$$\frac{U_B}{U_{TP}} = \frac{1}{1 - 0.61Ca^{0.33}} \quad \text{Eq. 2.14}$$

$$\frac{U_B}{U_{TP}} = \frac{1}{\left(1 - 2\frac{\delta_{B-B'}}{d_H}\right)^2 - \left(1 - \frac{\pi}{4}\right)\left(1 - 2\frac{\delta_{B-B'}}{d_H} - \frac{w_{film}}{d_H}\right)^2} \quad \text{Eq. 2.15}$$

Yue et al. (2008) studied the Taylor flow hydrodynamics and proposed Eq. 2.15 for the bubble velocity in square microchannels, assuming that the liquid film is at rest at small Ca (<0.04). In these channels the bubble would be expected to have a non-axisymmetric shape under such Ca as seen in Figure 2.13, where $\delta_{B-B'}$ and w_{film} are the film thickness surrounding the body of the bubble and the width of the film in the axial plane respectively (Figure 2.13).

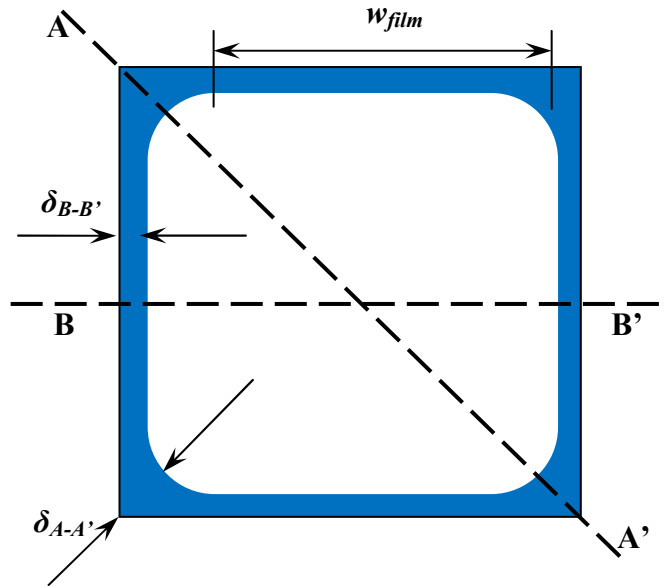


Figure 2.13 Liquid film shape in square microchannel with non-axisymmetric bubble ($Ca < 0.04$, Yue et al. 2008).

2.5.4 Film thickness

At proper contact angle and capillary number as discussed in Section 2.4, the Taylor bubbles are separated from the capillary wall by a very thin liquid film. Shear stress on the bubbles from the film is much smaller than from the wall the bubbles usually travel with a velocity U_B slightly greater than the volume-average liquid velocity U_{TP} . The

difference determines the flow rate in the liquid film Q_{film} from simple mass balance on the cross section of the bubble cylindrical body (Eq. 2.16).

$$Q_{film} = (U_B - U_{TP}) \frac{\pi d^2}{4}, U_{TP} = \frac{4(Q_L + Q_G)}{\pi d^2} \quad \text{Eq. 2.16}$$

where Q_G and Q_L are flowrate of gas and liquid phase respectively.

$$\frac{\delta}{d} = 0.66Ca^{2/3} \quad \text{Eq. 2.17}$$

$$\frac{\delta}{d} = \frac{0.66Ca^{2/3}}{\left(1 + 3.33Ca^{2/3}\right)} \quad \text{Eq. 2.18}$$

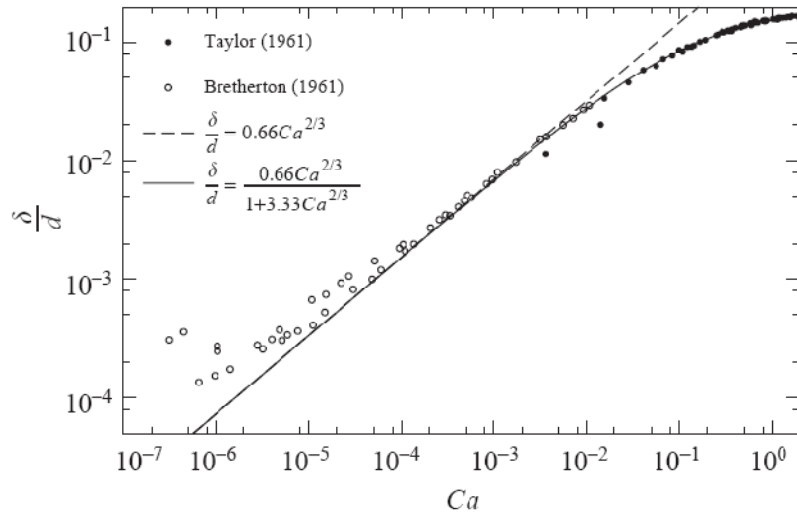


Figure 2.14 Film thickness as a function of the capillary number Ca . Bretherton used aniline and benzene, while Taylor used a syrup–water mixture, glycerine and lubricating oil. [Kreutzer et al., \(2005b\)](#).

Early experimental investigations by [Fairbrother and stubbs \(1935\)](#) yielded an empirical correlation for the ratio of the cross section of the capillary occupied by a wetting film. For Ca up to 10^{-2} , the fraction was found to be proportional to the square root of Ca . [Taylor \(1961\)](#) extended this upper limit to 10^{-1} and pointed out that at high Ca the ratio approach asymptotically a constant value of 0.56 instead of following the square root correlation. Other correlations of film thickness found in literature were mostly a function of Ca as well. [Bretherton \(1961\)](#) used lubrication analysis for the transitional region between the bubble front and the cylindrical bubble body and proposed a dimensionless film thickness Eq. 2.17. Figure 2.14 shows how the dimensionless film thickness changes with Ca . The deviation of the slope from 2/3 was attributed to the

increasing importance of Marangoni effects at small Ca (Bretherton, 1961). Other reports gave the same order of magnitude for the film thickness but with slightly different slopes. For example Fairbrother and Stubbs (1935) found 0.5, Irandoust and Andersson (1989) found 0.54 and Halpern et al. (1998) found 0.52. The slope difference could be due to the different wall roughness effects. Aussillous and Quéré (2000) presented a correlation (Eq. 2.18) that accurately fitted to data of Bretherton (1961) and Taylor (1961) for a wide capillary range from 10^{-4} to 10^0 and will be used in this thesis.

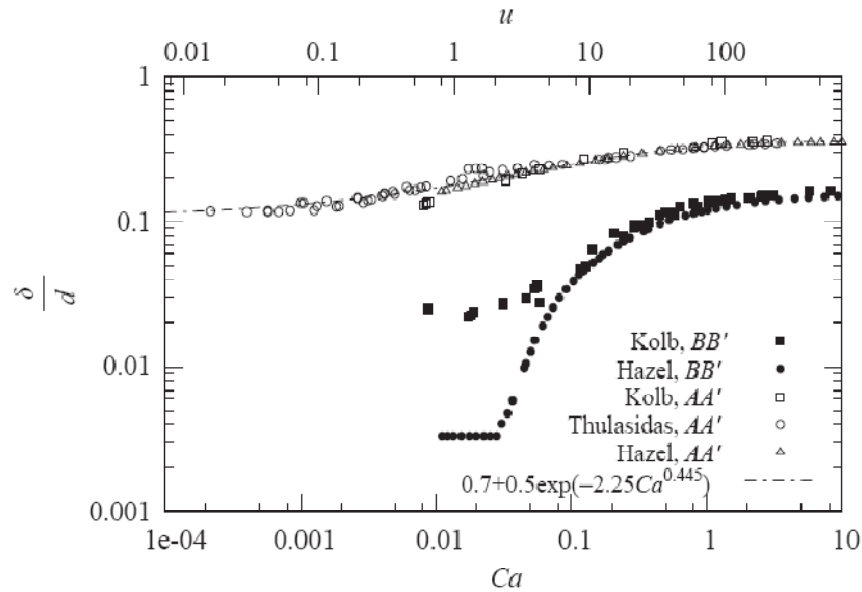


Figure 2.15 Dimensionless film thickness versus Ca in square capillaries. On the top axis, the velocity of the bubble is plotted, assuming water-like properties $\mu_L = 10^{-3} \text{Pa s}$ and $\sigma = 0.073 \text{ N/m}$ (Kreutzer et al., 2005b).

In non-circular channels the presence of corners causes non-uniformities in the film thickness. A schematic graph of the liquid film in square capillaries is shown in Figure 2.13. Kreutzer et al. (2005b) summarized in Figure 2.15 film thickness from experimental data by Thulasidas (1995) and Kolb and Cerro (1991), and from numerical simulations by Hazel and Heil (2002). In A-A' direction, the film thickness approach a non-zero asymptote at high Ca which shows that a constant liquid film exists in the corners even at very low velocities. The data of Kolb and Cerro (1991) and Hazel and Heil (2002) in direction BB' deviated from each other when $Ca < 0.1$ but showed that the film thickness approaches an asymptotic value at a Ca smaller than 0.04. For $Ca > 3$ the bubble shape becomes axisymmetric similar to that in circular channels. This was verified in the numerical study of Taha and Cui (2006a) as discussed in Section 2.5.1. In summery, the region of $Ca < 0.04$ is usually of interest in monolithic reactors. The

dimensionless film thickness in A-A' direction is constant, which was 0.0025 in Hazel and Heil (2002) and 0.02 in Kolb and Cerro (1991). A close examination of the experimental conditions is recommended when using the correlations. For the diagonal direction A-A', Kreutzer et al. (2005b) fitted the experimental bubble diameter with the following corrections:

$$\frac{d_{B,A-A'}}{d_c} = 0.7 + 0.5 \exp(-2.25Ca^{0.445}) \quad \text{Eq. 2.19}$$

2.5.5 Flow patterns in liquid slugs

The description of flow patterns in liquid slugs dates back to the pioneering work of Taylor (1961), who postulated the main features of the possible flow patterns (Figure 2.16). At high Ca , for $m > 0.5$, a complete bypass flow pattern was envisaged (Figure 2.16a) and there is no recirculation forms in the liquid slugs. At small Ca , for $m < 0.5$, two possible patterns were sketched. In one case, a stagnation ring formed around the bubble cap with the stagnation point at the bubble cap tip (Figure 2.16b). In the other case, two stagnation points appeared inside the liquid slug and at the bubble tip (Figure 2.16c). Taylor's speculations of patterns (a) and (b) were confirmed experimentally by Cox (1964) and Thulasidas et al. (1997). Thulasidas et al. (1997) suggested that pattern (a) appeared at $Ca > 0.47$ and (b) at $Ca \leq 0.15$ for Re ranging from 10^{-4} to 2.

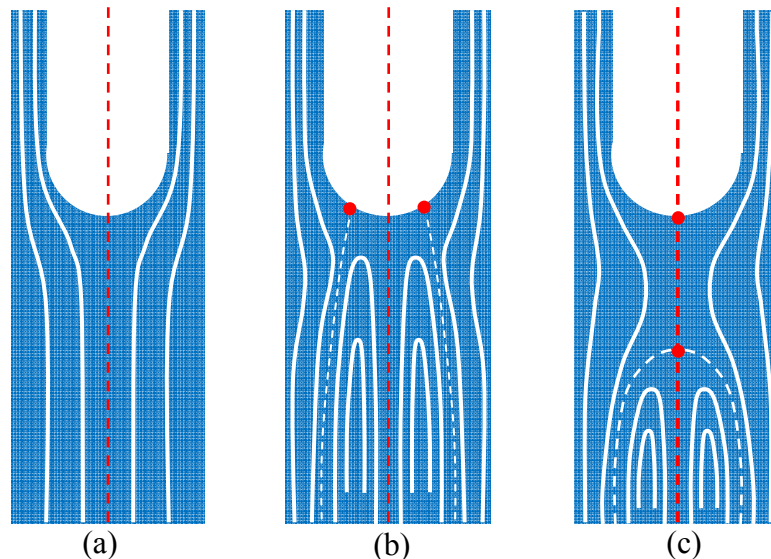


Figure 2.16 Sketch of liquid streamlines for the flow of elongated bubbles in capillaries. (a) $m > 0.5$, total bypass; (b),(c) $m < 0.5$, formation of stagnation ring. The quantity m is

$$\text{defined as } \frac{U_B - U_{TP}}{U_B} \quad (\text{Taylor, 1961}).$$

Numerical confirmations were also available from [Martinez and Udell \(1989\)](#) at Ca of 0.7 corresponding to $m = 0.5$, and [Taha and Cui \(2006b\)](#) (Figure 2.17). The latter observed that with increasing Ca , the vortex in the liquid slug becomes smaller and the radial position of the vortex centre shifts towards the capillary axis until the bypass streamlines are fully developed. In another numerical study of [Giavedoni and Saita \(1997\)](#) at $Re = 0$, all three patterns were observed where (c) only appeared as a transition pattern within a narrow Ca range from 0.6 to 0.69. The $Ca < 0.6$ value for (b) was suggested in their study.

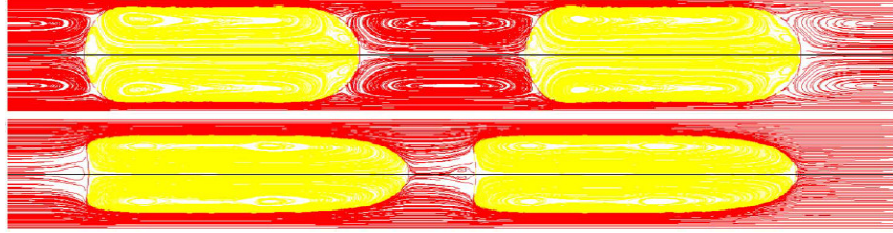


Figure 2.17 Velocity field in Taylor flow inside circular capillaries ($d = 2\text{mm}$) with a reference frame moving with the bubble ([Taha and Cui, 2006b](#)). $Ca = 0.032$ for the top pattern, and the streamlines bow sharply to complete the vortex path similar to Figure 2.16 (b); in the bottom one, $Ca = 0.924$ and the vortex is hardly seen to form a bypass pattern similar to Figure 2.16 (a).

$$r^0 = r \frac{\sqrt{2 - \Psi}}{\sqrt{2}}, \Psi = \frac{U_B}{U_{TP}} \quad \text{Eq. 2.20}$$

$$r^1 = r \sqrt{2 - \Psi}, \Psi = \frac{U_B}{U_{TP}} \quad \text{Eq. 2.21}$$

Since small Ca is of interests to this study, pattern (b) will be relevant in most cases given that pattern (c) only exists within a narrow range of Ca . A close examination of pattern (b) shows that the streamline across the stagnation points separates the flow into film and recirculation regions with no convective exchange between the two. Liquid in the film region flows past the bubbles from the downstream slug to the upstream one, obstructing any direct contact between the circulating vortex and the wall. Therefore, Taylor flow involves an essentially diffusive step across the film region and an essentially convective step in the recirculation region, characterized by a loop-shaped motion with a stagnation area in the centre. At small Ca in circular channels when the film is thin, the film thickness between the slug and the wall is comparable to that between the bubble and the wall. While at large Ca or in non-circular channels with corners, the film thickness between the slug and the wall has to be determined from the position of the dividing streamline. The radial position of both the centre of the toroidal

vortex r^0 and of the stagnation streamline r^l was given in Eq. 2.20 and Eq. 2.21 (Thulasidas et al., 1997).

2.5.6 Mass transfer

Microchannel reactors take advantage of dramatically reduced heat and mass transfer limitations, resulting in highly efficient, ultra-compact systems that exhibit performances superior to conventional systems. This is particularly true for reactors operating in Taylor flow, where the existence of Taylor bubbles modifies the single-phase liquid flow pattern, decreasing axial and improving radial mixing by the presence of vortices. The large exchange area in the film and slug contributes to the increased mass transfer and this feature becomes more important as the size of the microchannel decreases. For example, Vandu et al., (2005) investigated mass transfer characteristics of monolith reactors operating in Taylor flow and compared them with conventional internal airlift and bubble column reactors, concluding that the volumetric mass transfer coefficient, $k_L a$, is significantly higher in monolith reactors than in the other two configurations.

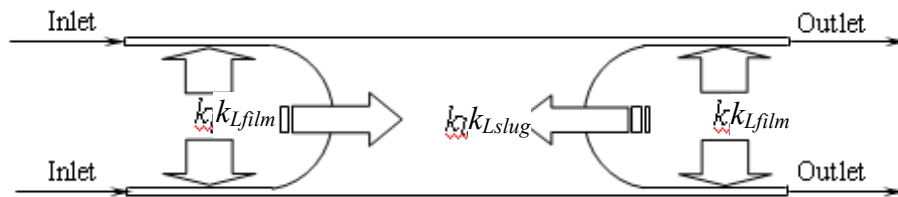


Figure 2.18 Mass transfer in a Taylor flow unit cell. The horizontal arrows: gas to liquid mass transfer occurring into the liquid slug from the bubble caps; The vertical arrows: gas to liquid mass transfer occurring into the liquid film from the bubble.

In Taylor flow, each unit cell (a slug with two half bubbles or a bubble and a slug) resembles a reactor (Figure 2.18). The stagnation streamlines (Figure 2.16) divide the flow into the film region and the slug region (where recirculation happens). A gas component can be transferred to the two regions directly and there is only diffusive transport between these two regions. Because of the different interfacial areas and diffusion lengths in the two regions, it is more accurate to use separate gas-liquid mass transfer coefficients, namely k_{Lfilm} for the film and k_{Lslug} for the slug region (Figure 2.18). The overall mass transfer coefficient can then be expressed as:

$$k_L a = k_{Lfilm} a_{film} + k_{Lslug} a_{slug} \quad \text{Eq. 2.22}$$

Most of gas-liquid chemical processes involve mass transfer of one or more species from the gas to the liquid phase while reaction follows if one or more reactants exist in the bulk liquid. Usually, the transfer proceeds along the following steps:

Step 1: Diffusion of reactants from the gas phase to the gas-liquid interface.

Step 2: Diffusion of the reactants from the interface towards the bulk of the liquid phase.

Step 3: Chemical reaction within the liquid phase.

Step 4: Diffusion of the reactants initially present within the liquid phase and reaction products within the liquid phase due to the concentration gradients created by the chemical reaction.

Step 1 does not provide any mass transfer resistance if there is no concentration gradient in the gas, i.e. pure gas. Even if the gas phase is a mixture, the resistance can be ignored compared to that in the liquid phase. *Steps 2* and *3* cannot be eliminated except under limiting conditions which depend on the relative dominance of the kinetic or mass transfer rates as well as the specific area.

A number of investigators have attempted to calculate the mass transfer coefficients for physical gas absorption. [Irandoust et al. \(1992\)](#) studied experimentally oxygen absorption into water, ethanol and ethylene glycol and used penetration theory and the correlation by [Clift et al. \(1978\)](#) to develop a mass transfer model that included contributions from the bubble cap and from the film side of the bubble to the liquid. A correction factor needed to be applied to match the theoretically derived k_La with the experimental data while the results indicated that both bubble caps and the bubble side in the film contributed to mass transfer. [Berčič and Pintar \(1997\)](#) studied methane absorption in water and developed an equation for the mass transfer coefficient using a CSTR by-pass model (Eq. 2.23). k_La was found to depend on slug length only, which can probably be attributed to the relatively large bubble lengths (overall unit cell length is up to 0.22m) used in the study where the film becomes quickly saturated and unable to contribute further to gas absorption. A Computational Fluid Dynamics (CFD) study for mass transfer in capillaries under Taylor flow was carried out by [van Baten and Krishna \(2004\)](#), who confirmed that both the bubble caps and the film side of the bubble contribute to mass transfer. A correlation was developed for k_La (Eq. 2.24) using penetration theory which compared favourably with the CFD results. For rather short unit cells (with most $L_{UC} < 0.025\text{m}$), [Vandu et al. \(2005b\)](#) developed a k_La correlation (Eq. 2.25) based on the $k_{L,film}$ suggested by [van Baten and Krishna \(2004\)](#), assuming that the film contribution was dominant. A value of 4.5 for C_I was found to fit best the

experimental data of air absorption in water in 1-3mm diameter capillaries of circular and square cross-sections. For short contact times, i.e. short bubble length at the same bubble velocity, mass transfer was found to be a function of channel dimension (Eq. 2.24 and Eq. 2.25). [Yue et al. \(2007\)](#) investigated CO₂ physical and chemical (into NaHCO₃/Na₂CO₃ buffer solution and NaOH solution) absorption in a rectangular microchannel ($d_H = 667\mu\text{m}$) and derived a correlation for the mass transfer coefficient under slug flow (Eq. 2.26).

$$k_L a = 0.111 \frac{(U_G + U_L)^{1.19}}{((1 - \varepsilon_G)L_{UC})^{0.57}} \quad \text{Eq. 2.23}$$

$$k_L a = 2 \frac{\sqrt{2}}{\pi} \sqrt{\frac{DU_B}{d}} \frac{4}{L_{UC}} + \frac{2}{\sqrt{\pi}} \sqrt{\frac{DU_B}{\varepsilon_G L_{UC}}} \frac{4\varepsilon_G}{d} \quad \text{Eq. 2.24}$$

$$k_L a = C_1 \sqrt{\frac{DU_G}{L_{UC}}} \frac{1}{d_H} \quad \text{Eq. 2.25}$$

$$Sh_L \cdot a \cdot d_H = 0.084 Re_G^{0.213} Re_L^{0.912} Sc_L^{0.5} \quad \text{Eq. 2.26}$$

2.6 Microstructured reactors

Various types of reactors have been used in traditional chemical engineering for gas-liquid reactions, e.g. agitated tank, slurry, bubble column, packed bed, spray column, falling-film, loop, trickle-bed, static mixer, spinning disk. These reactors have been well studied and most are used in industry. There are various criteria for selecting a reactor type such as production output, reaction rate, residence time, volumetric ratio of phases, exothermicity, heating-cooling requirements, ease of scale-up, etc. ([Hessel et al., 2005](#)). According to the literature the liquid side volumetric mass transfer coefficient $k_L a$ and specific area a are typically in the order of $10^{-4}\text{-}1\text{s}^{-1}$ and $10\text{-}1000\text{m}^2/\text{m}^3$ ([Yue et al., 2007](#)). With the advances in microengineering technology, some of these reactors are scaled down, e.g. falling-film and bubble column reactors, to benefit from the large surface-to-volume ratio in small scales. Therefore, a new family of reactors using microengineered structures appeared that attract increasing attention. According to [Comyns \(2007\)](#), microstructured reactors are (generally, but not exclusively) reactors with three-dimensional structures, with some inner dimension under a millimetre in size, and more specifically between ten and a hundred micrometres. They are used for liquid phase, gas-liquid and gas phase reactions. In addition, many new types of microstructured reactors have also been developed, such as mesh reactor and Taylor flow microreactor. These reactors extend the capabilities of conventional ones due to the significantly enhanced heat and mass transfer rates achieved in the small dimensions.

According to Hessel et al., 2005, $k_L a$ of the order of 10s^{-1} and specific areas as high as $50000\text{m}^2/\text{m}^3$ have been achieved in gas-liquid microstructured reactors, which are significant improvements compared to conventional gas-liquid contactors. Other advantages of microstructured reactors include improved reaction control and safety. The advantages represent a means for process intensification and make microstructured reactors suitable especially for fast exothermic reactions, e.g. fluorination, oxidations, sulfonations, photochemical and polymerization reactions (Löb et al., 2004; Chambers et al., 2004; Müller et al., 2005; Jähnisch et al., 2004, Lida et al., 2008), where microstructured reactors demonstrated performance advantages in terms of selectivity, space-time yield and safety. However, these devices have been relatively expensive due to the lack of an adequate low-cost manufacturing procedure and investigations of microstructured reactors have been limited in the lab with few examples of commercialisation (Brophy, 2005). The boost of the idea of “lab on a chip” accelerates the progress in microengineering technology that is important for the development of microstructured reactors. From chemical engineering point of view, flow consistency that would need to be overcome for a successful commercialization of the devices, flow characterization, as well as reactor scale-out, remain challenging topics.

2.6.1 Contact principles for gas-liquid microreactors

Normally, the design of microstructured reactors follows one of two contact principles for the gas and liquid phases. The first one is to keep both phases continuous and use the reactor to create an interface between them. In the other principle one phase is dispersed into the other using an appropriate inlet or a micromixer upstream of the reaction section. Reactors employing these principles are named *continuous-phase microreactors* and *dispersed-phase microreactors* respectively (Hessel et al., 2005).

2.6.1.1 Continuous-phase microreactors

In the continuous-phase microreactor, the gas and liquid phases are fed into the reactor separately and form two streams inside the reactor with an interface between them. Ideally, the two streams are withdrawn separately at the reactor outlet; therefore, it is not common for continuous-phase microreactors to be integrated with a gas-liquid separator. The falling-film and mesh reactors are two examples in this category.

Falling-film microreactor works by creating a thin falling liquid film on a wetted solid support under the action of gravity (Figure 2.20a). The solid support can be either a thin wall or stack of pipes. Depending on the liquid properties and its flowrate, the following

2. Literature Survey

flow regimes can occur: corner rivulet flow, falling film flow with dry patches and complete falling film flow (Figure 2.19b, Zhang et al., 2009). Conventional falling film reactors generate films with thickness of the order of 0.5-3mm (Dabir et al., 1996; Karimi and Kawaji, 1998) while in falling film microreactors, film thicknesses under 100 μ m have been reported (Jähnisch et al., 2000; Zanfir et al., 2005), leading to more than one order of magnitude higher specific area compared to conventional ones (up to 20000m²/m³ vs. 300-600m²/m³). Its relatively simple and well defined geometry has allowed number of models to be developed to characterise the falling film reactor such as 2D model by Zanfir et al., 2005, 3D simulations by Al-Rawashdeh et al., 2008, while it has also been used in pilot scale for the oxidation of an organic compound (Vankayala et al., 2007).

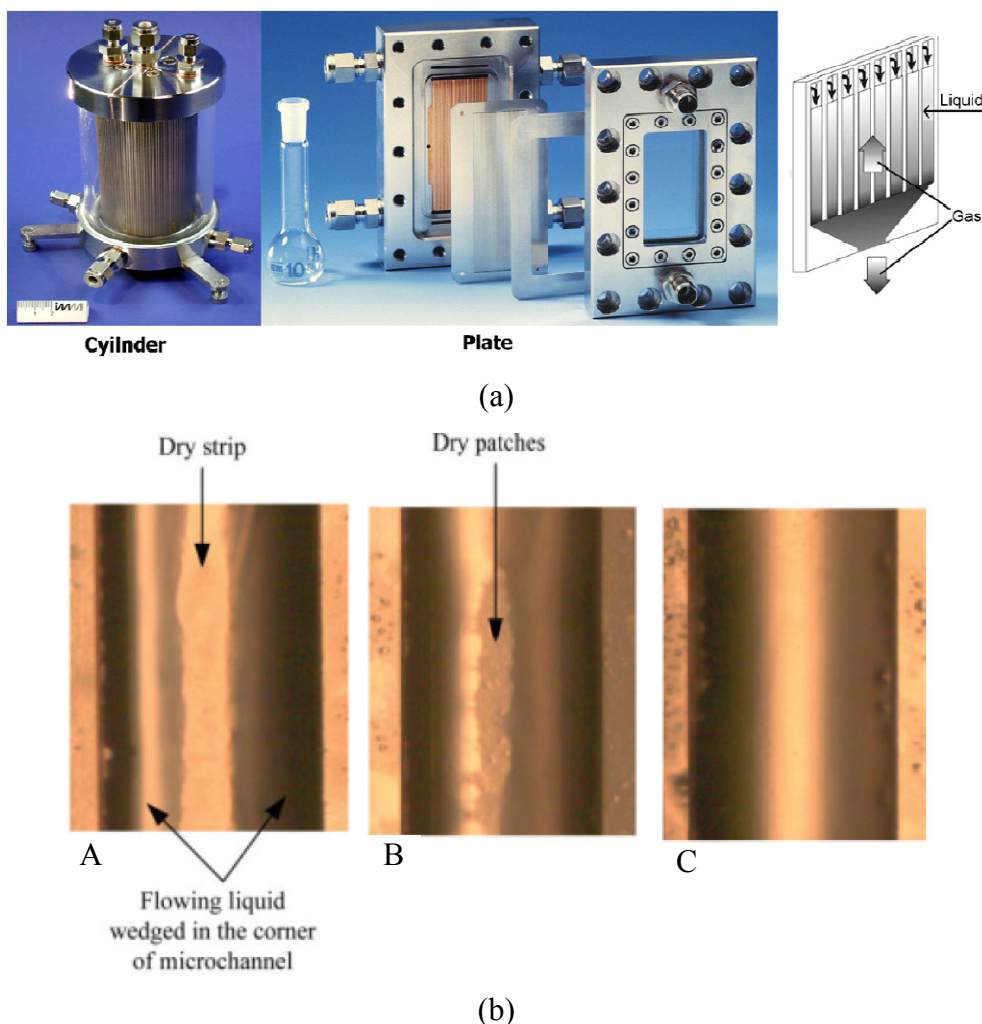


Figure 2.19 (a) Falling-film microreactor and schematic showing the gas-liquid contacting (Al-Rawashdeh et al., 2008); (b) flow patterns observed in falling-film microreactor (Zhang et al., 2009). A: corner rivulet flow; B: falling film flow with dry patches; C: complete falling liquid film flow.

In Mesh microreactor the gas-liquid interface is stabilized by well-defined openings on the plate that separates the two phases (Figure 2.20). The fluid layers have to be thin enough to promote fast mass and/or heat transfer (Hessel et al., 2005). The opening dimensions are typically in the range of 1-10 μm to stabilize the interface (Hessel et al., 2005), making this type of microreactor exclusively to micro-scale. Both co-current and counter-current operations are possible and the two phases ideally remain separated at the outlet. The pressures of the two phases have to be accurately controlled to prevent intermixing, which is technically demanding and limits the range of flowrates that can be used. In addition, significant axial dispersion can be present for typical liquid-phase diffusivity values (Hardt et al., 2002).

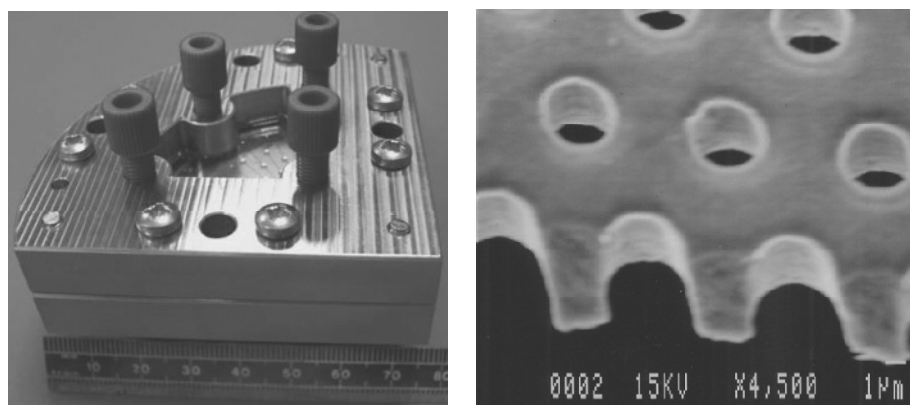


Figure 2.20 Assembled mesh microreactor and a scanning electron micrograph of the mesh pores (Wenn et al., 2003).

One special type of continuous-phase microreactor is the annular flow microreactor, where a thin annular liquid film surrounds a gas core (Section 2.2). The reactor in this case is a channel (as in the dispersed-phase microreactors) but the gas velocity and the gas-to-liquid flowrate ratio are very high. However, in contrast to other continuous phase microreactors, there is no need to manipulate the two phase pressures in order to keep the phases separate.

2.6.1.2 *Dispersed-phase microreactors*

The dispersed-phase microreactors are normally a channel or tube with or without some internal structures. The gas-liquid dispersion is created at the reactor inlet, where various designs have been suggested, e.g. T-junction, flow-focusing inlet, etc. The gas and liquid phases are separately brought into the reaction channel and they mix at the inlet. For multiple feed structure, a micromixer may be added upstream of the gas and liquid inlet to induce fluid lamellae (Hessel et al., 2000). Due to the intermixed nature of

the system, a gas-liquid separator may be needed if the phases are to be collected separately. Depending on the gas and liquid superficial velocities and flow control mechanism, different flow patterns can form inside the reaction channel.

One of the most frequently encountered flow patterns is Taylor flow (Figure 2.3) which apart from the large surface to volume ratio, also offers advantages such as high radial mixing, low axial dispersion and control of each unit cell (Section 2.5) as an individual reactor. This pattern is also encountered in monolith reactors and has received a lot of attention (Section 2.5). In microreactors, Taylor flow is adopted for both multiphase and single phase reactions. In the former, the dispersed phase contains a reactant and the reaction occurs either in the liquid or at the reactor wall. In the latter, an inert gas stream is introduced to create Taylor bubbles that enhance the mixing in the liquid. Gas (G-L) and liquid (L-L) configurations can be used to create segments of the reaction phase (Song et al., 2003; Yen et al. 2005). Normally G-L flow is preferred because it offers the following advantages (Yen et al. 2005): firstly, the system has better performance in reactions with elevated temperature since most solvents are expected to experience increased miscibility at high temperatures. Secondly, gas-liquid Taylor flow can be operated under a very large range of bubble velocities (over two orders of magnitude) and therefore reaction timescales. Finally, for liquid phase reactions, the reactive phase is the continuous phase which makes easy additional injection of reactants or withdrawal of reactant aliquots.

Hessel et al. (2000) and Haverkamp et al. (2006) used arrays of microchannels operating in Taylor flow and referred to them as microbubble column. In microbubble columns, bubbly flow (Figure 2.2) is the dominant flow pattern; however, coexistence of different flow patterns has been observed and was attributed to the maldistribution of the flows at the inlet (Hessel et al., 2000). Besides of the same operating bubbly flow regime, one microbubble column resembles its conventional counterpart (bubble column) in terms of structure and contacting principle. The determinant distinction between the two reactor types is the residence time, which is of the order of seconds or below in microbubble column and hours (pilot or industrial scale with tube length in the order of metres or several tens of metres) in conventional bubble columns (Haverkamp et al., 2006).

Foam microreactor is characterized by small bubbles that form in a micromixer at the inlet, packed together in the reaction channel, with dimensions normally in the millimetre range (Hessel et al., 2005). Coalescence of bubbles along the reactor length

is not uncommon, but can be controlled by modifying the viscosity and surface tension when the reaction chemistry is not affected (Hessel et al., 2005).

In contrast to the continuous-phase microreactors, a large range of gas to liquid flowrate ratios is possible and a wide range of flow regimes can be realized in dispersed-phase microreactors. Each flow unit for dispersed flow, e.g. a unit cell in Taylor flow (Section 2.5), can be treated as an individual reactor that can be individually analysed. Axial dispersion is greatly reduced in dispersed-phase microreactors, especially in Taylor flow microreactors, which limits the occurrence of back-mixing and improves residence time distribution. Because of the laminar flow, the consistency in the formation frequency of the dispersed phase and thus the interfacial area can be well manipulated (Teh et al., 2008). However, only co-current operation is possible, which may limit their applications. In addition, extra efforts may be required to separate the phases at the reactor outlet while the dispersed phase may undergo coalescence along the reaction channel, which will alter the interfacial area and the performance of the microreactors.

2.6.2 Structure design of microstructured reactors

The geometric structure of microreactors, including the inlet and the outlet, plays an important role in determining its performance, because it can affect mixing rates, hydrodynamics, and heat and mass transfer. For example, a number of investigations have shown that Taylor flow hydrodynamics and mass transfer performance depend on slug length (Irandoust et al., 1992; Kreutzer, 2003) which depends on the geometry of the inlet (Garstecki et al., 2006). Kreutzer et al. (2005c) studied maldistribution of the feed in monolith reactors during scaling-up and reported that the extent of maldistribution depended on the distributor used while a static mixer system was a better distributor than a nozzle. In addition, operations such as reactant injection, phase separation, local temperature and concentration gradient control, reaction quenching, can also be achieved through appropriate channel structure.

A number of designs have been suggested in the literature for the microreactor inlet, main channel, and outlet, which are reviewed below. Some designs are not for gas-liquid systems, e.g. water-oil system (Song et al., 2003), but they provide insights for the structure design for microreactors and thus are included.

2.6.2.1 Inlet design

The inlet is an important part of the microreactor particularly for the dispersed flow regimes because they bring together the phases and affect the mechanism of dispersed

phase formation and its size which will influence the interfacial area and mixing. As a result, there have been quite a few studies on inlet geometries that resulted in a variety of inlet designs. The T-junction is one of the widely adopted inlet configurations, in which the two phases join at opposite directions (Figure 2.21a). It is also common that one phase is fed into the main channel while the other joins at 90° (Figure 2.21b, e.g. [Garstecki et al., 2006](#)). When the inlet channels for the dispersed and continuous phases join at an angle $<180^\circ$, the inlet design is known as a Y-junction (Figure 2.21c, e.g. [Kumar et al., 2007](#)). When two inlet channels are used for either the gas or liquid phase and they flank the inlet channel of the other phase, a cross-junction is formed (Figure 2.21d, e.g. [Cubaud et al., 2005](#)). When the two inlet channels in the cross-junction join the third inlet channel at an angle less than 90° , then a flow-focusing inlet is formed (Figure 2.21e, e.g. [Haverkamp et al., 2006](#)). It is worth to note that the dimensions of all the inlet channels are not necessarily the same among themselves or with the main channel.

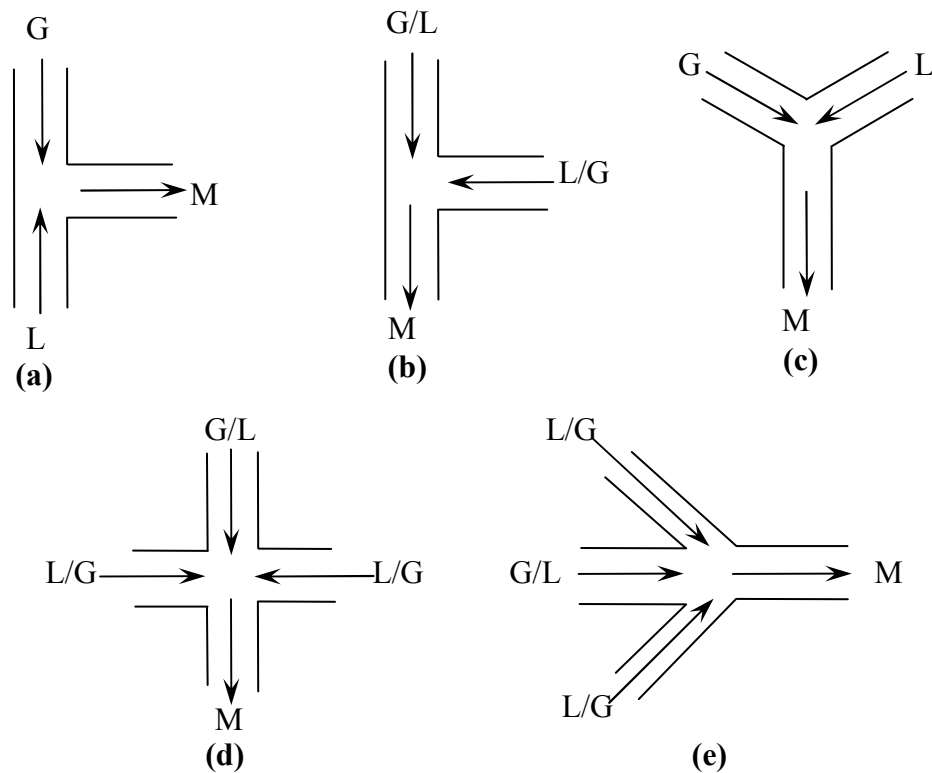


Figure 2.21 Various inlets developed from the T- junction. G: gas inlet; L: liquid inlet; M: main channel. (a) T-junction with the gas and liquid inlet channel perpendicular to the main channel; (b) T-junction with either the gas or liquid inlet channel in the direction of the main channel; (c) Y-junction inlet; (d) cross-junction inlet; (e) flow-focusing inlet.

Garstecki et al. (2006) studied droplet formation (air/water or oil/water) in a square T-junction similar to that shown in Figure 2.21b with the continuous phase in line with the main channel. All channels had a height of 33 or 79 μm , the dispersed phase inlet channel width was 50 or 100 μm and the inlet width connecting the main channel was 50, 100 or 200 μm . They found out that the inlet geometry influenced the drop formation mechanism. To be able to promote the squeezing mechanism (see Section 2.5.2), the inlet channel width had to be wider than the channel height and the width of the inlet should be ≥ 0.5 times of width of the main channel. Provided that these are satisfied, the bubble length was proportional to the width of the main channel (Eq. 2.9).

The effect of the angle at which the two inlet channels join was studied by Tan et al. (2009) using a Y-junction inlet with the gas inlet channel in the direction of the main channel and the liquid inlet channel joining them on the side (Figure 2.22). The fluid system was air/glycerol. When $\omega < 90^\circ$, bubble length was observed to decrease with increasing ω . The opposite was found to be true when $\omega > 90^\circ$. The bubble length can be predicted by Eq. 2.10.

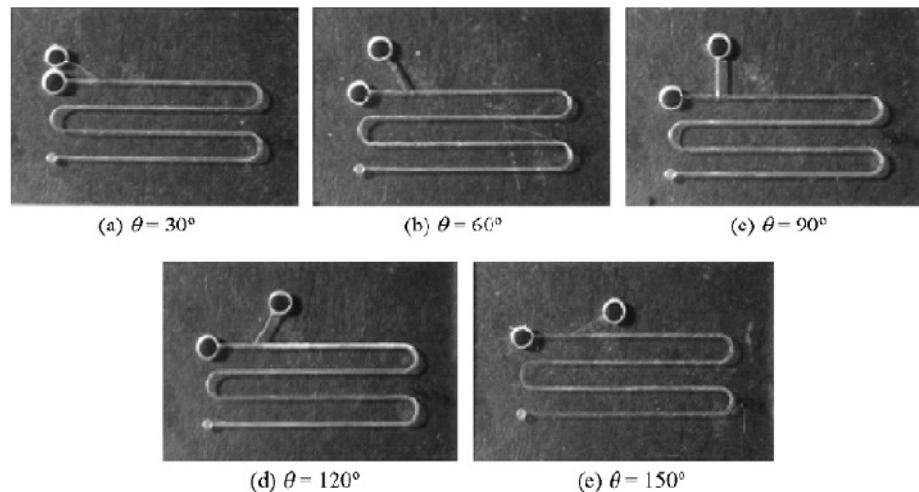


Figure 2.22 T- and Y-junction inlet with different angles (Tan et al., 2009).

The inlet channel dimensions were also found to influence the bubble/slug length as reported by Amador et al. (2004), who studied bubble formation from orifice, T- and Y-junctions. Experimental results showed that the bubble length was proportional to the gas inlet channel size (Figure 2.23a and b) but was not affected significantly by the liquid inlet channel size (Figure 2.23b and c). Qian and Lawal (2006) carried out a numerical study on Taylor flow formation in a T-junction microchannel. They reported the same effect of gas inlet channel size on bubble length as that by Amador et al. (2004). Besides, bubble length was found to be a function of T-junction orientation. By using T-junctions as shown in Figure 2.21a, bubble length was found to be similar using

2. Literature Survey

inlet orientation as in Figure 2.23a, but longer bubble was resulted using inlet orientation as in Figure 2.23b. Bubble and slug lengths from these inlets are as shown in Figure 2.24. In addition, they found that the degree of mixing at the inlet affected bubble size (see also Section 2.5.2). When the fluids split into many layers that alternate with each other at the inlet bubble and slug lengths were shorter (Figure 2.25).

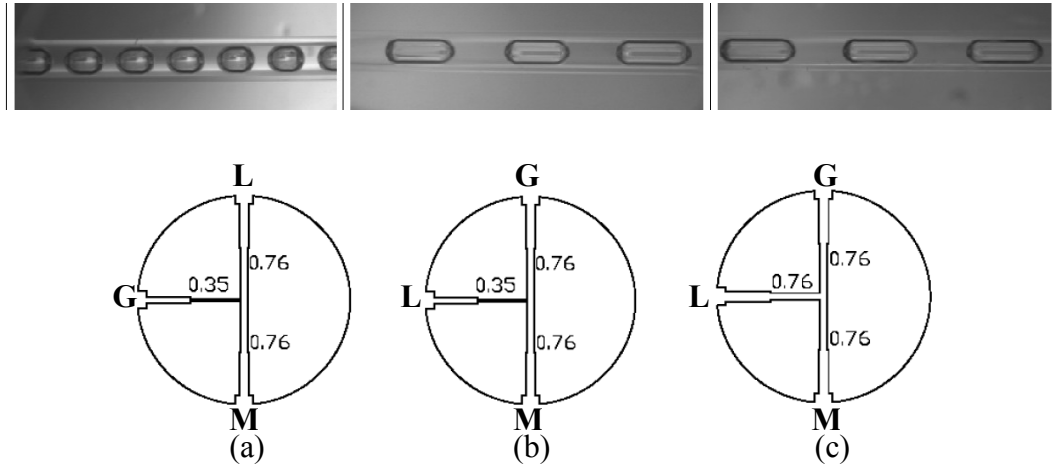


Figure 2.23 Effect of inlet channel size on bubble length (Amador et al., 2004).

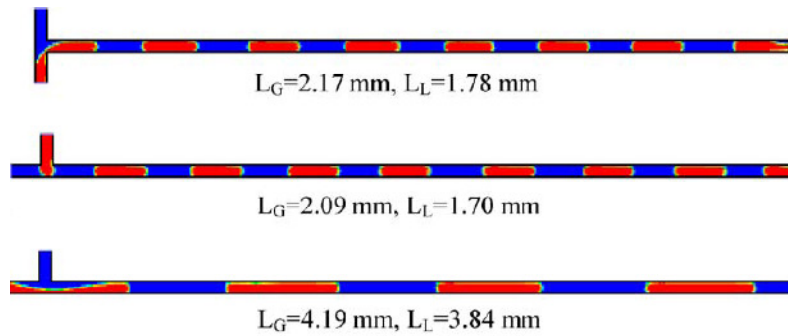


Figure 2.24 Effect of T-junction orientation on gas and liquid slug length (Qian and Lawal, 2006). The red and blue stand for the gas and liquid phase respectively.

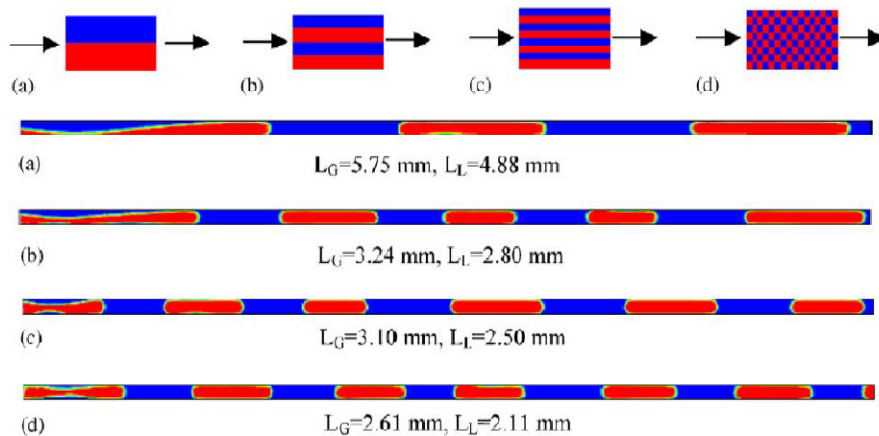
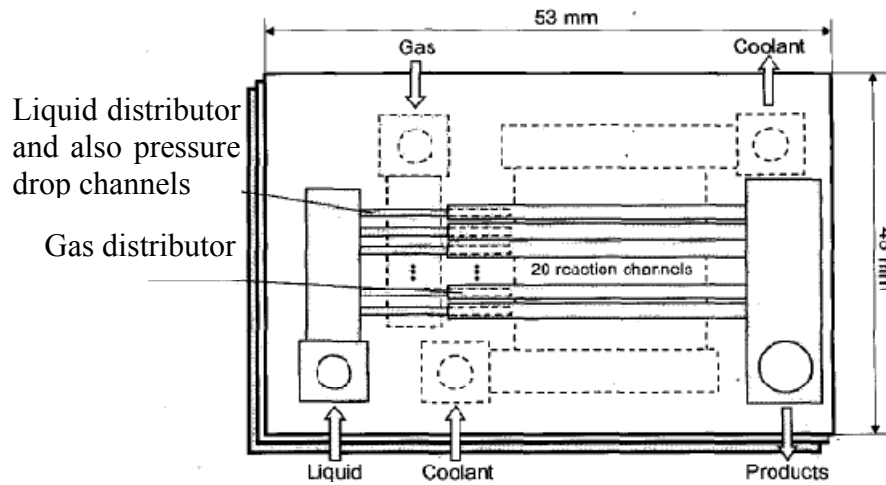


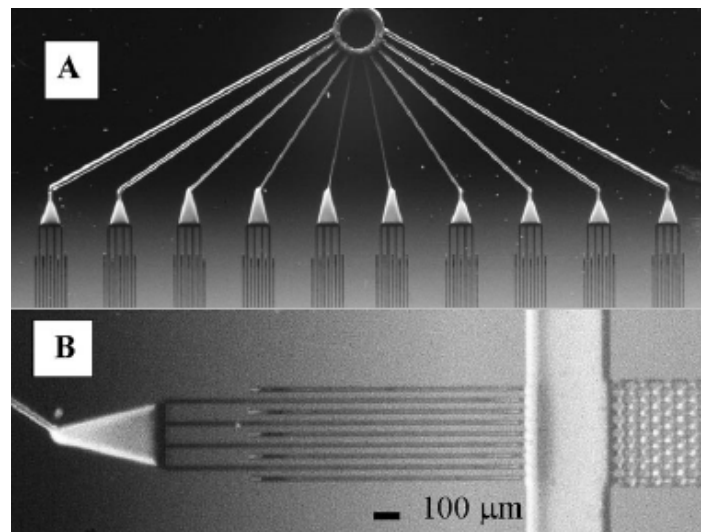
Figure 2.25 Effect of inlet mixing on gas and liquid slug length (Qian and Lawal, 2006).

During microreactor scale-out, the inlets (manifolds) should be designed to achieve equal flow distribution and reactant mixing. For dispersed-phase microreactors, bubble formation in the different scale-out channels is not simultaneous, which results in pressure fluctuations at the individual inlets and therefore, flow instabilities, channelling and unequal flow distribution between channels occur (Hessel et al., 2005). To prevent flow maldistribution, de Mas et al., (2003a) suggested that the gas and liquid should be introduced through individual inlet “pressure-drop” channels, which would exert much higher pressure drop than that across the reaction channels and limit the “cross talk” between them. A schematic of pressure-drop channels is given in Figure 2.26a from de Mas et al., (2003b). To achieve an even distribution, Losey et al. (2002), divided the gas inlet into 10 channels with different widths depending on their channel length (Figure 2.26b). Wada et al. (2006) suggested a design, where the gas flow was distributed through multi-stage equal-armed bifurcating channels as seen in Figure 2.26c. In micro scale, the dispersed phase tends to coalesce rapidly under the large interfacial forces, which makes mixing of the gas and liquid phases problematic. For gas-liquid reaction systems, a number of mixing mechanisms has emerged that are borrowed from liquid system. The most frequently adopted mechanism is lamination of the fluid streams. For example, Losey et al. (2002) further divided each of the 10 gas streams into 4 smaller streams in channel sizes of 25 μm (Figure 2.26b), the same dimension to the liquid inlet. Both phases form multiple laminae that alternated with other when they came into contact so that the diffusion path was significantly shortened. However, the dimensions of the laminating channels can not be too small because surface tension effects would become prohibitively large. This design is known as “splitting up and interleave” (Losey et al., 2002) and it suits many systems especially for those that the gas-liquid reaction is initiated upon two-phase contact. For systems that an inert gas phase is used to improve the reactive liquid phase mixing and/or to reduce axial dispersion, i.e. in Taylor flow, chaotic mixing use of unsteady fluid flow to stretch and fold a volume of fluid, Song et al., 2003) can be used.

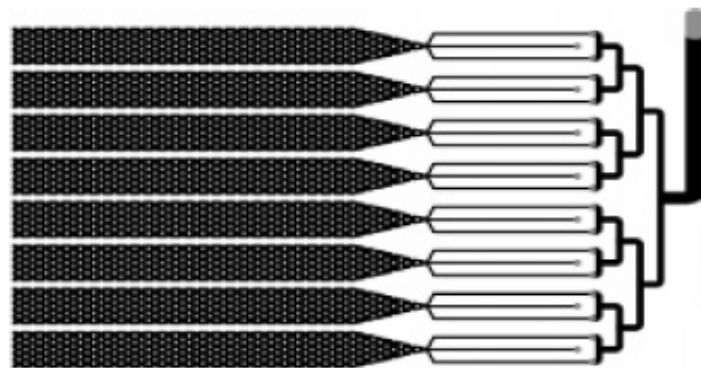
2. Literature Survey



(a)



(b)



(c)

Figure 2.26 Inlet design examples for flow even distribution during scale-out. (a) Inlet pressure-drop channels to prevent cross talk between main channels (de Mas et al., 2003b); (b) gas distribution channels of different length and size and liquid distributor that also serve as pressure-drop channels (Losey et al., 2002). In B, Gas inlet is split into 4 streams and then interleaved with 5 liquid inlet streams; (c) gas distribution channel with multi-stage equal-armed bifurcating channels (Wada et al., 2006).

Yen et al., (2005) studied the preparation of CdSe quantum dots, which was a liquid phase reaction and suffered from slow mixing and broad residence time distribution in conventional batch reactors. By introducing an inert gas of argon, Taylor flow was formed in a microchannel reactor. To further accelerate the mixing, a meandering channel was used at the reactor inlet to enhance the mixing between the two halves of the liquid slug, as seen in Figure 2.27. The reaction yield and size distribution were significantly improved and the reaction time was shortened. The enhanced performance in curved tubes is due to the secondary flows (Dean vortices) that are generated under unbalanced centrifugal forces (Kumar et al., 2007). The flow is stretched and folded, and leads to a rapid, exponential decrease of the striation length – distance for mixing by diffusion (Song et al., 2003).

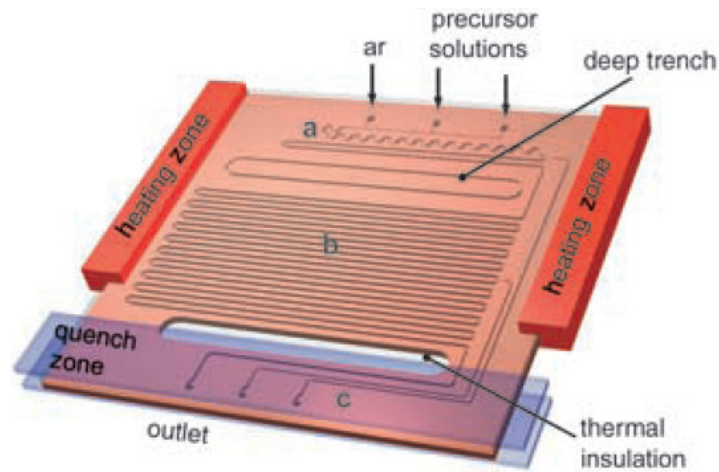


Figure 2.27 Inlet design example to improve the reactive phase mixing by forming Taylor flow using an inert gas and initiating chaotic mixing by travelling the flow in a meandering channel (Yen et al., 2005).

2.6.2.2 Main channel design

The main channel is the environment where the reaction occurs. Apart from the normal straight channels, structures have been added in some designs to improve mixing and increase the specific area. In many microdevices the use of curved meandering geometries are very common because they are compact and can reduce the residence time distribution (for single phase flow). Song et al. (2003) used a meandering main channel for a water-based phase reaction. An inert immiscible oil stream was added to form Taylor flow while the reactive streams formed the dispersed phase (Figure 2.28a). They found that the unsymmetrical recirculation within the droplets rapidly mixes the reactants. This could mean that either the reaction conversion is higher for the same reactor length or the reactor length can be shortened. However, when a two-phase

reaction took place in similar designs, little change to reaction conversion was found compared to straight channels. (Lida et al., 2009) studied polymerizations of styrene in cyclohexane in aluminium microchannel reactors. Taylor flow in a microchannel was used to achieve good heat dissipation and reactant mixing. Apart from straight channels, they also carried out the reaction in periodically pinched, obtuse zigzag, and acute zigzag channel microreactors, as shown in Figure 2.28b. Reaction conversion was reported to be similar in all four designs (Lida et al., 2009).

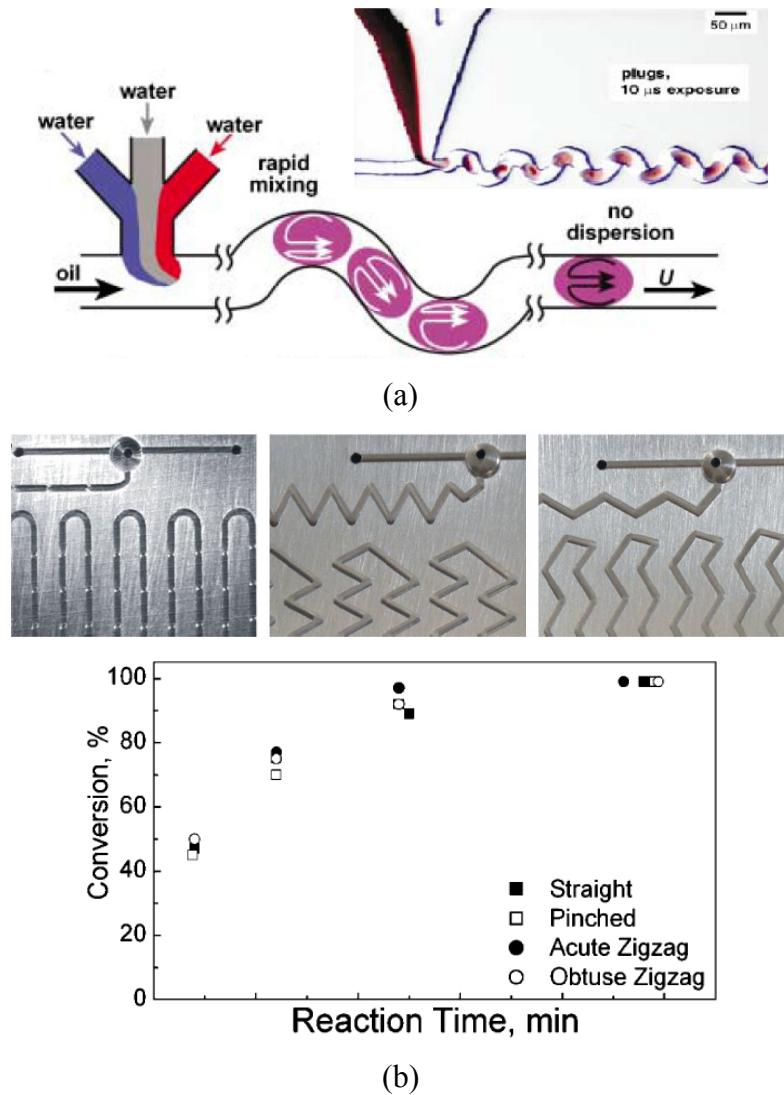


Figure 2.28 Examples of curved main channels. (a) Inert oil phase suspends the reactive phase in meandering microchannels. Channels were 45 μ m deep; inlet channels were 50 μ m and meandering channels were 28 μ m wide; $Re \sim 5.3$ (water), $Re \sim 2.0$ (oil) (Song et al., 2003); (b) channels with periodically pinched, obtuse zigzag, and acute zigzag structures and the reaction conversion achieved (Lida et al., 2009). The channels are rectangular with cross section of 790 μ m wide and 500 μ m deep, and 2 m length.

Internal structures in the channels have also been used to improve mixing and increase the interfacial area in multiphase reactions. Losey et al. (2002) studied the catalytic hydrogenation of cyclohexene to cyclohexane (gas-liquid-solid reaction with the solid phase is the catalyst) in a multi-microchannel reactor, an analogue to packed bed reactors. In conventional laboratory reactors, the reaction can be limited by the rate of gas absorption into the liquid, the distribution of reagents throughout the packed-bed, or the diffusion within the porous catalyst itself. Instead of packing catalysts in the microchannel as in a packed bed reactor, the reaction channel was designed to contain erected catalyst posts as seen in Figure 2.29a. The surface area was further increased by creating striations on the post (Figure 2.29b). The k_{La} was found to be $3-7s^{-1}$, comparable to that observed in packed-bed microreactor with $50\mu m$ diameter catalyst particles and more than 100 times larger than that in conventional laboratory devices. In the post design, the catalysts were allowed to be integrated with the bed and provided better control in catalyst size and distribution and void fraction compared to packed bed.

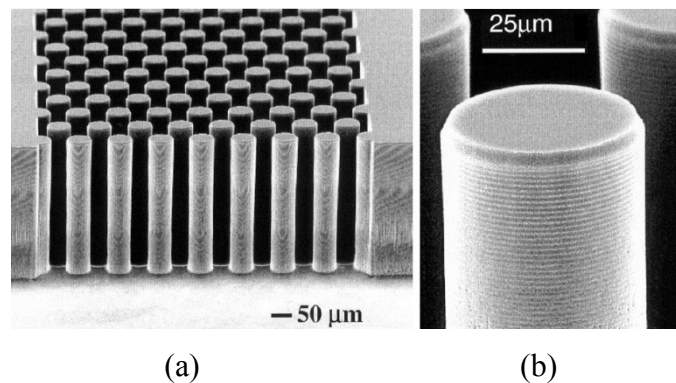


Figure 2.29 Microchannel fabricated with catalyst posts to improve gas-liquid contact. The posts are $50\mu m$ in diameter and $300\mu m$ high, arranged in staggered arrays in channels $300\mu m$ deep, $625\mu m$ wide and 20 mm long. (a) Microstructured catalyst supports prior to porous silicon formation; (b) View of micron scale striations on the posts. Losey et al. (2002).

2.6.2.3 Outlet design

The outlet design affects the reactor performance by influencing the flow stability. In addition, the advances in microengineering technology allow integration in the outlet a number of post-reaction processes such as reaction quenching, gas-liquid phase separation, etc., all are associated with the reactor outlet.

Amador et al. (2004) found that if the outlet was open to the atmosphere, there were pressure fluctuations each time a Taylor bubble burst at the outlet, which would not

only affect the movement of the other Taylor bubbles in the main channel but also the bubble formation at the inlet. To reduce the fluctuation, they used a disengagement chamber (a liquid reservoir) after the capillary outlet (Figure 2.30) to prevent direct bubble burst into the atmosphere. However, there was still a sudden change in the bubble curvature radius from the tube diameter to the disengagement chamber where it becomes spherical. [van Steijn et al. \(2008\)](#) studied this problem under Taylor flow by observing the flow under high speed camera. They found that the pressure fluctuations were associated with bubble entrance to and exit from the main channel and could be decomposed into contributions from the pump, inlet and outlet. Of these, the outlet gave the largest fluctuations. To reduce them, they suggested to smoothly increasing the cross-section of the outlet in order to gradually change the interfacial tension force. When two phases are to be separated, e.g. for downstream measurements or for product collection, a separator is needed. The most common way to separate a gas-liquid mixture is to use gravity as in large scale systems phase separations. Other integrated outlet designs for phase separation are also reported.

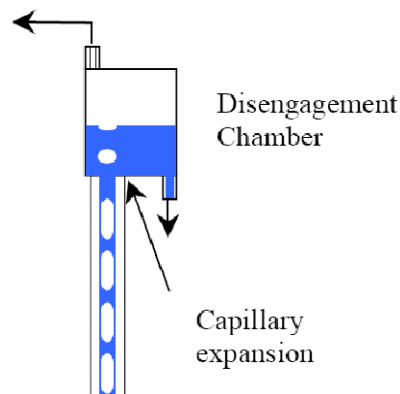


Figure 2.30 Disengagement chamber design at the capillary outlet to reduce pressure fluctuations ([Amador et al., 2004](#)).

[Günther et al. \(2003\)](#) designed an integrated gas-liquid separator, which applied a negative differential pressure through a microcapillary array at the channel outlet (Figure 2.31a). The separator was improved to include only 16 capillaries (Figure 2.31b) that lined up on one side of the channel at the outlet. The differential pressure should be smaller than the capillary pressure across the microchannel structure. The capacity of the separator could be determined from the number of capillaries, their cross sections and lengths. Therefore, a complete phase separation could be expected as long as the applied pressure differential did not exceed the capillary rise pressure in the individual capillaries and the flow rates were below the design limit.

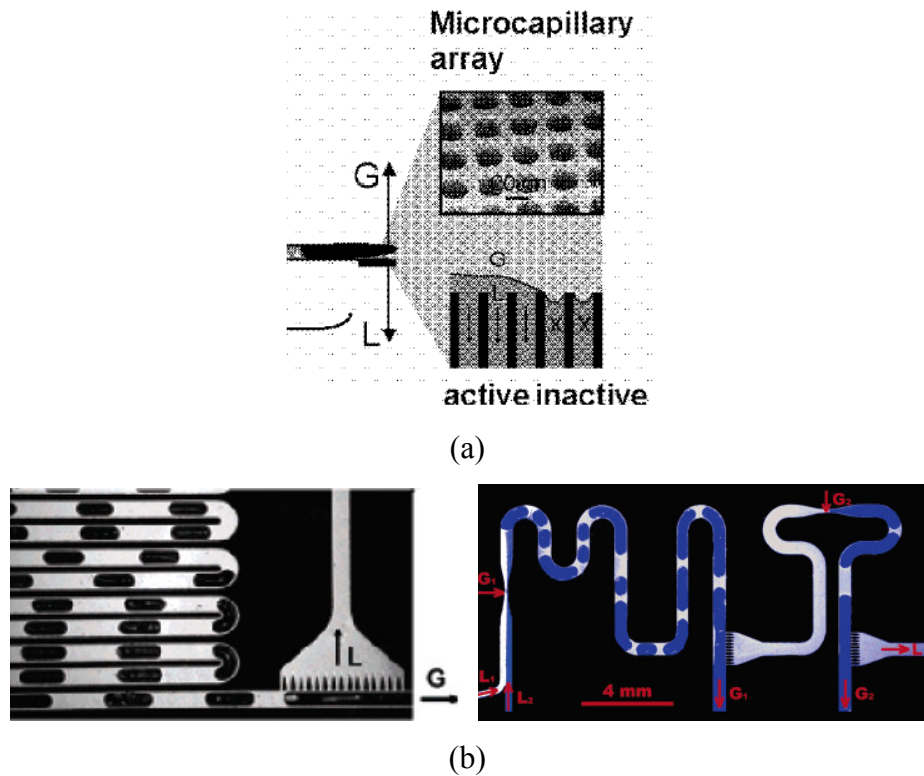


Figure 2.31 Gas-liquid separator design by applying a negative differential pressure. (a) separator with a microcapillary array (several thousands of 20 μ m capillaries on a 3mm diameter array). [Günther et al. \(2003\)](#); (b) single-stage and two-stage separator, providing an integrated design for liquid mixing (through first-stage separator) and the subsequent reaction (through second-stage separator). The liquid is drawn through 16 capillaries of 20 μ m wide. [Günther et al. \(2005\)](#).

2.7 Concluding remarks

Microstructured reactors offer improved reactor performance and safety compared to conventional large scale reactors and provide large opportunities either for carrying out difficult (or even unattainable with the current systems) reactions or for improving the process performance (economical or environmental). The reduced dimensions of microstructured reactors means that phenomena such as surface forces, wettability, flow confinement and channel design are important. However, these are not usually considered in large scale systems. The studies available in microchannels, which were reviewed above, are still not complete but provide a basis for the work in this thesis.

Most of the gas-liquid two-phase flow patterns found in large channels have also been observed in mini- and microchannels. However, new features that are specific to small dimensions are also observed (Section 1.1 and 2.2). This motivates the studies in Chapters 3 and 4 on gas-liquid flow patterns in microchannels and their differences from large scale systems. As the most encountered gas-liquid flow pattern, Taylor flow

has attracted much more attention than others (Section 2.5). Literature showed that bubble/slug lengths are important in determining mass and heat transfer but cannot be calculated directly. Various bubble/slug length correlations have been proposed (Section 2.5.2), but most of them focused on variables that are frequently used in large scale flow systems, such as flowrates and volume fraction. In addition, there are still large discrepancies in bubble/length predictions by these correlations. More recent work indicated that bubble/slug lengths also depended significantly on inlet conditions. Therefore, the aim of the work in Chapters 5 and 6 is to obtain bubble/slug lengths for the current system and understand how various inlet designs (Section 2.6.2.1) affect them. For mass transfer and reaction in microstructured reactors, various main channel designs, reviewed in Section 2.6.2.2, have been used in the literature to mainly promote fluid mixing. These approaches were utilized in Chapter 7 where a fast gas-liquid reaction is studied. The necessity of gas-liquid separation in reactive systems is expected and this forms part of the investigations in Chapter 7 and ideas from Section 2.6.2.3 provide a good starting point. One of the objectives of this thesis is to formulate numerical models that can extend the study beyond the capability of experiments and this is realized in Chapter 5 and 8 for the parametric study on bubble length and mass transfer in microchannels. The mass transfer study is as a result of insights obtained from work discussed in Section 2.5.6 for systems without reactions. Using the numerical model from Chapter 8 and with the knowledge of the various microstructured reactors developed in Section 2.6, in Chapter 9 the performance of different types of gas-liquid microreactors for a real industrial system is investigated.

Chapter 3
Review on Gas-Liquid Two-Phase Flow
Transitions in Microchannels

Nomenclature

a	Coefficient, -
b	Coefficient, -
d	Diameter, m
k	Channel roughness, m
Q	Volumetric flowrate, m ³ /s
U	Velocity, m/s
\bar{U}	Normalized velocity, $\bar{U}_{LS} = U_{LS}/(a + b\theta) = 1$, -

Greek Symbols

α	Volume fraction, -
μ	Dynamic viscosity, Pa·s
ρ	Density, kg/m ³
σ	Surface tension, N/m
θ	Contact angle, °

Dimensionless Numbers

Ca	Capillary number, $\mu_L(U_{GS}+U_{LS})/\sigma$
Re_{GS}	Gas Reynolds number, $\rho_G U_{GS} d / \mu_G$
Re_{LS}	Liquid Reynolds number, $\rho_L U_{LS} d / \mu_L$
Su	Suratman number, $Re_{LS}^2 / Ca = \rho_L \sigma d / \mu_L^2$
We_G	Gas Weber number based on actual gas velocity, $\rho_G U_G^2 d / \sigma$
We_L	Liquid Weber number based on actual liquid velocity, $\rho_L U_L^2 d / \sigma$
We_{GS}	Gas Weber number based on superficial gas velocity, $\rho_G U_{GS}^2 d / \sigma$
We_{LS}	Liquid Weber number based on superficial liquid velocity, $\rho_L U_{LS}^2 d / \sigma$
We'_{GS}	Gas Weber number based on density difference, $(\rho_L - \rho_G) U_{GS}^2 d / \sigma$
We'_{LS}	Liquid Weber number based on density difference, $(\rho_L - \rho_G) U_{LS}^2 d / \sigma$

Subscripts

G	Gas
GS	Gas phase superficial
H	Hydraulic

3. Review on Gas-Liquid Two-Phase Flow Transitions in Microchannels

<i>L</i>	Liquid
<i>LS</i>	Liquid phase superficial

Flow Patterns

<i>A</i>	Annular flow
<i>B</i>	Bubbly flow
<i>C</i>	Churn flow
<i>I</i>	Intermittent flow
<i>STD</i>	Surface tension dominated flow (bubbly, Taylor)
<i>T</i>	Taylor flow
<i>T-A</i>	Taylor-annular flow (transition from Taylor to annular flow)
<i>TR</i>	Transition flow
<i>W</i>	Wavy flow

3.1 Introduction

Compared to macro-systems, there are three major differences in flows in microchannels. Firstly, the relative importance of surface over volume forces increases. Secondly, Reynolds number is usually small and laminar flow is established, where viscous forces dominate over inertial ones. Thirdly, effects of wall roughness, wettability and flow confinement become important. Because of these differences the flow pattern boundary predictions that exist for two-phase flows in large diameter tubes cannot satisfactorily be applied to microchannel flows (Damianides and Westwater, 1988; Fukano et al. 1993). There exists a significant amount of work that attempts to characterize gas-liquid flows in microchannels (e.g. see review papers by Ghiaasiaan and Abdel-Khalik, 2001; Akbar et al., 2003). A number of investigators have attempted to produce universal flow regime maps (Akbar et al., 2003; Cubaud and Ho, 2004; Hassan et al., 2005; Waelchli and von Rohr, 2006). However, with decreasing characteristic length scales, flow patterns and their transitions are increasingly influenced by tube wall wetting properties and channel inlet geometry (Galbiati and Andreini, 1992), which limit most of the reported results to specific systems. Systematic studies are required to understand how flow pattern formation and transition are subject to the influence of various parameters and to interpret the differences that have been reported in the literature.

In this chapter, parameters influencing gas-liquid two-phase flow pattern transitions in microchannels are reviewed. The effects of flow orientation, channel geometry, channel dimension, channel surface properties, fluid properties and inlet conditions on flow patterns and their transition boundaries are considered. Finally, universal flow regime transition lines proposed in the literature are compared against available experimental data to evaluate their applicability.

3.2 Parameters influencing flow regimes and their transitions

Gas-liquid two-phase flow patterns forming in microchannels are reviewed in Section 2.2 and literature studies on this topic are summarized in Table 2.1. The effects on flow patterns and their transitions of parameters that have been identified as important in Table 2.1 will be discussed in this section.

3.2.1 Flow orientation

Gravity is not expected to play a role in microchannel flow for channel sizes up to about 2 mm as was seen in Section 1.1. Fukano and Kariyasaki (1993) from experimental

investigations in horizontal and vertical upward and downward flows, found that in channels smaller than 2.4mm bubbles started to be axisymmetrically distributed on the cross section of horizontal channels, while flow patterns were not affected by flow direction. In contrast, Hassan et al. (2005) suggested different universal flow pattern maps for horizontal and vertical channels between 0.1 and 1mm in diameter using literature data. As can be seen from Figure 3.1 bubbly flow in vertical channels is extended to lower U_{LS} than in horizontal ones perhaps because buoyancy in vertical channels favours bubble detachment at the inlet and assists the formation of small bubbles. In addition, annular flow in vertical channels is shifted to lower U_{GS} compared to horizontal ones, indicating a larger effect of inertia assisted by buoyancy over surface tension forces in vertical channels. However, because of lack of further studies the effect of gravity on microchannel flow patterns is not conclusive.

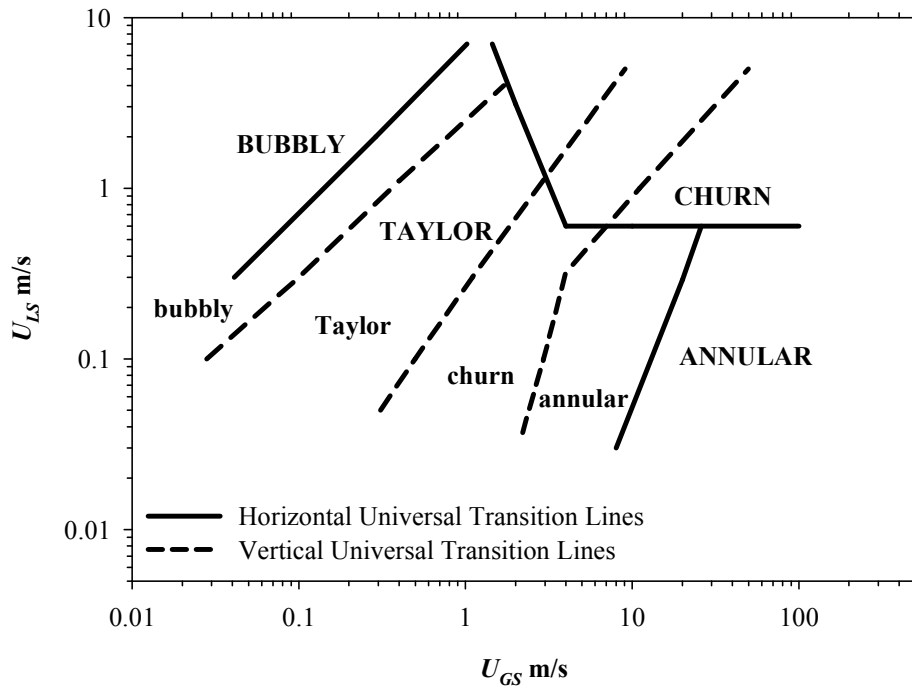


Figure 3.1 Comparison of flow pattern transitions in horizontal and vertical channels (Hassan et al., 2005). Regimes in capital are for horizontal flow map, and ones in lower case are for vertical flow map.

3.2.2 Channel size

Channel size is the most direct parameter that differentiates macro- and micro-channel flows and studies in small channels with different sizes are widely available. Coleman and Garimella (1999) investigated flow patterns formed in capillaries with diameters $1.3 < d < 5.5$ mm. The results shown in Figure 3.2 reveal that the main differences between

the small tubes (1.3, 1.75 and 2.6mm) compared to the large one (5.5mm) was the suppression of stratified flow (wavy) and the extension of Taylor flow (intermittent) to much higher U_{LS} and U_{GS} . Among the small tubes a decrease in tube size shifted the transitions from Taylor (intermittent) to bubbly (bubble) flow, from Taylor to Taylor-annular flow (wavy-annular) and from Taylor-annular to dispersed flow to progressively higher U_{GS} and U_{LS} . There was, however, little effect of tube size on the transition from Taylor-annular to annular and from annular to dispersed flow. The effect of tube size on the expansion of the Taylor regime could be attributed to two phenomena. Firstly, it is more possible that bubbles of similar volume will fill the channel cross section in small tubes compared to large ones, resulting in the expansion of the Taylor regime over bubbly flow as channel dimension decreases. Secondly, dominance of surface tension over inertial forces with decreasing channel size means that the formed bubble surfaces are not easily disrupted through coalescence (to form a continuous core) or breakup (to smaller bubbles) which explains the extension of the Taylor regime into higher U_{GS} and U_{LS} . At higher gas and liquid fluxes, however, inertia will eventually dominate and the transition to annular flow is independent of channel dimension.

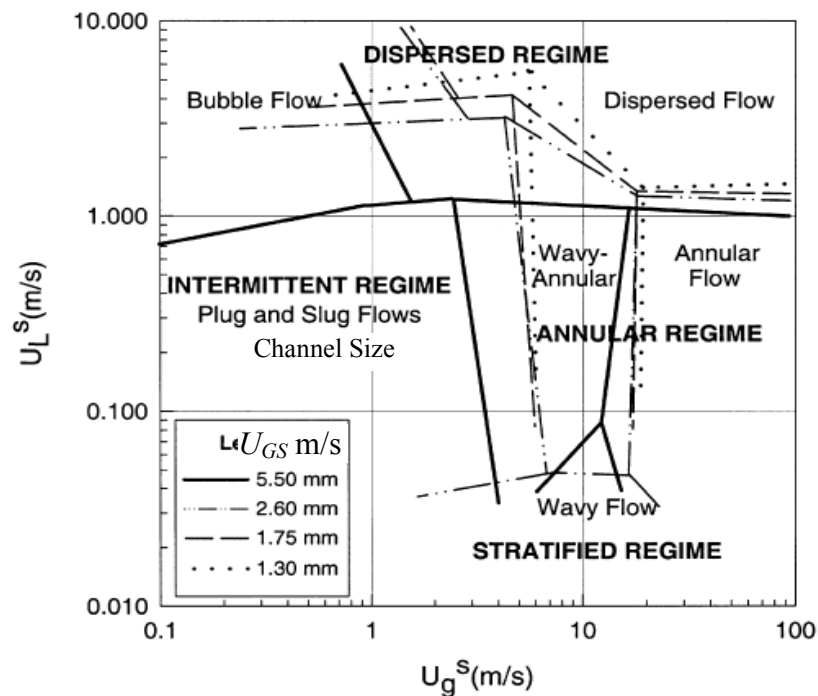


Figure 3.2 Comparison of flow pattern transitions in circular channels with different internal diameters (Coleman and Garimella, 1999).

Zhao and Bi (2001) studied air-water flow in triangular channels of hydraulic diameters 2.886, 1.443 and 0.886mm. They observed that the bubbly regime shrinks when the channel size is reduced from 2.886 to 1.443mm and is replaced in the 0.886mm tube by

a capillary bubble flow (grouped into bubbly flow as in Section 2.2), which occupies a very different area in the map (Figure 3.3). As channel size decreased, Taylor flow extended to higher U_{GS} and U_{LS} , whereas the churn flow occupied a smaller area of the map by moving to higher gas velocities, especially in the 0.886mm tube. The transition to the inertia dominated annular flow varied only slightly with channel size. Extension of the Taylor flow pattern to higher U_{GS} with decreasing channel size was also found by [Yue et al. \(2008\)](#) for rectangular channels with hydraulic diameters 667 μm (aspect ratio is 2), 400 μm (aspect ratio is 1) and 200 μm (aspect ratio is 1) and pure CO_2 /water system. However, the transitions from Taylor to bubbly and from Taylor-annular to annular flow did not follow a certain trend with diminishing channel size, probably because the rate of CO_2 absorption into the water that would affect the gas volume and velocity depended on channel size and aspect ratio.

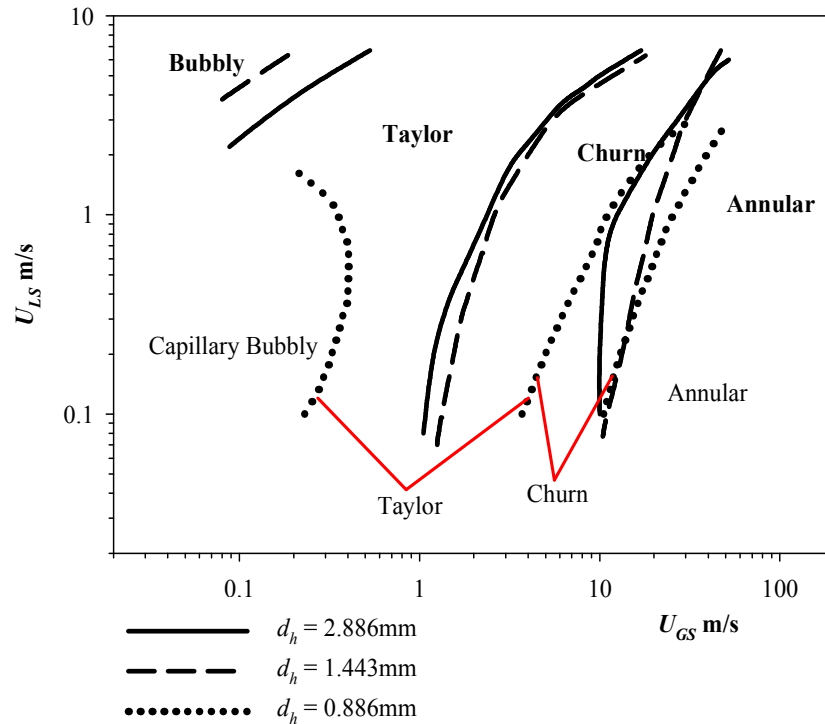


Figure 3.3 Comparison of flow pattern transitions for upward flow in triangular mini channels with different hydraulic diameters ([Zhao and Bi, 2001](#)). Regime names in bold font refer to the 2.886 and 1.443mm channels, while names in normal font refer to the 0.886mm channel.

In very small channels transitions between the different patterns happen over a large area of the map, while under the same conditions more than one patterns may co-exist as was found by [Kawahara et al. \(2002\)](#) at high gas and liquid velocities (multiphase

flow in their study). In addition, in many cases some of the patterns do not form at all. For example Kawahara et al. (2002) did not observe any bubbly or churn flows while Chung and Kawaji (2004) obtained essentially only Taylor flow in their studies.

3.2.3 Channel geometry

In the study by Triplett et al. (1999) air-water flows in different channel geometries were considered. From Figure 3.4, in the non-circular channels compared to the circular ones the transition to the liquid inertia dominated churn flow was shifted to lower U_{LS} and the transition to annular flow took place at lower U_{GS} . The transition to churn flow however, was supported by only a few data points. In non-circular channels liquid tends to be pulled into the channel corners; this will increase the cross sectional area occupied by the liquid and decrease the area occupied by the gas at the core that leads to increased gas velocity and an earlier transition to annular flow. Similar effect of channel shape on the transition to annular flow was found by Coleman and Garimella (1999), in rather large circular and rectangular channels (aspect ratio = 0.725) with hydraulic diameter of 5.5mm. They found, however, the opposite trend to that by Triplett et al. (1999) for the churn flow transition and argued that the film pulled into the corners is stabilised and does not break up because of increased surface tension effects.

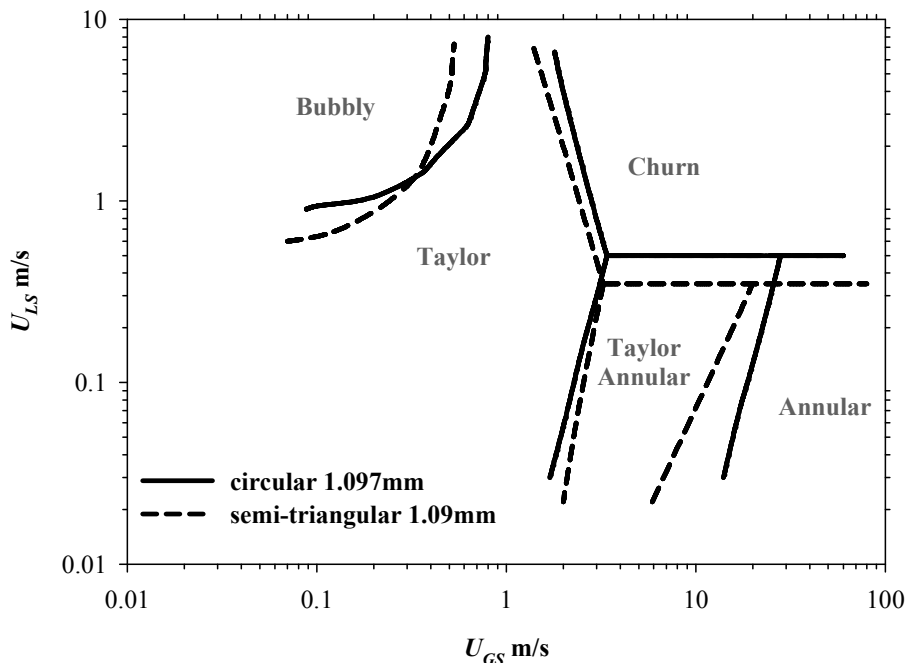


Figure 3.4 Comparison of flow pattern transitions in circular ($d = 1.097\text{mm}$) and semi-triangular channels ($d_H = 1.09\text{mm}$) (Triplett et al., 1999).

3.2.4 Wall wetting conditions

Barajas and Panton (1993) investigated the effect of contact angle, θ , of the liquid with the wall on flow patterns in a 1.6mm tube. As can be seen from Figure 3.5, wavy (stratified flow) flow in the system with $\theta = 34^\circ$ was at first replaced by rivulet flow when $\theta \geq 61^\circ$ which broke up into several rivulets at even higher contact angles (less hydrophilic walls). In addition, with increasing contact angle, the transition from rivulet to annular flow moved to higher U_{LS} . This is because the increased contact angle inhibited the liquid from spreading on the tube wall, which was more obvious in the non-wetting system ($\theta > 90^\circ$), where almost half of the annular area in the map was replaced by rivulet and multirivulet flows. Also in the non-wetting system the transition to bubbly and dispersed patterns occurred at lower U_{LS} , while there was no significant difference in the cases of lower contact angles. The non-wetting channel wall would favour the distortion of the gas-liquid interface and promote the breakage of the phases into bubbles or drops. There was however, little effect of contact angle on the transitions occurring with increasing gas velocity, apart from the transition from Taylor-annular (slug) to annular flow in the non-wetting system.

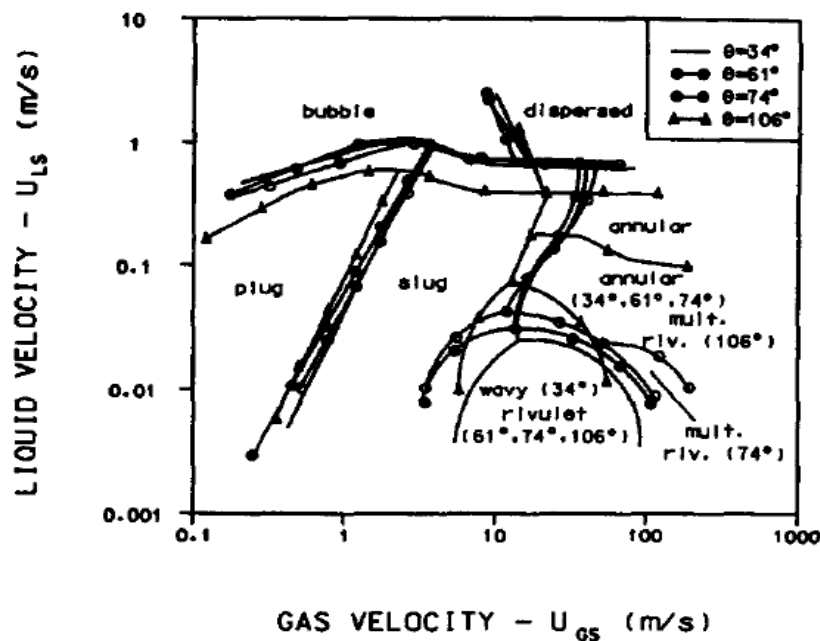


Figure 3.5 Effect of contact angle on flow pattern transitions for air-water flows (Barajas and Panton, 1993). $d = 1.6\text{mm}$.

The study of Barajas and Panton (1993) was confirmed and extended by Lee and Lee (2008), in which flows were further classified into two groups: wet and dry, depending on the existence of a continuous liquid wetting phase. For example, the rivulet flow

observed in Barajas and Panton (1993) is considered to be dry flow because there is no continuous liquid film. Lee and Lee (2008) found that both superficial liquid velocity and contact angle θ affect the transition from dry to wet flows. They suggested that a normalized liquid superficial velocity, $\bar{U}_{LS} = U_{LS}/(a + b\theta) = 1$, where a and b are numbers depending on wetting conditions, can be used to identify the boundaries of wet and dry flows in channels with different wettability (see Table 2.1). Dry flow can appear even in wetted channels depending on U_{LS} , e.g. at $U_{LS} < 0.018$ in a glass channel ($\theta = 30^\circ$ for water) and at $U_{LS} < 0.025$ m/s at a Teflon channel ($\theta = 43^\circ$ for methanol). In less wetted channels ($50^\circ < \theta < 90^\circ$), dry to wet transition takes place at U_{LS} common to two-phase flow operations, e.g. $U_{LS} \approx 0.17$ m/s for air-water flow in 2mm polyurethane tube.

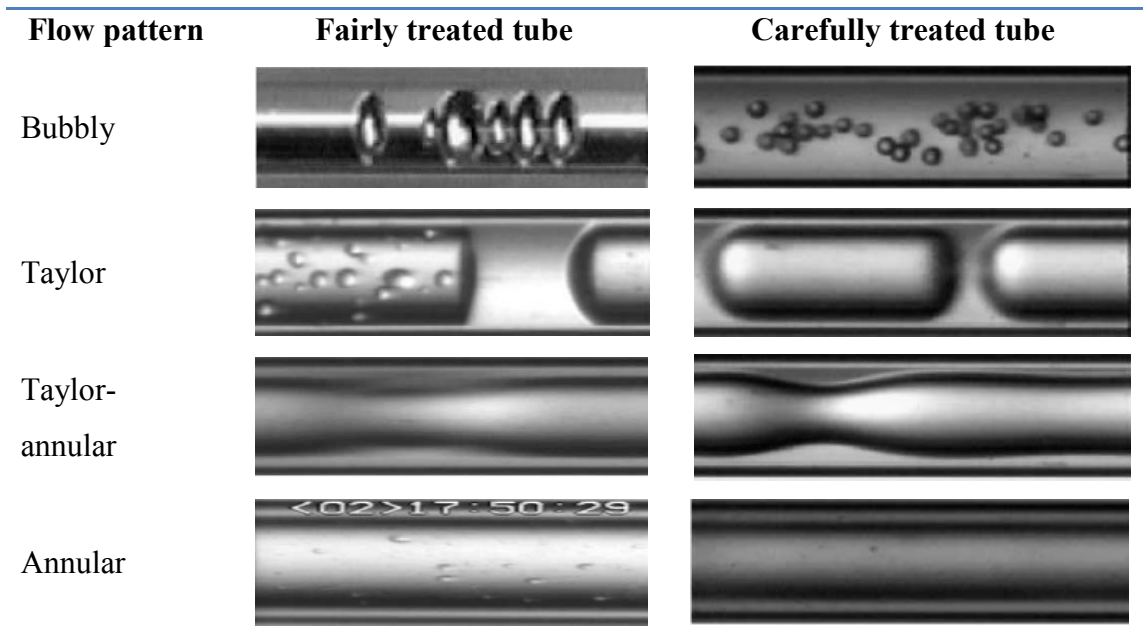


Figure 3.6 Two-phase flow patterns in a 100 μ m quartz tube. In the left column, the tube is fairly treated by drawing ethanol through the test section. In the right column, the tube is carefully treated with the combination of mechanical cleaning with a soft brush and ultrasonic vibration in a pool of high purity distilled water, ethanol and dilute hydrochloric acid (Serizawa et al., 2002).

Serizawa et al. (2002) by treating the tube surface found that flow patterns were sensitive to wall surface conditions. As can be seen in Figure 3.6, flow patterns appeared more regular in a carefully treated quartz tube, e.g. bubble coalescence was inhibited, while the small liquid drops on the tube wall were replaced by a continuous liquid film in Taylor flow. Therefore, contamination changes the wall wettability, discouraging the spreading and stabilization of the liquid film in this case. Lee and Lee

(2006), however reported that contamination increased the wall hydrophilicity for air/water flow in polyurethane tube ($d = 2\text{mm}$, $\theta = 75^\circ$) and shifted the dry-wet flow transition from $U_{LS} = 0.17\text{m/s}$ to $U_{LS} = 0.05\text{m/s}$. This is probably related to the marginally wetted nature (i.e. $50^\circ < \theta < 90^\circ$, Lee and Lee, 2006) of the polyurethane tube, where the existence of contaminants favours the water phase spread comparatively. Depending on wall wetting properties Cubaud et al. (2006) separated flows to hydrophilic and hydrophobic ones (Figure 3.7). In hydrophobic flows the liquid does not lubricate the wall well and hysteresis and friction effects during the movement of the three phase (gas-liquid-solid) contact line make the flow asymmetric with respect to the axial direction.

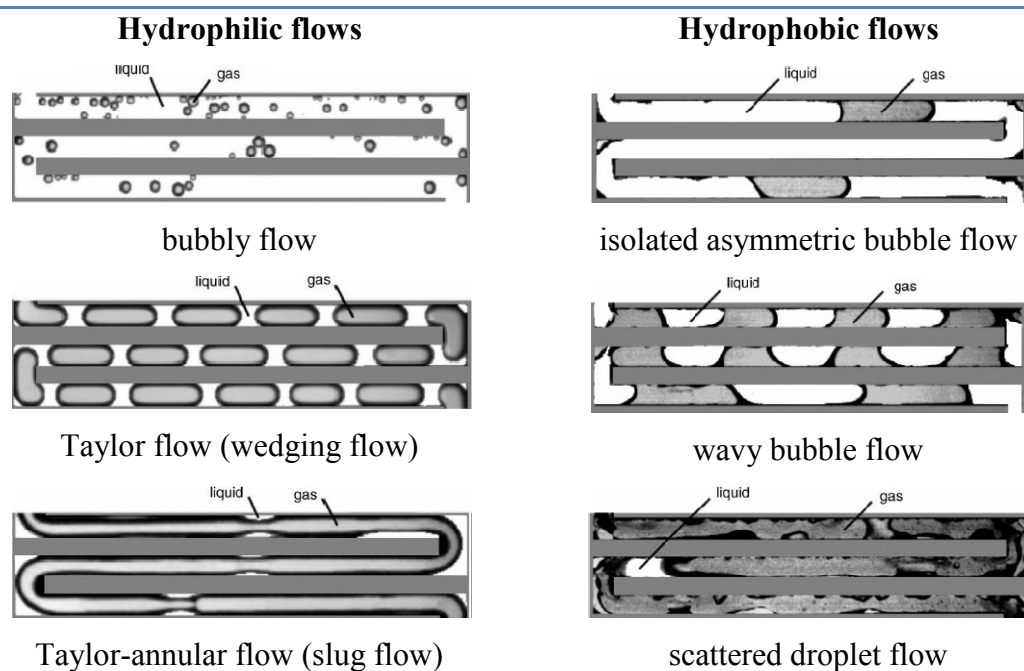


Figure 3.7 Effect of wall wettability on flow pattern morphologies for air/water flows in a square channel with $d_H = 525\mu\text{m}$ (Cubaud et al., 2006). The hydrophilic flows were realised in a silicon channel with glass top ($\theta \approx 9^\circ$ for silicon and $\theta \approx 25^\circ$ for glass); the hydrophobic flows were realised in the same channel with Teflon coating ($\theta \approx 120^\circ$).

3.2.5 Fluid properties

The effect of surface tension on the flow pattern transition lines was investigated experimentally by Pohorecki et al. (2008) in a rectangular microchannel (0.2mm wide and 0.55mm deep) using both water ($\sigma = 0.073\text{N/m}$) and ethanol ($\sigma = 0.024\text{N/m}$) as the liquid phase. There was not enough data to establish the transition from bubbly to Taylor flow but Taylor to Taylor-annular transition was found to shift to lower U_{GS} with increasing surface tension.

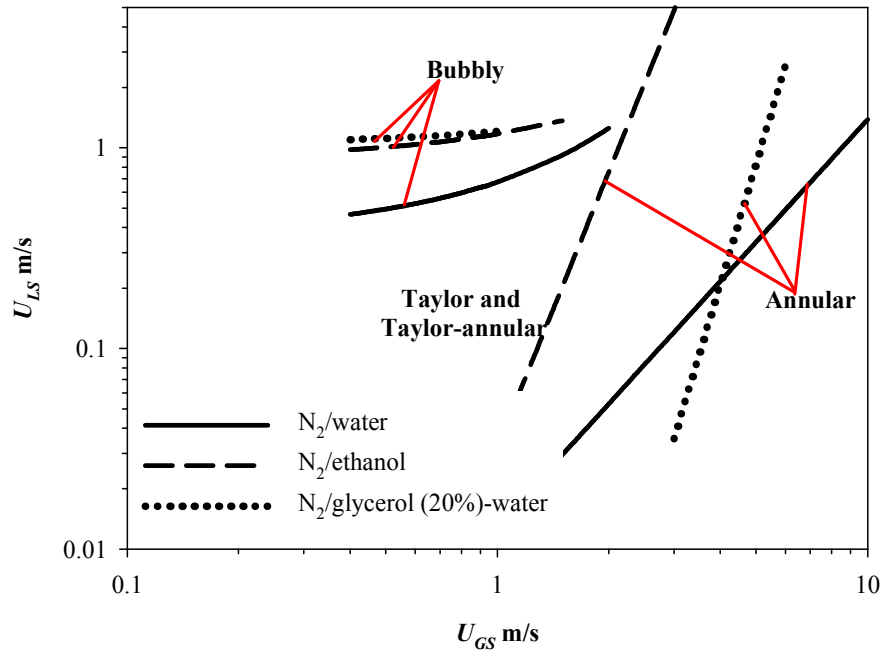


Figure 3.8 Effect of liquid surface tension and viscosity on flow pattern transitions in a rectangular microchannel with hydraulic diameter $d_H = 187.5\mu\text{m}$. The lines have been fitted to data presented by [Waelchli and von Rohr \(2006\)](#). The transition boundaries for bubbly and annular flows have been drawn in the figure while the patterns between these two lines are Taylor and Taylor-annular flows.

The opposite trend however, for the Taylor-annular flow transition was found by [Waelchli and von Rohr \(2006\)](#) from experiments in rectangular silicon microchannels ($d_H = 187.5$ and $218\mu\text{m}$). As can be seen in Figure 3.8, in N_2/water system ($\sigma = 0.073\text{N/m}$, $\mu = 0.001\text{Pa s}$) the Taylor-annular flow transition shifted to higher U_{GS} compared to the $\text{N}_2/\text{ethanol}$ system ($\sigma = 0.022\text{N/m}$, $\mu = 0.0011\text{Pa s}$). In addition, with the higher surface tension system bubbly flow shifted to lower U_{LS} . The same trends were also reported by [Yang and Shieh \(2001\)](#) ($d = 1\text{-}3\text{mm}$) using air/water ($\sigma = 0.0721\text{N/m}$) and vapour/liquid R-134a ($\sigma = 0.0075\text{N/m}$).

The disagreement could be a result of different inlets used in the studies. From the Y-junction inlet of [Pohorecki et al. \(2008\)](#), larger bubbles are expected from a higher surface tension liquid (Section 5.3.2.2), which explains the shift of the Taylor-annular flow transition to lower U_{GS} and would potentially extend Taylor flow to higher U_{LS} . In contrast, in both studies by [Waelchli and von Rohr \(2006\)](#) and [Yang and Shieh \(2001\)](#) there was upstream of the test section a mixing chamber with mesh structure just after the two fluids had joined. The two phases are expected to be broken within this mixing

chamber and the final drop size would be a result of both break up and of any subsequent coalescence. It appears that higher surface tension in this case favours the formation of smaller bubbles which would explain the shift of the Taylor to bubbly flow transition to lower U_{LS} and of the Taylor-annular transition to higher U_{GS} .

Waelchli and von Rohr (2006) also studied the effect of viscosity using a N₂/ 20% glycerol in water system ($\sigma = 0.073\text{N/m}$, $\mu = 0.00156\text{Pa}\cdot\text{s}$) which was reported to have the same surface tension as N₂/water but 50% higher viscosity. The Taylor to bubbly flow transition in N₂/glycerol-water system occurred at higher U_{LS} , while the transition to annular flow occurred at higher U_{GS} compared to that of N₂/water at the low liquid velocities but at lower U_{GS} at the high liquid velocities. The authors did not explain the observed results and little information is available in the literature on the effect of viscosity on flow patterns in channels with size less than 1mm. However, a similar shift with increased liquid viscosity of the Taylor to bubble transition in superficial liquid over gas velocity maps was reported by Furukawa and Fukano (2001) for a 19.2mm diameter pipe.

3.2.6 Inlet conditions

There have been a large number of studies on the effect of inlet conditions on bubble sizes in microchannels which revealed their dependence on size of inlet channels, angle and particular configuration that the two phases join as well as phase flowrates (Amador et al., 2004; Qian and Lawal, 2006; Garstecki et al., 2006). Although the bubble size will also determine whether the pattern is Taylor or bubbly flow, this transition has not been explicitly investigated. Studies on the effect of inlet on flow pattern transition boundaries are relatively few. Haverkamp et al. (2006) used two types of cross flow inlet, one with the phases joining perpendicularly and the other with the phases joining smoothly almost in parallel with each other, and observed a profound effect of the inlet type on the air-water flow patterns formed; for example the transition from Taylor (slug) to churn flow was shifted to higher gas velocities in the smooth inlet.

3.3 Flow regime prediction

The different regimes are often represented in two dimensional flow pattern maps, with the two coordinates representing some appropriate hydrodynamic parameters. The most popular coordinates are U_{GS} vs. U_{LS} , but dimensionless numbers have also been used. Examples from microgravity systems include Su vs. Re_{GS}/Re_{LS} (Jayawardena et al., 1997), We_{GS} vs. We_{LS} (Zhao and Rezkallah, 1993), We_G vs. We_L based on actual gas and

liquid velocities (Rezkallah, 1996). Void fraction is sometimes used to define transition boundaries in maps based on superficial velocities (Zhao and Rezkallah, 1993; Bousman et al., 1996; Cubaud and Ho, 2004).

Currently, no universal flow pattern map exists which includes all parameters influencing gas-liquid two-phase flows in microchannels. Akbar et al. (2003) summarized literature flow regime transitions in a map using the gas and liquid Weber numbers as coordinates and suggested that Weber number is more appropriate coordinate than the commonly used U_{GS} vs. U_{LS} . The proposed map worked well for experimental data obtained in air-water systems in horizontal channels with diameters around 1mm, both circular and non-circular. Hassan et al. (2005) proposed universal flow regime maps based on superficial velocities that were different for horizontal and vertical channels using their own and a number of other literature studies (Damianides, 1987; Fukano et al., 1989; Triplett et al., 1999; Kawahara et al., 2002; Pehlivan, 2003; Xu et al., 1999; Mishima et al., 1993). The proposed lines for horizontal channels predicted satisfactorily flow pattern transitions even at channels smaller than 1mm, e.g. 100 μ m (Kawahara et al., 2002). Cubaud and Ho (2004) from studies in square microchannels of size 200 and 525 μ m, proposed that pattern transitions in a map based on superficial velocities could be given in terms of volume fraction. In particular, the transitions from bubbly to Taylor, Taylor to Taylor-annular and Taylor-annular to annular flows take place at liquid volume fractions ($\alpha_L = Q_L / (Q_G + Q_L)$) equal to 0.75 ($U_{LS} = 3U_{GS}$), 0.04 ($U_{LS} = 0.042U_{GS}$) and 0.005 ($U_{LS} = 0.005U_{GS}$) respectively. These boundaries were not affected by microchannel size contrary to what was found in mini- and macro-channels (Bousman et al., 1996). Waelchli and von Rohr (2006) suggested a universal map based on their own experimental data in rectangular microchannels with 187.5 μ m and 218 μ m hydraulic diameter, using three liquid phases with different properties. For the map five dimensionless numbers were combined, based on a least square fit method, to give $10^7 Re_{LS}^{0.2} We'_{LS}{}^{0.4} (k/d_H)^5$ as ordinate and $Re_{GS}^{0.2} We'_{GS}{}^{0.4}$ as abscissa, where k/d_H is the relative roughness. The proposed pattern transition lines predicted well their data.

The above universal maps are compared in Figure 3.9 to Figure 3.12 against two sets of experimental data by Yang and Shieh (2001) and Chung and Kawaji (2004), obtained in horizontal circular tubes of 2mm and 250 μ m diameter respectively, that have not been used for their derivation. The coordinates used by Waelchli and von Rohr (2006) were modified to omit the effect of wall roughness.

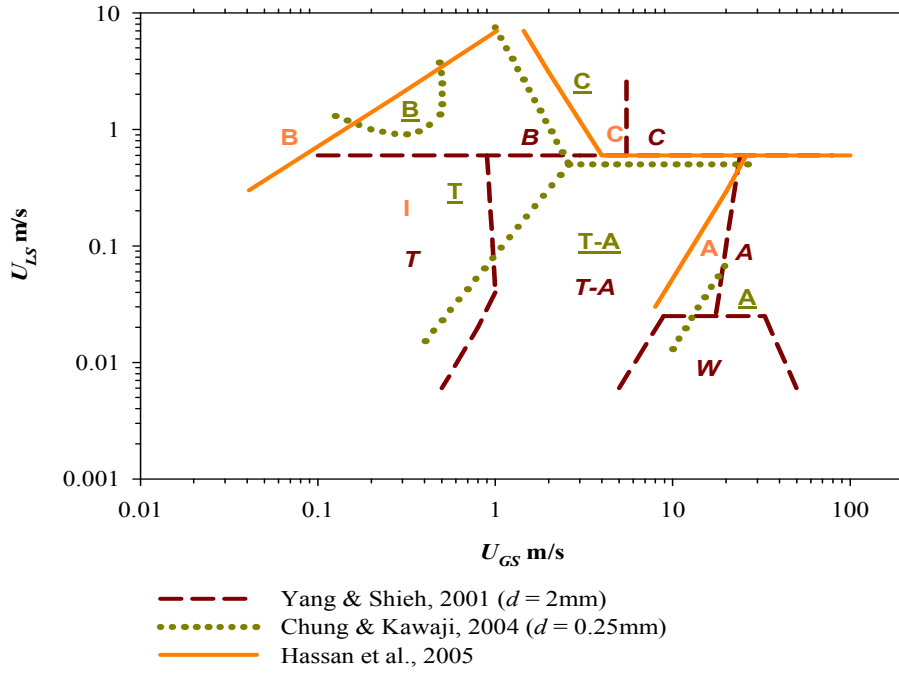


Figure 3.9 Comparison with the universal flow regime map by Hassan et al. (2005). Letters in normal, italic and underscore fonts stand for data by Hassan et al. (2005), Yang and Shieh (2001), and Chung and Kawaji (2004) respectively.

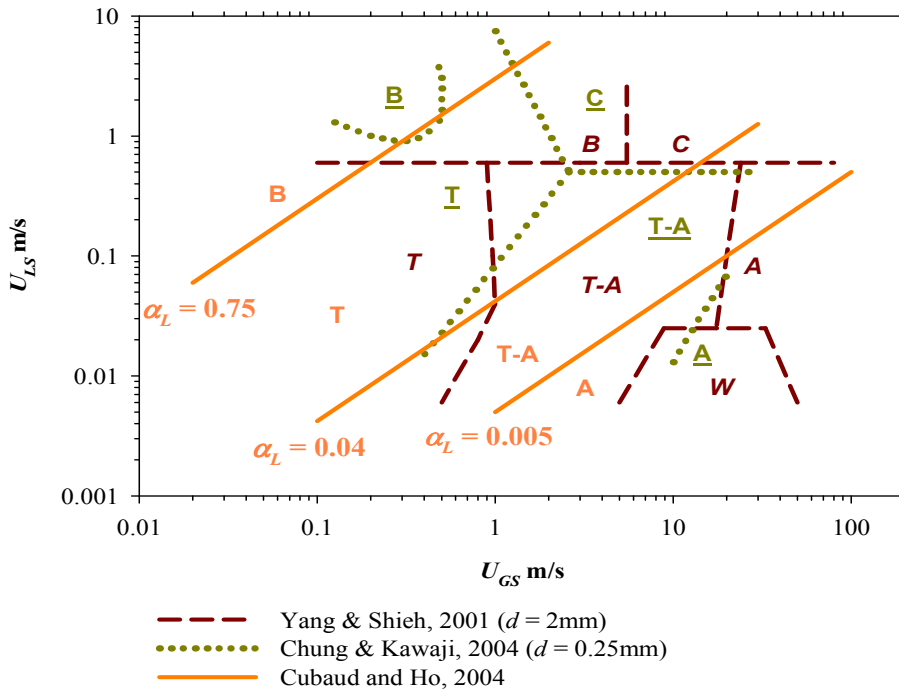


Figure 3.10 Comparison with the universal flow regime map by Cubaud and Ho (2004). Letters in normal, italic and underscore fonts stand for data by Cubaud and Ho (2004), Yang and Shieh (2001), and Chung and Kawaji (2004) respectively.

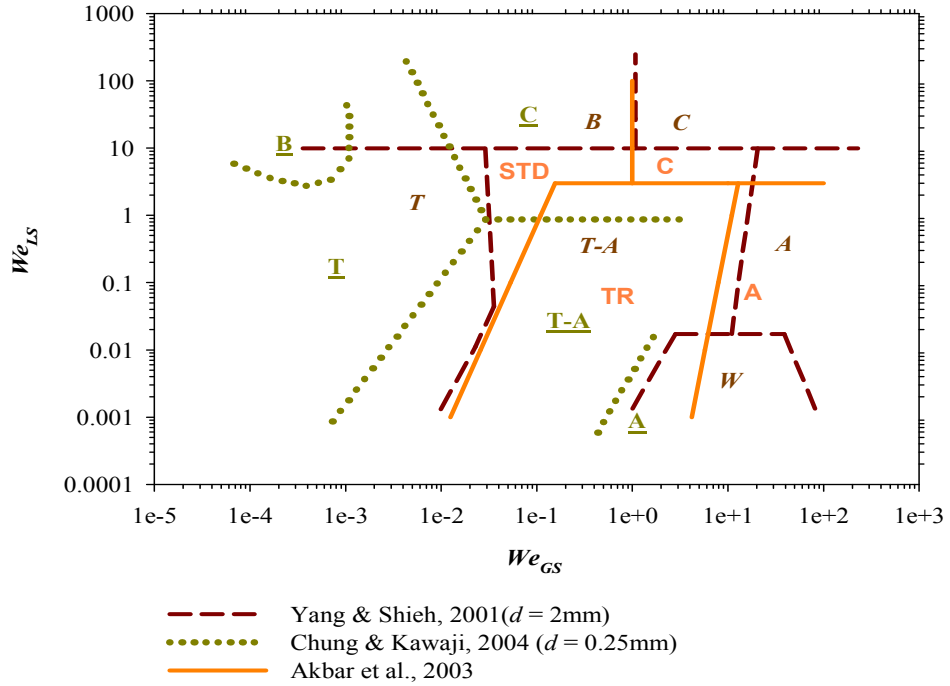


Figure 3.11 Comparison with the universal flow regime map by Akbar et al. (2003). Letters in normal, italic and underscore fonts stand for data by Akbar et al. (2003), Yang and Shieh (2001), and Chung and Kawaji (2004) respectively.

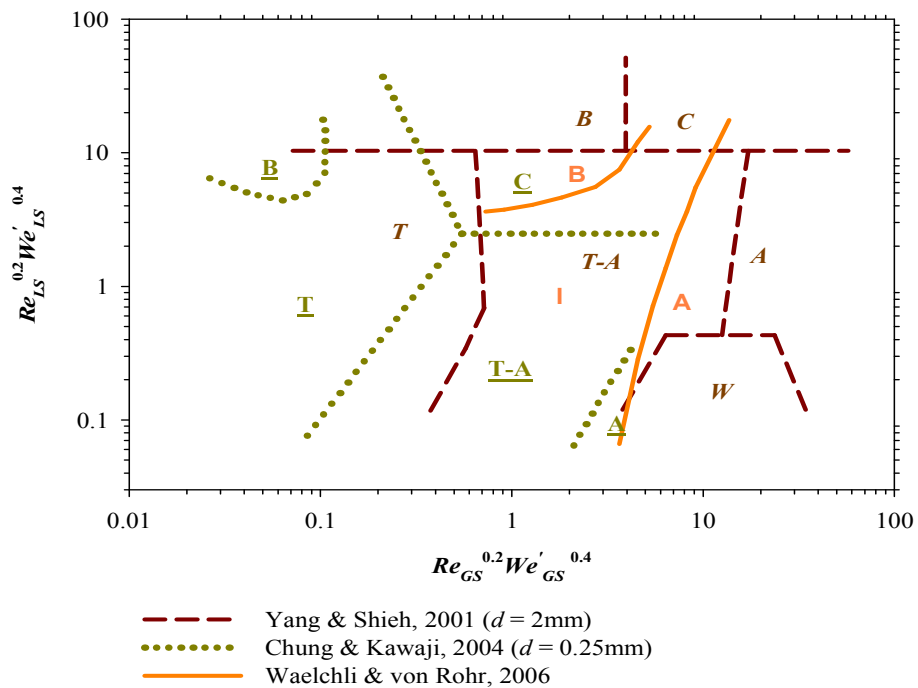


Figure 3.12 Comparison with the universal flow regime map by Waelchli and von Rohr (2006). Letters in normal, italic and underscore fonts stand for data by Waelchli and von Rohr (2006), Yang and Shieh (2001), and Chung and Kawaji (2004) respectively.

The transition lines by Hassan et al. (2005) based on superficial velocities predict the pattern boundaries satisfactorily for both examples (see Figure 3.9), apart from the transition to bubbly flow. It is possible that different inlet conditions may have contributed to this discrepancy. The transition lines based on volume fraction by Cubaud and Ho (2004) appear in Figure 3.10 to have lower slopes than the experimental ones leading to larger discrepancies from the experimental data than those suggested by Hassan et al. (2005). The transition lines in Weber number coordinates suggested by Akbar et al. (2003) predict satisfactorily the transitions in the large channel of 2mm, but not in the small one of 250 μm (Figure 3.11). The lines proposed by Waelchli and von Rohr (2006) predicted better the transitions in the large 2mm channel than in the small one (see Figure 3.12) but had the least accuracy among the three universal maps considered here.

From the above comparisons it appears that a universal flow pattern map based on U_{GS} - U_{LS} coordinates predicts the flow pattern transitions with good accuracy for the examples examined. However, by using such coordinates the effects of other parameters that can influence flow patterns, such as channel diameter and surface tension, are not reflected on the transition lines. Such parameters are included when dimensionless numbers are used as coordinates, but this leads to, in some cases, large discrepancies. Changes in the dimensionless numbers *because of changes in some parameters affect all the transition lines contrary to what was found experimentally*. For example, changes in channel dimensions have been found experimentally to affect the transition to bubbly and to Taylor-annular, but not to annular flow. If however, dimensionless numbers which contain the channel dimension, such as Reynolds or Weber numbers, are used as coordinates in a flow pattern map all the transition lines including that to annular flow will be affected. In addition, inlet conditions can strongly influence flow patterns (Section 3.2.6) and these are not usually taken into account in the prediction of flow pattern transition lines.

3.4 Conclusions

Knowledge of flow patterns forming under given inlet and operational conditions is essential for predicting the behaviour of gas-liquid microsystems. However, there is no generalised flow pattern map that includes the effects of all parameters affecting pattern transitions. The available literature indicates that the parameters that affect most these patterns and their transitions are channel size, phase superficial velocities, liquid phase surface tension and channel wettability while channel geometry has a small effect. Due

to the limited amount of data available it was not possible to conclude on the effect of flow orientation and liquid viscosity.

Universal flow regime maps suggested in the literature (Akbar et al., 2003; Cubaud and Ho, 2004; Hassan et al., 2005; Waelchli and von Rohr, 2006) were tested against patterns formed in a 2mm (Yang and Shieh, 2001) and a 250 μ m (Chung and Kawaji, 2004) channels. The results indicated that the maps based on the simplest coordinates, $U_{GS} - U_{LS}$, represented best the transitions between the different patterns for both channel dimensions tested.

With decreasing channel dimension surface and interfacial forces become dominant. As a result, properties such as wall wetting characteristics (Lee and Lee, 2008), wall roughness and contamination level (Serizawa et al., 2002) and inlet conditions (Haverkamp et al., 2006) will affect the flow patterns formed. Numerical simulations can help investigate the effects of different parameters and inlet conditions on flow patterns formed but at least with commercial CFD codes the handling of interfaces and contact lines still remains a challenge. Controlled experiments, with the advantages offered by the development of the microfabrication techniques, e.g. well defined wall wetting characteristics or roughness and specific inlet geometries will offer useful insights that can be implemented in theoretical models for flow pattern transitions based on physical principles.

Chapter 4
Effect of Inlet Conditions on Gas-Liquid Flow
Regimes in Microchannels

Nomenclature

d	Characteristic dimension, m
Q	Volumetric flowrate, m ³ /s
U	Velocity, m/s
V	Volume, m ³

Dimensionless Numbers

We_{GS}	Gas Weber number based on superficial gas velocity, $\rho_G U_{GS}^2 d / \sigma$
We_{LS}	Liquid Weber number based on superficial liquid velocity, $\rho_L U_{LS}^2 d / \sigma$

Subscripts

B	Bubble
C	Channel or capillary
GS	Gas phase superficial
I	Inlet
LS	Liquid phase superficial

Flow Patterns

A	Annular flow
B	Bubbly flow
C	Churn flow
T	Taylor flow
$T-A$	Taylor-annular flow

Inlet Configurations

CGP	Cross flow layouts with gas inlet parallel to the main flow
CLP	Cross flow layouts with liquid inlet parallel to the main flow
G	Gas inlet
L	Liquid inlet
M	Main channel
T	T-junction inlet
Y	Y-junction inlet

4.1 Introduction

As shown in Chapter 3, with decreasing characteristic length scales, flow patterns and their transitions are increasingly influenced by tube wall wetting properties and channel inlet geometry, which limit most of the reported results to specific systems. However, there are limited studies on the effect of inlet geometry on flow patterns and their transitions in small channels. [Haverkamp et al. \(2006\)](#) characterized gas-liquid flow patterns in single and multiple rectangular microchannels and reported that the inlet mixer design affected the flow transition boundaries. There is more work available on the effect of inlet geometry on Taylor flow as seen in Section 2.5. Taylor bubble lengths were found to depend significantly on the gas inlet size ([Amador et al., 2004](#); [Qian and Lawal, 2006](#); [Garstecki et al., 2006](#)) and the inlet tee orientation ([Qian and Lawal, 2006](#)). In this chapter, the effect of inlet geometry on the gas-liquid flow patterns and their transitions in microchannels with different sizes were investigated experimentally and the results for the different conditions were compared against each other and with literature data.

4.2 Experimental setup

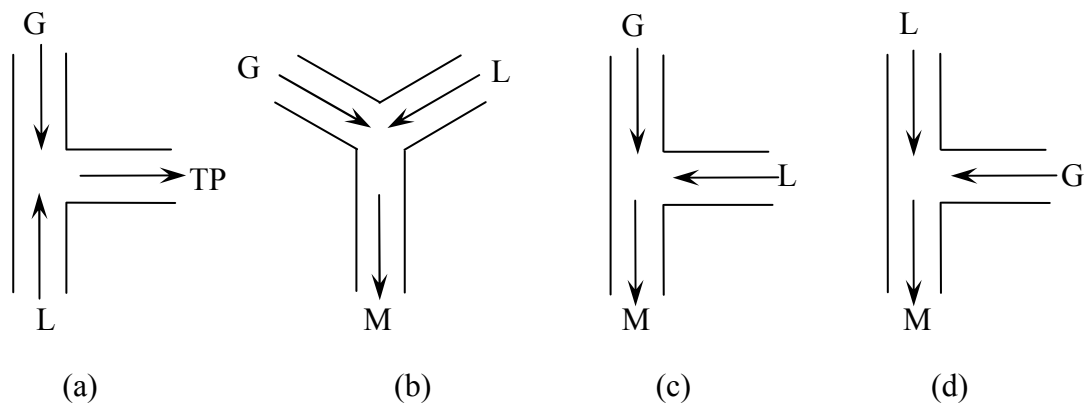


Figure 4.1 Inlet configurations. (a) T; (b) Y; (c) CGP; (d) CLP. G: gas inlet; L: liquid inlet; M: main channel.

The experiments were carried out in polyphenylsulfone circular capillaries (Radel R tubing from Upchurch Scientific) that have readily wetted surfaces. Capillaries with two different internal diameters of 0.5mm and 0.75mm and overall length of 0.2m were used. The two fluids joined in PEEK inlet junctions (Upchurch Scientific) with hole sizes of 0.5mm, 1mm and 1.25mm and four different configurations (see Figure 4.1); a T-junction (T), a Y-junction (Y), and two layouts developed from T-junction where either

gas (CGP) or liquid (CLP) enter with direction parallel to the main flow and the other phase enters with direction perpendicular to that of the flow.

Nitrogen and deionised water were used as test fluids while the experiments were carried out in room temperature and atmospheric pressure at outlet. Air was supplied from a gas cylinder and was regulated by two Brooks 5850 series mass flow controllers with flowrates between 0.3-20ml/min and 20-200ml/min respectively. Water was introduced using a KNAUER HPLC liquid pump with flowrates up to 50ml/min. The flows were recorded 0.15m downstream of the inlets with a high-speed video camera (Photron FASTCAM MC-1) with image resolution up to 512x512 pixels, using recording speeds 2000-5000fps and a shutter speed up to 160000s.

4.3 Results and discussions

4.3.1 Flow patterns

Five main flow patterns were observed, namely bubbly, Taylor, churn, Taylor-annular, and annular flows (Figure 4.2). Characteristics of each flow pattern are in Section 2.2.

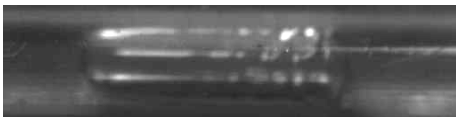
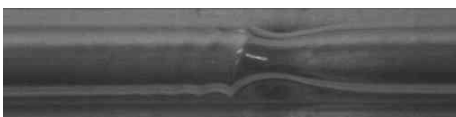
Bubbly		$d_C = 0.75\text{mm}, d_I = 0.5\text{mm},$ $U_{GS} = 0.097\text{m/s}, U_{LS} = 0.385\text{m/s}$ Inlet configuration: T
Taylor		$d_C = 0.75\text{mm}, d_I = 0.5\text{mm},$ $U_{GS} = 0.338\text{m/s}, U_{LS} = 0.269\text{m/s}$ Inlet configuration: T
Churn		$d_C = 0.5\text{mm}, d_I = 1.25\text{mm},$ $U_{GS} = 17.8\text{m/s}, U_{LS} = 4.23\text{m/s}$ Inlet configuration: T
Taylor-annular		$d_C = 0.5\text{mm}, d_I = 1.25\text{mm},$ $U_{GS} = 11.9\text{m/s}, U_{LS} = 0.192\text{m/s}$ Inlet configuration: T
Annular		$d_C = 0.5\text{mm}, d_I = 1.25\text{mm},$ $U_{GS} = 19.8\text{m/s}, U_{LS} = 0.0448\text{m/s}$ Inlet configuration: T

Figure 4.2 Flow patterns observed in various capillaries and gas-liquid flowrates. Flow is from right to left.

4.3.2 Effect of inlet size

The flow regime maps in the 0.5mm capillary are shown in Figure 4.3 for two T-inlets with sizes 0.5mm (symbols) and 1.25mm (lines). It can be seen that Taylor flow (T) dominates for a wide range of gas and liquid superficial velocities. With the large inlet ($d_I = 1.25\text{mm}$), bubbly flow does not appear for the range of flowrates investigated while the boundaries of Taylor-annular and churn flow appear at lower gas velocities compared to the small one. Annular flow also appears at the highest gas superficial velocity. These changes are attributed to the increased surface tension force in the large inlet compared to the small one that tends to keep the forming bubbles attached (see Section 5.3.2.2). As a result bubbles larger than the channel size will be produced and no bubbly flow will occur. In order to establish bubbly flow even higher liquid flowrates will be necessary to detach the gas bubbles before their size grows large.

From Figure 4.4, where Taylor bubble volumes, V_B , for three inlet sizes are compared, it can be seen that bubble volume increases with inlet size for the same liquid flowrate. The bubble volumes are averaged over 500 bubbles for each flow condition. The same effect of inlet size on bubble length was observed by [Qian and Lawal \(2006\)](#). The increasing attaching surface tension forces explain also the transition to Taylor-annular flow at lower superficial gas velocities in the large inlet compared to the small one (Figure 4.3). This effect is, however, not very pronounced because at the high gas flowrates where this transition occurs inertia forces begin to dominate and the effect of surface tension forces diminishes. Similar results for the transition from Taylor to bubbly flow were also found in the 0.75mm capillary (Figure 4.5). In this larger channel though, the effect of surface tension forces was less significant and the transitions from Taylor to Taylor-annular and churn flows that are primarily inertia dominated were not affected significantly by the inlet size (Figure 4.5).

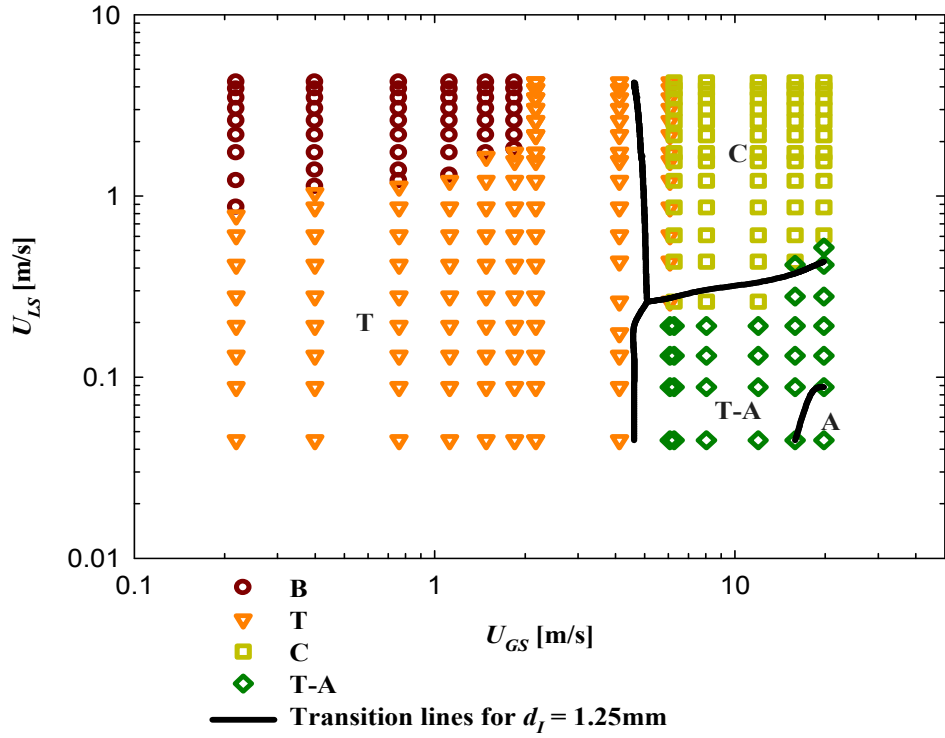


Figure 4.3 Effect of inlet size on flow pattern transitions. $d_C = 0.5\text{mm}$, T inlet configuration. Colored symbols represent the flow patterns for $d_I = 0.5\text{mm}$. Black solid lines represent the flow pattern transition lines for $d_I = 1.25\text{mm}$.

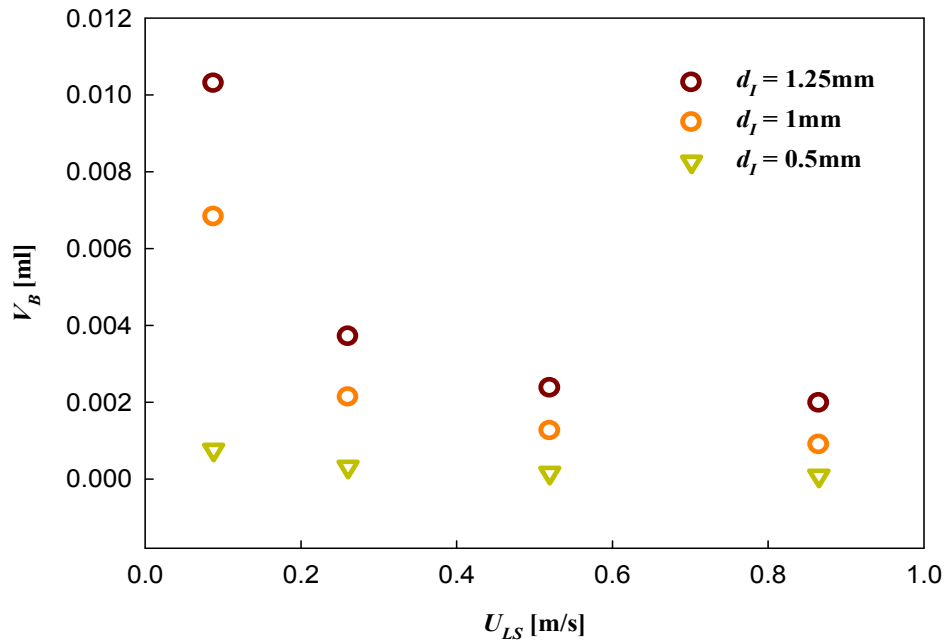


Figure 4.4 Taylor bubble volume for different inlet sizes. $d_C = 0.5\text{mm}$, $U_{GS} = 0.761\text{m/s}$, T inlet configuration.

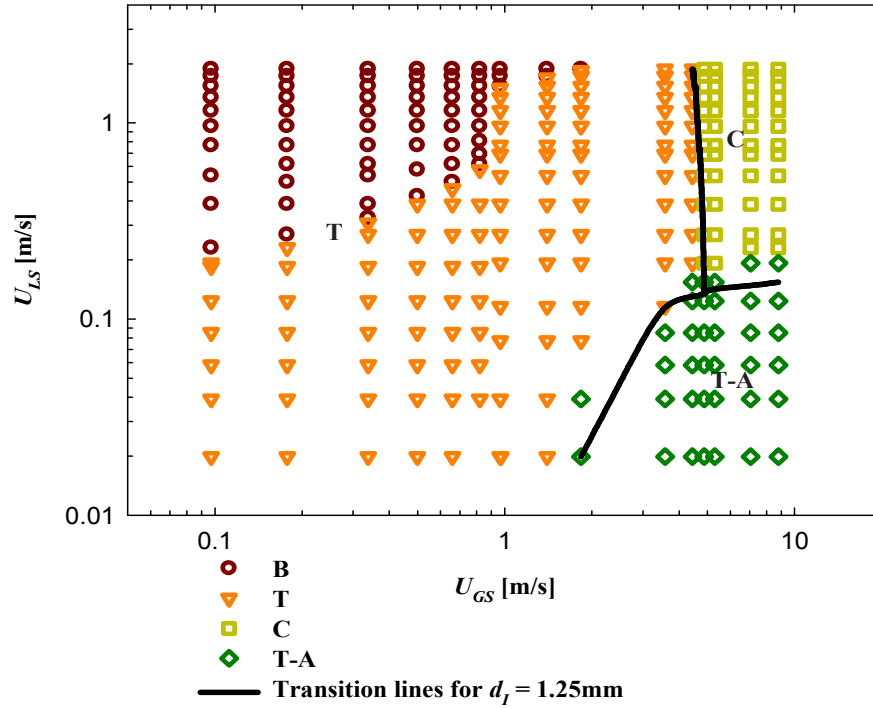


Figure 4.5 Effect of inlet size on flow pattern transitions. $d_C = 0.75$ mm, T inlet configuration. Symbols represent the flow patterns for $d_I = 0.5$ mm. Black solid lines represent the flow pattern transition lines for $d_I = 1.25$ mm.

4.3.3 Effect of inlet configuration

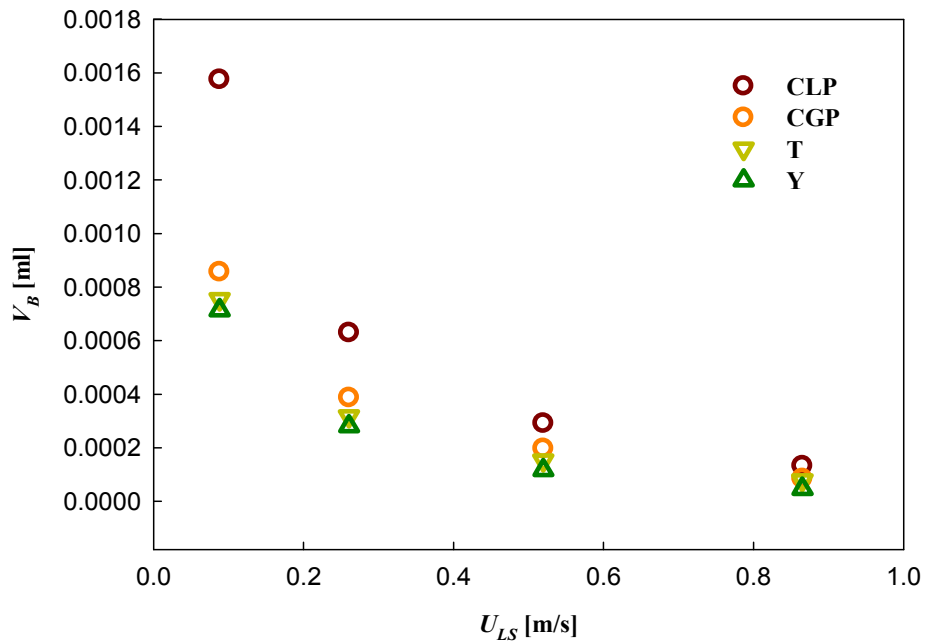


Figure 4.6 Taylor bubble volume for different inlet configurations shown in Figure 4.1. $d_C = 0.5$ mm, $d_I = 0.5$ mm, $U_{GS} = 0.761$ m/s.

The effect of inlet configuration on bubble size during Taylor flow is shown in Figure 4.6 for channel size $d_C = 0.5\text{mm}$ and the same inlet diameter $d_I = 0.5\text{mm}$ but different gas-liquid contacting configurations. The cross flow configuration CLP was found to generate larger bubbles compared to the others. However, the difference in bubble volume resulting from the variation in the inlet configuration is much less than that resulting from the inlet size and is not expected to affect significantly flow pattern transitions. The same results were also observed in the capillary $d_C = 0.75\text{mm}$ with inlet size $d_I = 0.5\text{mm}$.

4.3.4 Effect of capillary size

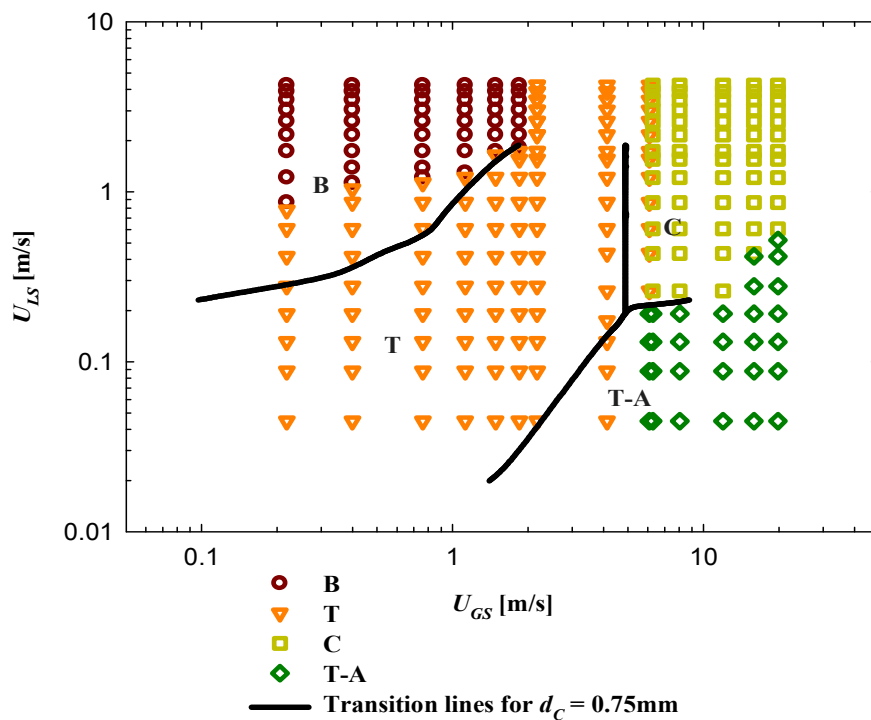


Figure 4.7 Effect of capillary size on flow pattern transitions. $d_I = 0.5\text{mm}$, T inlet configuration. Symbols represent flow patterns for $d_C = 0.5\text{mm}$. Black solid lines represent the transition lines for $d_C = 0.75\text{mm}$.

The effect of capillary size on flow pattern transitions can be seen in Figure 4.7 for a T-junction inlet of 0.5mm . In the larger channel transition from Taylor to bubbly and to Taylor-annular flow appears at lower liquid and gas superficial velocities respectively. Figure 4.8 shows that similar bubble volumes are achieved in both capillary sizes, apart from the very low liquid flowrate. This suggests that although similar bubbles are generated from the same inlet, the earlier transition to bubbly flow in the large capillary

than in the small one happens because the formed bubbles are smaller than the channel in the former case but not in the latter. In addition, in the large capillary the effect of surface tension force is reduced, which makes it easier for long Taylor bubbles to join and the pattern to change to Taylor-annular or churn flow.

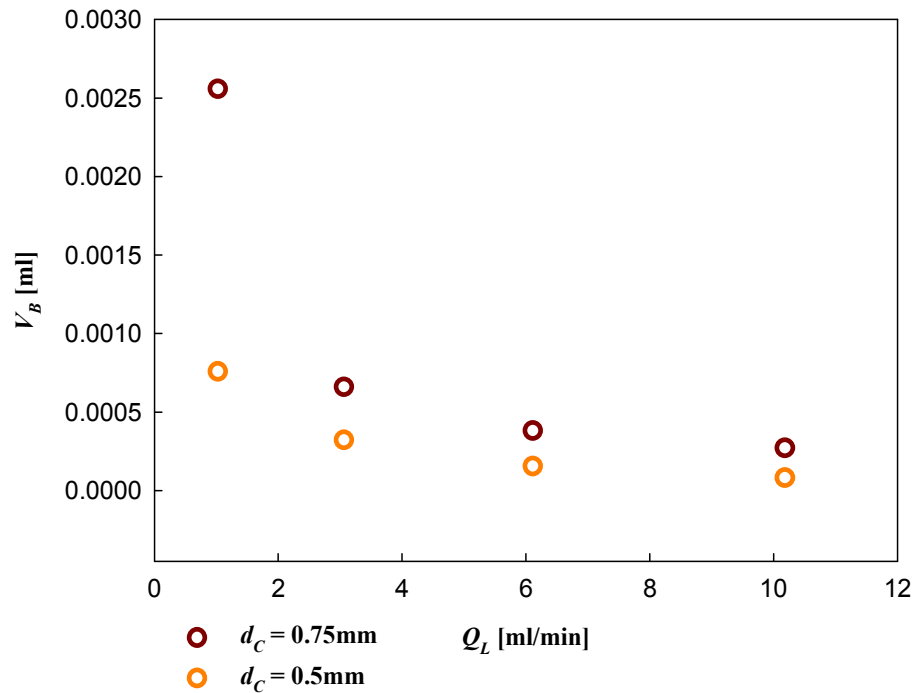
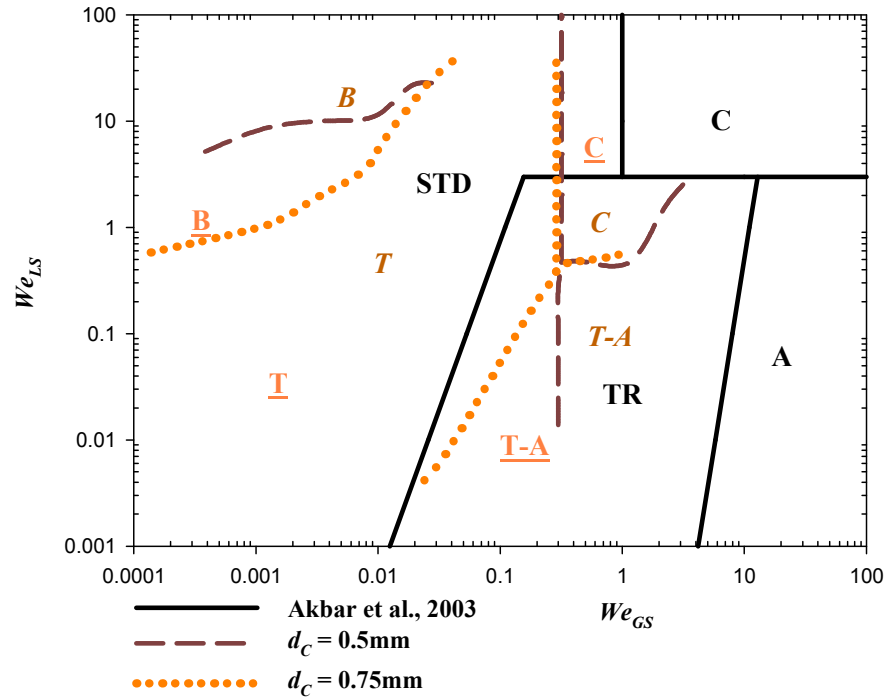


Figure 4.8 Taylor bubble volume for different capillary sizes. $d_I = 0.5\text{mm}$, $Q_G = 8.96\text{m/s}$, T inlet configuration.

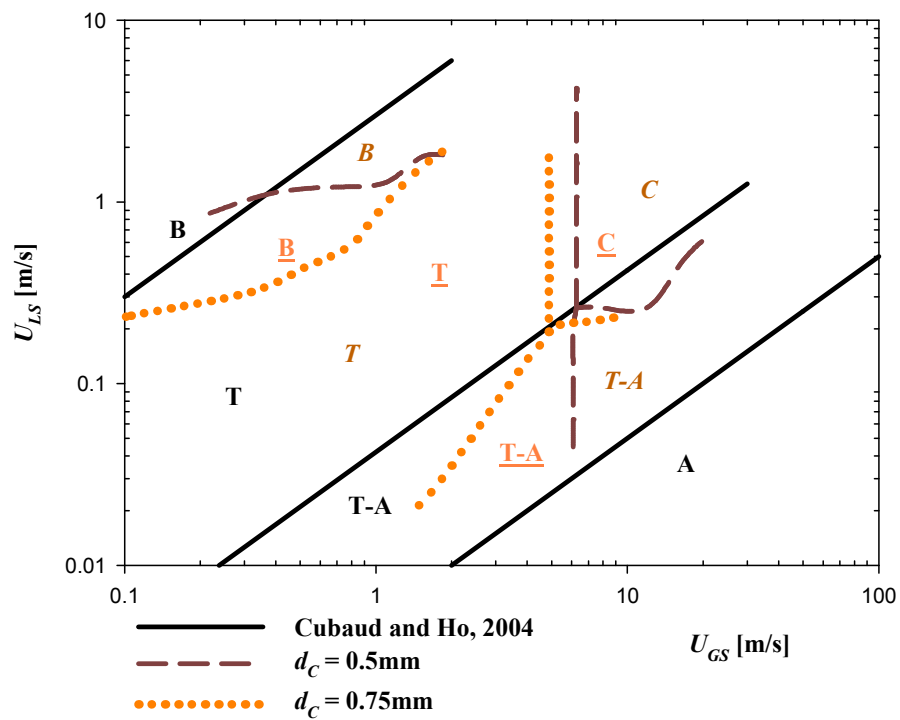
4.3.5 Comparison with literature

The flow pattern transitions for different capillary sizes were compared against literature universal flow regime maps in Figure 4.9. It was found that transition lines based on liquid volume fractions, as suggested by [Cubaud and Ho \(2004\)](#) (see Figure 4.9b), predicted the experimental data better than those by [Akbar et al. \(2003\)](#) (Figure 4.9a) and [Hassan et al. \(2005\)](#) (Figure 4.9c). This observation agreed with Section 3.3 that universal flow maps using U_{GS} vs. U_{LS} predict better the flow transitions. It should be noted that effects of inlet size and configuration were not reflected by the literature universal flow regime maps.

4. Effect of Inlet Conditions on Gas-Liquid Flow Regimes in Microchannels



(a)



(b)

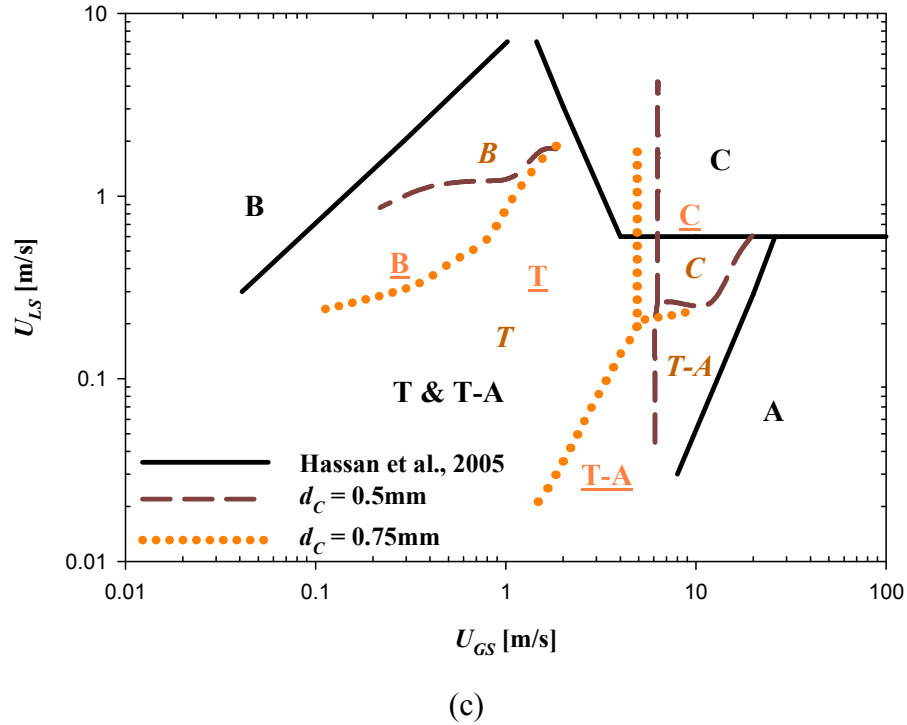


Figure 4.9 Comparison of flow pattern transitions with the literature universal flow regime maps by (a) Akbar et al. (2003), (b) Cubaud and Ho (2004) and (c) Hassan et al. (2005). $d_I = 0.5\text{mm}$, T inlet configuration. Symbols in plain, italic and underlined are for the literature, flows in 0.5mm capillary and flows in 0.75mm capillary respectively.

4.4 Conclusions

The effects of inlet size and configuration and channel size on gas-liquid flow patterns and their transitions in microchannels were investigated experimentally. The transition from Taylor to bubbly flow at low gas and high liquid superficial velocities did not occur when the inlet size was increased; as a result there was no bubbly flow when the large inlets were used. The inlet size also affected but to a lesser degree the transitions from Taylor to Taylor-annular and to churn flows at high gas superficial velocities. The inlet configuration and particularly the CLP one (cross flow with liquid parallel to the two-phase flow) was found to affect bubble size but not to the same extent as the inlet size. When the same inlet size and configuration were used, the size of the main capillary channel was found to have little effect on flow pattern transitions apart from the change from Taylor to bubbly flow. The flow pattern boundaries were predicted reasonably well by the transition lines suggested by Cubaud and Ho (2004).

Chapter 5

CFD Simulations of the Effect of Inlet Conditions on Taylor Flow Formation

Nomenclature

d	Internal or hydraulic diameter, m
\bar{F}	Dimensionless force term in momentum equation, -
g	Gravitational constant, m/s ²
h	Height of a rectangular channel, m
L	Length, m
p	Pressure, Pa
\bar{p}	Dimensionless pressure, $p/\rho U_{TP}^2$, -
Q	Volumetric flowrate, m ³ /s
r	Radius, m
t	Time, s
\bar{t}	Dimensionless time, tU_{TP}/d_C , -
u	Velocity, m/s
\bar{u}	Dimensionless velocity, u/U_{TP} , -
U	Velocity, m/s
w	Width of a rectangular channel, m

Greek Symbols

α	A constant of order one, -
ε	Volume fraction of fluid, -
μ	Dynamic viscosity, Pa s
$\bar{\mu}$	Dimensionless dynamic viscosity, -
ρ	Density, kg/m ³
$\bar{\rho}$	Dimensionless density, -
σ	Surface tension, N/m
$\bar{\sigma}$	Dimensionless surface tension, -
θ	Current contact angle, °

Dimensionless Numbers

Ca	Capillary number, $\mu_L U_B/\sigma$
------	--------------------------------------

Subscripts

<i>B</i>	Bubble
<i>C</i>	Channel or capillary
<i>G</i>	Gas
<i>GS</i>	Gas phase superficial
<i>L</i>	Liquid
<i>LS</i>	Liquid phase superficial
<i>N</i>	Gas nozzle
<i>S</i>	Slug
<i>TP</i>	Two-phase
<i>UC</i>	Unit cell

5.1 Introduction

As one of the dominant two-phase flow patterns in microchannels, Taylor flow is characterised by periodic occurrence of elongated capsular bubbles with an equivalent diameter several times that of the channel. The bubbles are separated by liquid slugs while only a thin liquid film (usually a very small percentage of the channel diameter) exists between them and the channel wall.

A number of investigations have shown that Taylor flow hydrodynamics and mass transfer performance are slug length dependent (Section 2.5). From inlet gas and liquid flowrates, the slug to bubble length ratio can be determined (Thulasidas et al., 1995). Their absolute values, however, will depend on the dynamics of the two-phase contacting at the inlet, as shown in Section 2.5.2. Bubble/slug lengths correlations in the literature are presented in Table 2.3. Several more recent studies, e.g. by Amador et al. (2004), Qian and Lawal (2006) and Garstecki et al. (2006), showed the significant effect of inlet geometry on bubble/slug lengths. In Chapter 2, it also showed that inlet sizes and configurations affect the Taylor bubble size and thus the flow regime transitions.

The simple and periodic morphology of Taylor flow and the laminar flow characteristics in microchannels make the system particularly suited for investigations through Computational Fluid Dynamics (CFD) simulations. A number of studies exists on the CFD modelling of hydrodynamics and mass transfer of Taylor bubbles within microcapillaries or channels (see for example Taha and Cui, 2006; van Baten and Krishna, 2004, 2005). In these studies the Taylor bubbles are taken to be fully formed and their lengths are assumed. Qian and Lawal (2006) studied numerically Taylor bubble formation at the inlet of a microchannel implementing CFD with the Volume of Fluid (VOF) model. However, coarse grids were used in their study and the thin film surrounding the bubbles was not observed; this could have affected the mechanism of bubble formation and subsequently bubble size.

In this chapter, CFD modelling is used to study the formation of Taylor bubbles in a capillary with a co-flow inlet configuration. The effect on bubble sizes of inlet conditions such as fluid velocities and gas nozzle size as well as surface tension and wall wetting properties, are investigated. The results are compared with experimental data from a similar system by Amador et al. (2004) and with other literature correlations.

5.2 Flow system and model formulation

The formation of Taylor bubbles is investigated in a capillary with 1mm internal diameter and smooth walls. A co-flow configuration is used at the inlet where the gas enters in the centre of the channel via a nozzle while the liquid flows around the nozzle as an annulus. Taylor bubble formation in the same design has been investigated experimentally (Amador et al., 2004), providing bubble sizes for comparison with the simulation results. The range of nozzle sizes and the inlet conditions investigated are summarised in Table 5.1.

Table 5.1 Simulation parameters used for the investigation of Taylor flow formation

Inlet condition	Value
Fluid pair	Air/water; air/octane; air/semi-octane
Gas nozzle size (ID/OD)	0.11/0.21 mm; 0.34/0.64 mm
Gas superficial velocity U_{GS}	0.01 - 0.033 m/s
Liquid superficial velocity U_{LS}	0.01 - 0.02 m/s
Contact angle	0°; 60°; 180°

Air is selected as the gas phase and paired with three different liquid phases, water, octane and “semi-octane”, whose physical properties are listed in Table 5.2. Semi-octane is a hypothetical fluid used for the simulation, that has the same density and viscosity as water, but its surface tension is that of octane. It is used to isolate the effect of surface tension on the bubble formation mechanism.

Table 5.2 Fluid properties used in the simulations of Taylor flow formation

Fluid	ρ (kg/m ³)	μ (Pa s)	σ (N/m)
Air	1.19	$1.7 \cdot 10^{-5}$	-
Water	998	0.001	0.07226
Octane	703	0.00052	0.02149
Semi-octane	998	0.001	0.02149

The CFD software CFX 4.3 (by ANSYS) is used for the simulations, which employs the VOF model for tracking the gas-liquid interface. The main advantage of VOF, compared to other front capturing methods, is its inherent volume conserving nature; this provides a good base to compare the simulated bubble volumes formed at the inlet

with those measured experimentally (Amador et al., 2004). The model assumes negligible effects of gravity, surface tension gradient (Marangoni effect) and gas compressibility. The transport equations are discretised by the finite volume method, applying a ‘HYBRID’ differencing scheme while pressure and velocity are coupled using the SIMPLEC algorithm. Surface tension is included as an extra body force in the momentum equation via the Continuum Surface Force (CSF) model. A very small time step ($1E-4\bar{t}$) is used to allow frequent interface profile modifications through a surface sharpening algorithm. At the wall, the interface normal and the interface curvature are modified according to the contact angle given.

The solution domain and its boundary conditions are depicted in Figure 5.1. The solution domain is constructed as a two-dimensional axisymmetric geometry in cylindrical coordinates, consisting of a main channel (right hand block in Figure 5.1) with a length three times that of the channel diameter and a gas nozzle (left hand block in Figure 5.1) with various widths but constant length of $0.3d_c$. Structured grids are generated in the blocks, which allow straightforward indexing of the nodes or control volumes and facilitate the formulation of the algebraic equations. Close to the wall region of the main channel the grid is refined so that the liquid film between the Taylor bubble and the wall can be captured. No-slip boundary condition is applied to all wall areas, indicated in Figure 5.1 by the hatched pattern. A *surface sharpening* algorithm is used that modifies the volume fractions of the two fluids at the end of each time step. The interface is placed at the cells where the volume fractions of the two fluids are equal to 0.5. A grid sensitivity analysis was carried out by monitoring both the velocity along the symmetry axis and the bubble volume. A grid size of 0.01 (grid dimension in both length and width) is selected, that results in velocity and bubble volumes very similar to those found with a smaller grid size of 0.005. With a grid size of 0.01 the number of computational cells is determined to be around 2×10^4 .

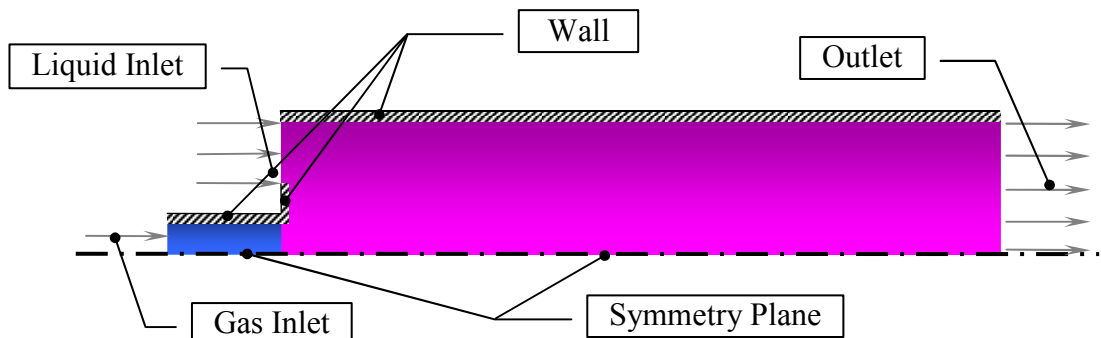


Figure 5.1 The solution domain with its boundary conditions.

The simulations were performed in an IBM RS/6000 workstation with Power 3 II processor, and the average running time for each case was approximately five days.

The governing equations are momentum balance (Eq. 5.1) and continuity equation (Eq. 5.2), where \bar{u} , \bar{p} , \bar{t} and \bar{F} are dimensionless velocity vector, pressure, time and a body force term respectively. When a control volume is not entirely occupied by one phase, mixture properties are applied as shown in Eq. 5.3 and Eq. 5.4. The density $\bar{\rho}$ and viscosity $\bar{\mu}$ are found from the volume fraction weighted averages of the respective single phase properties. For two-phase flow, the volume fraction of one phase is tracked by solving a phase marker function Eq. 5.5 and that of the other is derived from Eq. 5.6. All equations have been non-dimensionalised using as reference length the capillary diameter, d_C ; reference velocity the two-phase average velocity in the capillary, U_{TP} ; and reference time t , the ratio d_C/U_{TP} . The fluid properties in dimensionless form are given in Eq. 5.7 to Eq. 5.11.

$$\frac{\partial(\bar{\rho}\bar{u})}{\partial\bar{t}} + \bar{\nabla} \cdot (\bar{\rho}\bar{u}\bar{u}) + \bar{\nabla}\bar{p} = \bar{\nabla} \cdot \left[\bar{\mu}(\bar{\nabla}\bar{u} + \bar{\nabla}\bar{u}^T) \right] + \bar{F} \quad \text{Eq. 5.1}$$

$$\frac{\partial\bar{\rho}}{\partial\bar{t}} + \bar{\nabla} \cdot (\bar{\rho}\bar{u}) = 0 \quad \text{Eq. 5.2}$$

$$\bar{\rho} = \bar{\rho}_G \varepsilon_G + \bar{\rho}_L \varepsilon_L \quad \text{Eq. 5.3}$$

$$\bar{\mu} = \bar{\mu}_G \varepsilon_G + \bar{\mu}_L \varepsilon_L \quad \text{Eq. 5.4}$$

$$\frac{\partial\varepsilon_G}{\partial\bar{t}} + \bar{u} \cdot \bar{\nabla}\varepsilon_G = 0 \quad \text{Eq. 5.5}$$

$$\varepsilon_G + \varepsilon_L = 1 \quad \text{Eq. 5.6}$$

$$\bar{\rho}_G = \frac{\rho_G U_{TP} d_C}{\mu_L} \quad \text{Eq. 5.7}$$

$$\bar{\mu}_G = \frac{\mu_G}{\mu_L} \quad \text{Eq. 5.8}$$

$$\bar{\rho}_L = \frac{\rho_L U_{TP} d_C}{\mu_L} \quad \text{Eq. 5.9}$$

$$\bar{\mu}_L = \frac{\mu_L}{\mu_L} = 1 \quad \text{Eq. 5.10}$$

$$\overline{\sigma} = \frac{\sigma}{\mu_L U_{TP}} \quad \text{Eq. 5.11}$$

5.3 Results and discussions

5.3.1 Bubble formation mechanism

Bubble formation in the small gas nozzle (0.11mm ID) for the air-water system is depicted in Figure 5.2 and Figure 5.3 for two extreme scenarios: $\theta = 0^\circ$ and a $\theta = 180^\circ$. A multistage mechanism that consists of the expanding, contracting and necking stages is observed; these descriptions refer to the movement of the gas-liquid interface at the lower end of the bubble close to the nozzle. In the initial expanding stage (Figure 5.2A-C and Figure 5.3A-C) the liquid is displaced by the emerging gas while the gas-liquid interface moves away from the tube central axis. As the bubble is pushed forward in the channel, the interface retracts back towards the central axis (contracting stage, Figure 5.2D, Figure 5.3D-E). It is the expanding and contracting stages that contribute mostly to the bubble volume. As the bubble grows further in the radial direction and starts blocking the channel leaving only a thin liquid film close to the wall, liquid pressure builds up upstream. The lower end of the bubble is squeezed and as a result a neck forms that connects the bubble body with the tip of the gas (Figure 5.2E, F and Figure 5.3E). This is the necking stage, which takes place quickly in only several hundred time steps or less (e.g. 0.007s in Figure 5.2) compared with several thousand time steps needed for the previous stages (e.g. 0.032s in Figure 5.2). Finally the neck pinches off and the bubble moves downstream (Figure 5.2G and Figure 5.3F). During these stages, the bubble shape changes. When gas phase first emerges, the bubble assumes a spherical shape as it is still away from the side channel wall (Figure 5.2A, B and Figure 5.3A, B). As it expands, the middle part of the bubble grows quickly in the radial direction and forms a spherical zone, which has a smaller diameter than the spherical segment at the top (Figure 5.2C and Figure 5.3C). At the end of the contracting stage, the lower part of the bubble lifts gradually and takes the shape of a truncated cone with the apex in contact with the nozzle (Figure 5.3D). In the case of $\theta = 180^\circ$, gas is now the wetting phase and spreads to the wall to become the continuous phase as soon as the bubble forms (Figure 5.3G).

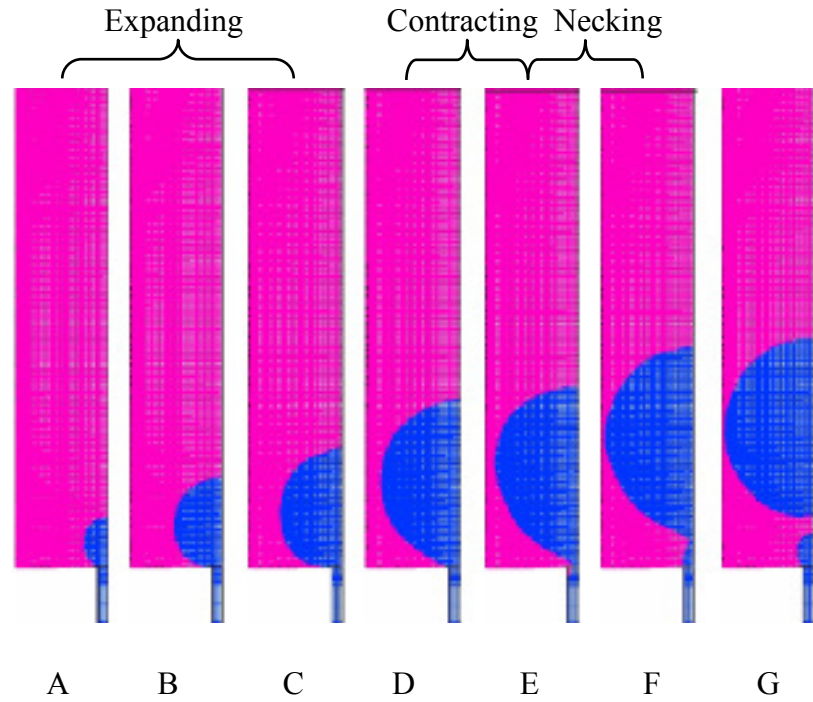


Figure 5.2 Bubble formation in air-water system with $\theta = 0^\circ$. $d_C = 1\text{mm}$, $d_N = 0.11\text{mm}$, $U_{GS} = 0.0155\text{m/s}$, $U_{LS} = 0.02\text{m/s}$, at times A: 0.0014s, B: 0.007s, C: 0.014s, D: 0.028s, E: 0.0322s, F: 0.0378s, G: 0.0392s.

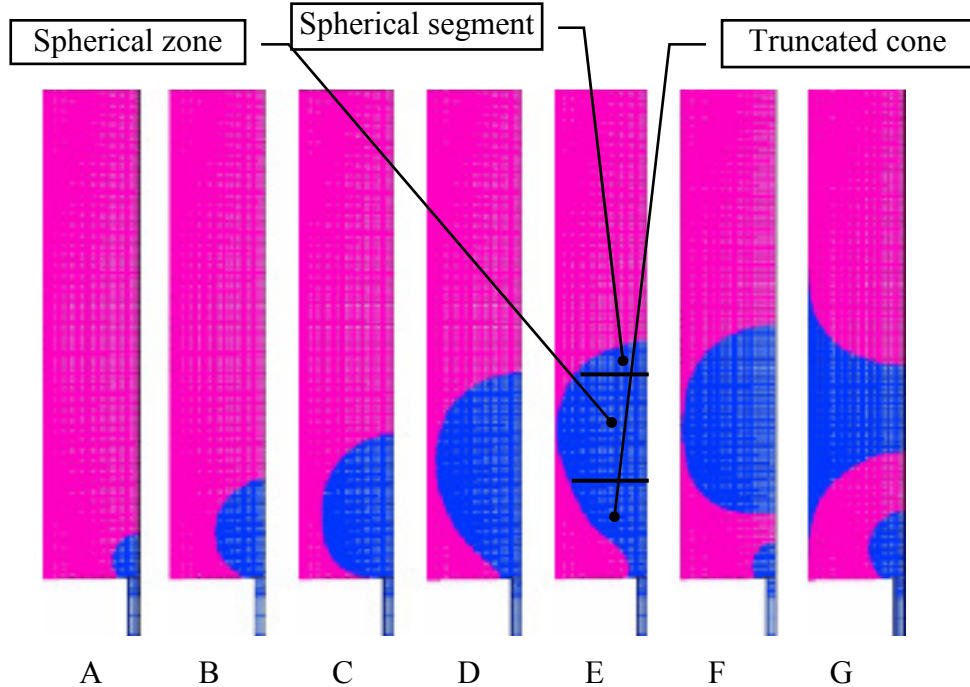


Figure 5.3 Bubble formation in air-water system with $\theta = 180^\circ$. $d_C = 1\text{mm}$, $d_N = 0.11\text{mm}$, $U_{GS} = 0.0155\text{m/s}$, $U_{LS} = 0.02\text{m/s}$, at times A: 0.0014s, B: 0.007s, C: 0.021s, D: 0.035s, E: 0.0406s, F: 0.0434s and G: 0.0462s.

During bubble formation for both contact angles studied, the expanding and contracting stages are accompanied by a movement of the three phase contact line along the top nozzle wall. The results of the current study, in accordance to the observations by Gnyloskurenko et al. (2003), suggest that the three phase contact line moves as shown schematically in Figure 5.4.

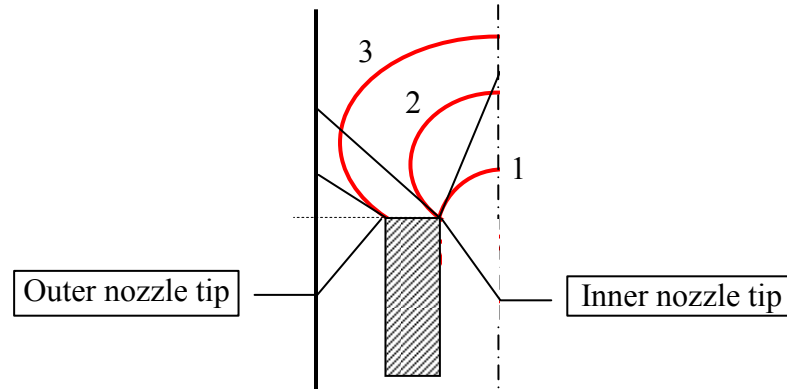


Figure 5.4 The movement of the three phase contact line on the top wall of the nozzle during bubble formation at very low gas flowrates.

At position 1 the meniscus is at the inner wall of the nozzle with current contact angle θ . With increasing gas pressure, if there is contact angle hysteresis, the contact angle will change to acquire its advancing value before the three phase contact line slides towards the outer nozzle wall (from position 2 to position 3). As the bubble expands, liquid builds up behind it and the liquid pressure becomes higher than the gas pressure. This pressure difference would resist further movement of the contact line towards the outer nozzle wall. When the contact angle attains its receding value (if that is different from the equilibrium one), the movement of the contact line will be reversed, i.e. from the outer towards the inner nozzle wall. As seen from Figure 5.2 and Figure 5.3, the movement of the contact line depends on the wetting conditions of the system. In the case of $\theta = 180^\circ$, the complete movement of the contact line (position 2 to position 3 and to position 2 again) occurs after 0.04s, slower than that in the case of $\theta = 0^\circ$, which is within 0.028s. As a result, the base of the forming bubble has a wider periphery for longer time in the less wetting case while all other operating conditions are the same.

No contact line movement along the nozzle wall was observed with the large nozzle size, $d_N = 0.34\text{mm}$, at the stored time intervals. This is perhaps because, the larger nozzle size reduces the pressure difference between the gas and the liquid at the contact point, according to Laplace equation (Eq. 5.12, $2r = d_N$ at the contact point) and this pressure difference may not be sufficient to initiate movement of the contact line. In addition, the

larger nozzle size increases the liquid phase inlet velocity for the same flowrate which, because of drag force, would cause the bubble to move downstream faster than in the case of small nozzle. All these contribute to the disappearance of contact line movement within the time interval used.

$$p_G - p_L = \frac{\sigma}{2r} \quad \text{Eq. 5.12}$$

5.3.2 Effect of inlet conditions on bubble size

Bubble length is often used in the literature to compare bubble sizes during Taylor flow (Table 2.3). To compare with experiments the formed bubble volume is used instead. The use of the VOF model means that the CFD simulations are computationally very expensive. In order to reduce computational time, the formation of only one or two Taylor bubbles is modelled for each case.

5.3.2.1 Effect of gas and liquid velocity

As can be seen from Figure 5.5 and Figure 5.6 the bubble volume increases with increasing gas and decreasing liquid superficial velocity respectively. The results agree very well with experimental data obtained in an identical system (Amador et al., 2004). By increasing U_{GS} , the rate that the gas enters the forming bubble increases. Although the detaching effect of the gas momentum flux would also increase and shorten the bubble formation time, it is compensated by the faster gas injection rate. With increasing U_{LS} , the detaching effect of liquid drag force increases, and smaller bubbles are formed.

5.3.2.2 Effect of liquid property

Three liquid phases, water, octane and semi-octane are used here to study the dependence of bubble sizes on surface tension, density and viscosity of the liquid phase. Figure 5.7 shows that the volume of bubbles produced in the octane system is smaller than that in the water system under the same conditions. In semi-octane, which has the density and viscosity of water but the surface tension of octane (Table 5.2), the bubble volumes are almost the same as those obtained in octane. This suggests that bubble size is mainly affected by surface tension and only slightly by density and viscosity. Compared to water, in octane the reduced attaching effect of the surface tension force causes the bubbles to detach earlier and smaller bubbles form. Both Laborie et al. (1999) and Qian and Lawal (2006) also found that increase in surface tension increased slightly bubble size while viscosity had almost no influence.

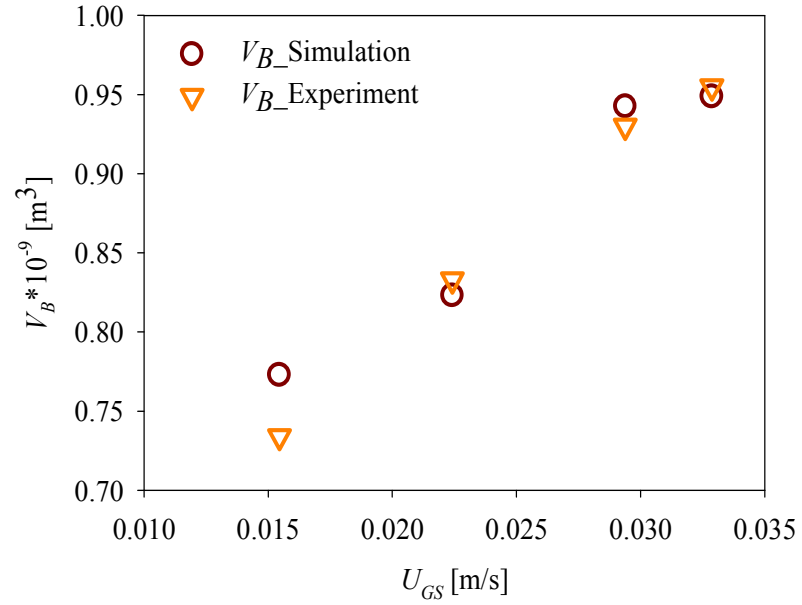


Figure 5.5 Effect of gas velocity on bubble volume. $d_C = 1\text{mm}$, $d_N = 0.11\text{mm}$, $U_{LS} = 0.02\text{m/s}$, $\theta = 0^\circ$, air-water system.

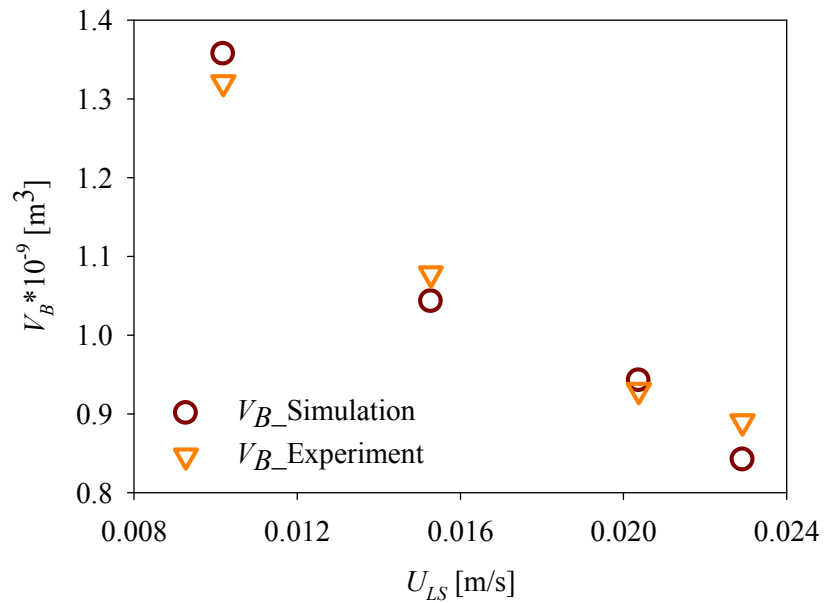


Figure 5.6 Effect of liquid velocity on bubble volume. $d_C = 1\text{mm}$, $d_N = 0.11\text{mm}$, $U_{GS} = 0.0294\text{m/s}$, $\theta = 0^\circ$, air-water system.

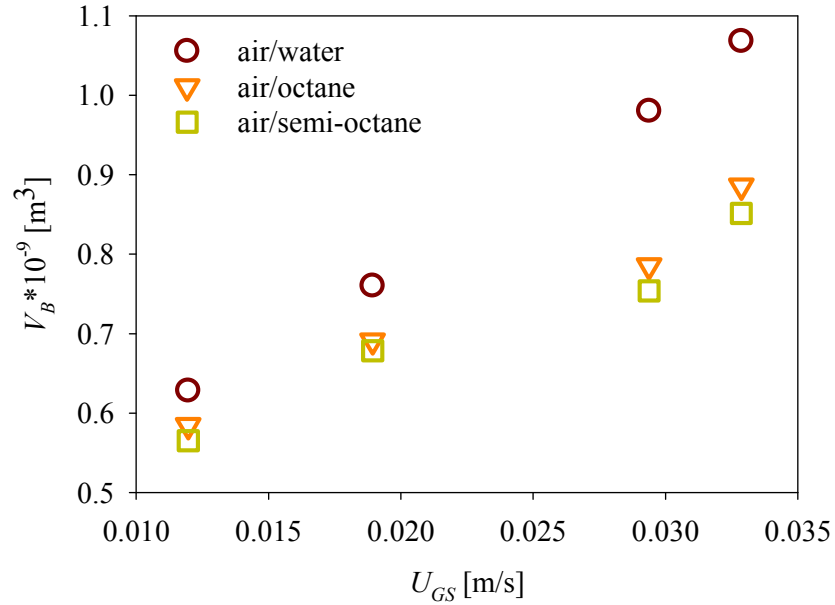


Figure 5.7 Effect of fluid property on bubble volume. $d_C = 1\text{mm}$, $d_N = 0.34\text{mm}$, $U_{LS} = 0.02\text{m/s}$, $\theta = 0^\circ$.

5.3.2.3 Effect of nozzle size and its wall thickness

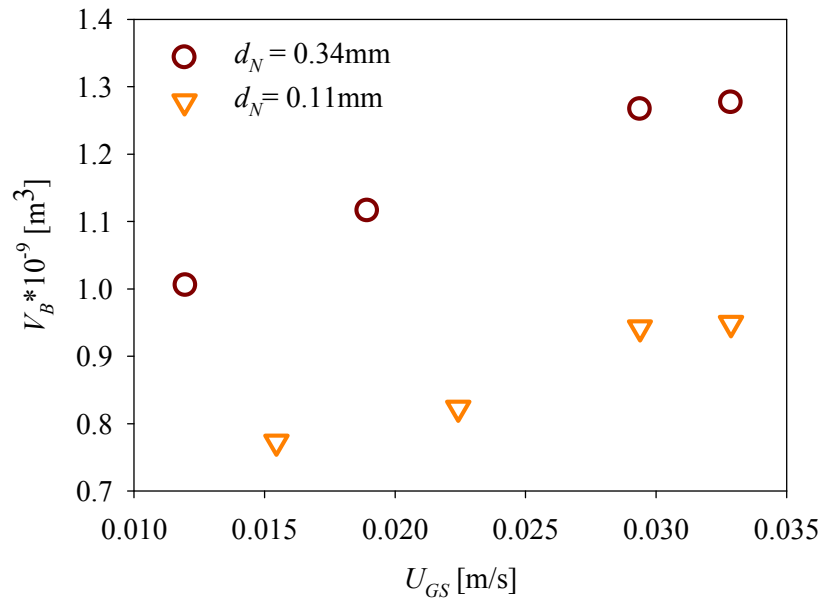


Figure 5.8 Effect of gas nozzle size on bubble volume. $d_C = 1\text{mm}$, $U_{LS} = 0.02\text{m/s}$, $\theta = 0^\circ$, air-water system.

As can be seen from Figure 5.8, increasing the nozzle size from 0.11mm to 0.34mm results in an increase in bubble volume. The nozzle size can affect bubble formation in two ways: for the same gas flowrate the gas flux in the large nozzle, which has a

detaching effect, decreases; in addition, the increased periphery of the large nozzle increases the surface tension force which has an attaching effect. Both help to extend the bubble formation time and thus its size.

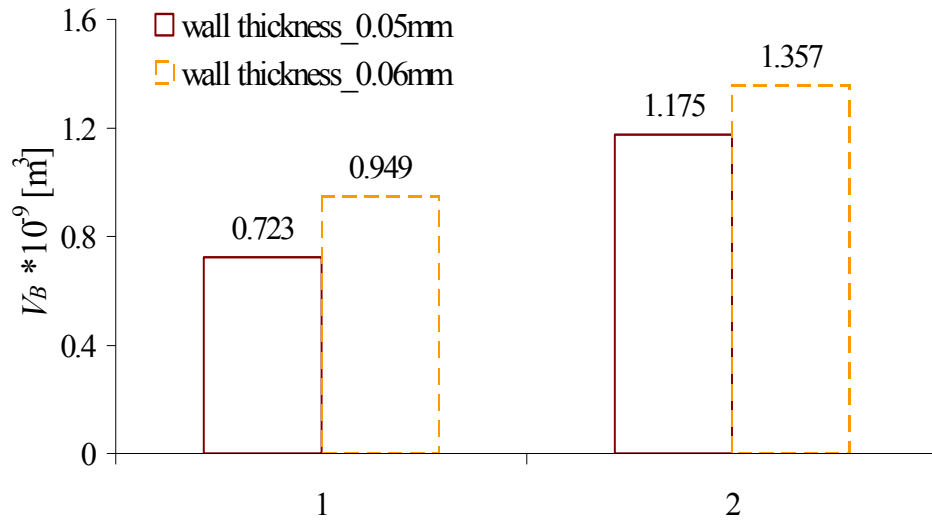


Figure 5.9 Effect of wall thickness on bubble volume. Case 1: $U_{GS} = 0.0329\text{m/s}$, $U_{LS} = 0.02\text{m/s}$; Case 2: $U_{GS} = 0.0294\text{m/s}$, $U_{LS} = 0.01\text{m/s}$. $d_C = 1\text{mm}$, $d_N = 0.11\text{mm}$, $\theta = 0^\circ$, air-water system.

Apart from the nozzle size, its wall thickness also seems to play a role on bubble size, as can be seen from Figure 5.9, where larger bubbles are observed for the thicker wall. As discussed before, the three-phase contact line can recede and advance along the top nozzle wall during bubble formation. Therefore, for a thicker wall more time is taken by the contact line to move outwards and inwards on the nozzle wall which allows extra time for the bubble to grow. However, when there is no contact line movement along the nozzle wall as in the case of $d_N = 0.34\text{mm}$, the effect of nozzle wall thickness will probably be absent.

5.3.2.4 Effect of wall wetting condition

To investigate the effect of wetting conditions on bubble size, three equilibrium contact angles are examined for the air-water system (Table 5.1). From Figure 5.10 it can be seen that as the wettability of the liquid worsens, i.e. equilibrium contact angle changes from 0° to 60° , bubble size increases by 7.2% (Figure 5.10a and b respectively). At time $t = 0.03\text{s}$, under the same operating conditions, when the first bubble has already detached for $\theta = 0^\circ$ and $\theta = 60^\circ$, it is still attached to the gas nozzle for $\theta = 180^\circ$, indicating that a larger bubble size will eventually form. Contact angle would affect the

movement of the three phase contact line on the top wall of the nozzle as well as the shape of the gas-liquid interface at the inlet and consequently the amount of gas entering the bubble. These results agree with the experimental observations by [Byakova et al., \(2003\)](#) but are opposite to the numerical predictions of [Qian and Lawal \(2006\)](#). In the latter, no liquid film around the bubble was observed and a three phase contact line existed on the capillary wall downstream of the inlet. As a result, gas-liquid interface changed from concave to convex on the liquid side when θ changed from 0° to 180° ; this change in shape affected the measured bubble length which was found to be inversely proportional to θ when the liquid phase was wetting but proportional to it for a non-wetting liquid.

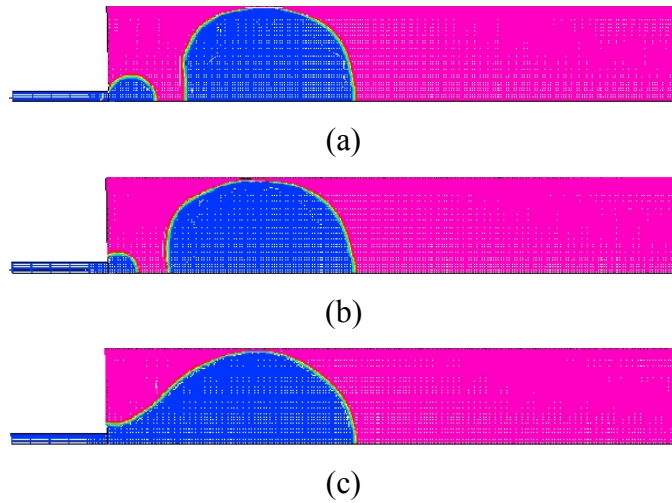


Figure 5.10 Effect of contact angle on bubble volume: (a) $\theta = 0^\circ$, $V_B = 0.773 \cdot 10^{-9} \text{ m}^3$; (b) $\theta = 60^\circ$, $V_B = 0.829 \cdot 10^{-9} \text{ m}^3$; (c) $\theta = 180^\circ$. $d_C = 1 \text{ mm}$, $d_N = 0.11 \text{ mm}$, $U_{GS} = 0.0155 \text{ m/s}$, $U_{LS} = 0.02 \text{ m/s}$, $t = 0.03 \text{ s}$, air-water system.

5.3.3 Bubble size comparison with literature

As shown in Section 5.3.2 and also in the literature (Section 2.5.2), the geometry of the inlet plays a significant role on the size of the formed bubbles and slugs. A number of correlations have been suggested in the literature for predicting Taylor bubble sizes (Table 2.3) that use various inlets (see Table 5.3). Even when T-junctions are used, the dimensions of the side inlet channels and the angles they join the main channel are not consistent. As such the correlations would only be able to predict sizes in the particular systems they were derived from. Despite these differences, however, the simulated data are compared in this section with the currently available literature correlations in order to evaluate their generality and ability to predict bubble/slug sizes during Taylor flow in microchannels.

For the comparison, the Taylor bubble lengths from this study are needed and these were obtained by measuring the axial distance between the front and the rear of the bubble. The comparisons with the literature correlations are depicted in Figure 5.11. When only a correlation for the slug length is given (e.g. Eq. 2.5), it is transformed to bubble length via Eq. 5.13 according to Liu et al. (2005). The gas fraction term ε_G in each case is estimated as suggested by the respective author.

$$L_B = L_{UC} \varepsilon_G = \frac{L_S}{\varepsilon_L} \varepsilon_G = \frac{L_S}{(1 - \varepsilon_G)} \varepsilon_G \quad \text{Eq. 5.13}$$

Table 5.3 Conditions used in literature and this work for determining bubble length

Literature	d_C [mm]	U_S [m/s]	Gas-liquid inlet
Kreutzer (2003)	1.56	$U_{GS} + U_{LS} < 0.75$	Liquid distributor
Garstecki et al. (2006)	$h: 0.033$ $w: 0.05 \sim 0.2$	$U_{GS}: 0.044 \sim 0.61$ $U_{LS}: 0.063 \sim 0.51$	T-junction
Qian and Lawal (2006)	1	$U_{GS}: 0.01 \sim 0.25$ $U_{LS}: 0.01 \sim 0.25$	T-junction
Laborie et al. (1999)	1~4	$U_{GS}: 0.1 \sim 0.74$ $U_{LS}: 0.1 \sim 1$	Porous membrane
Liu et al. (2005)	0.9~3	$U_{GS}: 0.008 \sim 0.7$ $U_{LS}: 0.008 \sim 0.5$	PVC T-connection
Akbar and Ghiaasiaan (2006)	0.1~1	$0.5 < U_{GS} + U_{LS} < 1.6$	No inlet given
This study	1	$U_{GS}: 0.01 \sim 0.033$ $U_{LS}: 0.01 \sim 0.02$	Co-flow annular configuration

As can be seen in Figure 5.11, Eq. 2.5 (Kreutzer, 2003) and Eq. 2.9 (Garstecki et al., 2006, with $\alpha = 0.57$ that fitted the data better than $\alpha = 1$) predict well the current data, but all others overpredict them. Apart from the different inlet configurations, another reason for the discrepancy could be the wider range and larger values of channel size and superficial gas and liquid velocities (wide range of Ca) used in the literature than in the current study (Table 5.3). The model by Garstecki et al. (2006) that predicts the data well, was developed particularly for low Ca , as those encountered in the present study. Furthermore, it is interesting, that the agreement is better with those correlations where volume fraction is included (Kreutzer, 2003; Qian and Lawal, 2006; Garstecki et al.,

2006). This would imply that the bubble length is affected by the gas/liquid flowrate or velocity ratio ($\varepsilon_L^{-1} \approx 1 + U_{GS}/U_{LS}$ from the definition of liquid volume fraction) more than by the other parameters. When Liu et al. (2005) and Laborie et al. (1999) used the two velocities separately, e.g. expressed in Re_G and Re_L , rather than as a ratio, larger deviation was observed.

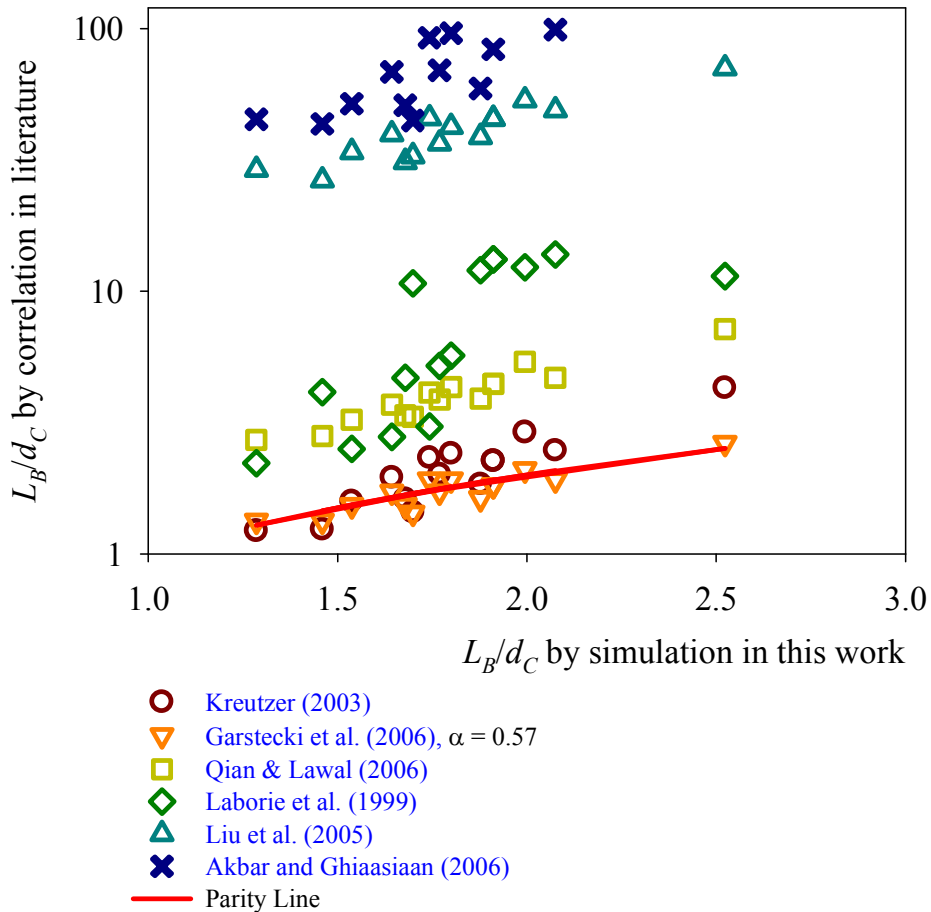


Figure 5.11 Comparison of simulated dimensionless bubble lengths with those predicted by literature correlations.

Interestingly, the correlation by Qian and Lawal (2006) that contains the volume fraction and was derived for velocity ranges and channel size very similar to those used here, still overpredicts the data, despite slightly. Apart from the inlet configurations this discrepancy could also be due to the ratio of gas inlet to main channel used. This ratio was one in the study by Qian and Lawal (2006) but is about 1/9 in the present study. It was discussed in Section 5.3.2.3 that by increasing the gas inlet size larger bubbles are produced.

5.4 Conclusions

The mechanism of Taylor bubble formation at the inlet of a microchannel and the ensuing bubble size were studied for very low superficial gas velocities ($U_{GS} < 0.04\text{m/s}$) using CFD modelling. The effects on bubble volume of gas/liquid velocities, liquid properties, contact angle, gas nozzle size and its wall thickness were examined. Bubble volumes obtained agreed well with experimental results for an identical system. It was found that bubble formation follows three stages, namely expanding, contracting and necking. The first two stages that correspond respectively to outward and inward movement of the gas-liquid interface close to the nozzle contribute mostly to bubble size. For the smaller gas nozzle size used, $d_N = 0.11\text{mm}$, the three phase contact line was found to slide along the top of the nozzle wall outwards and inwards during the expanding and contracting stages respectively. This was not observed for the large nozzle used ($d_N = 0.34\text{mm}$). The bubble shape deviated from spherical for most of the bubble formation time.

It was found that increasing the gas or decreasing the liquid velocity increases the bubble size. Surface tension was found to have a greater effect on bubble size than viscosity and density. Large nozzle size as well as large contact angle favoured the formation of larger bubbles. In the case of the small nozzle, increased nozzle thickness was also found to produce larger bubbles.

The bubble sizes were found numerically agreed better with those literature correlations that included phase fraction or ratios of superficial phase velocities. Inlet size and contacting configuration, which have been found to affect bubble size, were not taken into account in the literature correlations and would contribute to the discrepancies observed.

Chapter 6

Microreactor Design and Taylor Bubble Length Prediction

Nomenclature

A	Cross sectional area, m^2
d	Characteristic dimension, m
f	Frequency, 1/s
h	Height, m
Q	Volumetric flowrate, m^3/s
w	Width, m

Greek Symbols

ε	Volume fraction, -
σ	Surface tension, N/m

Dimensionless Numbers

Ca	Capillary number, $\mu_L U_B / \sigma$
------	--

Subscripts

b	Bubble
C	Channel or capillary
G	Gas
Gin	Gas inlet
L	Liquid
Lin	Liquid inlet
uc	Unit cell

Inlet Configurations

G	Gas inlet
H	Horizontal
L	Liquid inlet
M	M-junction inlet
T	T-junction inlet
V	Vertical
Y	Y-junction inlet

6.1 Introduction

The sizes of the bubbles and liquid slugs are very important for determining pressure drop and mass transfer rates during Taylor flow. A number of correlations have been suggested in the literature for the prediction of bubble size (Table 2.3). However, the inlet configuration that has been found to play an important role is not usually taken into account. Although bubble and slug sizes can be calculated via Computational Fluid Dynamics (CFD) simulations (e.g. Chapter 5) for different test section configurations, the computations tend to be expensive because of the 3D models required for the non-circular channels normally encountered in micro-applications. Experiments can provide valuable information on the variation of bubble and slug sizes under different conditions and inlet channel geometries. The results obtained can be used to predict bubble and slug sizes in the later on chapters. The fabrication of the microreactors is initially described. This is followed by parametric studies on the effect of inlet conditions on bubble frequency/size and size distribution that are necessary for the final section, where bubble frequency correlations are obtained for the system of interest and will be used to predict bubble size in the following chapters.

6.2 Microreactor fabrication

Single channel microreactors of various designs were fabricated in-house. Using engraving (Roland EGX-400 Flatbed Engraving Machine), the channels were made on transparent acrylic sheets (RS Components Ltd). The fabrication procedure is described below:

- (1) The reactor geometry was first drawn in AutoCAD and imported to the engraving software.
- (2) A piece of acrylic sheet (95x95x2mm) was fixed to the Engraving Machine's Super Sticky Mat (Mastergrave Ltd) and the zero point was determined.
- (3) A cutter size was chosen, which gives the width of the channel, while the channel depth was set from the software. The cutter spindle (rotating) speed and linear speed were also set for the channel depth and length.
- (4) The channels were engraved at selected conditions and at progressively larger depth, which aimed to improve the channel quality. Usually 0.2mm depth was machined in each run.

(5) The fabricated sheets were washed in supersonic bath with 5% Decon 90 solution (to remove any impurities and grease) and deionised water (to remove any residual Decon 90 solution). The sheets were then wiped with isopropanol and blow dried with nitrogen supplied from a gas cylinder.

(6) The sheets were placed in an enclosed rack with holding arms that separate them from each other. A few drops of Methyl methacrylate in a Petri dish were left in the rack for at least 2 hours to enable the chemical to vaporise and coat the sheets, assisting the bonding.

(7) Two sheets (the top and the bottom layer as seen in Figure 6.1) were carefully aligned to be a reactor chip (with gloves on to prevent contamination) using 2.5mm nylon screws cut to length which were inserted in alignment holes on the acrylic sheets. Each chip was then wrapped with aluminium paper and placed within an aluminium bonding jig (100mm x 100mm) that had screws along its four edges (Figure 6.1). A torque driver was used to tighten all screws to 1Nm initially, and then 2Nm all round. The bonding jig was additionally pressed with a U-clamp at the centre of the clamp to help distribute the pressure evenly. This is important for achieving uniform bonding in the next step.

(8) The system was left in an oven at 90°C for 48 hours and then was cooled down overnight. The sealing was checked in a water bath.

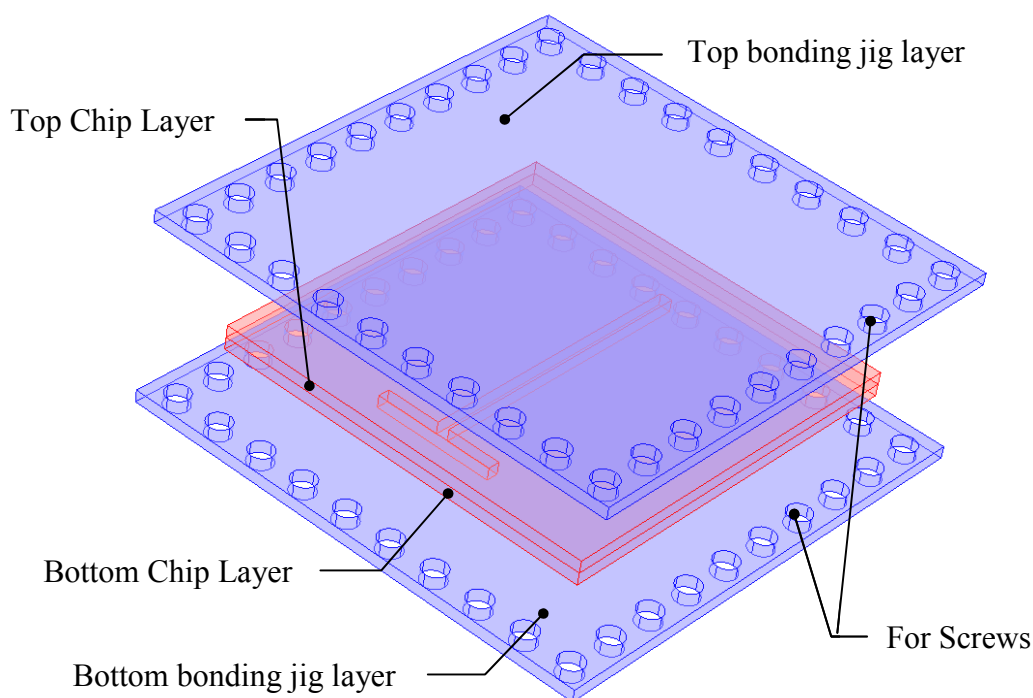
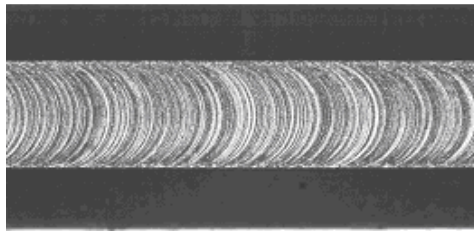
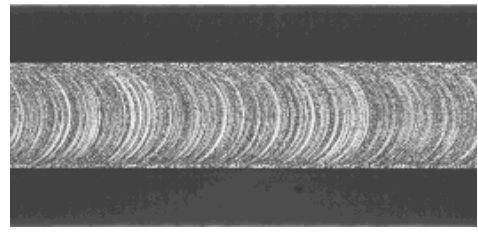


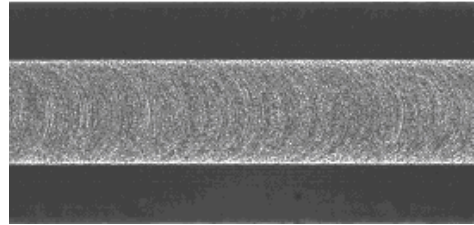
Figure 6.1 Layout of a reactor chip and the bonding jig for diffusion bonding.



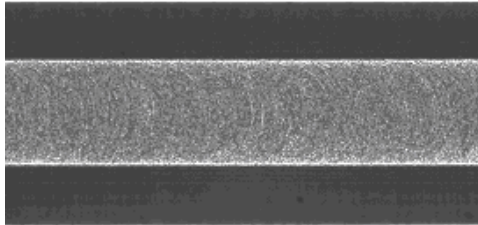
(a) linear speed: 0.01mm/s; spindle speed: 3000rpm; no cooling;



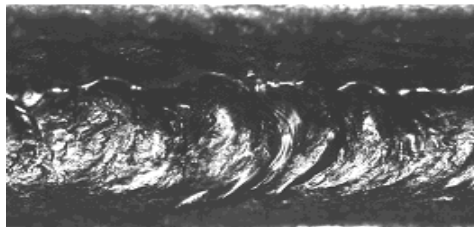
(b) linear speed: 0.01mm/s; spindle speed: 3000rpm; air cooling;



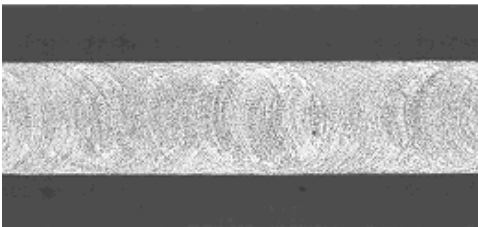
(c) linear speed: 0.01mm/s; spindle speed: 8000rpm; no cooling;



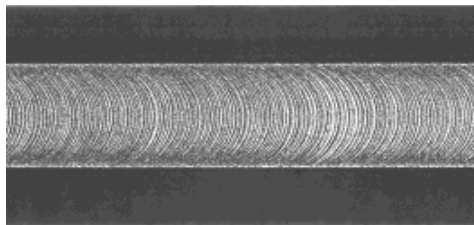
(d) linear speed: 0.01mm/s; spindle speed: 8000rpm; air cooling;



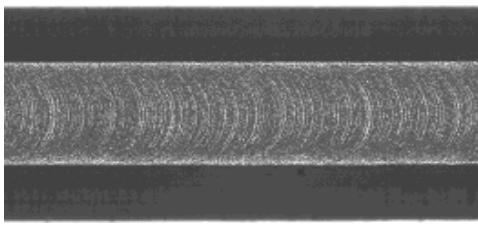
(e) linear speed: 0.01mm/s; spindle speed: 20000rpm; no cooling;



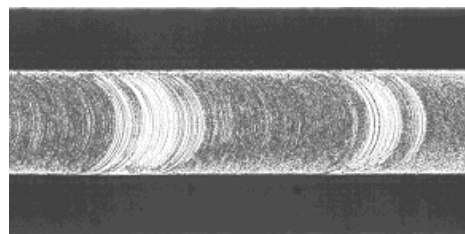
(f) linear speed: 0.01mm/s; spindle speed: 20000rpm; air cooling;



(g) linear speed: 1mm/s; spindle speed: 8000rpm; no cooling;



(h) linear speed: 1mm/s; spindle speed: 8000rpm; air cooling;



(i) linear speed: 0.01mm/s; spindle speed: 20000rpm; lubricant cooling;

Figure 6.2 Photographs of channel bottom under different engraving conditions. Cutter tip size: 0.1mm, channel depth: 0.5mm.

During the production, different cutter spindle and linear speeds were tried as well as different cooling methods in order to improve the quality of the channels. As can be seen in Figure 6.2, when the cutter spindle speed increases from 3000 to 20000rpm (Figure 6.2b, d, and f), the channels become smoother and the irregularities at the channel bottom are less visible. Another way to improve the channel quality is to reduce cutter linear velocity. The fringes at the channel bottom are less visible when the linear speed is 0.01mm/s, the lowest speed that the machine can have, compared to that of 1mm/s (Figure 6.2g vs. c and h vs. d). By using air cooling (Figure 6.2b, d, f, h), channels are smoother than those without cooling (Figure 6.2a, c, e, g) because the air flow effectively removes the waste materials while it also cools the cutter tip. Air blow is necessary at high spindle speeds (Figure 6.2e), as without it waste material collects at the channel bottom while excessive heat is not effectively removed and can melt the channel material locally. The use of lubricant oil for cooling was also tried (Figure 6.2i). However, the quality of surfaces produced was poor with waste accumulating intermittently. As a result, a low cutter linear speed of 0.01mm/s, a high cutter spindle speed of 20000rpm and air cooling were used for the microreactor fabrication.

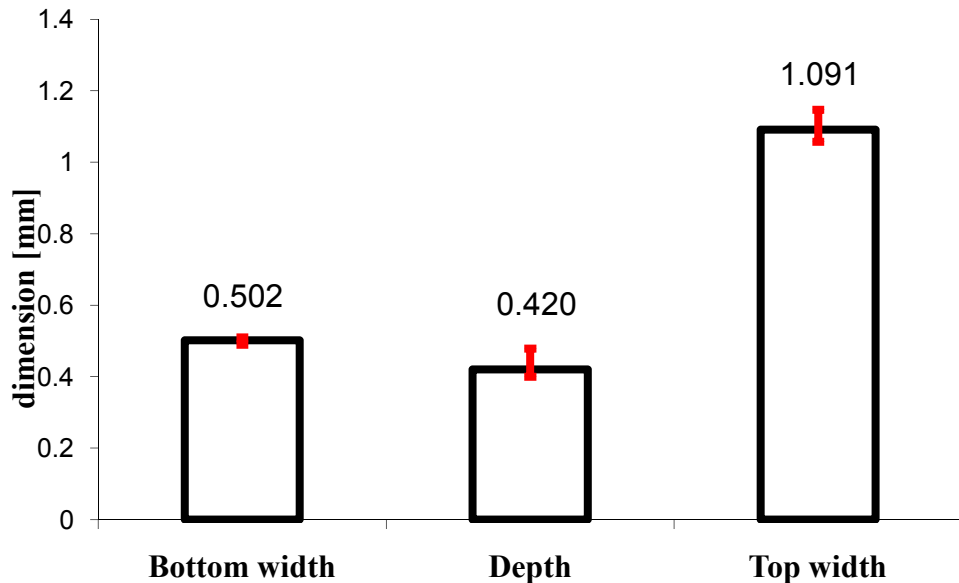


Figure 6.3 Average top and bottom width and the determined channel depth for channels engraved under the same conditions. Cutter tip: 0.5mm, channel depth: 0.5mm.

In order to check the uniformity of the channels produced in this way, the channel top and bottom widths are measured and channel depths are calculated. Seven channels, fabricated on different acrylic chips under the same engraving conditions, are used for this study. Top and bottom widths are measured along each channel at five locations.

With known channel geometry (Figure 6.4b), the channel depth for each location can be calculated. An Olympus inverted microscope GX51 with a 20X objective and an installed camera is used to capture the channel top or bottom images, which are then analyzed (Aequitas). The average channel top and bottom width and channel depth from all measurements/calculations are plotted in Figure 6.3 with error bars given (the maximum and the minimum deviation from the average). The channel bottom width hardly varies because the same cutter tip is used. It is worth noting that the reactor has a truncated trapezium cross section (Figure 6.4b) due to the tapered cutter tip (Figure 6.4a), which leads to variations in channel top width when fabricating channels of different depths. The differences in channel depth are attributed to the soft adhesive mat placed underneath the plate to keep it in place on the engraving machine and the uneven thickness of the acrylic sheet.

The following drawbacks have been recognized for these in-house made chips. Firstly, acrylic is not a good wetting material for a water based liquid phase. Secondly, the engraving technology could not deliver high quality finish in channels of small dimensions. The channel depth is non-uniform and the channel surface is relatively rough. However, this way of fabrication has low cost and short production cycle (usually 4 days), which is convenient when different reactor prototypes need to be studied.

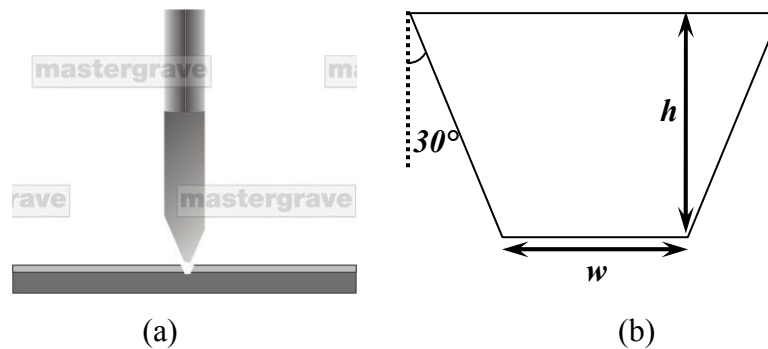


Figure 6.4 (a) Cutter shape (Mastergrave Ltd, the supplier) and (b) the produced channel cross section profile. w and h are channel bottom width and channel depth respectively.

6.3 Microreactor inlet design

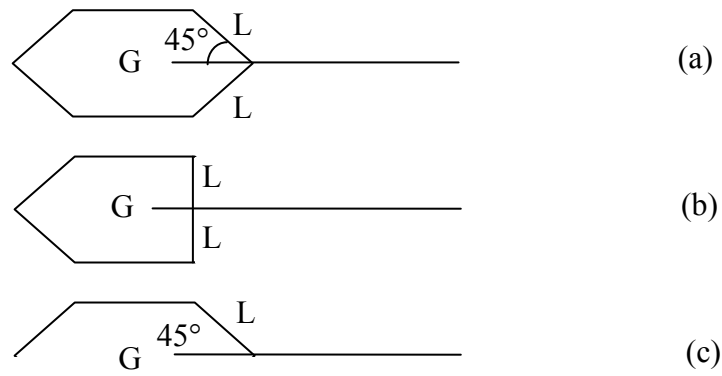


Figure 6.5 Inlet configurations used in the inlet design study.

Different inlets were tested to investigate their effect on Taylor flow stability. The cutter tip size used was 0.5mm. By varying the channel depth (0.3mm and 0.5mm), two hydraulic diameters of 0.613 and 0.4mm were obtained. The inlet configurations (Section 2.6.2.1) used are the flow focusing design, where two flanking side inlets join a third inlet at 45° (Figure 6.5a) and 90° (Figure 6.5b), and a Y-junction where the channels join at 45° (Figure 6.5c). Air/water and air/octane fluid pairs were tested in five scenarios shown in Table 6.1.

Table 6.1 Testing scenarios in the inlet design study.

Scenario	d_H [mm]	$d_{H,Gin}$ [mm]	$d_{H,Lin}$ [mm]	Gas-liquid contact [°]	Inlet configurations (Figure 6.5)
A	0.613	0.613	0.613	45	Double L flank G (a)
B	0.613	0.4	0.613	45	Double L flank G (a)
C	0.613	0.613	0.4	45	Double L flank G (a)
D	0.613	0.613	0.613	90	Double L flank G (b)
E	0.613	0.613	0.613	45	Single L flank G (c)

6.4 Experimental setup

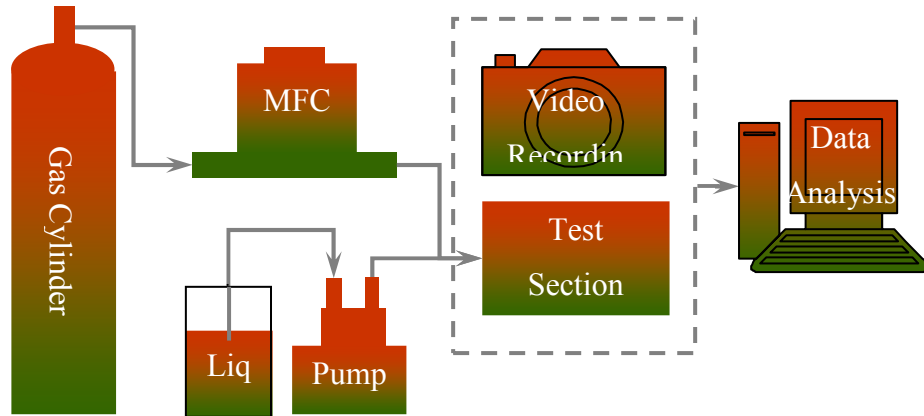
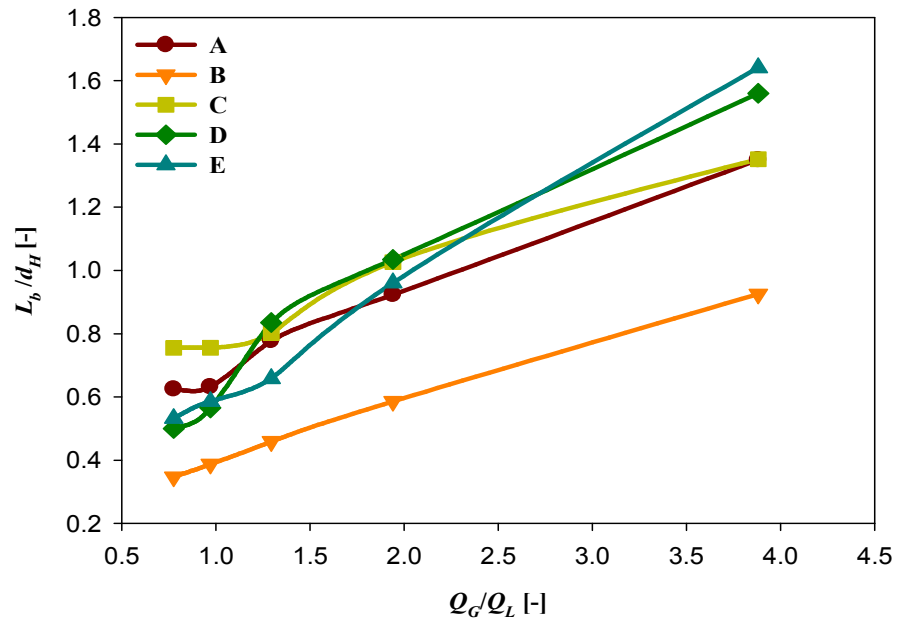


Figure 6.6 Experimental schematic for the investigation of microreactor inlet design.

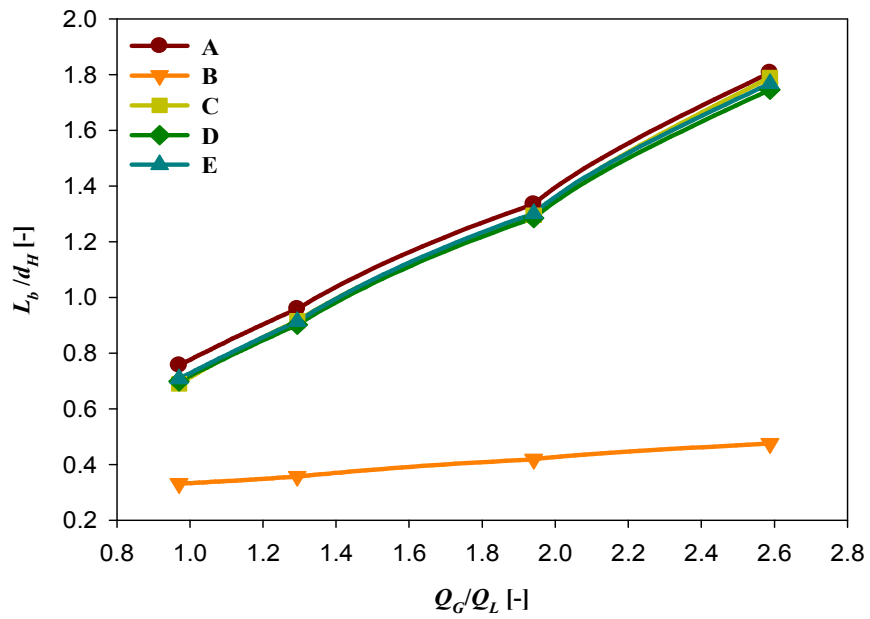
The experimental set up is shown in Figure 6.6. The gas phase was nitrogen and the liquid phase was either water or octane that have different surface tension, σ (water: 0.07226 Pa s, octane: 0.02149 Pa s). The nitrogen flow was supplied from a gas cylinder and regulated with a Bronkhorst EL-FLOW F-110C mass flow controller with a range 0.01-1 ml/min. The liquid was introduced by using a MiliGat pump (0 – 6 ml/min). Bubble formation was captured with a high-speed video system Kodak HS 4540, which can record between 30 and 4500 frames per second (fps) in full frame mode and 9000-40500 fps in segmented frame mode. Data were collected in a PC and analyzed. The unit cell (one bubble and one slug) or bubble frequencies were obtained by counting the number of bubbles within a time period. From the bubble frequency bubble length was calculated (Appendix A). In addition, bubble lengths were also measured in some cases directly from the recorded images using the image analysis software Aequitas. About 5-80 bubbles were then used to calculate an average in each case.

6.5 Results and discussions

6.5.1 Inlet design



(a)



(b)

Figure 6.7 Dimensionless bubble length obtained under different testing scenaria. (a) air/water system; (b) air/octane system. $Q_G = 0.932\text{ml/min}$.

As can be seen in Figure 6.7, all scenarios produce similar bubble lengths, apart from scenario B, in which the gas inlet size is smaller than the others. It is clear that the gas inlet size has a significant effect on bubble sizes. The effect of liquid inlet size is small. The standard deviation of the measured bubble lengths for the three scenarios that have the same inlet size is shown in Figure 6.8. It can be seen that scenarios D and E produce more uniform bubble sizes compared to scenario A. It was observed during the experiments that in scenario A, where gas and liquid join at 45° , the bubble neck did not break at the inlet but further downstream in the main channel and at varying locations. This could be a result of the uneven channel sizes fabricated (Section 6.2), which leads to nonuniform liquid flow in the two branches of the double flank (Figure 6.5a and b). This is expected to affect more the bubble formation in the 45° inlet configuration compared with the 90° one (Figure 6.5a), because the bubble neck is more easily pushed forward to the main channel under the liquid drag force and is broken in a non-consistent way by the asymmetric liquid flows. Although scenario D and inlet design (b) also give small standard deviation, in order to avoid any effect of any asymmetry in the two liquid inlets it was decided to use design (c) and scenario E in the following work.

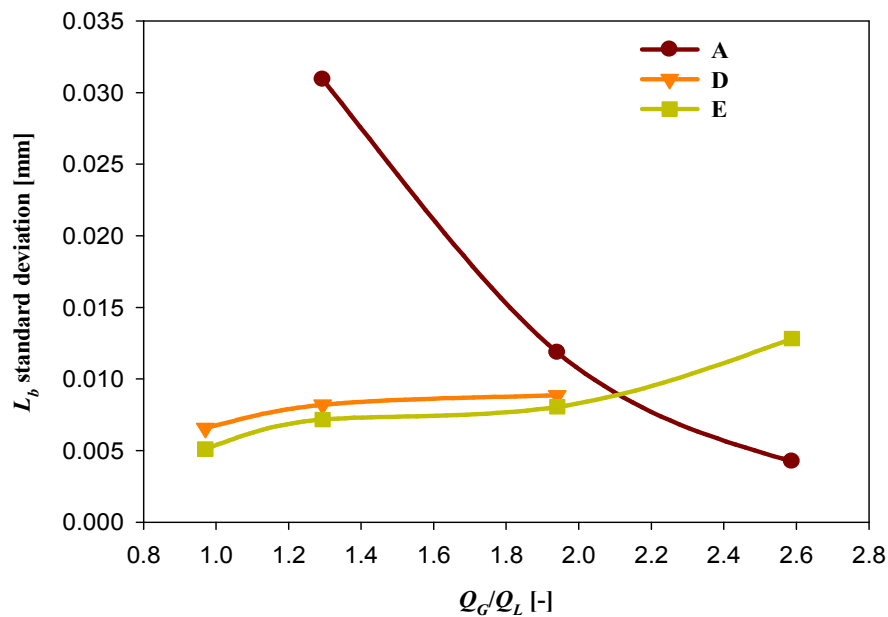


Figure 6.8 Bubble size standard deviation under different testing scenarios. $Q_G = 0.932\text{ml/min}$.

6.5.2 Effect on bubble length of inlet conditions

It was shown in the previous section that single-gas, single-liquid inlet design (Figure 6.5c) produce more uniform bubble sizes with the fabrication technology used (Section

6.2). This design is adopted in this section. A cutter with tip size of 0.5mm (channel bottom width) was used and three depths of 0.25mm, 0.5mm and 0.8mm were considered, producing channel hydraulic diameters of 0.345mm, 0.577mm and 0.816mm respectively; these refer to the inlet or the main channels.

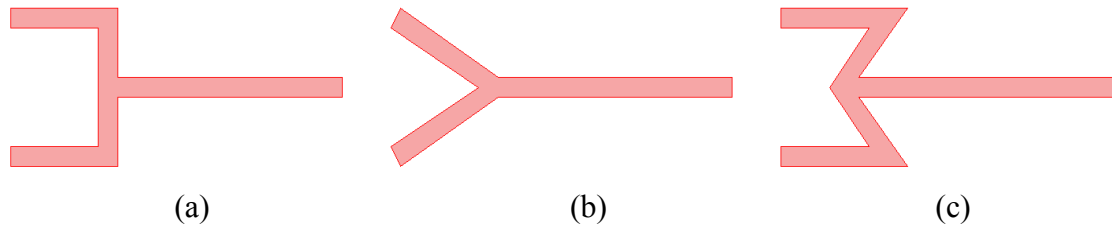


Figure 6.9 Inlet configurations used in the parametric study on bubble sizes. (a) T-junction; (b) Y-junction; (c) M-junction.

Apart from inlet conditions such as gas and liquid flowrates, liquid surface tension and gas inlet size (Section 5.3.2, Section 6.5.1), it has been found that the degree of mixing of the two fluids at the inlet can also affect bubble size (Qian and Lawal, 2006). Therefore, three inlet configurations T-, Y-, and M- junction are studied (Figure 6.9) because it is expected that the mixing quality will be different due to their different mixing volume. The unit cell frequency is recorded during the experiment, from which bubble length is obtained (Appendix A).

6.5.2.1 Effect of channel orientation

Bubble size in the T-junction is studied with the main channel placed either vertically and upward flow or horizontally. In the latter case, the chip is vertical, and one inlet is placed on top of the other while either gas or liquid can flow through it. As shown in Figure 6.10, there is little difference among the three cases when $Q_L \geq 4\mu\text{l/s}$. At small liquid flowrates ($Q_L < 4\mu\text{l/s}$), the horizontal channel with the liquid phase in the upper inlet gives the longest bubble length while the vertical orientation produced the shortest bubbles. At low liquid velocities, the bubble is detached from the inlet following the liquid pressure squeezing mechanism (Garstecki et al., 2006, see Section 2.5.2). Under the slight effect of gravity, the film thickness at the upper side of the main channel is thinner when liquid flows from the lower inlet than from the upper one. This leads to an increase of the squeezing effect on the bubble neck for the former case that results in a faster bubble break-up. Since the effect on bubble length of inlet orientation is small, it is not included in the bubble size correlations later on.

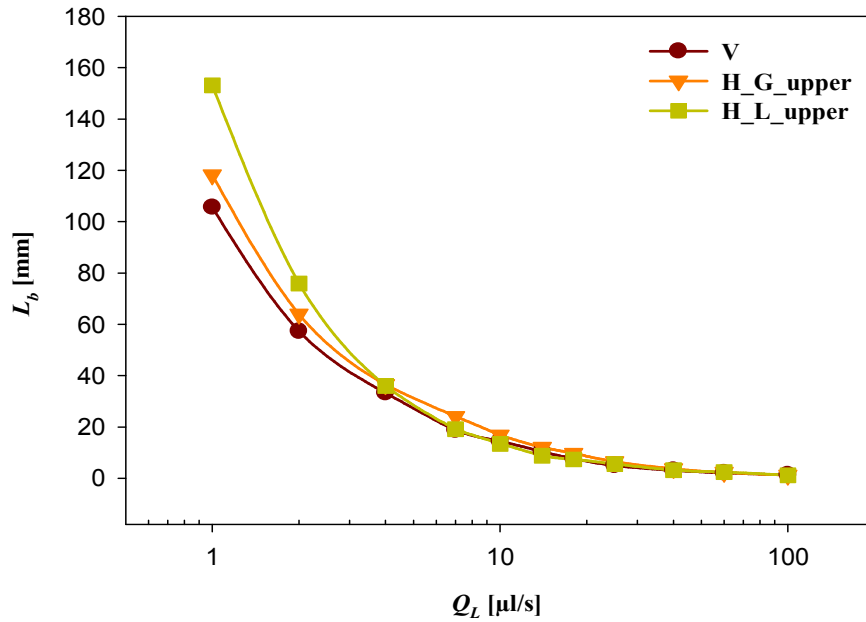
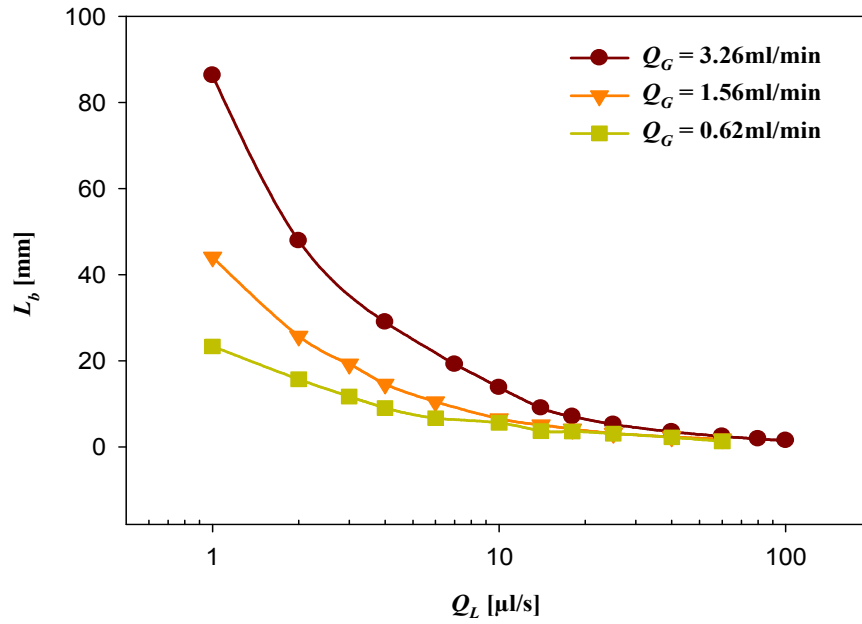


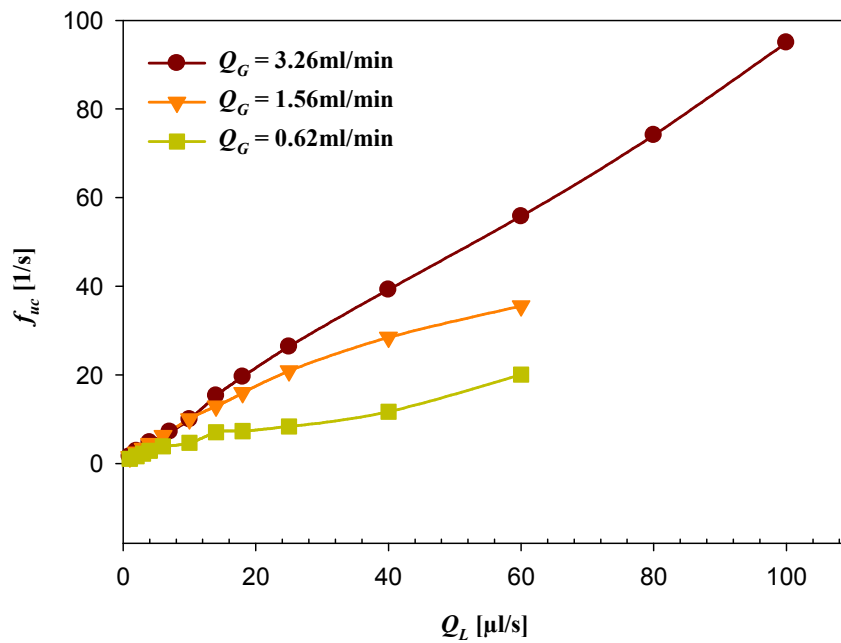
Figure 6.10 Effect of inlet orientation on bubble length. $Q_G = 3.26\text{ml/min}$, $d_H = 0.577\text{mm}$, $d_{H,Gin} = 0.577\text{mm}$, $d_{H,Lin} = 0.577\text{mm}$, liquid phase: water, inlet configuration: T-junction. V: vertical; H_G_upper: horizontal with gas phase in the upper inlet; H_L_upper: horizontal with liquid phase in the upper inlet.

6.5.2.2 Effect of gas and liquid flowrate

Gas and liquid flowrates have been found to affect significantly the size of the Taylor bubbles at Capillary numbers, Ca , less than $1.3\text{E-}3$ (for discussion see Chapter 5). The effect of gas and liquid flowrates is investigated in the current set up for a larger range of Ca up to $1.1\text{E-}2$ and is shown in Figure 6.11 for a test section with $d_H = 0.577\text{mm}$ and gas inlet equal to 0.577mm . As can be seen in Figure 6.11a, bubble length increases with increasing gas flowrate, Q_G , and decreasing liquid flowrate, Q_L . In addition, the frequency of the unit cell, f_{uc} , also increases with increasing gas or liquid flowrates (Figure 6.11b), resulting in shorter unit cells.



(a)



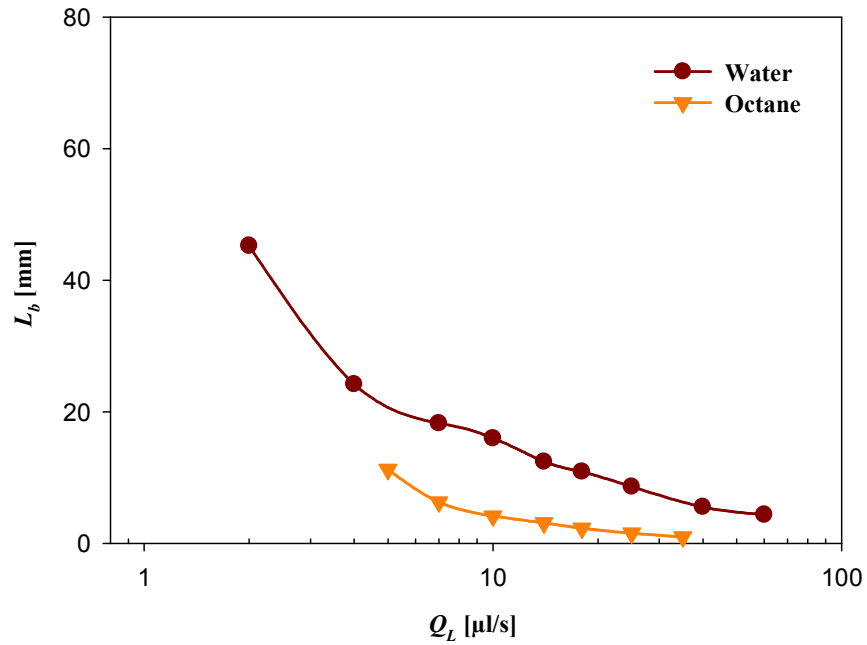
(b)

Figure 6.11 Effect of gas and liquid flowrate on (a) bubble length and (b) unit cell frequency. $d_H = 0.577$ mm, $d_{H,Gin} = 0.577$ mm, $d_{H,Lin} = 0.577$ mm, liquid phase: water, inlet configuration: Y-junction, orientation: vertical upflow.

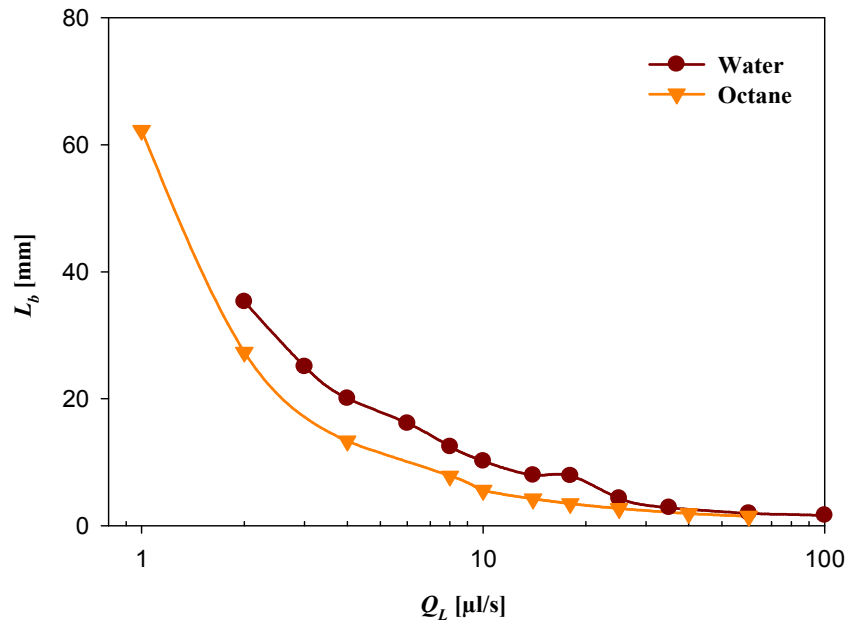
6.5.2.3 Effect of surface tension

To investigate the effect of surface tension, experiments were carried out with both water ($\sigma = 0.07226$ N/m) and octane ($\sigma = 0.02149$ N/m) as the liquid phase. In agreement

with the findings of Section 5.3.2.2, longer bubbles are generated in the nitrogen-water system that has higher surface tension (Figure 6.12). The increased attaching effect of surface tension force in water at the test section inlet during bubble formation explains the difference. Similar trends were found for the other channel sizes used.



(a)



(b)

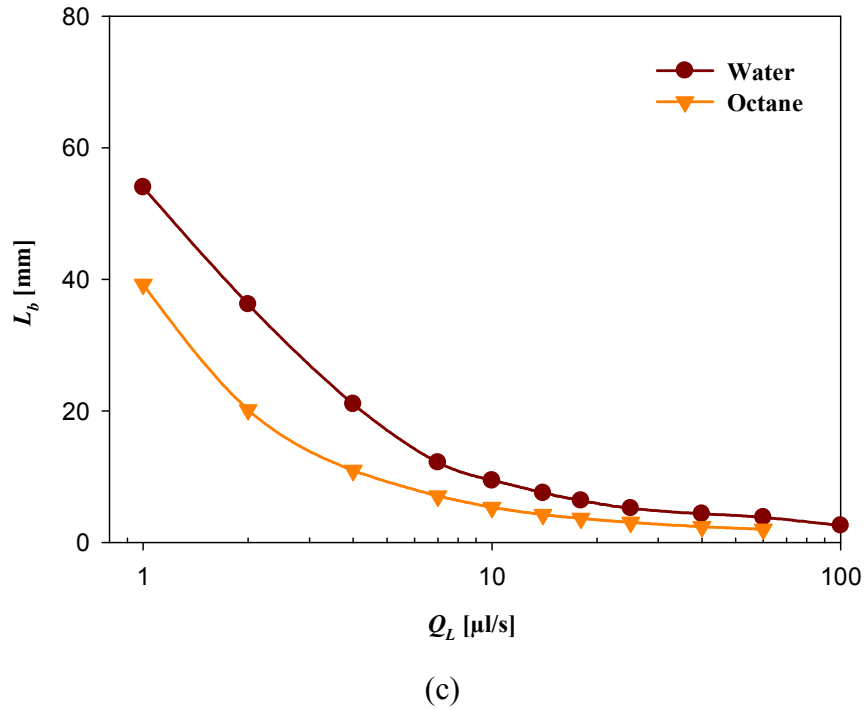


Figure 6.12 Effect of liquid phase surface tension on bubble length. (a) $d_H = 0.345$ mm; (b) $d_H = 0.577$ mm; (c) $d_H = 0.816$ mm. $Q_G = 1.56$ ml/min, $d_{H,Gin} = 0.577$ mm, $d_{H,Lin} = 0.577$ mm, inlet configuration: T-junction, orientation: horizontal.

6.5.2.4 Effect of gas inlet size

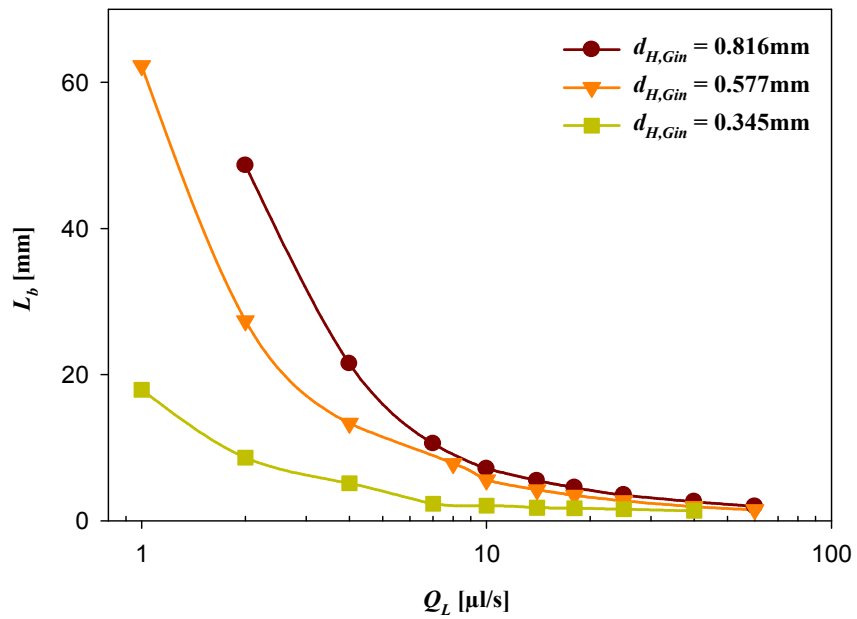


Figure 6.13 Effect of gas inlet size on bubble length. $Q_G: 1.56$ ml/min, $d_H = 0.577$ mm, $d_{H,Lin} = 0.577$ mm, liquid: octane, inlet configuration: T-junction, orientation: horizontal.

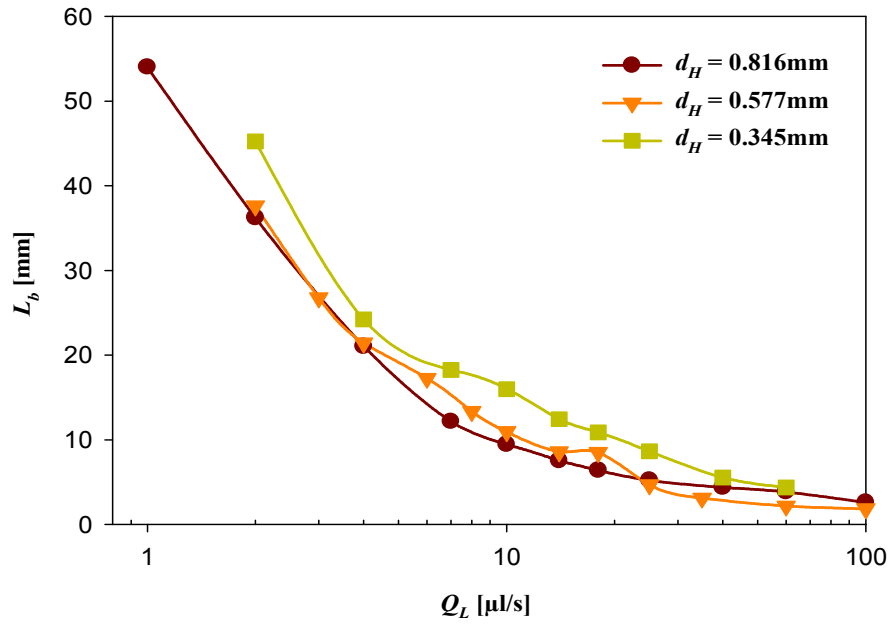
Three gas inlet sizes were investigated and their effect on bubble length is shown in Figure 6.13. Bubble length is found to increase with gas inlet size, in agreement with CFD simulations (Section 5.3.2.3). The rate of bubble length increase however, is reduced as the inlet size increases, probably because the effect of surface tension is weakened at larger dimensions.

6.5.2.5 Effect of main channel size

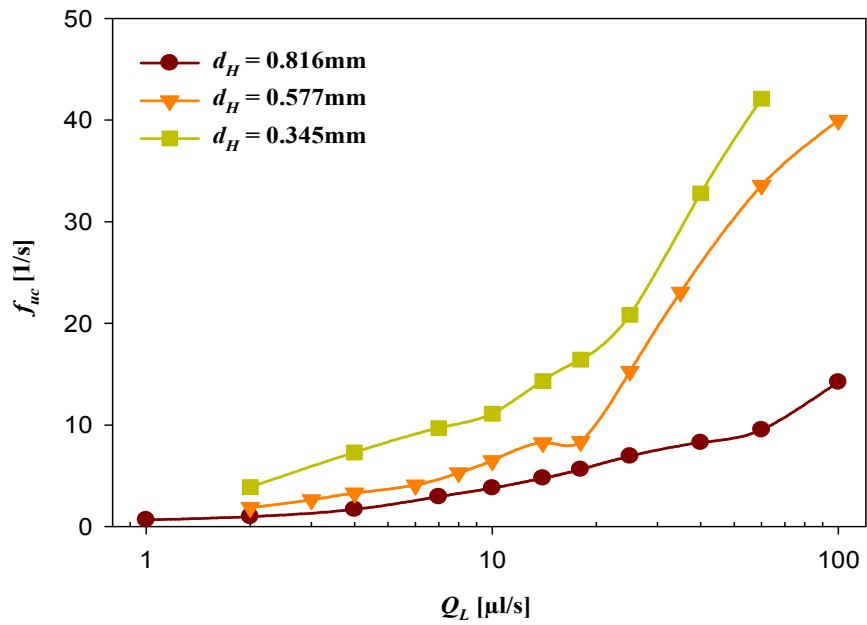
It was shown in Section 4.3.4 that bubbles flowing in small channels are elongated compared to those in large channels but the unit cell frequency was the same. This is because the same inlets (commercial T-junctions) were used and were not integrated with the main channel. Bubble elongation was therefore due to the smaller cross sectional area in the small channels compared to the large ones.

The inlets used in this chapter are fully integrated with the main channel (Figure 6.9). Bubble lengths are found to be similar in channels of different size when the same inlet design is used (Figure 6.14a). A further examination reveals that the unit cell frequency is higher in the small channels compared to the large ones (Figure 6.14b), which means that smaller bubble volumes are produced in the small channels. This is because in small channels bubbles are confined by the channel walls which limit their cross sectional growth during formation at the inlet. At the same time the liquid shear on the bubbles is increased due to the increased liquid superficial velocity in the small channels compared to the large ones for the same flowrate. Both these phenomena contribute to an earlier detachment of bubbles in the small channels compared to the large ones. The above observations apply to the octane system as well.

The results from the non-integrated (Figure 4.8) and integrated (Figure 6.14) inlets suggest that channel size will affect bubble formation only in the latter case. With non-integrated inlets, different channel sizes will only modify bubble length because of the different cross sectional areas.



(a)



(b)

Figure 6.14 Effect of main channel size on bubble length (a) and unit cell frequency (b). Q_G : 1.56ml/min, $d_{H,Gin} = 0.577\text{mm}$, $d_{H,Lin} = 0.577\text{mm}$, liquid: water, inlet configuration: T-junction, orientation: horizontal.

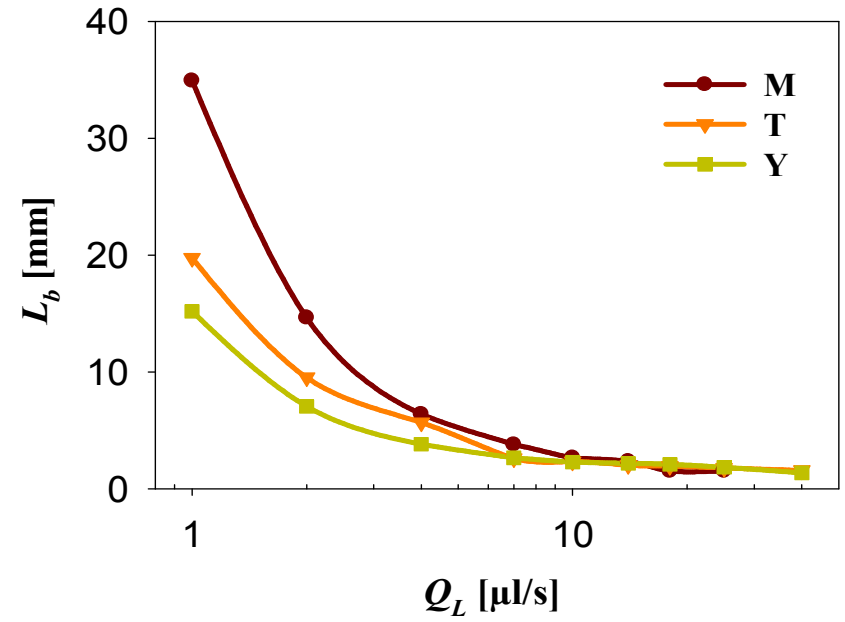
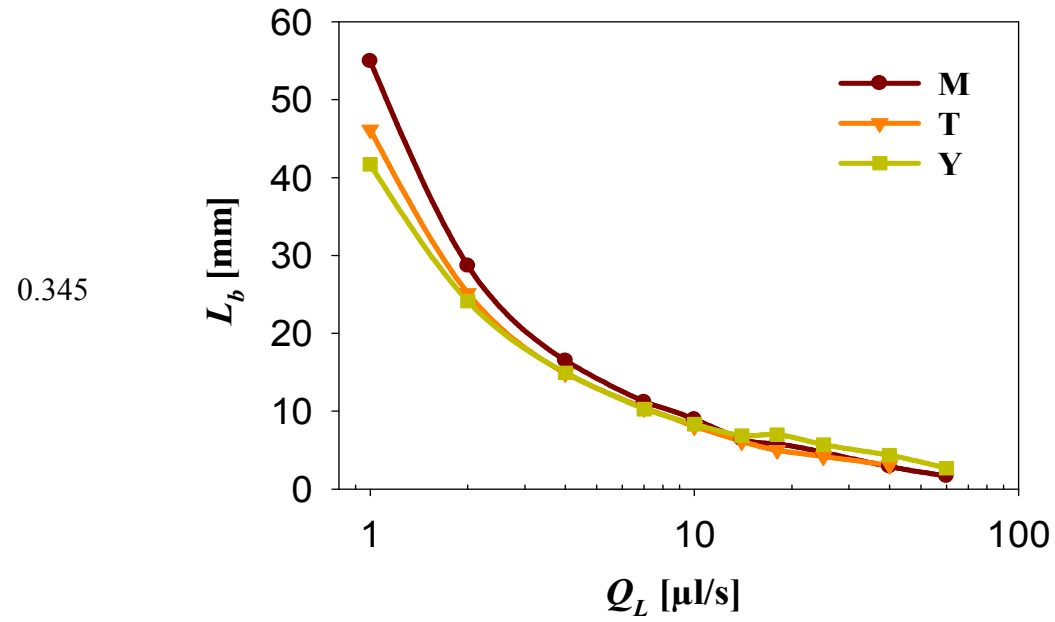
6.5.2.6 Effect of inlet configuration

The bubble lengths for the three inlet configurations are presented in Figure 6.15 for all three gas inlet sizes and two different liquids. In general, the largest bubbles are produced in the M-junction, followed by those in the T-junction while the smallest bubbles form in the Y-junction. According to [Qian and Lawal \(2006\)](#), bubble size would depend on the quality of the mixing between the two fluids at the channel inlet; good mixing would result in small bubbles (Figure 2.25). The different inlets used here have different volumes for the mixing of the two phases; better mixing is expected when the mixing volume is small. T-, Y- and M-inlet has an inlet mixing volume of 0.475 μ l, 0.483 μ l and 1.444 μ l respectively. The M-inlet with the largest mixing volume would be expected to create large bubbles, while the Y-inlet with the smallest volume will create small bubbles. The differences between the inlets become less significant as the bubble size decreases with increasing liquid flowrate. Similar results were found for the intermediate gas inlet size (0.577mm and 0.816mm). The bubble size fluctuation observed when the M-junction is used could be due to the sharp edges in the M-junction that create irregular flow patterns in the liquid which affect bubble formation in a non-predictable way.

$d_{H, \text{Gin}}$ mm

Air/water

Air/octane

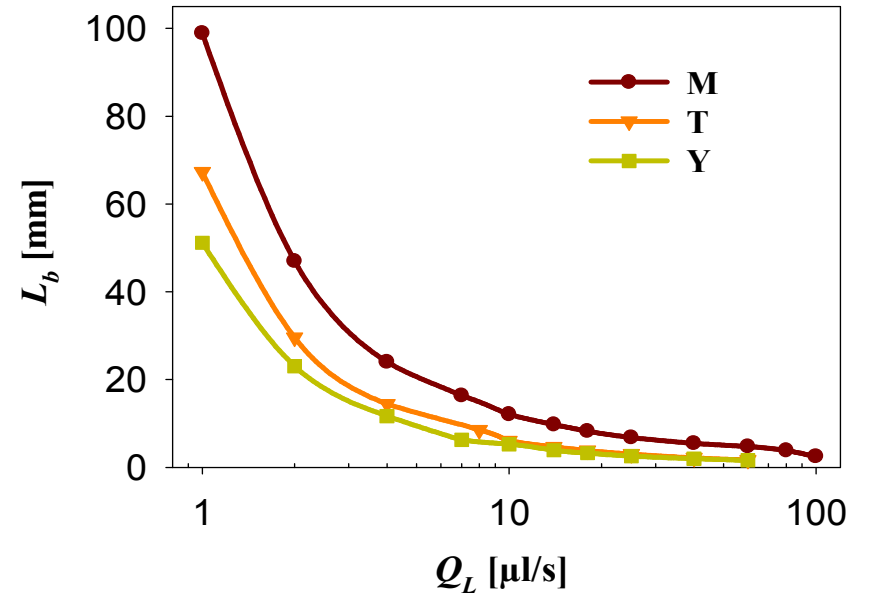
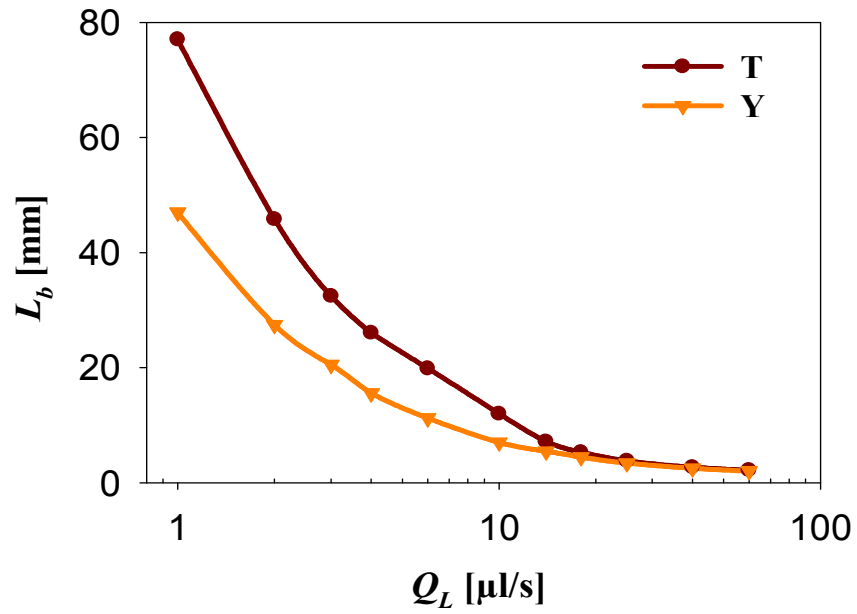


$d_{H,Gin}$ mm

Air/water

Air/octane

0.577



$d_{H,Gin}$ mm

Air/water

Air/octane

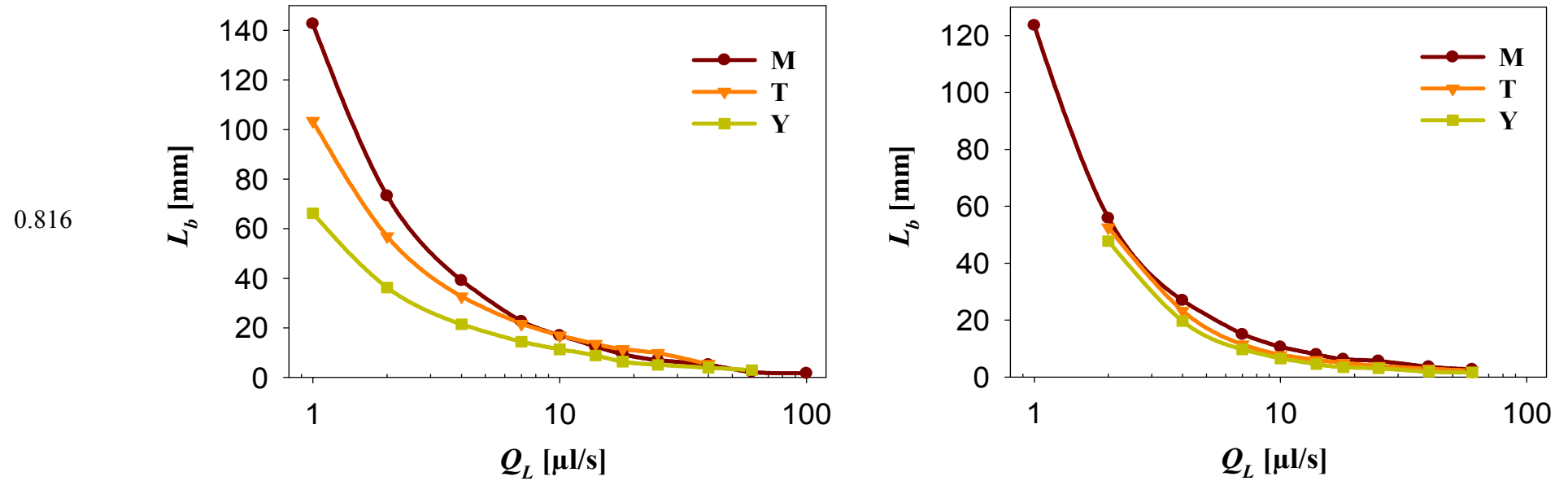


Figure 6.15 Bubble lengths under different inlet configurations. Q_G : 1.56ml/min, $d_H = 0.577\text{mm}$, $d_{H,Lin} = 0.577\text{mm}$, orientation: horizontal for the main channel.

6.5.3 Prediction of bubble length

For the application of microreactors operating in Taylor flow it is important to be able to predict bubble lengths from information available on channel geometry and operating conditions. A number of correlations have been suggested in the literature (see Section 2.5.2). Section 5.3.3 indicated that correlations including phase fraction predict bubble lengths obtained from CFD simulations better than those which did not account for phase fraction. Therefore the correlations developed by [Kreutzer \(2003\)](#) (Eq. 2.5), [Qian and Lawal \(2006\)](#) (Eq. 2.8) and [Garstecki et al. \(2006\)](#) (Eq. 2.9), that include phase fraction, are compared against the experimental data in Figure 6.16. Only data recorded from the T-junction inlet are used. In addition, data at very high or very low liquid flowrates are not included because only a few experiments were carried out at these conditions. It can be seen from Figure 6.16 that in most cases the correlation from [Garstecki et al. \(2006\)](#) underpredicts the results probably because it applies to low Ca flows where bubbles form through the squeezing mechanism. The [Qian and Lawal \(2006\)](#) equation performs the best among the three, probably because it includes the effect of surface tension. The widely scattered results, however, suggest that none of these correlations works well for the current system since the effect of gas inlet size is not taken into account.

To develop a correlation for the current system the unit cell frequency is used, because it is the parameter that is measured experimentally. The unit cell frequency or bubble length was found to be mainly affected by gas and liquid flowrates, surface tension, gas inlet size and main channel size. Although the inlet configuration was important, it cannot be easily quantified and different correlations are developed for the T- and Y-junctions respectively, because they are more commonly encountered in microreactor applications compared to the M-junction.

The unit cell frequency is found to be correlated best with the following parameters: homogeneous liquid fraction, ε_L ($\varepsilon_L = Q_L/(Q_G+Q_L)$), gas inlet cross sectional area, A_{Gin} , channel cross sectional area, A_C and capillary number, Ca . Since less data was available for the Y-junction test section on the effect of main channel size, the same exponential factor for A_C is used as that for the T-junction. The unit cell frequency correlations for the T- and Y-junctions are given in Eq. 6.1 and Eq. 6.2 respectively.

$$f_{uc,T} = 4.389 \times 10^4 \varepsilon_L^{0.694} A_{Gin}^{-0.534} A_C^{0.453} Ca^{1.294} \quad \text{Eq. 6.1}$$

$$f_{uc,Y} = 2.97 \times 10^4 \varepsilon_L^{0.821} A_{Gin}^{-0.355} A_C^{0.453} Ca^{0.984} \quad \text{Eq. 6.2}$$

From the unit cell frequency bubble length can be calculated according to Appendix A.

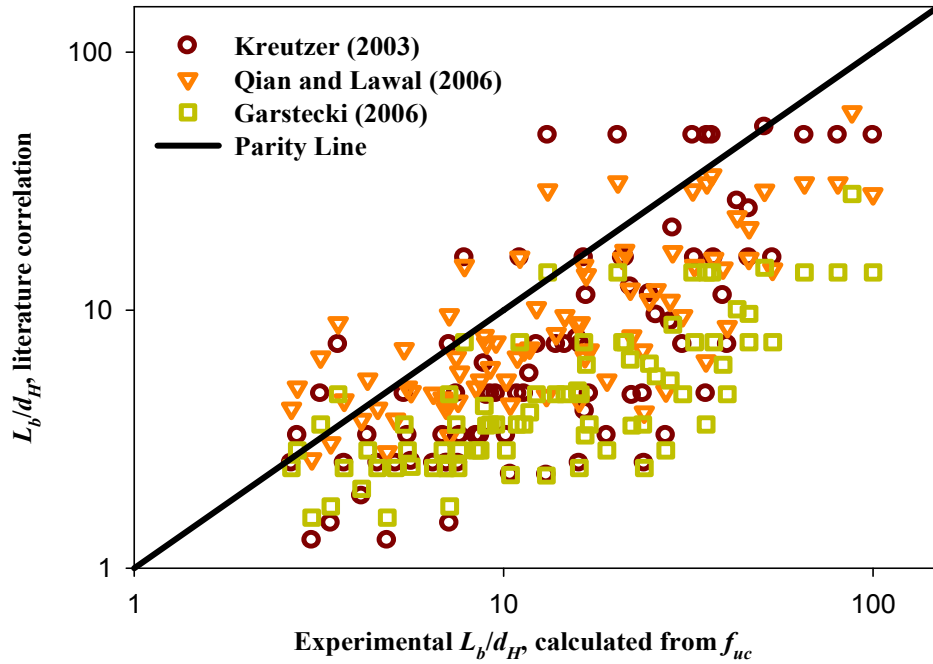


Figure 6.16 Comparison of bubble lengths calculated from literature correlations and experimental recorded unit cell frequency. Q_G : 0.62~3.26ml/min, Q_L : 2~18 μ l/s, d_H : 0.345~0.816mm, $d_{H,Gin}$: 0.345~0.816mm, liquid: water and octane, inlet configuration: T-junction, orientation: horizontal.

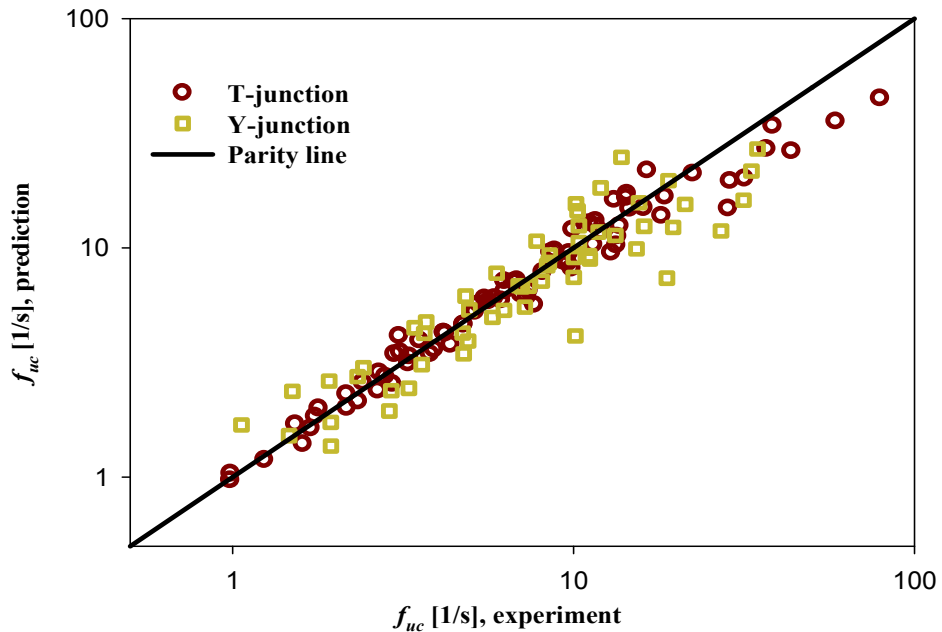


Figure 6.17 Comparison between experimentally recorded unit cell frequencies and predicted ones using Eq. 6.1 and Eq. 6.2.

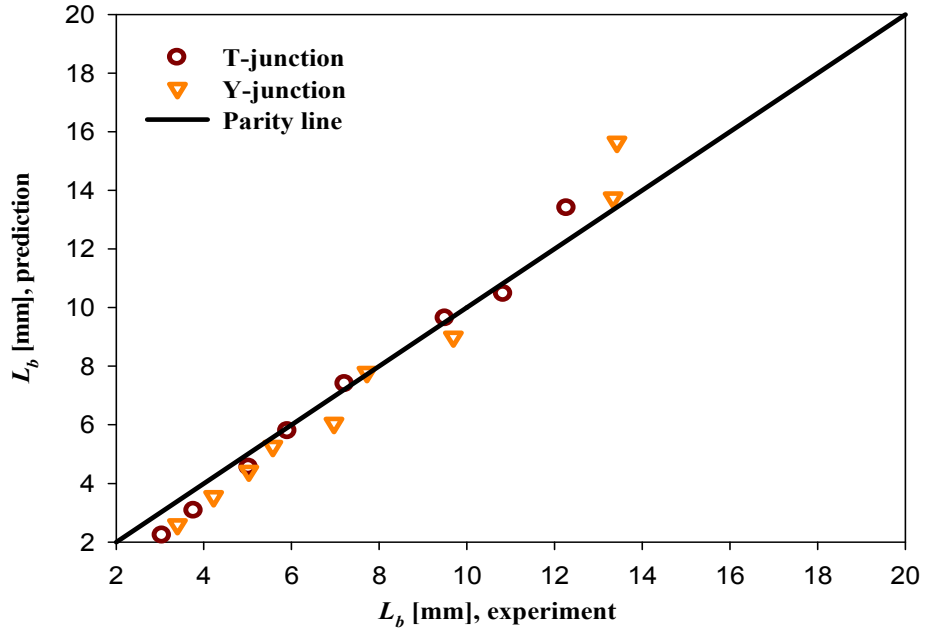


Figure 6.18 Comparison of bubble lengths measured from experimental images with those calculated from Eq. 6.1 and Eq. 6.2. Q_G : 0.62~3.26ml/min, Q_L : 2~18 μ l/s, d_H : 0.345~0.816mm, $d_{H,Gin}$: 0.345~0.816mm, liquid: water and octane, orientation: horizontal.

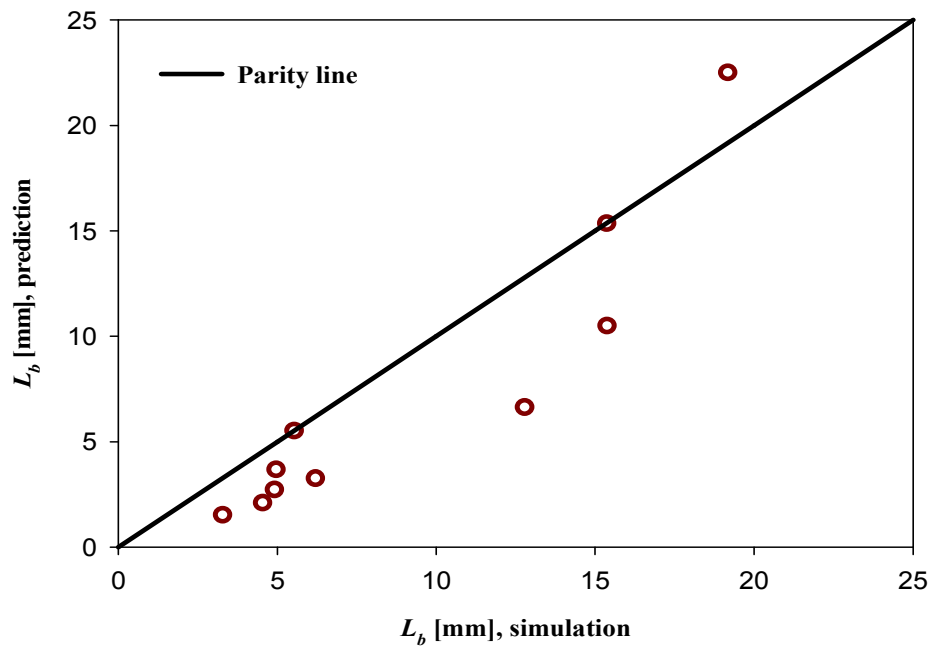


Figure 6.19 Comparison between simulated bubble lengths (Qian and Lawal, 2006) with those calculated from Eq. 6.1 and Eq. 6.2. U_{GS} : 0.05~0.1m/s, U_{LS} : 0.02~0.2m/s, d : 3mm, d_{Gin} : 3mm, liquid: water, orientation: vertical, inlet: T-junction.

The unit cell frequency predictions are plotted against the experimental data in Figure 6.17. The standard deviation of bubble frequency for the T- and Y-junctions is 11% and 19% respectively. With the Y-junction it was seen that bubbles break up away from the inlet, further inside the channel at locations which varied. This may have contributed to the larger deviation with this inlet compared to the T-junction. The bubble lengths predicted from the above correlations are found to be in good agreement with bubble lengths measured from recorded images (Figure 6.18). Reasonable agreement is also found when the correlation for the T-junction is used to predict the experimental bubble lengths cited by [Qian and Lawal \(2006\)](#) as can be seen in Figure 6.19.

6.6 Conclusions

This chapter focuses on microreactor design and Taylor bubble size prediction, preparing for the mass transfer and reaction studies. The fabrication of acrylic chips is introduced and the procedures followed to improve the channel quality are discussed. In the study of inlet design, bubble lengths are found to be significantly influenced by gas inlet size while there is little effect of liquid inlet size, gas-liquid inlet orientation and the number of inlets. However, single flanking inlet and a 90° angle between the gas and the liquid are found to produce narrow bubble length distributions. In the new designs using single gas and liquid inlet, bubble lengths were obtained during gas-liquid Taylor flow in microchannels using different inlet geometries. It was found that the bubble length increased with increasing gas flowrate, gas inlet size and liquid surface tension and decreasing liquid flowrate. From the different inlets used the M-junction, that had the largest mixing volume, produced longer bubbles while the Y-junction with the smallest mixing volume gave shorter bubbles. Available literature correlations did not predict satisfactorily the experimental bubble lengths. Two correlations were developed, one for the T- and the other for the Y-junction, to predict unit cell frequencies from which bubble lengths can be estimated. The correlations were found to predict well experimental bubble lengths obtained from video images as well as the data by [Qian and Lawal \(2006\)](#).

Chapter 7
Mass Transfer and Reaction in Taylor Flow
Microreactor

Nomenclature

a	Minor axis of the ellipse
b	Major axis of the ellipse
A	Interfacial area, m^2
C	Concentration, mol/l
C^*	Interfacial concentration, mol/l
d	Diameter, m
D	Diffusivity, m^2/s
F	Mole flowrate, kmol/s
h	Channel depth, m
h_i	Parameter, -
He	Henry's constant, $atm\ m^3/mol$
I	Ionic strength, $kmol/m^3$
k	Reaction rate constant, $m^3/(kmol\ s)$
k_L	Liquid side mass transfer coefficient, mol/s
l	Reactor length, m
L	Length, m
n	Normal direction
P	Pressure, atm
Q	Volumetric flowrate, m^3/s
r	Reaction rate
R	Gas constant, $0.082\ m^3\ atm/(K\ kmol)$
R'	Radius of the bend of the meandering channel
t	Time, s
T	Temperature, K
U	Velocity, m/s
\bar{u}	Velocity, m/s
w	Channel width, m
V	Volume, m^3
x	Radial coordinate, m
$X\%$	CO_2 absorption fraction, -
y	Volume fraction, -
z	Axial coordinate, m
Z	Valence, -

Greek Symbols

α	Specific area, m^2/m^3
μ	Dynamic viscosity, $\text{Pa}\cdot\text{s}$
ρ	Density, kg/m^3
σ	Surface tension, N/m
δ	Film thickness, m
ε	Volume fraction, -
δ	Film thickness, m
Ψ	Liquid utilization, $\text{mol CO}_2/\text{ml NaOH solution}$

Dimensionless Numbers

Ca	Capillary number, $Ca = \frac{\mu_L U_B}{\sigma}$
De	Dean number, $De = Re(d_H/R')^{0.5}$
Re	Reynolds number, $Re_G = \frac{\rho_G U_{TF} d_H}{\mu_G}$

Subscripts

B	Bubble
C	Channel
CO_2	Related to carbon dioxide
CO_3^{2-}	Related to carbonate
$film$	Film region
G	Gas
H	Hydraulic
HCO_3^{2-}	Related to bicarbonate
i	Chemical species
j	Grid cell
in	Inlet
L	Liquid
OH	Related to hydroxide
Out	Outlet
S	Slug
UC	Unit cell

water Related to water
vol Volume

7.1 Introduction

In this chapter CO₂ absorption in an aqueous NaOH solution is investigated during Taylor flow in single microchannel reactors. Improved mass transfer is expected because of the large specific area of this pattern. However, the axial symmetry of the flow and the stagnant zones in the liquid slugs can still impose mass transfer limitations especially in the case of fast reactions as is the CO₂ chemical absorption. To improve the reactor performance and overcome the mass transfer limitations, process intensification can be used. In [Commenge et al. \(2005\)](#), two types of process intensification were identified. *Global intensification* is where the characteristic dimensions are reduced while still achieving the same absorption. *Local intensification* is where appropriate structured geometries are implemented that act locally on the flow or the operating conditions in order to increase transfer rates without changing the characteristic dimensions of the unit. An example of the latter is given by [Losey et al. \(2002\)](#), where 50µm diameter posts were placed in the 600µm reaction channel (Figure 2.29) resulting in 30-70 times improvement in mass transfer coefficient in the catalytic hydrogenation of cyclohexene to cyclohexane compared to laboratory scale packed-bed reactors.

In this chapter, different channel configurations such as meandering and bifurcating ones are used for local intensification. Bifurcating channels break the Taylor bubbles into smaller ones and result in increased contact area between the two phases and renewal of the liquid film around the bubbles. In addition, the original liquid slugs are broken as well into two parts and new vortices form in them that improve mixing ([Link et al., 2003](#)). Meandering channels break the symmetrical flow in the liquid slug and have been found to accelerate mixing ([Günther et al., 2004](#)).

The investigations are both experimental and theoretical. Experiments are carried out in in-house fabricated microchannel reactors of characteristic dimension less than 1mm. CO₂ volume fraction in the gas phase is measured to calculate the reaction conversion, which are compared with the simulation results. A gas-liquid two-phase model is formulated, which uses the experimental operating conditions as the inputs.

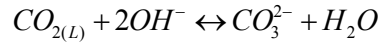
7.2 Reaction system

CO₂ absorption into aqueous alkaline solutions has many applications in industry, such as CO₂ removal from synthesis gas in ammonia production ([Farrauto & Bartholomew, 1997](#)), environmental applications ([Aroonwilas et al., 1999](#)) and CO₂ removal from flue

gases (Freguia & Rochelle, 2003). It is an intrinsically very fast and homogeneous reaction (Danckwerts, 1970), making it a suitable system to study in small channels. During absorption the following reactions occur:



The overall reaction can be written as



Reaction (i) represents the process of physical dissolution of gaseous CO_2 into the liquid solution. As the rate of this process is comparatively very high, the equilibrium at the interface can be described by Henry's law:

$$C_{CO_2(L)}^* = HeP_{CO_2} \quad \text{Eq. 7.1}$$

where $C_{CO_2(L)}^*$ is the equilibrium concentration of carbon dioxide at the gas-liquid interface, P_{CO_2} is the partial pressure of CO_2 in the gas phase and He is the equilibrium solubility of CO_2 in the liquid phase. The value of He can be calculated using Eq.7.2 (Schumpe, 1993), where C_i and h_i are the concentration and a parameter characteristic to each ion in the solution, while h_G is the absorbed gas in the liquid phase (Table 7.1, Schumpe, 1993). At 293 K, the equilibrium solubility of CO_2 in water is $0.039 \text{ kmol/m}^3 \text{ atm}$.

$$\log(He / He_{water}) = -\sum_i (h_i + h_G) C_i \quad \text{Eq.7.2}$$

Table 7.1 Values of h_i in calculating at 298K

i	Component	$h_i, \text{ m}^3 \text{ kmol}^{-1}$
1	Na^+	0.1171
2	OH^-	0.0756
3	CO_3^{2-}	0.1666
G	$\text{CO}_{2(L)}$	-0.0183

Reaction (iii) is an ionic reaction whose rate is significantly higher than that of reaction (ii). Therefore, reaction (ii) governs the overall rate of the process and follows second-order kinetics (Pohorecki and Moniuk, 1988):

$$r = -k_{OH^-} C_{OH^-} C_{CO_2(L)} \quad \text{Eq.7.3}$$

The equilibrium constant of reaction (ii) at ambient temperature is about $6 \cdot 10^7 \text{ m}^3/\text{kmol}$ (Astarita, 1967) and it can be considered as practically irreversible. The rate constant k_{OH^-} for reaction (ii) was given by Pohorecki and Moniuk (1988) as:

$$\log(k_{OH^-}) = 11.916 - \frac{2382}{T} + 0.221I - 0.016I^2 \quad \text{Eq.7.4}$$

The solution ionic strength, I , can be calculated from the ion concentration C and its valence Z (Eq.7.5)

$$I = 0.5 \sum_i C_i Z_i^2 \quad \text{Eq.7.5}$$

With known P_{CO_2} and C_{OH^-} , the reaction rate of CO_2 absorption can be calculated by solving simultaneously Eq. 7.1 - Eq.7.5 (Zanfir et al., 2005).

7.3 Reactor design

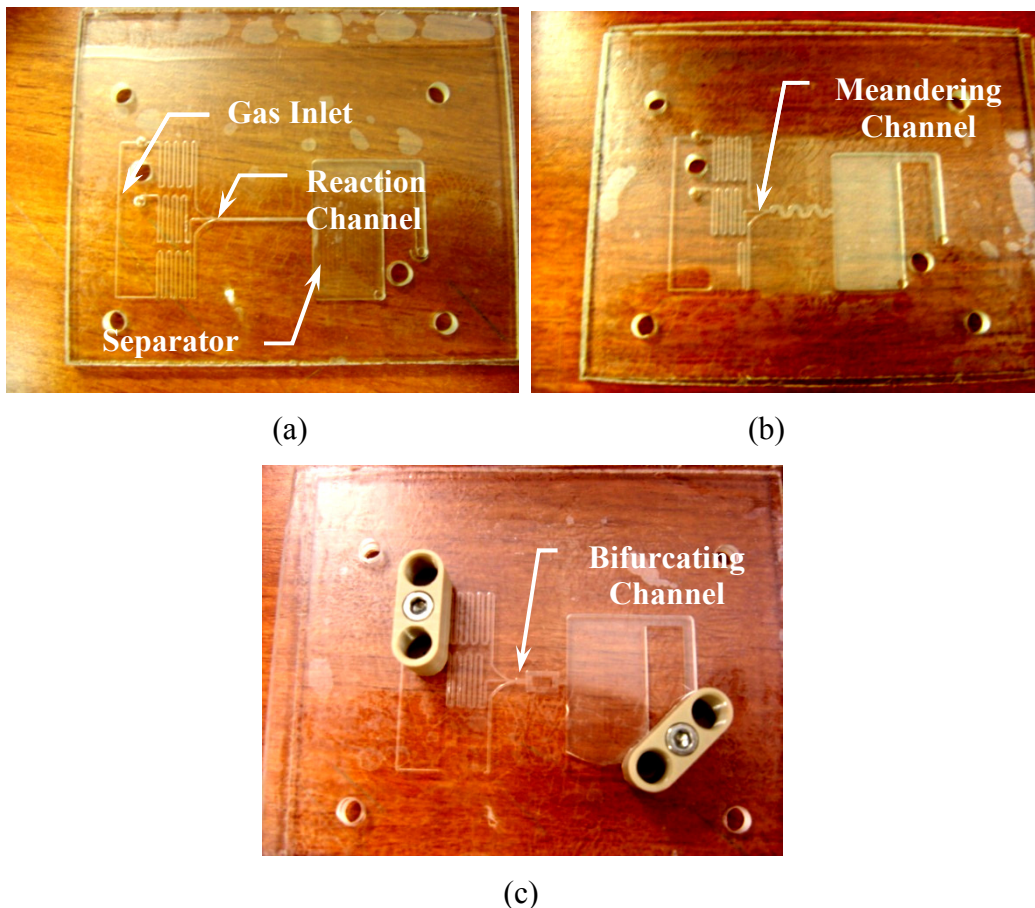
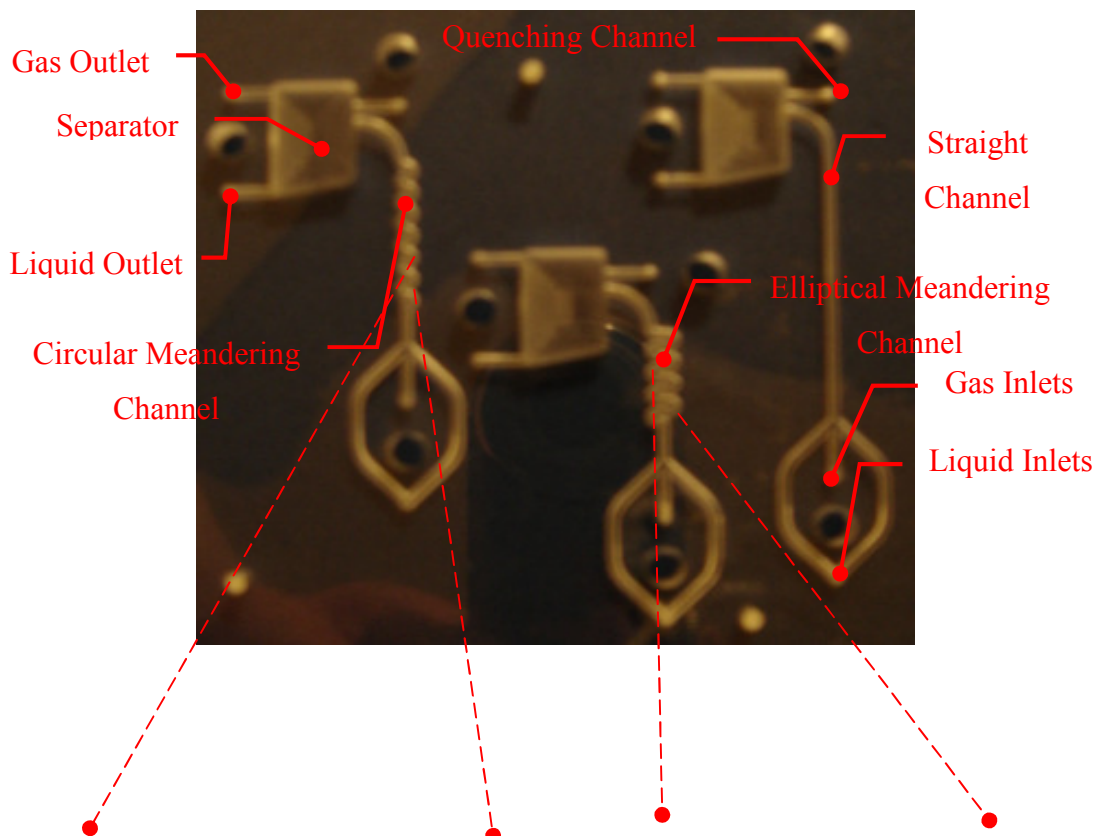


Figure 7.1 Series I reactor design – without reaction quenching channel. (a) straight channel; (b) meandering channel; (c) bifurcating channel.

To study the local process intensification during the two phase reaction, single channel microreactors of different geometries were designed and fabricated (see Section 6.2 for fabrication process). Two reactor series were made. Series I included three designs, namely straight channels of different dimensions, circular meandering channels with bends that are semicircular and bifurcating channels. The inlet in all designs was with the gas feed smoothly flanked between two identical liquid feed channels. The smooth flow-focusing inlet as shown in Figure 7.1 was based on a design by [Haverkamp et al. \(2006\)](#) who found that bubble size distribution was narrower using this design than using a T-mixer. Before both the gas and liquid inlets, there were meandering channels smaller in size than the inlet channels that reduced pressure fluctuations at the inlet (see Section 2.6.2.1 for detail). At the end of the reaction channel there was a gas-liquid separator (Figure 7.1a) where the fluids separated under gravity. Series II reactors were designed to study the effect of channel dimension and local structure on process intensification. They included straight channels of different widths and lengths and meandering channels of different curvature ratios. As shown in Figure 7.2, the gas-liquid separation chamber was improved to include a quenching channel, where an acid stream was brought in to terminate the CO₂ absorption process by reacting HCl with the residual NaOH. In Series II reactors the effect of residence time, mixing quality in the meandering channel and further reactions in the separation chamber were investigated.



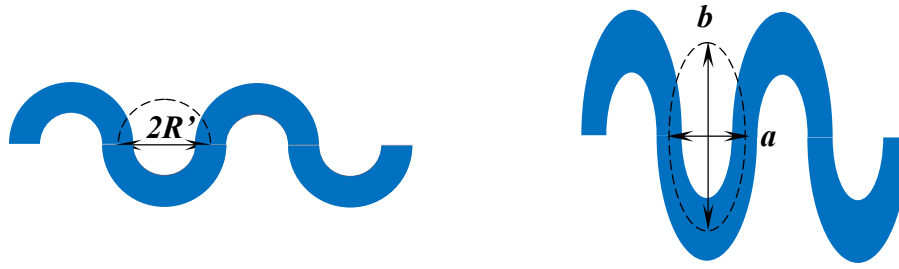


Figure 7.2 Series II reactor design – with reaction quenching channel.

Channel specifications for both design series are shown in Table 7.2, where w , h and l are the designed bottom width, the depth and the centreline length (along the channel profile for non-straight channels) of the channel; R' is the radius of the bend of the circular meandering channel; a and b are the minor and the major axis of the ellipse respectively of the elliptical meandering channel. From Section 6.2, there will be slight channel dimension deviation from the designed value, especially the channel depth, and the cross section of all channels is of truncated trapezium shape as shown in Figure 6.4. All these are linked to the fabrication technique used for this study. In Series I reactors, the same l is used for all channels in order to achieve equivalent reactor volumes. The actual reactor volume is measured by monitoring the amount of water injected from a syringe with a volume of the same order as that of the reactor. The result shows that the volume difference among the three reactors is within 1%.

Table 7.2 Dimensions of single channel microreactors in design Series I and II.

Series	Channel Structure	Design Dimension [mm]	d_H [mm]
I	Straight	$w: 1; h: 0.2; l: 20$	0.331
	Straight	$w: 0.5; h: 0.2; l: 20$	0.291
	Circular meandering	$w: 1; h: 0.2; l: 20, R' = 1$	0.331
	Bifurcating	$w: 1; h: 0.2; l: 20$	0.331
II	Straight	$w: 0.5; h: 0.25; l: 20$	0.345
	Straight	$w: 0.5; h: 0.5; l: 15, 20, 25, 40, 50$	0.577
	Straight	$w: 0.5; h: 0.8; l: 20$	0.816
	Circular meandering	$w: 0.5; h: 0.5; l: 20, R' = 1.4, 2.54$	0.577
	Elliptical meandering	$w: 0.5; h: 0.5; l: 50. a = 1.4, b = 4.1; a = 1.4, b = 9.6$	0.577

7.4 Experimental set up

The experimental set up is shown in Figure 7.3. A gas mixture of nitrogen and carbon dioxide (CO₂: 20%vol) is supplied from a gas cylinder and regulated with a Bronkhorst EL-FLOW F-110C mass flow controller for flows between 0.01-1 ml/min. The liquid phase, 0.2M sodium hydroxide solution, is pumped through a MiliGat pump (0-6 ml/min). The gas and liquid join at the inlet of the test section. After the reactor they separate at the separation chamber and the gas is led to a Gas Chromatograph to measure the residual CO₂ volume fraction. The liquid phase is continuously removed by a peristaltic pump from Grant Instrument Inc. Given that the reaction system is exothermic and the reaction rate is very sensitive to temperature, the test section is placed into a water bath kept at a constant temperature of 19 °C. The operating conditions (Table 7.3) for the gas and liquid phases are chosen to ensure that the mole flowrate F of NaOH is always more than that of CO₂ ($F_{NaOH}/F_{CO_2} > 3.8$).

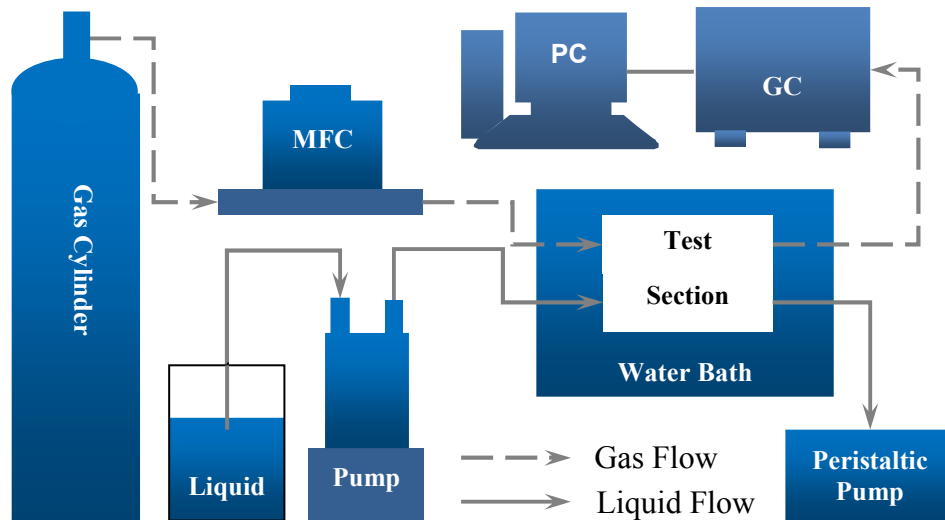


Figure 7.3 Schematic experimental set up for the investigation of mass transfer and reaction in Taylor flow microreactors.

Table 7.3 Operating conditions used in the CO₂ absorption experiment

Conditions	Values
Gas flowrate	0.41ml/min – 1.5ml/min
Liquid flowrate	0.17ml/min - 3ml/min
Gas phase split	CO ₂ : 20.14vol%; N ₂ : 79.86vol%
Initial concentrations	CO ₂ : 0.00835mol/l; NaOH: 0.2mol/l
Temperature and pressure	T: 292K; atmospheric pressure

7.5 Model formulation

In the model it is assumed that gravity, surface tension gradient (Marangoni effect) and gas compressibility have negligible effects. The bubble is assumed to have a cylindrical body with spherical caps at the ends for the low Capillary numbers encountered in this study ($Ca < 10^{-3}$) (Bretherton, 1961), as shown in Figure 7.4. The experimental conditions, e.g. Q_G , Q_L and A_C , are used to predict the unit cell frequency (Eq. 6.2), from which the bubble/slug lengths are calculated (see Appendix A) and used for the simulations. As discussed in Section 7.3, the inlet design in this chapter is not identical to the Y-junction design in Chapter 6, used to obtain correlation Eq. 6.2. There would, therefore, be errors in predicting the unit cell frequency. However, Eq. 6.2 was used because it was developed for a system that is very similar to the one used here, i.e. using the same fabrication technique and material, while the geometry of the inlet was found not to affect significantly the average bubble/slug length. for unit cell frequency. The bubble volume decrease due to CO₂ absorption is assumed to be negligible. The solution domain consists of two sub-domains, depicted in Figure 7.4 by the white and shaded areas, representing the gas and the liquid respectively. In Van Baten and Krishna (2005), Taylor bubble was treated as a void and the mass transfer of a tracer was solved when the tracer concentration at the gas-liquid interface remained unchanged. When reaction occurs in the liquid phase, as in the current study, the same model setup leads to physically incorrect CO₂ conversion, i.e. > 100% (Appendix B). Update of the interfacial concentration after a time period (the CO₂ amount absorbed at the end of the period is subtracted from the initial one on calculating the interfacial CO₂ concentration) was also not satisfactory (Appendix B). Therefore, in this study both the gas and liquid domains were solved and the CO₂ concentration at the interface was updated after each time step. Initial simulations showed that convection in the gas phase can be omitted because of the large CO₂ diffusivity in gas that leads to small CO₂ concentration gradient. The governing equations are the Navier-Stokes and continuity equation for solving the liquid phase velocity field (Eq. 7.6, Eq. 7.7), convection-diffusion equation for solving the liquid phase mass transfer (Eq. 7.8) and diffusion equation for solving the gas phase mass transfer (Eq. 7.9). The reaction term in Eq. 7.8 refers to both the gas and liquid reactant as shown in Eq. 7.10 and Eq. 7.11.

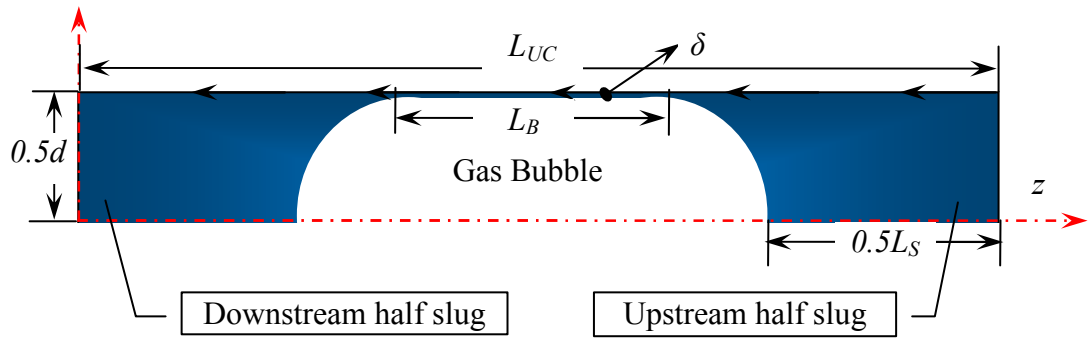


Figure 7.4 Geometry and boundaries of the computational domain

The simulations were carried out in the two-dimensional domain using axisymmetric cylindrical coordinates, in which the bubble was kept stationary while the wall moved with the bubble velocity in the direction opposite to the flow. For the boundary conditions of the hydrodynamic equations, the axial and radial velocity at the outer tube wall were set to $U_z = -U_B$ and $U_x = 0$ respectively where z and x are the axial and radial coordinates. Along the bubble surface, free slip boundary was used, i.e. $d\bar{u}/dn = 0$ where $d\bar{u}$ is the velocity component in the direction of the bubble surface and n is the normal direction to the bubble surface. For the mass transfer equations, along the bubble surface Henry's law constant was used to take into account the discontinuous concentration of CO_2 in the gas and liquid phases. Periodic boundary conditions were applied to the front and the back of the computational domain for velocity, pressure and concentrations, assuming that the inlet to the liquid slug is taken equal to the outlet. This assumption is only correct when the mass transferred during a time step is very small. [van Baten and Krishna \(2005\)](#) reported that error from this assumption was at most 0.03%.

Table 7.4 2D dimensional model details in gas domain for the Taylor flow reactor

$$\rho_L \frac{\partial \bar{u}}{\partial t} + \nabla \cdot \left(\rho_L \bar{u} \bar{u} - \mu_L \left(\nabla \bar{u} + (\nabla \bar{u})^T \right) \right) = -\nabla P \quad \text{Eq. 7.6}$$

$$\nabla \cdot \bar{u} = 0 \quad \text{Eq. 7.7}$$

$$\frac{\partial}{\partial t} C_i + \nabla \cdot (\bar{u} C_i - D_i \nabla C_i) = \begin{cases} r_i \\ 0 \end{cases} \quad \text{Eq. 7.8}$$

where

r_i is used for the reaction scenaria with $i = \text{CO}_{2(L)}$ and OH ;

0 is used for the physical absorption scenaria

$$\frac{\partial}{\partial t} C_{CO_2(G)} + \nabla \cdot (-D_{CO_2(G)} \nabla C_{CO_2(G)}) = 0 \quad \text{Eq. 7.9}$$

$$r_{CO_2(L)} = -k_{OH^-} C_{OH^-} C_{CO_2(L)} \quad \text{Eq. 7.10}$$

$$r_{OH^-} = -2k_{OH^-} C_{OH^-} C_{CO_2(L)} \quad \text{Eq. 7.11}$$

The equations were solved using a commercial finite element software (Comsol Multiphysics 3.3a). A free mesh with triangular elements was used, while along the bubble interface the mesh was refined to capture the steep concentration gradient in that region. Simulations were carried out in an Intel Pentium CPU processor with 3.20GHz, 2.0GB of RAM and the operating system was Windows XP x64 edition. Sensitivity studies on time step showed that a time step equal to 0.01s was satisfactory, i.e. there was little concentration discrepancy when a smaller time step, e.g. 0.005s, was used (Appendix C). Standard 2nd order elements were used for the velocity fields, 1st order elements for the pressure field and 3rd order elements for the mass transfer. The simulations were initially run in a steady-state mode to solve hydrodynamics in the liquid domain. The converged velocity field was then used as a starting point to solve the mass transfer in the liquid and in the gas domains simultaneously. Mass transfer was solved transiently to represent Taylor bubble movement downstream the reactor. Sensitivity analysis showed that the grid size should be less than 20 μ m in the sub-domains and less than 2 μ m along the gas-liquid interface to make CO₂ conversion independent of the grid size. The model was verified by comparing the velocity field in the liquid phase with the results by [van Baten and Krishna \(2005\)](#) (Appendix D).

The liquid phase properties are taken equal to those of water, i.e. density $\rho_L = 1000\text{kg/m}^3$ and viscosity $\mu_L = 0.001\text{Pa}\cdot\text{s}$. The diffusivity of CO₂ and of NaOH in the liquid phase is calculated by using Eq. 7.12 and Eq. 7.13 ([Zanfir et al., 2005](#)).

$$D_{CO_2(L)} = 1.97 \times 10^{-9} (1 - 0.129 C_{OH^-} - 0.261 C_{CO_3^{2-}}) \quad \text{Eq. 7.12}$$

$$D_{NaOH(L)} = 1.7 D_{CO_2(L)}^{1.35} \quad \text{Eq. 7.13}$$

7.6 Results and discussions

Mass transfer in the different cases was compared through CO₂ conversion, $X\%$, defined as the percentage of CO₂ transferred from the gas to the liquid phase. CO₂ conversions for experiments and simulations are calculated using Eq. 7.14 and Eq. 7.15 respectively. The derivation of Eq. 7.14 is explained in Appendix E, where sample calculations are also provided. In Eq. 7.15, vol is the volume of the grid (using the option of computing

volume values for axisymmetric modes) and V_G is the bubble volume that is assumed unchanged during the simulation.

$$X\% = \frac{(y_{CO_2,in} - y_{CO_2,out})}{(1 - y_{CO_2,out})y_{CO_2,in}} \% \quad \text{Eq. 7.14}$$

$$X_t \% = \left(1 - \frac{\sum_{j, \text{gasdomain}} vol_j C_{CO_2(G)} / V_G}{C_{CO_2(G),0}} \right) \% \quad \text{Eq. 7.15}$$

7.6.1 Series I reactors

CO₂ absorption experiments were carried out in Series I reactor (Table 7.2). The experimental operating conditions are then used as the simulation inputs (Section 7.5). Experimental and simulation results are presented in Table 7.5 and Table 7.6 respectively.

Table 7.5 Experimental conditions and results for Series I reactors of different structures. $Q_L = 2\mu\text{l/s}$, $d_H = 0.331\text{mm}$, $y_{CO_2,in}\% = 21.75\%$.

Structure	Q_G [ml/min]	$y_{CO_2,out}\%$ [-]	$X\%$ [-]
Straight	0.585	2.628	90.3
Straight	0.799	6.258	76.0
Straight	1.014	7.600	70.4
Straight	1.121	8.440	66.8
Meandering	0.585	1.558	94.3
Meandering	0.799	5.593	78.7
Meandering	1.014	7.536	70.7
Meandering	1.121	8.179	68.0
Bifurcating	0.585	4.39	83.5
Bifurcating	0.799	6.295	75.8
Bifurcating	1.014	6.987	73.0
Bifurcating	1.121	7.262	71.8

7. Mass Transfer and Reaction in Taylor Flow Microreactor

Table 7.6 Flow geometric values used in the simulations of series I straight channels, $y_{CO_2,in}\%$ = 21.75%.

d_H [mm]	l [mm]	Q_G [ml/min]	Q_L [μl/s]	A_C [mm ²]	U_{TP} [m/s]	Ca x 10 ⁴ [-]	U_B [m/s]	ε_L [-]	$1/f_{UC}$ [s]	L_{UC} [mm]	L_B [mm]	δ [μm]	α [m ² /m ³]	$y_{CO_2,out}\%$ [-]
0.331	20	0.585	2	0.223	0.053	0.729	0.056	0.170	0.310	17.31	14.03	1.72	9923	4.022
0.331	20	0.585	7	0.223	0.075	1.039	0.080	0.418	0.105	8.39	4.56	2.17	6941	1.692
0.331	20	0.585	15	0.223	0.111	1.535	0.120	0.606	0.053	6.28	2.15	2.78	4680	0.248
0.291	20	0.478	2	0.123	0.081	1.120	0.087	0.201	0.144	12.31	9.65	2.00	10941	0.334
0.291	20	0.692	2	0.123	0.110	1.522	0.118	0.148	0.137	16.08	13.52	2.43	11600	1.542
0.291	20	0.907	2	0.123	0.139	1.924	0.151	0.117	0.132	19.72	17.23	2.83	11970	3.515

The CO₂ conversions in Series I straight channel reactors are compared in Figure 7.5. It can be seen that the experimental results are underpredicted by the simulations. This discrepancy can partly be attributed to the axisymmetric channel and cylindrical bubbles with spherical cap used in the simulations. However, it is believed that the continuation of the reaction in the separation chamber, that is not taken into account in the modelling, is mainly responsible for this discrepancy given the fast rate of the reaction. The largest deviation occurred at the low conversion cases when higher CO₂ and NaOH concentrations are available in the separation chamber. The simulations agreed better with the experimental data at high conversions when most of the CO₂ had been consumed in the reactor channel and there was not much left to continue the reaction in the separation chamber.

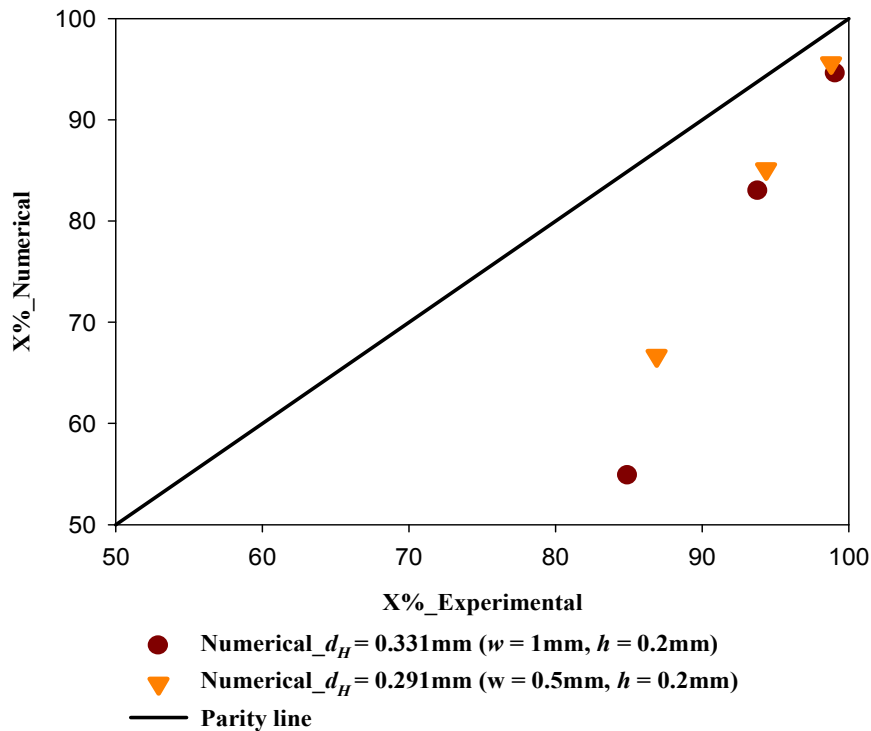


Figure 7.5 CO₂ conversion comparison between experimental and numerical results in Series I straight channel reactors.

The experimental results from the meandering and bifurcating channels are compared in Figure 7.6 against those from the straight channel with the same hydraulic diameter. The residence time in the abscissa is calculated using bubble velocity ($t = l/U_B$) and this is used for the rest of the chapter, where l is the central line length along the channel profile and U_B is calculated using the gas and liquid flowrate and the cross sectional area (Eq. 2.14). The CO₂ conversion in the bifurcating channel was higher but was only

slightly improved in the meandering channel as compared to the straight one. The channel splitting in the bifurcating geometry reduces the sizes of the bubbles and slugs. This creates new interfaces and at the same time disturbs the flow symmetry within the slugs which together with the decreased slug size improve the mixing in the slugs. These features will greatly enhance mass transfer and reaction conversion. The meandering channel aims to increase mixing in the slug by forming vortices at the bends that break the symmetry of Taylor flow. The Dean number ($De = Re(d_H/R')^{0.5}$) is often used to quantify the mixing caused by the vortices. However, improvements in mixing by the above approach did not seem to affect the mass transfer significantly. This is partly because of the small dimensions of the current system that could not result in Dean numbers that are large enough to improve mixing significantly. For example, [Jiang et al., \(2004\)](#) suggest a $De > 140$ for the flow pattern switch from two to four vortex version to improve the mixing significantly, much larger than the values of $10 < Re < 25$ in the current system (calculated using data in Table 7.2 and Table 7.3). As is also shown in Chapter 8, the liquid mixing in the slug is not as important when a fast reaction is present and the liquid reactant is in excess as CO_2 is rapidly consumed close to the interface.

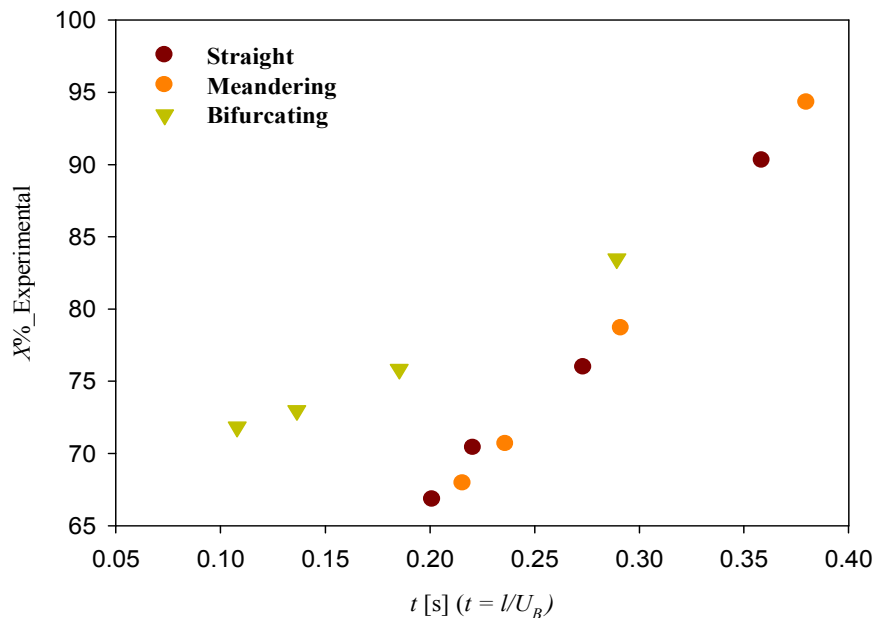


Figure 7.6 Experimental CO_2 conversions in Series I structured reactors. $d_H = 0.331\text{mm}$, $Q_L = 0.12\text{ml/min}$, $Q_G = 0.37\text{-}1.12\text{ml/min}$.

The investigations here are preliminary and better results could have been obtained if the structures of the bifurcating and meandering channels were improved. For example,

the splitting of the bubbles in the bifurcating channel was not always reproducible (Appendix F). This was partly attributed to the quality of the fabrication finish of the channel walls particularly at the corners. The outlet geometry of the channels may also have attributed as any pressure change due to bubble/slug recombination at the end of the bifurcating geometry would affect the conditions at the split point. In meandering channels a variety of parameters control the mixing quality, e.g. two-phase Reynolds number, channel dimension, the radius of the curvature, and it is possible that the geometric features chosen here are not the good ones.

7.6.2 Series II reactors

From Section 7.6.1, reactions taking place in the separation chamber is thought to contribute to the deviations between experiments and simulations. In order to eliminate these reactions, a quenching channel was added to the separation chamber in Series II reactors. Through the quenching channel, a 0.2M hydrochloric acid stream flowed into the separation chamber and terminated the reaction by contacting with the reactants stream (see Figure 7.2). In tests, where there is no reaction channel so that CO₂ and NaOH streams meet only at the separation chamber, the CO₂ absorption was found to decrease from 29.2% to 0.77% when the quenching stream was added, proving its effectiveness.

The experimental and simulation results in the Series II reactors are shown in Table 7.7 and Table 7.8. In order to investigate how reaction conversion changes with the residence time, channels with the same hydraulic diameter of 0.577mm but four different channel lengths, ranging from 15 to 40mm (Table 7.2), are studied for each flow condition (various liquid flowrates but constant gas flowrate). Results are presented in Figure 7.7, showing that with the elimination of further reaction in the separation chamber the experimental data are predicted well by the numerical model. Reaction conversions are found to increase with increasing residence time and liquid flowrate. For the latter, shorter bubble (Section 6.5.2.2) and thus larger specific area is obtained that contributes to the improved mass transfer. For $Q_L = 5\mu\text{l/s}$ in Figure 7.7 the conversion increases significantly in the first 0.1s and then changes more moderately. In this case, the bubble is long and the specific area is large that contributes to a very high conversion initially. However, the NaOH in the film is soon exhausted, as seen in Figure 7.8, which shows how NaOH is depleted in the upper and lower film region along the bubble length. As a result, part of the bubble surface in the film side does not contribute further to mass transfer.

Table 7.7 Experimental conditions and results for Series II channels of different structures. $Q_G = 1.4067\text{ml/min}$, $d_H = 0.577\text{mm}$, $y_{CO_2,in}\% = 23\%$.

Structure	R, a, b [mm]	l [mm]	Q_L [$\mu\text{l/s}$]	$y_{CO_2,out}\%$ [-]	$X\%$
Straight	-	20	5	12.12	53.85
Straight	-	20	10	8.93	67.16
Straight	-	20	15	7.22	73.93
Straight	-	20	20	5.5	80.52
Circular Meandering	$R = 1.4$	20	5	12.45	52.40
Circular Meandering	$R = 1.4$	20	10	9.16	66.26
Circular Meandering	$R = 1.4$	20	15	7.62	72.39
Circular Meandering	$R = 1.4$	20	20	6.7	75.96
Circular Meandering	$R = 2.54$	20	5	12.76	51.03
Circular Meandering	$R = 2.54$	20	10	9.43	65.16
Circular Meandering	$R = 2.54$	20	15	7.88	71.37
Circular Meandering	$R = 2.54$	20	20	6.99	74.83
Straight	-	50	2	12.85	50.62
Straight	-	50	5	7.47	72.98
Straight	-	50	10	3.87	86.53
Straight	-	50	15	3.53	87.76
Straight	-	50	20	3.15	89.13
Elliptical Meandering	$a = 1.4, b = 4.1$	50	2	13.18	49.20
Elliptical Meandering	$a = 1.4, b = 4.1$	50	5	6.58	76.43
Elliptical Meandering	$a = 1.4, b = 4.1$	50	10	3.66	87.29
Elliptical Meandering	$a = 1.4, b = 4.1$	50	15	2.37	91.88
Elliptical Meandering	$a = 1.4, b = 9.6$	50	2	13.63	47.16
Elliptical Meandering	$a = 1.4, b = 9.6$	50	5	7.21	74.0
Elliptical Meandering	$a = 1.4, b = 9.6$	50	10	3.34	88.43
Elliptical Meandering	$a = 1.4, b = 9.6$	50	15	2.87	90.12
Elliptical Meandering	$a = 1.4, b = 9.6$	50	20	2.52	91.35

7. Mass Transfer and Reaction in Taylor Flow Microreactor

Table 7.8 Flow geometric values used in the simulations of series II straight channels. $y_{CO_2,in}\% = 23\%$.

d_H [mm]	l [mm]	Q_G [ml/min]	Q_L [μ l/s]	A_C [mm ²]	U_{TP} [m/s]	Ca x 10 ⁴ [-]	U_B [m/s]	ε_L [-]	1/ f_{UC} [s]	L_{UC} [mm]	L_B [mm]	δ [μ m]	α [m ² /m ³]	$y_{CO_2, out}\%$ [-]
0.577	15	1.41	5	0.39	0.072	1.0	0.077	0.18	0.27	20.88	16.64	3.68	5638	14.2
0.577	15	1.41	10	0.39	0.085	1.17	0.091	0.3	0.15	13.58	8.95	4.09	4788	12.09
0.577	15	1.41	20	0.39	0.11	1.53	0.12	0.46	0.081	9.63	4.63	4.84	3676	7.47
0.577	20	1.41	5	0.39	0.072	1.0	0.077	0.18	0.27	20.88	16.64	3.68	5638	11.94
0.577	20	1.41	10	0.39	0.085	1.17	0.091	0.3	0.15	13.58	8.95	4.09	4788	8.89
0.577	20	1.41	20	0.39	0.11	1.53	0.12	0.46	0.081	9.63	4.63	4.84	3676	3.87
0.577	25	1.41	5	0.39	0.072	1.0	0.077	0.18	0.27	20.88	16.64	3.68	5638	9.89
0.577	25	1.41	10	0.39	0.085	1.17	0.091	0.3	0.15	13.58	8.95	4.09	4788	7.34
0.577	25	1.41	20	0.39	0.11	1.53	0.12	0.46	0.081	9.63	4.63	4.84	3676	3.53
0.577	40	1.41	5	0.39	0.072	1.0	0.077	0.18	0.27	20.88	16.64	3.68	5638	8.02
0.577	40	1.41	10	0.39	0.086	1.17	0.091	0.3	0.15	13.58	8.95	4.09	4788	5.55
0.577	40	1.41	20	0.39	0.11	1.53	0.12	0.46	0.081	9.63	4.63	4.84	3676	3.15
0.345	20	1.41	5	0.16	0.18	2.44	0.19	0.18	0.082	15.77	12.66	3.9	9332	15.4
0.345	20	1.41	10	0.16	0.21	2.87	0.23	0.3	0.045	10.28	6.87	4.32	7918	11.89
0.345	20	1.41	15	0.16	0.24	3.3	0.26	0.39	0.032	8.32	4.74	4.71	6872	9.38
0.345	20	1.41	20	0.16	0.27	3.73	0.3	0.46	0.024	7.3	3.61	5.08	6068	8.7

7. Mass Transfer and Reaction in Taylor Flow Microreactor

d_H [mm]	l [mm]	Q_G [ml/min]	Q_L [μl/s]	A_C [mm ²]	U_{TP} [m/s]	Ca x 10 ⁴ [-]	U_B [m/s]	ε_L [-]	1/ f_{UC} [s]	L_{UC} [mm]	L_B [mm]	δ [μm]	α [m ² /m ³]	$y_{CO_2, out}$ % [-]
0.577	20	1.41	5	0.39	0.072	1.0	0.077	0.18	0.27	20.88	16.64	3.68	5638	12.12
0.577	20	1.41	10	0.39	0.085	1.17	0.091	0.3	0.15	13.58	8.95	4.09	4788	8.93
0.577	20	1.41	15	0.39	0.097	1.35	0.1	0.39	0.11	10.98	6.13	4.47	4160	7.22
0.577	20	1.41	20	0.39	0.11	1.53	0.12	0.46	0.081	9.63	4.63	4.84	3676	5.5
0.816	20	1.41	5	0.77	0.037	0.51	0.039	0.18	0.66	25.85	20.5	3.37	4006	14.0
0.816	20	1.41	10	0.77	0.043	0.6	0.046	0.3	0.37	16.8	10.97	3.75	3404	11.09
0.816	20	1.41	15	0.77	0.05	0.69	0.053	0.39	0.26	13.57	7.47	4.11	2959	8.36
0.816	20	1.41	20	0.77	0.056	0.78	0.06	0.46	0.2	11.9	5.61	4.44	2616	6.63

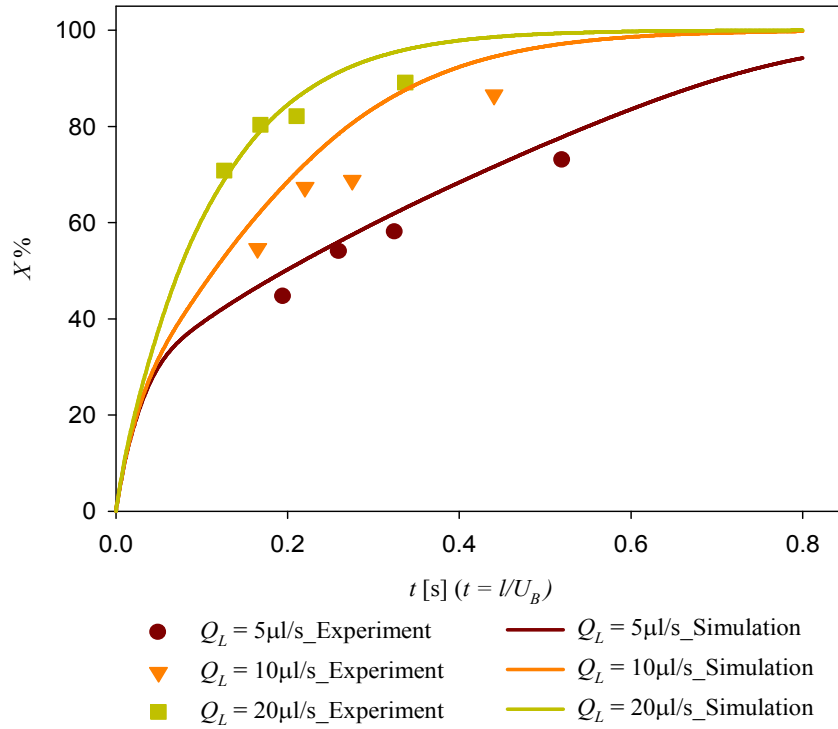


Figure 7.7 Experimental and simulation results for series II straight channel reactors. $d_H = 0.577\text{mm}$; $Q_G = 1.407\text{ml/min}$.

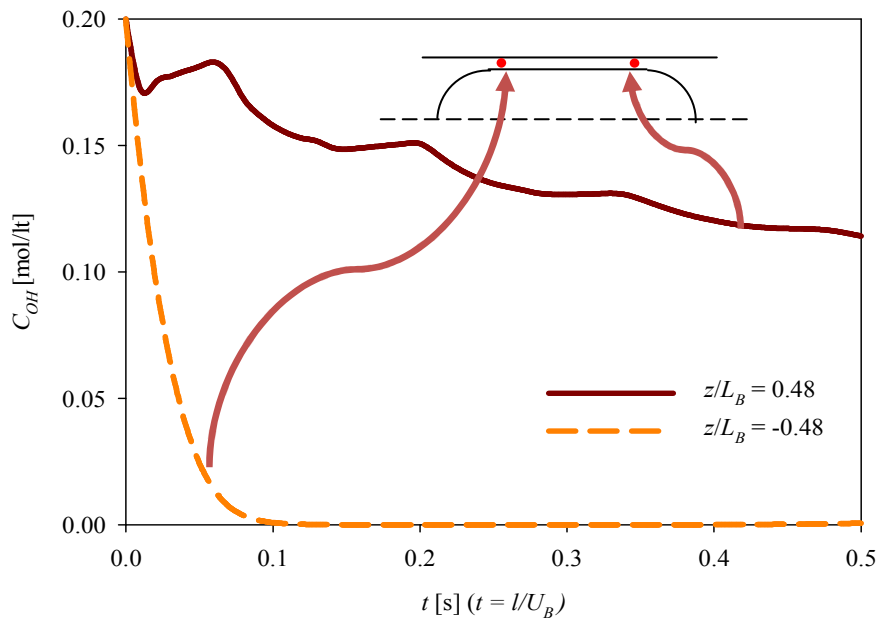
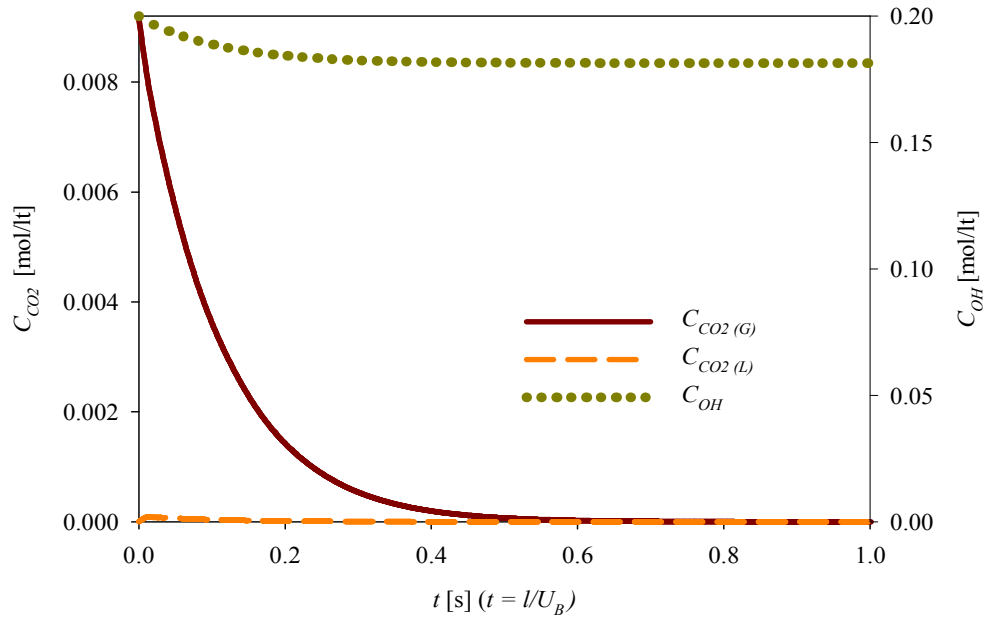
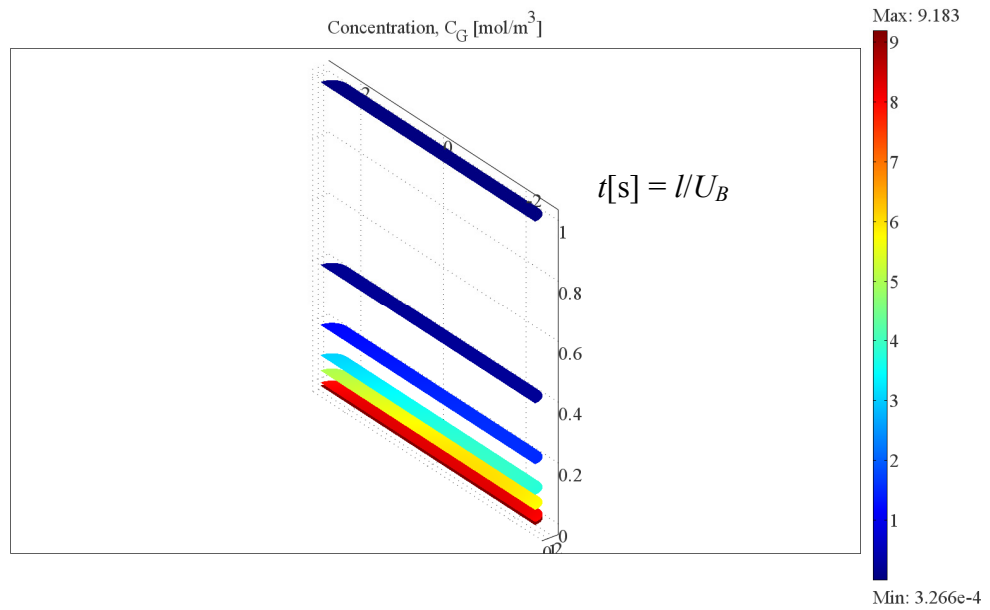


Figure 7.8 Point NaOH concentration in the upper and lower part of the bubble side film in a Series II straight channel reactor. $(x-0.5d_B)/\delta = 0.33$, $d_H = 0.577\text{mm}$, $Q_G = 1.407\text{ml/min}$, $Q_L = 5\mu\text{l/s}$.



(a)



(b)

Figure 7.9 Simulation results for a Series II straight channel reactor. $d_H = 0.577\text{mm}$, $Q_G = 1.407\text{ml/min}$, $Q_L = 20\mu\text{l/s}$. (a) average concentrations change with time; (b) CO_2 concentration profile in the gas bubble.

Typical simulation results are presented in Figure 7.9 for the average CO_2 and NaOH concentrations in the gas and liquid phases. The CO_2 in the gas is consumed quickly with time (Figure 7.9a) while there are very small concentration gradient (Figure 7.9b), verifying the assumption that in the gas phase mass transfer is fast. CO_2 in the liquid phase remains nearly at zero due to the reaction, as seen in Figure 7.9a. The NaOH

concentration does not reduce much towards the end of the reaction (CO_2 is nearly completely absorbed), showing that the number of moles of NaOH is in excess.

Experimental and numerical reaction conversions for channels with different sizes under the same gas and liquid flowrate are compared in Figure 7.10. As can be seen that the simulations predict well the experimental results and higher conversion is observed in smaller diameter channels at the same residence time. This is because smaller bubbles are present as the channel dimension decreases under the same flow conditions which result in larger specific area (Table 7.8).

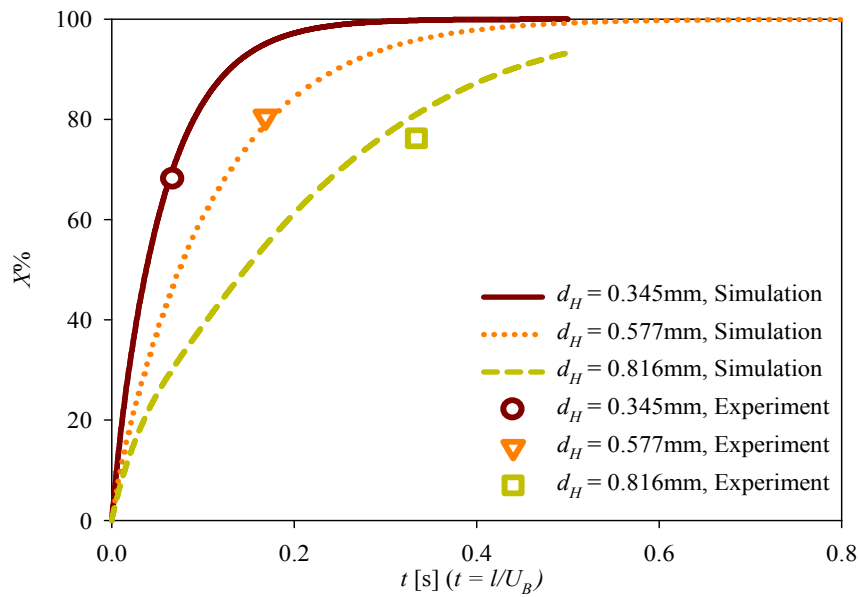


Figure 7.10 Effect of residence time on reaction conversion in Series II straight channel reactors with various characteristic dimensions. $Q_G = 1.407\text{ml/min}$, $Q_L = 20\text{ml/min}$.

The effect of channel geometry was investigated with the Series II meandering reactors. Circular meandering channels of different radius and elliptical meandering channels of different major axes were experimentally investigated and results are shown in Figure 7.11 and Figure 7.12 respectively against those from a straight channel of the same length. All channels had the same cross sectional area. Each experiment was repeated four times and the error bars are also shown in the figures. Conversions in the circular meandering channels were less than those in the straight channels and slightly decreased with an increase in the meandering channel curvature as shown in Figure 7.11. Bubble formation frequencies were found to be similar in all channels tested, as shown in Figure 7.13, thus excluding the effect of bubble/slug sizes on conversion. It seems that meandering channels have little effect on reaction conversion, because as discussed

before the effect of mixing in the slug does not affect significantly the mass transfer. The conversion differences between the elliptical meandering channels and the straight ones were even less as seen in Figure 7.12. Any variation could be a result of the sharp bends in the rather rough channels, which disturb the flow. Some results are found to be within the error range of the other structures (Figure 7.12).

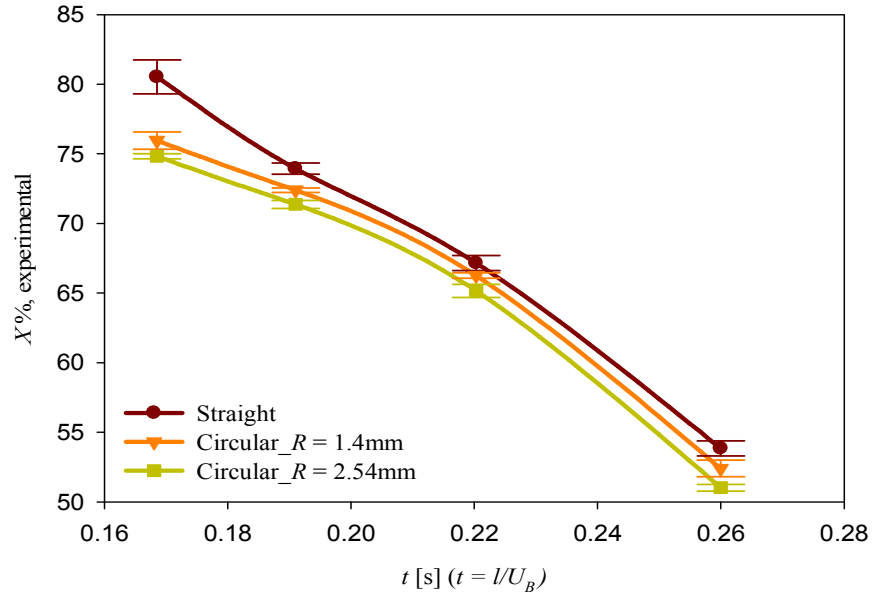


Figure 7.11 Experimental conversions in series II straight and circular meandering channel reactors. $Q_G = 1.407\text{ml/min}$, $Q_L = 5, 10, 15, 20\text{ml/min}$, $l = 20\text{mm}$.

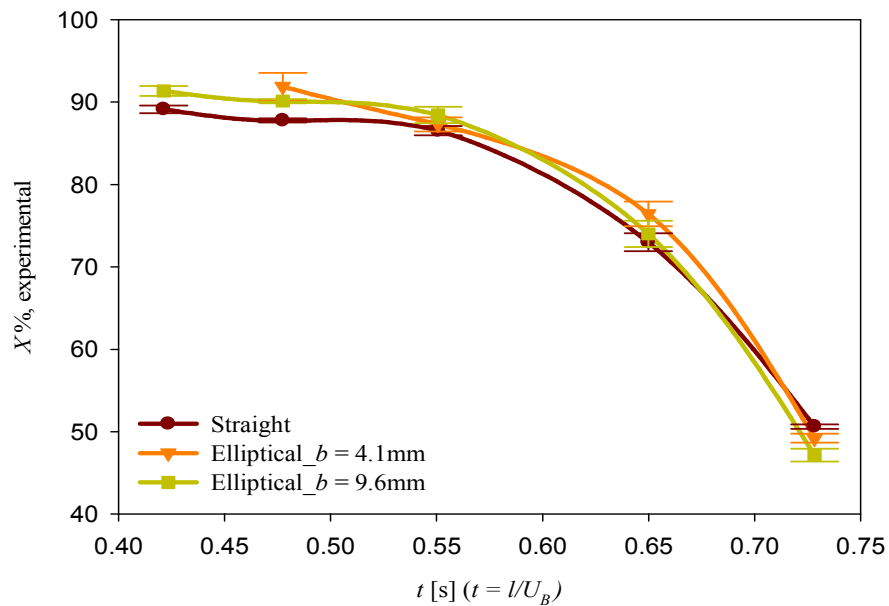


Figure 7.12 Experimental conversions in series II straight and elliptical meandering channel reactors. $Q_G = 1.407\text{ml/min}$, $Q_L = 5, 10, 15, 20\text{ml/min}$, $l = 50\text{mm}$, $a = 1.4\text{mm}$.

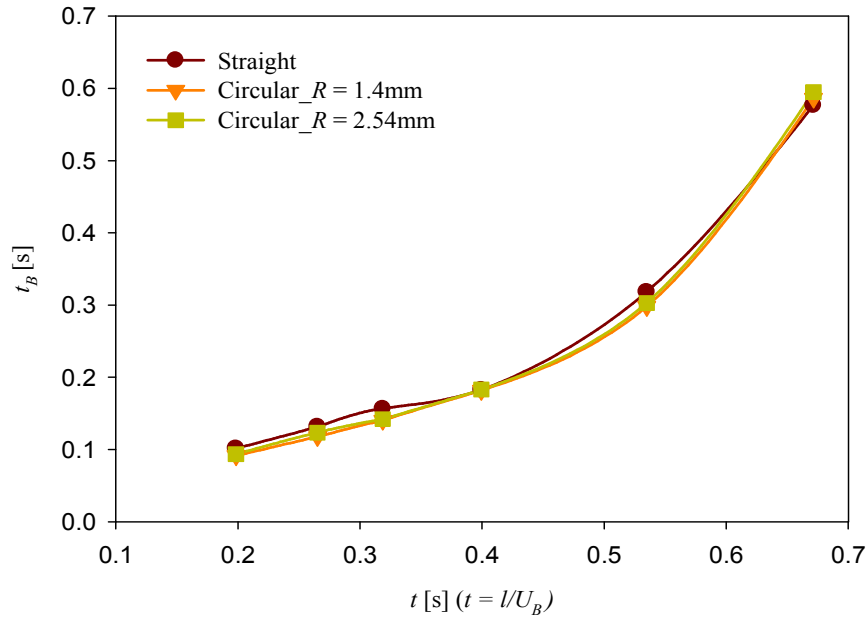


Figure 7.13 Bubble formation time t_B in Series II circular meandering channel reactors. $Q_G = 1.407\text{ml/min}$, $Q_L = 5, 10, 15, 20\text{ml/min}$, $l = 20\text{mm}$.

7.7 Conclusions

In this chapter, a gas-liquid two-phase reaction was studied in Taylor flow microchannel reactors of various designs. The reaction examined was CO_2 absorption into NaOH aqueous solution, a fast reaction system suitable for the investigation of the mass transfer performance of Taylor flow microreactors. Experimental results were compared with numerical simulations to evaluate the applicability of CFD as a modelling tool for the current system.

It was found that without quenching the reaction, it would continue to take place in the separation chamber and contribute to significant deviations from the real conversions. When acid quenching stream was added in Series II reactors, the extra absorption in the separation chamber was eliminated effectively and the agreements between the simulations and the experiments were satisfactory.

The CO_2 absorption was intensified in the bifurcating channels but not in meandering channels. In the former, higher conversions were found under the same operating conditions and channel dimensions than in straight channels. The increased mass transfer was mainly attributed to the reduced size of bubbles and slugs with splitting that renewed the interfacial area. However no significant improvements were seen with meandering channels both with Series I and II reactors.

7. Mass Transfer and Reaction in Taylor Flow Microreactor

In channels of different hydraulic dimensions, lower conversions were obtained in the larger channels under the same residence time. This was attributed to the smaller bubble size found in the small channels under the same gas and liquid flowrates that increase the available specific area for mass transfer. Reaction conversions were found to increase with residence time and with increasing gas to liquid flowrate ratio for the same residence time.

Numerical CFD simulations were found to be able to predict the experimental data well and can thus be recommended for further investigations.

Chapter 8
Numerical Parametric Study on Taylor Flow
Microreactor

Nomenclature

a	Specific area, m^2/m^3
A	Interfacial area, m^2
C	Concentration, mol/l
C^*	Interfacial concentration, mol/l
d	Diameter, m
E	Enhancement factor, -
F	Mole flowrate, kmol/s
k_L	Liquid side mass transfer coefficient, mol/s
l	Reactor length, m
L	Length, m
N	Number of mole, mol
t	Time, s
T	Temperature, K
U	Velocity, m/s
V	Volume, m^3
$X\%$	CO_2 absorption fraction, -
y	CO_2 volume fraction in gas mixture, -

Greek Symbols

μ	Dynamic viscosity, $\text{Pa}\cdot\text{s}$
ρ	Density, kg/m^3
σ	Surface tension, N/m
ε	Volume fraction in an unit cell, -
δ	Film thickness, m
Ψ	Liquid utilization, $\text{mol CO}_2/\text{mL NaOH solution}$

Dimensionless Numbers

Ca	Capillary number, $Ca = \frac{\mu_L U_B}{\sigma}$
------	---

Subscripts & Superscripts

B	Bubble
C	Channel

<i>Chemical</i>	Chemical absorption
<i>CO₂</i>	Related to carbon dioxide
<i>G</i>	Gas
<i>H</i>	Hydraulic
<i>in</i>	Inlet
<i>L</i>	Liquid
<i>NaOH</i>	Related to sodium hydroxide
<i>out</i>	outlet
<i>Physical</i>	Physical absorption
<i>S</i>	Slug
<i>t</i>	Time
<i>UC</i>	Unit cell

8.1 Introduction

In this chapter, mass transfer and reaction in the Taylor flow microreactor is further investigated. The literature studies (Section 2.5) revealed that many parameters, such as bubble velocity, bubble length, slug length, unit cell length and capillary size, affect mass transfer in Taylor flow, because the specific area of the unit cell changes with the bubble geometry. However, there are no parametric studies reported when chemical reaction is also present, despite the common use of Taylor flow in applications that involve reactions. In this chapter, parametric studies on the mass transfer during CO₂ absorption into aqueous alkaline solutions with and without reaction under Taylor flow in microchannels are carried out using the numerical model developed in Section 7.5. Simulations are particularly beneficial for carrying out parametric studies because the effects of the different parameters can be easily isolated, which is not always possible with experiments (for example in this case the bubble length from slug length).

For the study, the effect of a fast reaction on mass transfer is initially considered. This is followed by investigating the effect on mass transfer of the flow geometry such as bubble length, slug length and unit cell length and of the channel dimension. These results would help to design Taylor flow microreactors with improved performance.

8.2 Model formulation

Table 8.1 Reaction conditions for the numerical parametric study of Taylor flow microreactor

Conditions	Values
Gas phase	CO ₂ : 5vol%; N ₂ : 95vol%
Liquid Phase	Water; 0.2mol/l NaOH
Temperature and pressure	T: 298K; atmospheric pressure

The numerical model was described in Section 7.5. The simulations are mainly carried out in a 0.5mm diameter channel, apart from one case, with bubble and slug lengths ranging from $0.5d$ to $10d$ based on the experimental findings (Chapter 6). The reaction system of CO₂ absorption into NaOH (Section 7.2) is used and the reaction conditions are shown in Table 8.1. The study is carried out at atmospheric pressure and 298K. 0.2mol/l NaOH or water is used as liquid phase. Different from Chapter 7 where a 20%vol CO₂/N₂ mixture was used as gas phase, a 5%vol mixture is used in this chapter

so that the model assumption of negligible gas volume change due to CO₂ absorption is better satisfied. The operating conditions ensure that there is enough liquid reactant ($F_{NaOH}/F_{CO_2} > 10$) even under the highest gas to liquid volume ratio in the reaction scenario. The liquid phase properties are taken equal to those of water, i.e. density $\rho_L = 1000\text{kg/m}^3$, viscosity $\mu_L = 0.001\text{Pa}\cdot\text{s}$.

$$\Psi = \frac{F_{CO_2}^{In} - F_{CO_2}^{Out}}{Q_L^{In}} = \frac{Q_G^{In}}{Q_L^{In}} C_{CO_2}^{In} X_{CO_2} = \frac{V_B}{V_S} C_{CO_2}^{In} X_{CO_2} = \frac{\varepsilon_B}{1 - \varepsilon_B} C_{CO_2}^{In} X_{CO_2} \quad \text{Eq. 8.1}$$

$$\varepsilon_B = \frac{U_G}{U_B} \quad \text{Eq. 8.2}$$

$$\begin{aligned} k_L a &= \frac{U_L}{l} \ln \frac{C^* - C_{CO_2(L),in}}{C^* - C_{CO_2(L),out}} = \frac{U_L}{U_B t} \ln \frac{C^* - C_{CO_2(L),0}}{C^* - C_{CO_2(L),t}} \\ &= \frac{1 - 0.61Ca^{0.33} - \varepsilon_B}{t} \ln \frac{C^* - C_{CO_2(L),0}}{C^* - C_{CO_2(L),t}} \end{aligned} \quad \text{Eq. 8.3}$$

$$E_t = \left(\frac{\Delta N_{CO_2(L),chemical}}{\Delta N_{CO_2(L),physical}} \right)_t = \frac{N_{CO_2(L),0} - N_{CO_2(L),t,chemical}}{N_{CO_2(L),0} - N_{CO_2(L),t,physical}} \quad \text{Eq. 8.4}$$

The mass transfer performance of the different cases is compared through CO₂ absorption fraction, $X\%$ (Eq. 7.15), which is defined as the percentage of CO₂ transferred from the gas to the liquid phase. One drawback in using absorption fraction to assess mass transfer is that large absorption fraction can be achieved in an uneconomic way, e.g. by using a large amount of liquid reactant. To compare the performance of the reactors, a liquid utilization index, Ψ , defined by Eq. 8.1 (Zanfir et al., 2005) is also used. In Eq. 8.1, the gas to liquid volumetric flowrate ratio can be substituted by the bubble volume fraction using Eq. 8.2 (Liu et al., 2005), which can be calculated from the Taylor flow geometric information (Table 8.2). Because the liquid volume has been taken into account in the equation, interfacial area A will be compared hereafter when appropriate. A residence time t of 0.05s was selected for all simulations that ensured that in all cases the CO₂ absorption fraction was less than 100% and while there were still significant differences between the various cases in each parametric study.

For physical absorption, a plug flow model was used to estimate the mass transfer coefficient $k_L a$ (Eq. 8.3) from the simulations, where the ratio of liquid superficial velocity U_L to bubble velocity U_B can be obtained from Eq. 8.2 and Eq. 2.14 (Liu et al., 2005). An enhancement factor at time t , E_t , (Eq. 8.4) is also calculated in each case to compare the CO₂ chemical absorption with the physical one.

8. Numerical Parametric Study on Taylor Flow Microreactor

Table 8.2 Simulation parameters, mass transfer coefficient and the enhancement factor for various cases. $y_{CO_2,in} = 5\%$, $C_{NaOH,in} = 0.2M$, $t = 0.05s$.

Case	d [mm]	U_B [m/s]	L_S [mm]	L_B [mm]	L_{UC} [mm]	δ [μm]	$V_B \times 10^{10}$ [m ³]	$V_{UC} \times 10^{10}$ [m ³]	ε_B	$A \times 10^{-6}$ [m ²]	a [m ² /m ³]	$k_L a$ [s ⁻¹]	$k_L \times 10^{-4}$ [m/s]	$E_{t=0.05s}$ [-]
1	0.5	0	0.26	0.25	1	5	1.09	1.96	0.55	1.14	5800	0.68	1.17	10.7
2	0.5	0.01	0.26	0.25	1	5	1.09	1.96	0.55	1.14	5800	0.93	1.59	7.5
3	0.5	0.05	0.26	0.25	1	5	1.09	1.96	0.55	1.14	5800	1.41	2.43	4.9
4	0.5	0.1	0.26	0.25	1	5	1.09	1.96	0.55	1.14	5800	1.49	2.56	4.6
5	0.5	0.05	0.26	2	2.75	5	4.39	5.40	0.81	3.83	7100	0.86	1.21	8.9
6	0.5	0.05	0.26	5	5.75	5	10.0	1.13	0.89	8.45	7490	0.52	0.70	11.6
7	0.5	0.05	2	0.25	2.74	5	1.09	5.38	0.2	1.14	2120	0.73	3.43	3.4
8	0.5	0.05	5	0.25	5.74	5	1.09	11.3	0.10	1.14	1010	0.35	3.42	3.5
9	0.5	0.05	0.26	2	2.76	1	4.54	5.42	0.84	3.91	7210	0.39	0.54	18.1
10	0.5	0.05	0.26	2	2.66	50	2.85	5.22	0.54	3.02	5770	1.11	1.91	5.9
11	0.5	0.05	0.44	0.5	1.43	5	1.56	2.81	0.55	1.53	5420	1.30	2.39	5
12	0.5	0.05	1.54	2	4.03	5	4.39	7.92	0.55	3.83	4840	0.83	1.70	7.1
13	0.25	0.05	2.12	1.63	4	2	1.09	1.96	0.55	1.83	9330	0.86	0.92	9.6

8.3 Results and discussions

The geometric parameters of Taylor flow for each scenario are listed in Table 8.2, where the calculated $k_L a$ and E are also given.

8.3.1 Effect of fluid flow and chemical reaction

Three scenarios, mass transfer in a static system (diffusion only, $U_B = 0\text{m/s}$), mass transfer with flow, and mass transfer with flow and fast reaction present (CO_2 absorption into NaOH), are compared to show the effects on conversion and liquid utilization of recirculation in the slugs of Taylor flow and of chemical reaction. The simulations are performed for three bubble velocities, 0.01, 0.05 and 0.1m/s and the results are shown in Figure 8.1. In the physical absorption scenario, the utilization index, Ψ , and absorption fraction, X , are found to be larger in the cases with flow than in the static system and to increase with bubble velocity because at higher U_B the recirculation frequency is increased which improves the mixing. However, the increase in X and Ψ with U_B becomes less significant from $U_B > 0.05\text{m/s}$. It is expected that mass transfer between the bubble and the slug will be more significant in the first recirculation of the liquid in the slug when there is still no CO_2 in the liquid and a large concentration difference exists between the interface and the liquid. Interfacial mass transfer is expected to be less efficient in the following recirculations of the liquid when there will already be CO_2 in the liquid phase, particularly close to the interface, and the concentration gradient, necessary for the mass transfer, is reduced compared to the initial recirculation cycle. For the residence time examined (0.05s), the number of recirculations in the liquid for bubble velocities of 0.01, 0.05 and 0.1m/s is about 0.5, 2.5 and 5 respectively (the recirculation path is approximately $2(L_S + d/2)$ in these calculations). For $U_B = 0.01\text{m/s}$ the first recirculation cycle is not complete and the mass transfer performance can be improved by increasing the recirculation frequency, which is achieved by increasing U_B (Figure 8.1). Since the first recirculation is the most effective, any further increase in U_B does not improve significantly the mass transfer (see Figure 8.1) despite the increase in the recirculation frequency.

The utilization index and conversion are significantly improved in the presence of reaction (Figure 8.1) because in this case the absorbed CO_2 in the liquid is converted, thus maintaining the CO_2 concentration difference between gas and liquid necessary to drive the mass transfer. However, when reaction is present, bubble velocity and liquid circulation have only a small effect on X or Ψ . The results in Figure 8.1 show that

compared to the static scenario, X increases by 145% at $U_B = 0.1\text{m/s}$ in the physical absorption scenario while the increase is only 5% in the reaction scenario. The small improvement in the reaction scenario with bubble velocity is probably due to the better mixing in the liquid slug that allows more concentrated NaOH to approach the gas-liquid interface. Although bubble velocity has a minor effect on liquid utilization in the reaction scenario, higher bubble velocity at the same residence time means longer reactor, which is not appealing in terms of reactor cost.

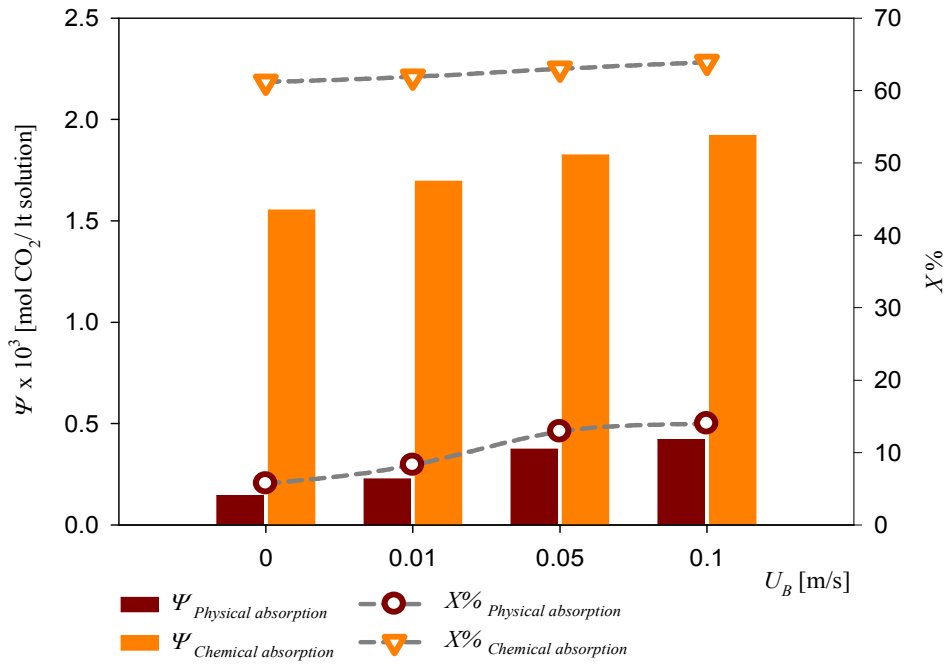
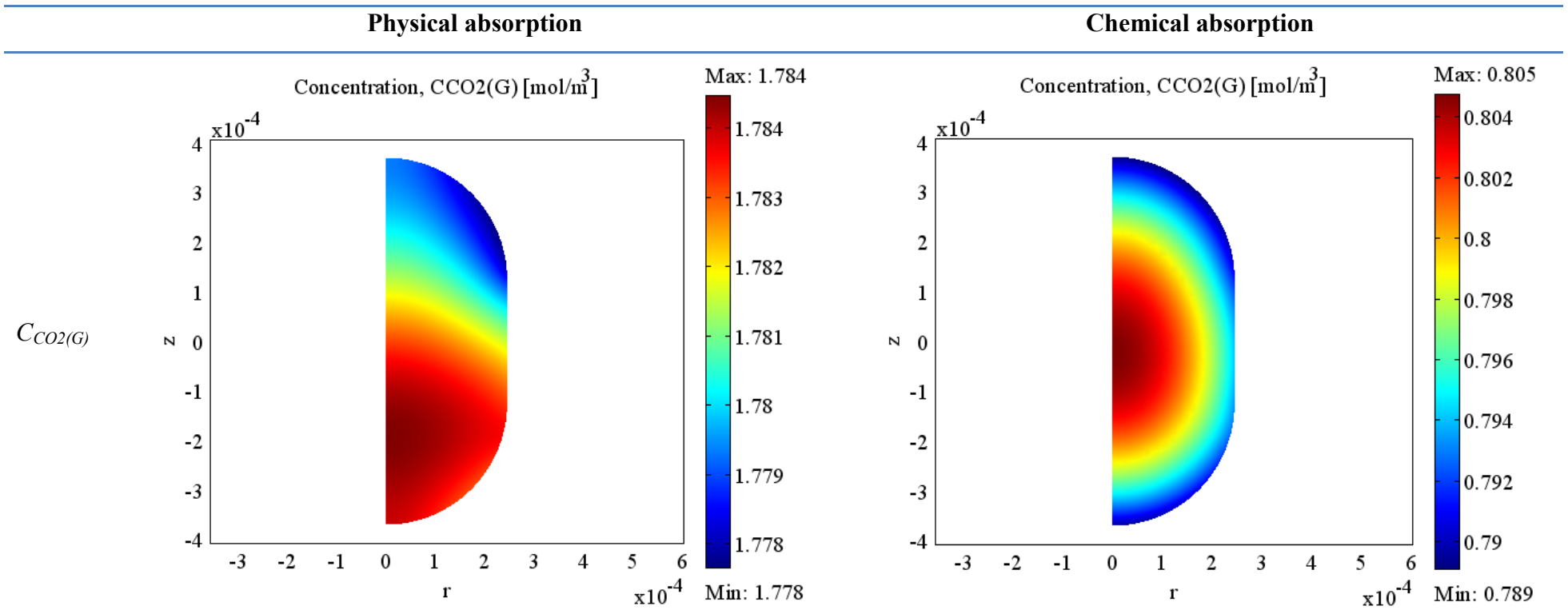


Figure 8.1 Effect of bubble velocity on liquid utilisation index and CO_2 absorption fraction. $d = 0.5\text{mm}$, $L_S = 0.26\text{mm}$, $L_B = 0.25\text{mm}$, $L_{UC} = 1\text{mm}$, $\delta = 5\mu\text{m}$, $t = 0.05\text{s}$. Case No. 1-4.

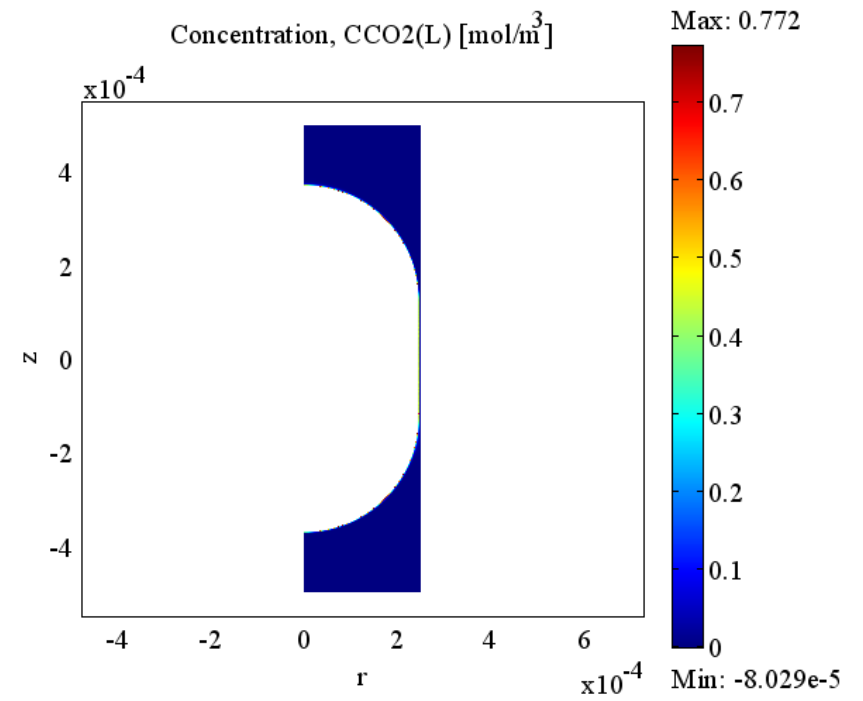
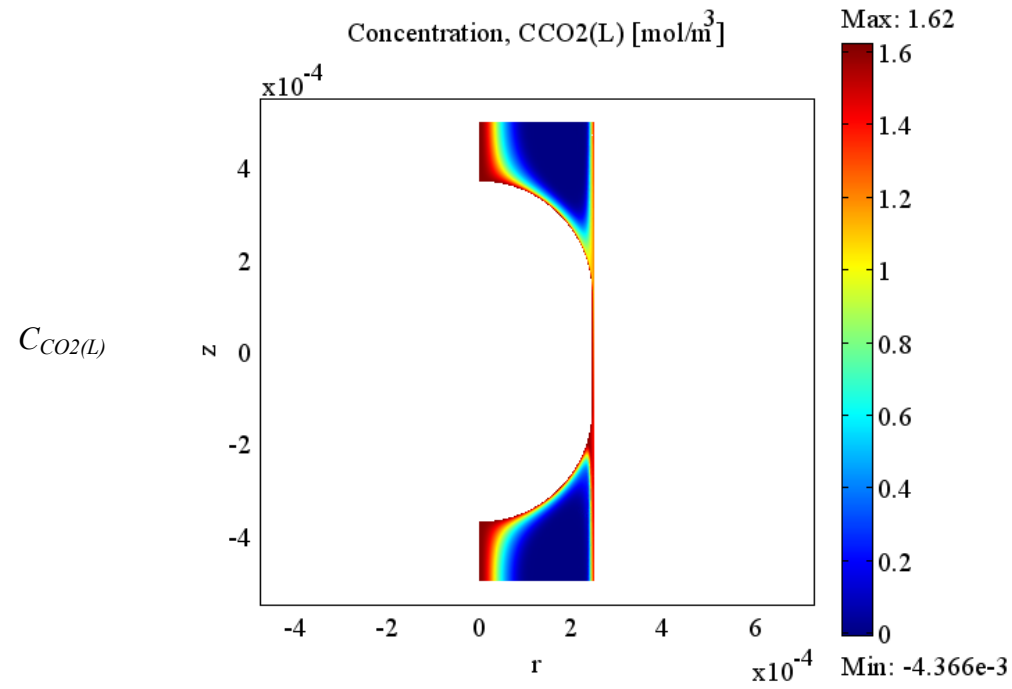
The values of the mass transfer coefficient, $k_L a$, for physical absorption and the absorption enhancement factor, E , when a chemical reaction is present are shown in Table 8.2. It can be seen that $k_L a$ increases with bubble velocity. Example CO_2 concentration in the gas and the liquid phases are given in Table 8.3. Within the liquid slugs, there are concentration gradients in the physical absorption case while during chemical absorption there is no CO_2 which explains the higher mass transfer in this case. The concentration gradients in the gas phase are very small in both physical and chemical absorption. The lack of symmetry in the physical absorption case seems to reflect the direction of the velocity.

Table 8.3 Example CO₂ concentration profiles. Case No. 3.



Physical absorption

Chemical absorption



8.3.2 Effect of bubble length

By increasing the bubble length, the interfacial area of the bubble is increased Table 8.2 together with the amount of CO₂ available in the gas phase for transfer. The mixing in the liquid bulk and the amount of NaOH remain the same due to the same slug size. From Figure 8.2 it can be seen that longer bubbles lead to significantly higher utilization index in both scenarios, which is attributed to two phenomena: larger V_B/V_S and larger interfacial area. As a result more CO₂ can transfer to the liquid within a certain time and react with NaOH. The utilization index is increased by 858% when bubble length extends from 0.25 to 5mm in the reactive case, but only by 300% during physical absorption probably because in this case the interface becomes quickly saturated with CO₂ and further mass transfer is slowed down. The absorption fraction, on the other hand, for both scenarios shows a decrease with L_B . This is because the increased amount of CO₂ that is transferred is offset by the larger amount of CO₂ present in the gas with increasing L_B . From Table 8.2 it can be seen that the mass transfer coefficient, $k_L a$, also decreases with bubble length. Although the specific area per unit volume, a , increases, in longer bubbles the film becomes saturated with CO₂ and this part of the bubble does not contribute further to mass transfer.

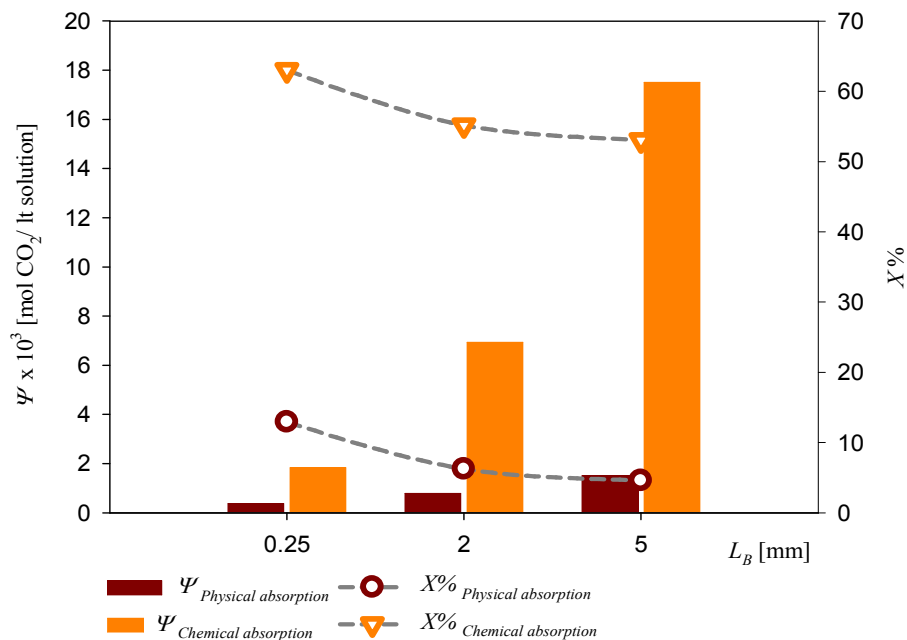


Figure 8.2 Effect of bubble length on liquid utilization index and CO₂ absorption fraction. $d = 0.5\text{mm}$, $U_B = 0.05\text{m/s}$, $L_S = 0.26\text{mm}$, $\delta = 5\mu\text{m}$, $t = 0.05\text{s}$. Case No. 3, 5 and 6.

8.3.3 Effect of slug length

The reactor performance for various slug lengths is shown in Figure 8.3, which demonstrates that short slugs significantly improve the liquid utilization index for both scenarios because of the reduced amount of liquid used, i.e. larger V_B/V_S (Table 8.2). In contrast in both scenarios, the CO₂ absorption fraction decreases or remains the same with decreasing slug length as shown in Figure 8.3. In the reaction scenario there is hardly any change in X because the bubble interfacial area available for mass transfer does not change while the amount of NaOH is in all cases in excess. The change in absorption fraction is more noticeable in the physical absorption scenario particularly when comparing $L_S = 0.26$ mm with the longer slugs. In the short slug more than one recirculation cycles take place within the residence time while in the long ones ($L_S = 2$ and 5mm) the first recirculation cycle is not complete which means that for the entire time of the simulation fresh liquid with no CO₂ comes in contact with the interface. The mass transfer coefficient, $k_L a$, decreases with slug length following the reduction in specific area (see Table 8.2).

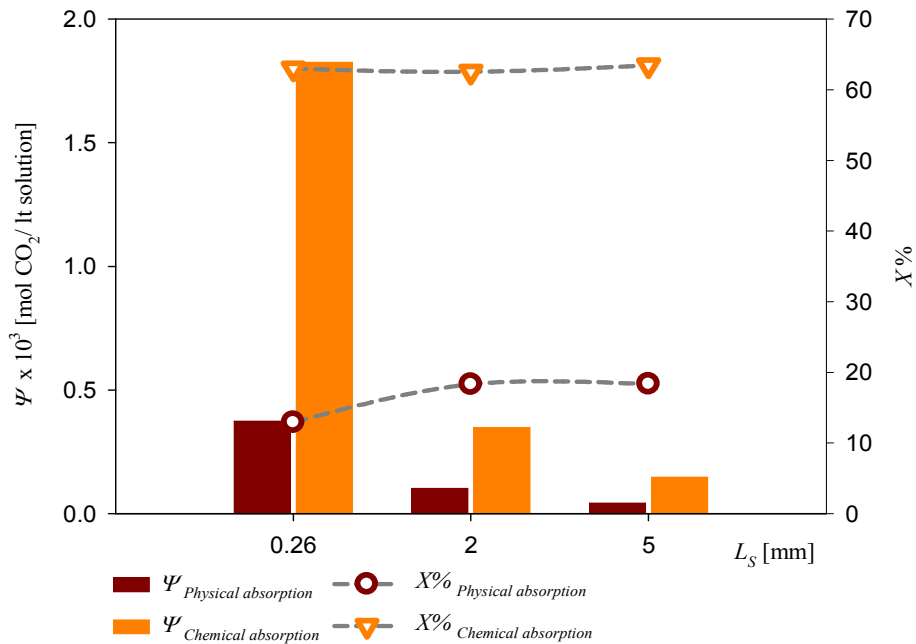


Figure 8.3 Effect of slug length on liquid utilization index and CO₂ absorption fraction.

$d = 0.5$ mm, $U_B = 0.05$ m/s, $L_B = 0.25$ mm, $\delta = 5$ μ m, $t = 0.05$ s. Case No. 3, 7 and 8.

8.3.4 Effect of film thickness

The film between the Taylor bubble and the wall is important as it determines the bubble movement in the channel while it connects adjacent liquid slugs. Three film thicknesses, 1 μ m, 5 μ m and 50 μ m, are studied for their effect on the reactor performance.

For the reaction scenario a thinner film results in larger interfacial area (Table 8.2) and V_B/V_S , which leads to increased liquid utilization as seen in Figure 8.4 (NaOH is not exhausted within the time examined even in the 1 μm film). The differences in Ψ are very small among the physical absorption cases and do not follow a trend with film thickness. A high utilization index is obtained with the 5 μm thick film, while when the film is too thin (1 μm) or too thick (50 μm), the utilization index is less (Figure 8.4). When the film is thin (1 μm) it quickly becomes saturated with CO_2 and can only absorb a small amount of CO_2 . Mass transfer will mainly happen through the interface from the bubble caps, which is 20% of the total, resulting in low liquid utilization. Furthermore, there is hardly any liquid transferring between slugs (Figure 8.5a) that could create concentration gradients in the slugs and improve mass transfer. When the film is thick (50 μm), a lot of liquid bypasses the bubble (Figure 8.5c) and remains unused (see Figure 8.6); V_B/V_S decreases by 72% that will reduce Ψ .

CO_2 absorption fraction generally increases with increasing film thickness as a result of decreasing bubble volume (Figure 8.4). The results are similar to those of decreasing bubble length (Figure 8.2).

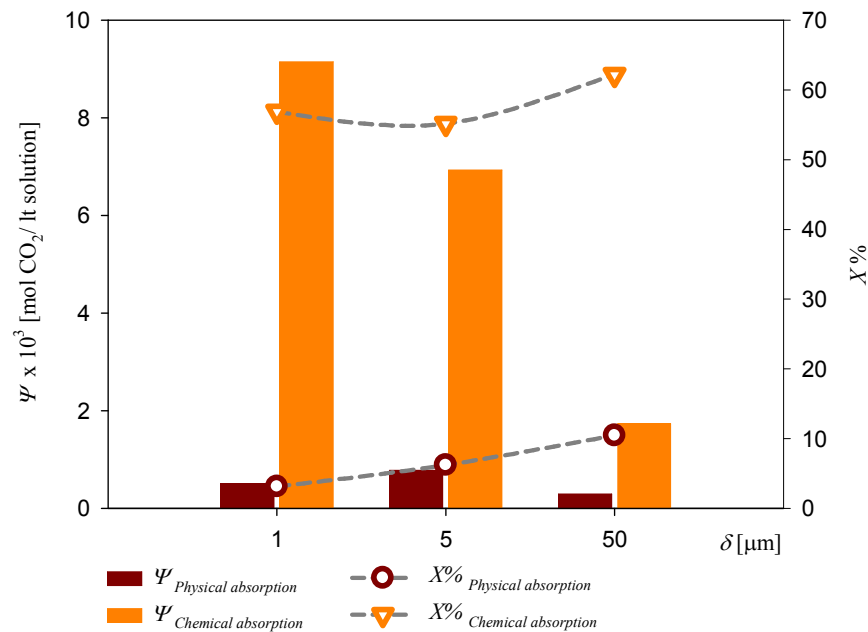


Figure 8.4 Effect of film thickness on liquid utilization index and CO_2 absorption fraction. $d = 0.5\text{mm}$, $U_B = 0.05\text{m/s}$, $L_S = 0.26\text{mm}$, $L_B = 2\text{mm}$, $t = 0.05\text{s}$. Case No. 5, 9 and 10.

The mass transfer coefficient, $k_L a$, is found to increase with film thickness (Table 8.2) although the specific area decreases. This observation is similar to that at increasing

bubble length. The film becomes saturated with CO₂ at thin film and part of the bubble does not contribute further to mass transfer.

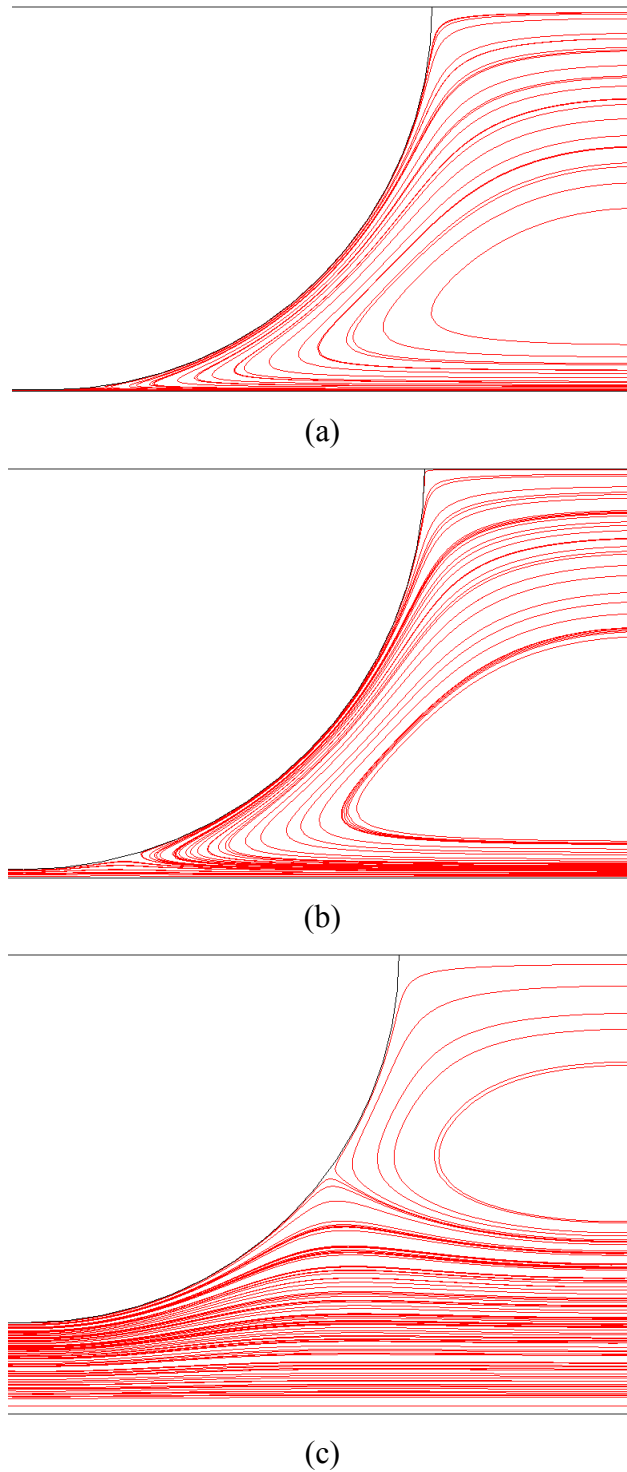


Figure 8.5 Streamline plot in liquid slug for cases with different film thickness. $\delta = 1\mu\text{m}$ (a), $5\mu\text{m}$ (b) and $50\mu\text{m}$ (c). $d = 0.5\text{mm}$, $U_B = 0.05\text{m/s}$, $L_S = 0.26\text{mm}$, $L_B = 2\text{mm}$, $t = 0.05\text{s}$. Case No. 5, 9 and 10.

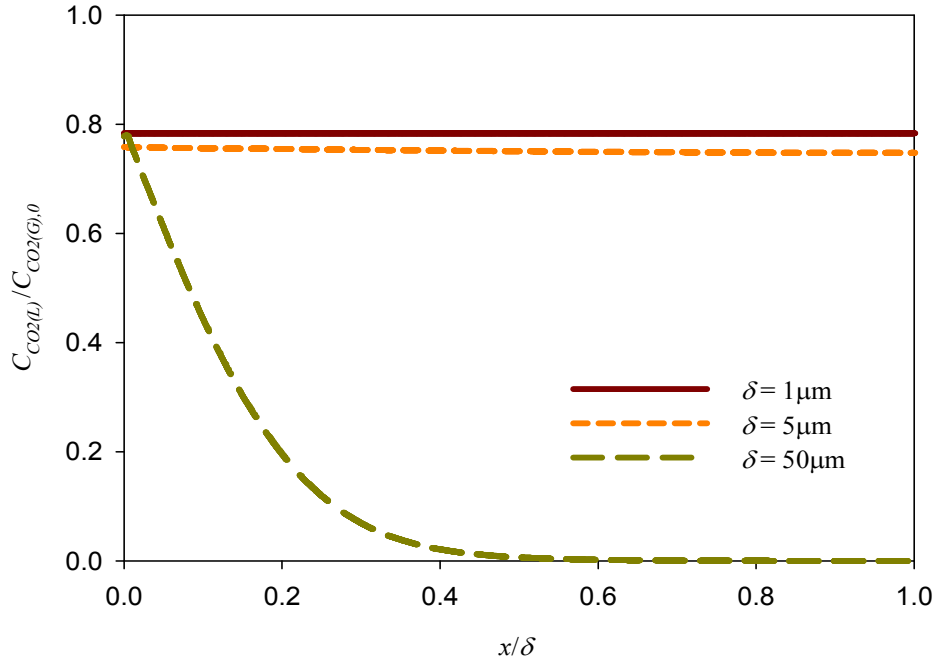


Figure 8.6 Transversal CO₂ concentration profile for cases with different film thickness. $d = 0.5\text{mm}$, $U_B = 0.05\text{m/s}$, $L_S = 0.26\text{mm}$, $L_B = 2\text{mm}$, $t = 0.05\text{s}$. Case No. 5, 9 and 10.

8.3.5 Effect of unit cell length

As was discussed in Chapter 5 bubble and slug lengths can vary depending on the inlet geometry. In this section the unit cell length is varied and with this the bubble and slug lengths in order to maintain the same gas to liquid volume ratio (ε_B), see Table 8.2.

As can be seen in Figure 8.7, Ψ decreases with increasing L_{UC} for both the reaction and the physical absorption scenaria. Since ε_B remains the same, the only parameter that can affect Ψ is CO₂ absorption fraction $X\%$. For both scenaria, the amount of CO₂ increases with increasing unit cell size as larger bubbles are present. In addition, the interfacial area also increases that would improve mass transfer (Table 8.2) but at a lower rate than the bubble volume. For example, the interfacial area increases by 336% when L_{UC} changes from 1mm to 4.03mm, while the respective increase in bubble volume is 403%. The overall result is a lower absorption fraction in the longer unit cell length for both chemical and physical absorption as can be seen in Figure 8.6. In the physical absorption case, the first recirculation cycle in the slug takes longer time in a longer unit cell (longer slugs), which would have improved the mass transfer (see discussion in Section 1.1.1). However, this improvement in mass transfer does not balance the increased amount of CO₂ present and the absorption fraction is still lower than in the

shorter unit cells. From Table 8.2 it can be seen that $k_L a$ decreases moderately with unit cell size in accordance with the decrease in specific area.

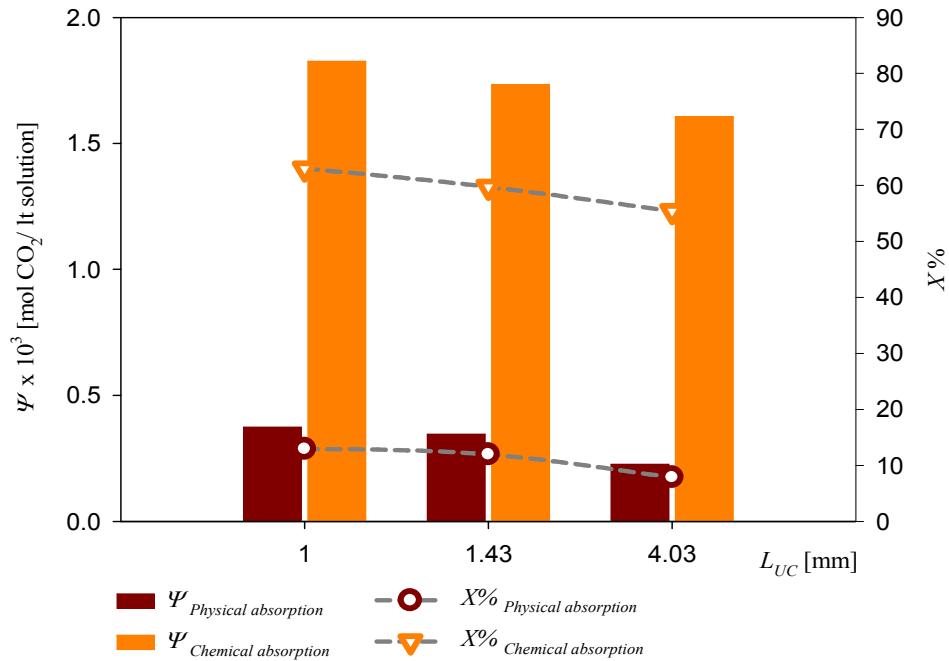


Figure 8.7 Effect of unit cell length on liquid utilization index and CO₂ absorption fraction. $d = 0.5\text{mm}$, $U_B = 0.05\text{m/s}$, $\varepsilon_B = 0.55$, $\delta = 5\mu\text{m}$, $t = 0.05\text{s}$. Case No. 3, 11 and 12.

8.3.6 Effect of channel dimension

To investigate the effect of channel size on mass transfer a channel size of 0.25mm is used in addition to the 0.5mm channel studied before. In order to keep the unit cell volume constant in the two channels, the unit cell length is extended in the 0.25mm channel by four times which means longer bubbles and slugs. The bubble and slug lengths are adjusted so that the gas to liquid volume ratio remains the same in the two cases (see Table 8.2). As can be seen in Figure 8.8, the absorption fraction and utilization index for the reaction scenario are higher in the small channel compared to the large one which is attributed to the larger interfacial area (Table 8.2). The opposite, however, is seen for the physical absorption scenario. This is because in the small channel the slug is extended by eight times in length (Table 8.2) and thus the time to complete a full recirculation reaches 0.09s. Therefore, at time of 0.05s, when the data is collected, only half recirculation is completed and this deteriorates the mixing in the liquid slug. As a result, better absorption fraction and utilization are obtained in the large channel in the physical absorption case.

$k_L a$ decreases as channel size decreases probably because the film which becomes quickly saturated and does not further contribute to mass transfer is extended in the small channel. Although k_L from the bubble cap increases in the small channel the corresponding specific area is small and the $k_L a$ associated with the bubble cap does not contribute sufficiently to the overall mass transfer coefficient.

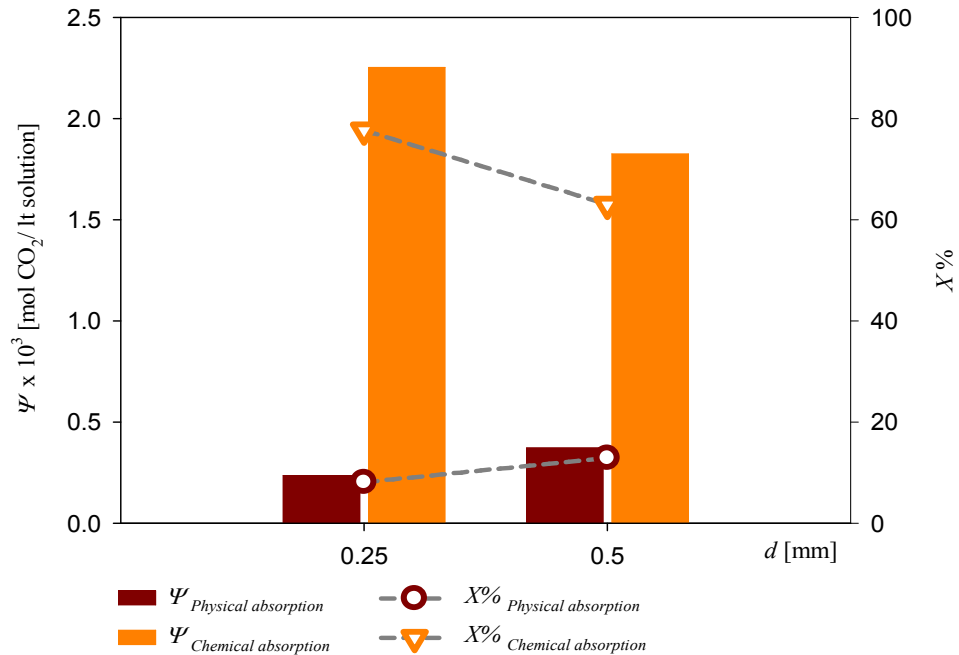


Figure 8.8 Effect of channel dimension on liquid utilization index and CO₂ absorption fraction. $U_B = 0.05\text{m/s}$, $\varepsilon_B = 0.55$, $V_{UC} = 0.196\mu\text{l}$, $t = 0.05\text{s}$. Case No. 3 and 13.

8.3.7 Mass transfer coefficient and enhancement factor

The mass transfer coefficients from the current simulations (see Table 8.2) are compared with those from literature correlations (Eq. 2.23 to Eq. 2.26) in Figure 8.9. In general, $k_L a$ from this study fall within the predictions of literature correlations. Better agreement is seen with Eq. 2.24 and Eq. 2.25. It is possible that higher $k_L a$ values were predicted by Eq. 2.24 compared to the current data because in this work narrow channels are used where the contribution of mass transfer from the bubble caps is not as significant as that from the film. When the mass transfer coefficient based only on the film size of the bubble is used, as in Eq. 2.25, the agreement is improved (see Figure 8.9). Eq. 2.23 by Berčić and Pintar (1997) underpredicts the mass transfer possibly because it was developed using long bubble lengths. Eq. 2.26 also underpredicts the current results probably because it was obtained at much higher gas and liquid velocities (10-300 times of those used in this study) (Yue et al., 2007). The $k_L a$ from physical CO₂

absorption found here vary from 0.4 to 1.5s^{-1} and the specific areas vary from 1000 to $10000\text{m}^2/\text{m}^3$. These values agree with the range reported by Yue et al. (2007) for similar gas-liquid contactors, i.e. k_{La} from 0.3 to 21s^{-1} and from 3400 to $9000\text{m}^2/\text{m}^3$, and outperform other contactors (see Table 2 in Yue et al., 2007).

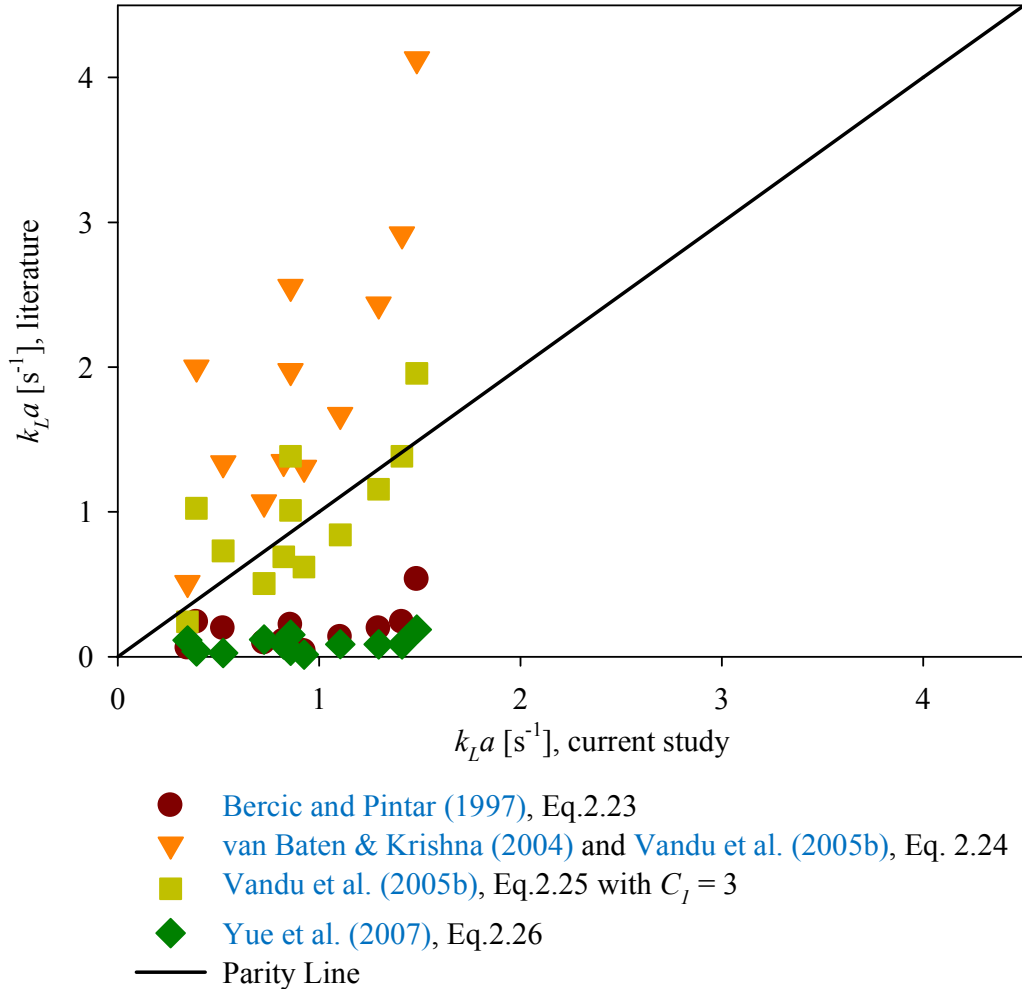


Figure 8.9 The comparison of k_{La} between simulation results (Table 8.2) and predictions by literature correlations (Eq. 2.23-Eq. 2.26). $t = 0.05\text{s}$.

The enhancement factors at $t = 0.05\text{s}$ for all the cases studied are calculated using Eq. 8.4 and the results are shown in Table 8.2. With the presence of chemical reaction, CO_2 absorption improves by 3 – 18 folds. E decreases with increasing bubble velocity because of the improved liquid slug mixing that enhances the physical absorption. At higher bubble length, E is found to be higher since the increased specific area at longer bubble helps to improve chemical absorption while there is little improvement in liquid slug mixing at constant liquid slug length. There is no significant effect of slug length

on E , because shorter slug decreases both the specific area and the liquid slug mixing that is important for chemical and physical absorption respectively. E decreases with film thickness because with the thin film case, the specific area is large while the liquid recirculation is restrained (Figure 8.5a). Similar to the effect of slug length, unit cell length does not affect E significantly because with longer unit cell, both the specific area and the liquid slug mixing are reduced. However, the liquid slug mixing is more significantly affected and this results in improvement in E . Large enhancement by chemical absorption is seen in the case with smaller channel because of the larger specific area and reduced liquid slug mixing at the record time of 0.05s (Section 8.3.6), which improves chemical absorption but reduces the physical one.

8.4 Conclusions

Numerical parametric studies on the effect on Taylor flow reactor performance of a number of variables were carried out in this chapter. By using CO₂ absorption in a NaOH aqueous solution, the effects of bubble velocity, bubble geometry and channel dimension were compared in the presence and absence of reaction. The reactor performance was evaluated using the CO₂ absorption fraction $X\%$ and the liquid utilization index Ψ .

CO₂ absorption were found to be significantly higher when reaction was present than when there was no reaction because the transferred CO₂ was consumed which led to a constantly large driving force across the interface for mass transfer. The simulation results showed that the CO₂ absorption fraction increased with increasing bubble velocity, slug length and film thickness, while it decreased with increasing bubble length and unit cell length. Interestingly, decreasing the channel size improved CO₂ absorption fraction for the reaction scenario but decreased absorption fraction in the physical absorption scenario. The effects of bubble velocity and slug length were relatively small while generally the effects on $X\%$ of the above parameters were more significant in the physical absorption cases.

Together with CO₂ absorption, the amount of gas and/or liquid present affects the liquid utilization index Ψ . Similar to $X\%$, Ψ was found to be higher in the reaction cases than in the physical absorption cases. When there was reaction, Ψ was found to increase with increasing bubble velocity and bubble length, and with decreasing slug length, unit cell length and channel dimension. The effect of bubble and slug length was significant. With physical absorption, the effects of various parameters were found to be more

moderate. Results showed that Ψ increased with increasing bubble velocity, bubble length and channel dimension and decreasing slug length and unit cell length.

In general, chemical absorption mainly depended on the *effective* specific area, which only took into account the interface that contributed to the mass transfer. Because in some cases, part of the interface did not absorb; for example, at long bubble length CO_2 circulated to the bubble side film region was absorbed by the upper part of the film and left the lower part ineffective. However, physical absorption was found to be affected by the mixing quality in the liquid slug, which was mainly contributed by the first recirculation.

The Mass transfer coefficient in this study was found to be ranged from $0.3\text{-}1.5\text{s}^{-1}$, which was in line with literature values for Taylor flow but higher than normal gas-liquid contactors. The Enhancement factor of chemical over physical absorption varied between 3 and 18. Enhancement was more significant at low bubble velocity, long bubble length, thin liquid film, short unit cell length and small channel dimension. The effect of slug length was small.

The above suggest that it is important to establish bubble and slug lengths in a Taylor flow reactor that improve mass transfer through appropriate inlet configuration.

Chapter 9
Microreactor Application Study on Fuel Gas
Absorption in Amine Solutions

Nomenclatures

<i>a</i>	Specific surface area, m^2/m^3
<i>A</i>	Reactor effective cross sectional area (not accounting for solid walls or interstices), m^2
<i>B</i>	A very large number, 10^5
<i>C</i>	Concentration, kmol/m^3
<i>d</i>	Channel size, equals to $\delta_G + \delta_L$, m
<i>D</i>	Diffusivity, m^2/s
<i>f</i>	Mole flux, $\text{mol}/(\text{m}^2 \text{ s})$
<i>F</i>	Mole flowrate, kmol/s
<i>g</i>	Gravitational acceleration, m/s^2
<i>h</i>	Reactor height, m
<i>He</i>	Henry's constant, $\text{atm m}^3/\text{mol}$
<i>I</i>	Ionic strength, kmol/m^3
<i>k_i</i>	Reaction rate constant for reaction i, $\text{m}^3/(\text{kmol s})$
<i>K_i</i>	Equilibrium constant for reaction i
<i>L</i>	Length, m
<i>l</i>	Reactor length, m
<i>M</i>	Molecular weight, kg/kmol
<i>n</i>	Number of plates/channels
<i>N</i>	Number of moles, kmol
<i>P</i>	Pressure, atm
<i>Q</i>	Total volumetric flowrate, m^3/s
<i>R</i>	Gas constant, $0.082 \text{ m}^3 \text{ atm}/(\text{K kmol})$
<i>R_i</i>	Chemical reaction rate for reaction i
<i>t</i>	Time, s
<i>T</i>	Temperature, K
<i>v</i>	Average velocity, m/s
<i>V</i>	Volume, m^3
<i>w</i>	Plate width, m
<i>x</i>	Transverse coordinate, m
<i>X</i>	CO_2 conversion
<i>y</i>	Axial coordinate, m
<i>z</i>	Molar fraction

Dimensionless Numbers

Ca Capillary number, $Ca = \frac{\mu_L U_B}{\sigma}$

Fo Mass Fourier number, $Fo = \frac{t_G}{\tau_D}$

Greek symbols

δ Film thickness, m

ρ Density, kg/m³

μ Viscosity, kg/(m s)

τ_D Diffusion time, s

ψ Utilization index, kmol CO₂/m³ amine solution

Φ Dimensionless constant

Subscripts

0 At inlet, $t = 0$

B Bubble

C Channel or capillary

CO_2 Related to carbon dioxide

e equilibrium

G Gas phase

$G \rightarrow L$ Gas to liquid phase

i Chemical species

L Liquid phase

Superscripts

in Flow into the system

out Flow out of the system

W In water

9.1 Introduction

The increasing awareness of climate change has called for reduction in CO₂ emissions of 50%-60% by 2050 (IPCC, 2007). Other industrial processes, where CO₂ plays a negative role include: presence of CO₂ in synthesis gas in ammonia production could poison the catalyst in the ammonia converter; and CO₂ in natural gas could increase transportation costs and reduce the energy level per unit gas volume. For various gas streams that contain a relatively low CO₂ concentration, CO₂ capture in a chemical solvent, usually amine, is by far the most cost effective and viable solution (Tobiesen and Svendsen, 2006). The amine groups of the alkanolamines provide the necessary alkalinity in the aqueous solution to react with CO₂ while the hydroxyl groups increase the water solubility.

Table 9.1 Advantages and disadvantages for various amines used in CO₂ absorption.

Amines	Advantages	Disadvantages
MEA	<ul style="list-style-type: none"> • relatively strong base with a fast reaction rate • high absorption capacity per weight due to its low molecular weight • less likely to undergo thermal degradation • reduce hydrocarbon loss when processing natural gas and refinery gas due to low solubility for hydrocarbons 	<ul style="list-style-type: none"> • higher stripping energy demand and cost due to high heat of reaction • more vaporization loss • more corrosive
DEA	<ul style="list-style-type: none"> • less reactive with COS and CS₂, suitable for gas streams with appreciable amount of these components • low vapour pressure benefits the low-pressure operations 	<ul style="list-style-type: none"> • vacuum distillation is required for reclaiming contaminated solutions • undergoes many irreversible reactions with CO₂, forming corrosive degradation products
MDEA	<ul style="list-style-type: none"> • higher capacity to absorb CO₂ • less volatile than DEA and MEA • lower energy demand for strippers • lower vapour pressure leads to smaller losses of solvent • does not degrade readily 	<ul style="list-style-type: none"> • slow rate of reaction with CO₂

The most frequently used alkanolamines include monoethanolamine (MEA), diethanolamine (DEA), and methyldiethanolamine (MDEA). The advantages and

disadvantages for various amines are summarized in Table 9.1. Due to some complementing features, different amines are usually blended to achieve the optimum performance when dealing with different gases. However, the corrosive characteristics of primary and secondary amines limit their fraction to below 20wt% MEA and 35wt% DEA respectively while the milder MDEA can be up to 50wt%.

Figure 9.1 shows a conventional process for CO₂ removal and recovery. The feed gas stream and the lean amine coming from the stripper contact countercurrently in the gas absorber, which is usually a packed bed or tray column. The amine is loaded with CO₂ when travelling down the column and leaves the bottom as a rich amine stream. After exchange heat with the lean amine, the hot rich amine is pumped to the top of the stripper, contacting with the stream from the reboiler at a reduced pressure (1-2atm) and elevated temperature (100-120°C), where the reaction of CO₂ with amines is reversed and pure CO₂ recovered. The lean amine solution is then pumped through the heat exchanger, where it is cooled and reused in the absorber (Oyenekan and Rochelle, 2006).

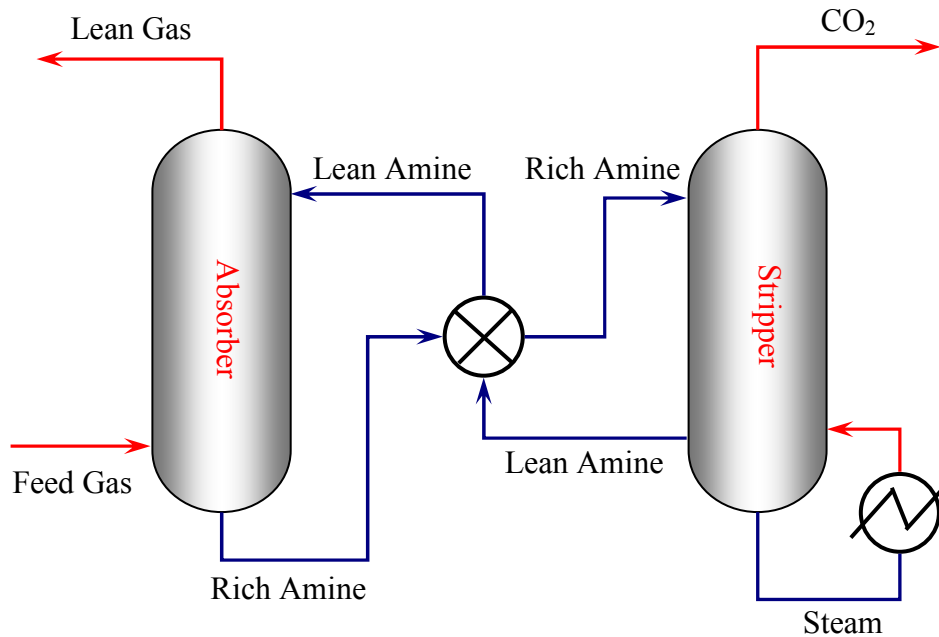


Figure 9.1 Conventional process flow diagram of CO₂ removal and recovery

In conventional process, problems such as flooding, channelling and foaming can be encountered (Feron and Jansen, 2002), leading to varying mass transfer regimes and problems for operation. The size of the units makes heat management difficult, which results in reaction rate variations due to uneven distribution of temperature. The accumulated heat along the absorber also contributes to solvent degradation which gradually reduces the capturing ability of the solvent in the recycle loop. In addition, the

dominant operating cost is the steam needed to run the reboiler of the stripping unit, which can account up to 90% of the total process energy requirements (Tobiesen and Svendsen, 2006).

To better address the problem of CO₂ capture and storage, new technologies are in great demand that should have the following potential benefits:

- Improve mass and heat transfer efficiency and uniformity between gas and liquid phase. Given that the reaction between CO₂ and amine solution is rather fast, mass transfer could be the rate limiting step during absorption and desorption. New contacting principles that provide large and stable contacting interface and improved mixing are potential solutions.
- Improve heat transfer and heat management. This helps to reduce solvent degradation in the absorber, intensify heat supply in stripper and improve heat exchanger efficiency.
- Increase solvent utilization efficiency, thus reducing the size of scrubbing plant and cost.

With the advent of microreaction technology, novel contacting principles and phase contactors/reactors have become available (Section 2.6.1). Microstructured reactors extend the range of capabilities of conventional systems especially in terms of enhanced mass and heat transfer mostly due to their large surface-to-volume ratio. Besides, sub-millimetre length scale shortens the diffusion time to sub-millisecond and can reduce concentration gradients and mixing length. As a result, microstructured reactors are particularly suitable for fast reactions that can be mass transfer limited.

9.2 System characterization

9.2.1 Operating conditions

The component and flowrate of feed gas and liquid phase is listed in Table 9.2. The CO₂ inlet fraction and exit concentration is 2.28% and 50ppm respectively, with the latter corresponding to a CO₂ conversion of 99.8%. Q_G and Q_L are the total gas and liquid volumetric flowrate respectively. The volumetric flowrate ratio of gas to liquid is 20.37, which for gas/liquid flow in a small channel corresponds to the operating line shown in Figure 9.2 (red dashed line). It can be seen that the system can be operated under Taylor, churn and Taylor-annular flow regimes. These flow patterns have been discussed in detail in Section 2.2. Since very small liquid volume fraction (around 5%) characterises the current system, the Taylor flow formed will appear as very long bubble and very

short liquid slug as seen in Figure 9.3. Hence, the film region will be the primary interface for the reaction. Therefore, this chapter starts with an investigation of falling film microreactor. The results will provide more information for reactions at the film region and an insight for the performance of other microreactors.

Table 9.2 Gas and liquid flow conditions that feed to the CO₂ absorber.

	Components	lbmol/h	mol/s	m ³ /s	mol/l	kg/s
Gas	H ₂	33	4.2	0.0016	0.0011	0.0083
	N ₂	3092	389.6	0.14	0.098	10.91
	CO ₂	1879.9	236.9	0.09	0.06	10.42
	H ₂ S	379.3	47.8	0.018	0.012	1.62
	H ₂ O	133.1	16.8	0.0064	0.0042	0.31
	CH ₄	69705.7	8782.9	3.34	2.22	140.53
	C ₂ H ₆	4411.2	555.8	0.21	0.14	16.67
	C ₃ H ₈	1632.6	205.7	0.078	0.052	9.05
	N-C ₄	1321	166.4	0.063	0.042	10.32
	Total	82587.8	10406.1	3.95	2.63	199.84
Liquid	H ₂ O	40371.6	5086.8	0.09	26.2	91.56
	CO ₂	70.5	8.9	0.00038	0.046	0.39
	H ₂ S	2.7	0.3	1.1E-05	0.0018	0.012
	MDEA	7054.8	888.9	0.1	4.58	105.78
	Total	47499.6	5984.9	0.19	30.83	197.74

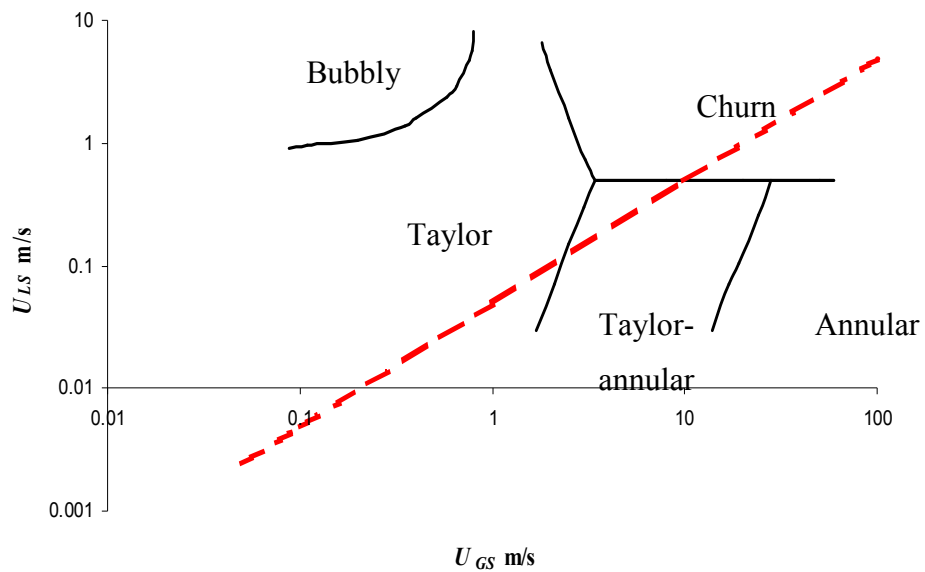


Figure 9.2. Possible flow patterns for the system under investigation. Based on the flow map of Triplett et al. (1999).

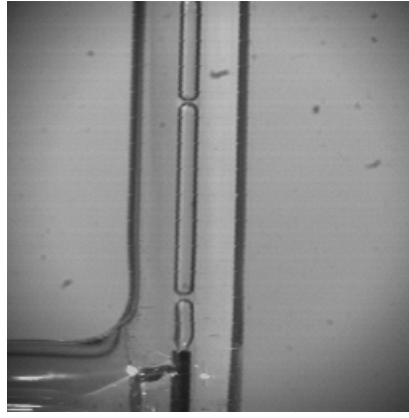


Figure 9.3. Representative Taylor bubble captured in a system with similar operating flowrates. $d = 1\text{mm}$, 20vol% CO_2 , 0.2M NaOH, $U_{GS} = 0.17\text{m/s}$, $U_{LS}/U_{GS} = 0.052$.

9.2.2 Reaction system

The reaction between CO_2 and tertiary amines are different from that with primary and secondary amine because CO_2 can not combine with the amine group directly, which results in lower rate of reaction compared to that with primary and secondary amines.

Donaldson and Nguyen (1980) proposed that the reaction mechanism between CO_2 and tertiary alkanolamines was a base catalyzed hydration process, reaction (i). Reactions (ii) ~ (v) also occur.



In most of the literature, the kinetics of CO_2 absorption in MDEA have been assumed to be pseudo-first order reaction (Blauwhoff et al., 1984; Haimour et al., 1987; Tomcej and Otto, 1989). However, great discrepancies on rate coefficient existed and an overestimation of the contribution of reaction (ii) has been suggested to be one of the reasons (Lettel et al., 1990). Rinker et al. (1995) examined the kinetics by both experiments and modeling, and reported that the contribution of reaction (ii) could neither be neglected nor could its rate expression be assumed to be pseudo-first order, otherwise the k_1 value obtained would be seriously overestimated especially at high temperature.

All reactions ((i)-(v)) are considered to be reversible. Reaction (i) and (ii) have finite reaction rate, which is given in Eq. 9.1 and Eq. 9.2. Reactions (iii) ~ (v) are types of proton transfer and are assumed to be instantaneous and at equilibrium. Based on a model that assumes all the above reactions are reversible, Rinker et al. (1995) proposed a rate constant, Eq. 9.3, for reaction (i) for the temperature range of 293-342K in 10wt% MDEA solution. This kinetic expression will be employed in this study initially, even though the mass fraction of MDEA is much larger (53.5wt%).

$$R_1 = -k_1[CO_2][R_3N] + \frac{k_1}{K_1}[R_3NH^+][HCO_3^-] \quad \text{Eq. 9.1}$$

$$R_2 = -k_2[CO_2][OH^-] + \frac{k_2}{K_2}[HCO_3^-] \quad \text{Eq. 9.2}$$

$$k_1 = 2.91E7 \exp\left(\frac{-4579}{T}\right) \quad \text{Eq. 9.3}$$

The value of k_2 is determined from the correlation of Pinsent et al. (1956):

$$k_2 = 10^{\left(13.635 - \frac{2895}{T}\right)} \quad \text{Eq. 9.4}$$

The value of equilibrium constant K_2 to K_5 is determined according to Eq. 9.5 with coefficients A , B , and C given in Table 9.3. K_1 is obtained from component balance, $K_1 = K_2/K_4$ (Rinker et al., 1995). In the present study, **only reaction (1) is considered in the simulations.**

$$\ln K_i = A + \frac{B}{T} + C \ln T \quad \text{Eq. 9.5}$$

Table 9.3. Coefficients in Eq. 9.5 used to calculate K_i for MDEA kinetics

K_i	A	B	C	Value at 320.4K
K_2	231.5	-12092.1	-36.8	9.3E-9
K_3	216.1	-12431.7	-35.5	1.2E-12
K_4	-56.2	-4044.8	7.8	6.0E-11
K_5	132.9	-13445.9	-22.5	1.5E-17

Reaction (i) is a reversible reaction and chemical equilibrium will be achieved after some time. Eq. 9.6 shows a “virtual” concentration of transferred CO_2 from the gas to liquid phase, which has been transformed to produce $MDEAH^+$ and HCO_3^- according to reaction (i). When R_1 is set to zero, Eq. 9.7 is obtained. The equilibrium concentration of each component is given in Eq. 9.8 to Eq. 9.10. By combining Eq. 9.6 to Eq. 9.10, the equilibrium conversion X_e can be calculated, and has a value of 93.4% for operating

conditions given in Table 9.2. Deviations could exist because the average CO₂ concentration in the liquid domain takes the value of that at the gas-liquid interface as shown in Eq. 9.8. The level of deviation will depend on the mass transfer in the liquid slug.

$$C_{CO_2(G \rightarrow L)} = -\frac{N_{CO_2(G \rightarrow L)}}{V_L} = \frac{C_{CO_2(G),0} Q_G X_e}{Q_L} \quad \text{Eq. 9.6}$$

$$K_1 [CO_2(L)]_e [MDEA]_e = [MDEAH^+]_e [HCO_3^-]_e \quad \text{Eq. 9.7}$$

$$[CO_2(L)]_e = HeP_{CO_2(G),e} = HeRTC_{CO_2(G),0}(1 - X_e) \quad \text{Eq. 9.8}$$

$$[MDEA]_e = C_{MDEA,0} - C_{CO_2(G \rightarrow L)} \quad \text{Eq. 9.9}$$

$$[MDEAH^+]_e = [HCO_3^-]_e = C_{CO_2(G \rightarrow L)} \quad \text{Eq. 9.10}$$

9.2.3 Physical properties

9.2.3.1 Gas phase

The gas phase density is valued by assuming an ideal gas mixture as in Eq. 9.11, where M is the molecular weight and z is the mole fraction.

$$\rho_G = \frac{P \sum_i z_i M_i}{RT} \quad \text{Eq. 9.11}$$

The gas phase viscosity is calculated by Eq. 9.12 (Wilke, 1950), where Φ is a dimensionless constant as defined in Eq. 9.13 with i and j are any two components in the mixture.

$$\mu_G = \sum_{i=1}^n \frac{\mu_i}{1 + \frac{1}{z_i} \sum_{\substack{j=1 \\ j \neq i}}^n z_j \Phi_{ij}} \quad \text{Eq. 9.12}$$

$$\Phi_{ij} = \frac{\left[1 + \left(\mu_i / \mu_j \right)^{0.5} \left(M_j / M_i \right)^{0.5} \right]^2}{\left(4 / \sqrt{2} \right) \left[1 + M_i / M_j \right]^{0.5}} \quad \text{Eq. 9.13}$$

CO₂ diffusivity in the gas phase mixture is taking the value from Zanfir et al. (2005).

9.2.3.2 Liquid phase

The density, viscosity and surface tension are taking values from [Rinker et al. \(1994\)](#) for 50wt% MDEA.

The solubility and diffusivity of CO₂ in aqueous MDEA solutions are estimated using the N₂O analogy technique. The Henry's law constant and diffusivity of CO₂ and N₂O in MDEA and pure water are related by the following equations:

$$\frac{He_{CO_2}^{MDEA}}{He_{CO_2}^W} = \frac{He_{N_2O}^{MDEA}}{He_{N_2O}^W} \quad \text{Eq. 9.14}$$

$$\frac{D_{CO_2}^{MDEA}}{D_{CO_2}^W} = \frac{D_{N_2O}^{MDEA}}{D_{N_2O}^W} \quad \text{Eq. 9.15}$$

where *W* refers to pure water. The value of $He_{CO_2}^W$ and $D_{CO_2}^W$ can be calculated from Eq. 9.16 ([Rinker et al., 1995](#)) and Eq. 9.17 ([Tamimi et al., 1994a](#)) respectively. Henry's constant of N₂O in pure water and MDEA use the value from [Tamimi et al. \(1994b\)](#) for a 30wt% MDEA aqueous solution.

$$He_{CO_2}^W = 23314 \exp\left(\frac{-1984.8}{T}\right) \quad \text{Eq. 9.16}$$

$$D_{CO_2}^W = 3.0654E^{-6} \exp\left(\frac{-2196.1}{T}\right) \quad \text{Eq. 9.17}$$

The diffusivity of MDEA in the liquid solution is correlated as in Eq. 9.18 ([Rinker et al., 1995](#)). The diffusivity of other ions are assumed to be equal to that of MDEA.

$$D_{MDEA}^L = 4.682E^{-14} \mu_L^{-0.569842} T \quad \text{Eq. 9.18}$$

The operating temperature and pressure and the values of physical properties are summarized in Table 9.4.

Table 9.4. Operating conditions for the reaction system

	Gas phase	Liquid phase
Temperature <i>T</i> [K]	313	320.4
Pressure <i>P</i> [atm]	67.46	67.25
Density ρ [kg/m ³]	50.54	1018.5
Viscosity μ [Pa s]	1.1E-5	2.57E-3
Diffusivity <i>D</i> [m ² /s]	$D_{CO_2}^G = 1.63E-5$	$D_{CO_2}^L = 1.40E-9$ $D_{MDEA}^L = 4.49E-10$
Henry's law constant <i>He</i> [atm m ³ /mol]	-	0.045
Reaction rate <i>k_l</i> [m ³ /(kmol s)]	-	18.1

9.3 Falling film reactor

Falling film is characterized by the motion of a thin layer of liquid over a solid surface under gravity. Advantages include excellent heat removal and reduced mass transfer resistance in the liquid side. It has been widely used as gas-liquid contactor, especially for reactions like sulfonation, chlorination, ethoxylation or hydrogenation (Section 2.6.1.1). The interfacial area for falling film reactors could be from 300 to 600 m²/m³ for conventional units (Farrauto and Bartholomew, 1997), while values larger than 10000 m²/m³ for a less than 100µm film are available in microreactors (Hessel et al., 2000).

In this section, a two dimensional model for both gas and liquid phase is formulated for CO₂ absorption into MDEA solutions. The model is firstly validated against the results from a similar system for CO₂ absorption (Zanfir et al., 2005). Then sensitivity studies on the reactor performance of gas and liquid film thickness, reaction rate, and MDEA concentration are carried out.

9.3.1 Model formulation

The falling film microreactor is designed to consist of plates of 4m width and an adjustable height packed in parallel (Figure 9.4). The dimensions are chosen according to the size of the conventional packed bed, which is 4.3m in diameter. The number of plates depends on the gas chamber size between two plates. Initially a plate thickness of 0mm is considered. No heat exchange plates are considered. Only one plate-gas chamber unit is studied in the simulations and a 2D area in the unit cross section is selected as the solution domain (Figure 9.5). The following assumptions apply:

- Uniform flow distribution is achieved among plates and gas chambers
- Uniform mass transfer and reaction along the plate width direction
- Isothermal reaction
- No axial and radial velocity distribution in either gas or liquid phase i.e. average velocity is applied over the domain
- Negligible physical property changes in gas phase and mass change in liquid phase resulted from CO₂ absorption due to its low volume fraction (2.28%)
- Negligible axial diffusion in both gas and liquid phase

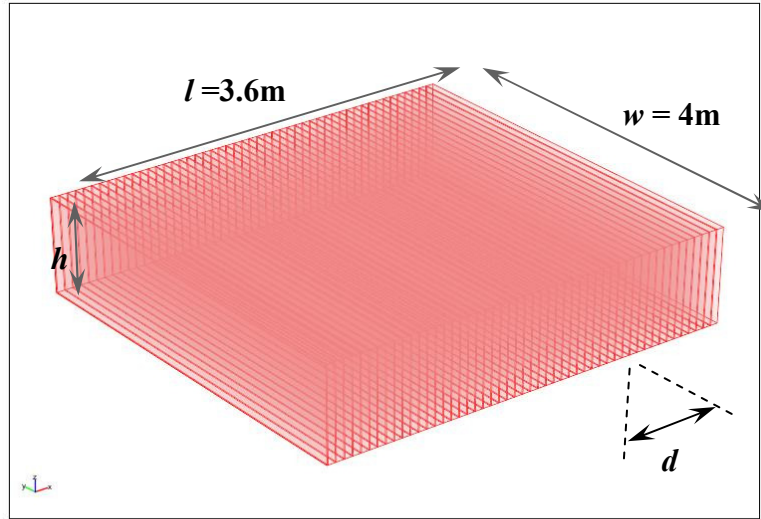


Figure 9.4. 3D view of a falling film microreactor that consists of a number of plates of 4m width, zero thickness and adjustable height, which are packed in parallel.

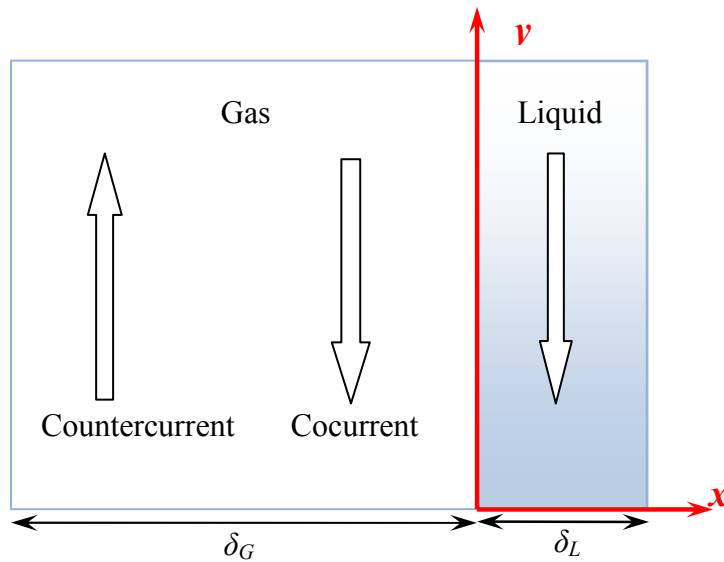


Figure 9.5. Simulation domains and boundaries for the falling film microreactor. The scale has been adjusted for better visualization.

The liquid film thickness (Eq. 9.21) is determined when coupling equations Eq. 9.19 and Eq. 9.20 (Bird et al., 2002), with either of which the average liquid velocity can be obtained. δ_L is film thickness, Q volumetric flowrate, n number of plates, w the width of each plate and v the average velocity.

$$v_L = \frac{\rho_L g \delta_L^2}{3\mu_L} \quad \text{Eq. 9.19}$$

$$v_L = \frac{Q_L}{nw\delta_L} \quad \text{Eq. 9.20}$$

$$\delta_L = \sqrt[3]{\frac{3Q_L\mu_L}{nw\rho_L g}} \quad \text{Eq. 9.21}$$

The average gas velocity is determined as Eq. 9.22 with δ_G the depth of gas chamber.

$$v_G = \frac{Q_G}{nw\delta_G} \quad \text{Eq. 9.22}$$

The reaction conversion X can be calculated from Eq. 9.23, where the CO_2 outlet concentration is averaged over the grid volume at the outlet of the gas domain.

$$X = \left(1 - \frac{\sum_{i,\text{outlet}} \text{vol}_i C_{\text{CO}_2(\text{G})}}{\sum_{i,\text{outlet}} \text{vol}_i C_{\text{CO}_2(\text{G})\text{inlet}}} \right) \quad \text{Eq. 9.23}$$

Model details including governing equations, initial conditions and boundary conditions for each domain are presented in Table 9.5 and Table 9.6 respectively. The gas phase average velocity is assigned positive value for countercurrent and negative value for cocurrent operations.

Table 9.5 2D model details in liquid domain for the falling film microreactor

Variables	C_i with $i = \text{CO}_2(\text{L}), \text{MDEA}, \text{MDEA}^+, \text{HCO}_3^-$	
Governing equations	$-D_i \frac{\partial^2 C_i}{\partial x^2} + v_L \frac{\partial C_i}{\partial y} - R_i = 0$	
Reaction term	$R_i = \begin{cases} -k_1 C_{\text{CO}_2(\text{L})} C_{\text{MDEA}} + \frac{k_1}{K_1} C_{\text{MDEA}^+} C_{\text{HCO}_3^-} & \text{for } i = \text{CO}_2(\text{L}), \text{MDEA} \\ k_1 C_{\text{CO}_2(\text{L})} C_{\text{MDEA}} - \frac{k_1}{K_1} C_{\text{MDEA}^+} C_{\text{HCO}_3^-} & \text{for } i = \text{MDEA}^+, \text{HCO}_3^- \end{cases}$	
Initial conditions	$C_{\text{CO}_2(\text{L})} = 0 \text{ mol/l}, C_{\text{MDEA}} = C_{\text{MDEA}^+} = C_{\text{HCO}_3^-} = 0 \text{ mol/l}$	
Boundary conditions	Inlet	$C_{\text{MDEA}} = 4.578 \text{ kmol/m}^3, C_i = 0 \text{ with } i \neq \text{MDEA}$
	Outlet	$\frac{\partial C_i}{\partial y} = 0$
	Wall	$\frac{\partial C_i}{\partial x} = 0$
	Gas-liquid interface	$C_{\text{CO}_2(\text{L})} = \text{HeRT} C_{\text{CO}_2(\text{G})}$ $\frac{\partial C_i}{\partial x} = 0 \text{ with } i \neq C_{\text{CO}_2(\text{L})}$

Table 9.6. 2D model details in gas domain for the falling film reactor

Variables	$C_{CO_2(G)}$	
Governing equations	$-D_G \frac{\partial^2 C_{CO_2(G)}}{\partial x^2} + v_G \frac{\partial C_{CO_2(G)}}{\partial y} - R_G = 0$	
Reaction term	$R_G = 0$	
Initial conditions	$C_{CO_2(G)} = 0.0598 \text{ mol/l}$	
Boundary conditions	Inlet	$C_{CO_2(G)} = 0.0598 \text{ mol/l}$
	Outlet	$\frac{\partial C_{CO_2(G)}}{\partial y} = 0$
	Wall	$\frac{\partial C_{CO_2(G)}}{\partial x} = 0$
	Gas-liquid interface	$C_{CO_2(L)} = HeRT C_{CO_2(G)}$

9.3.2 Model validation

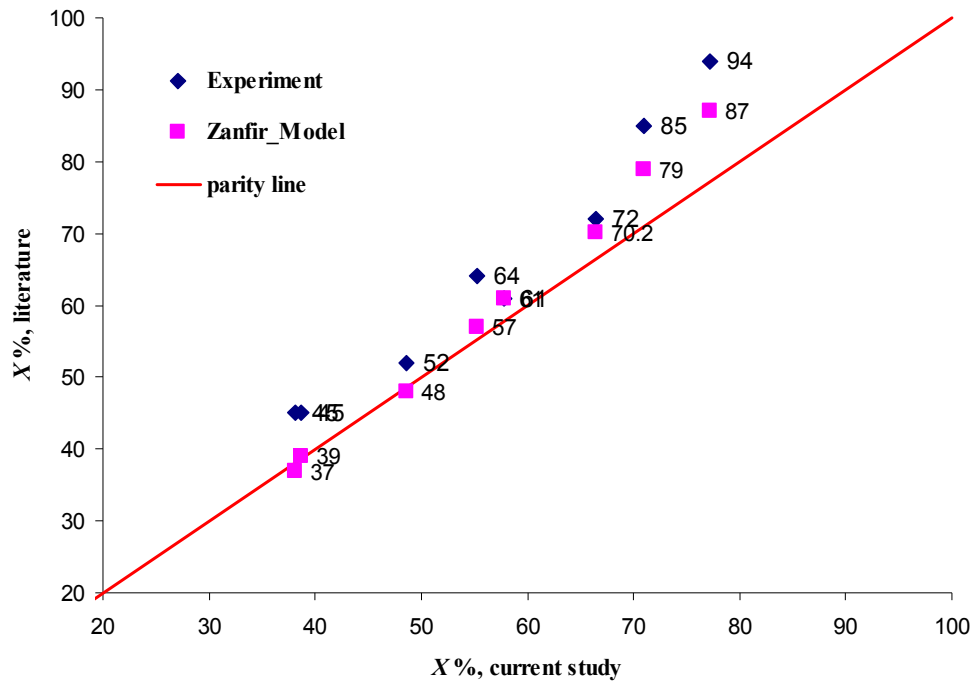


Figure 9.6 Model validation using the experimental and analytical modelling results from [Zanfir et al. \(2005\)](#).

The model described above is validated using results from [Zanfir et al. \(2005\)](#), who studied the CO₂ absorption in NaOH solutions using a falling film microreactor. The

reactor is a metal plate with 64 open top microchannels measured 300 μm wide, 100 μm deep and 66.4mm long and the gas chamber depth is 5.5mm. Low CO₂ mole fraction cases ($\leq 8\%$) at different NaOH concentrations are selected as benchmarks because changes in physical properties and mass due to CO₂ absorption are small. The reaction kinetics is discussed in Section 7.2. CO₂ absorption into NaOH solutions is a very fast process with the initial reaction rate ranging from 24.19 to 557.07kmol/(m³s) for NaOH concentrations from 0.1M to 2M. The comparison is plotted in Figure 9.6 with very good agreement at low CO₂ conversion cases. The deviation at higher conversion could be due to the gradually improper assumptions used in the current model, such as constant gas phase velocity and negligible physical property changes in gas phase.

9.3.3 Preliminary results and discussions

9.3.3.1 Base case characterization

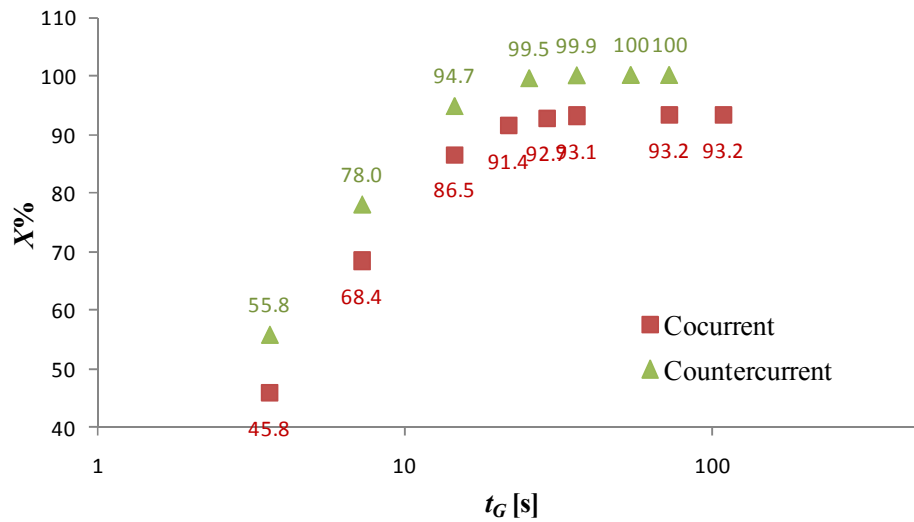
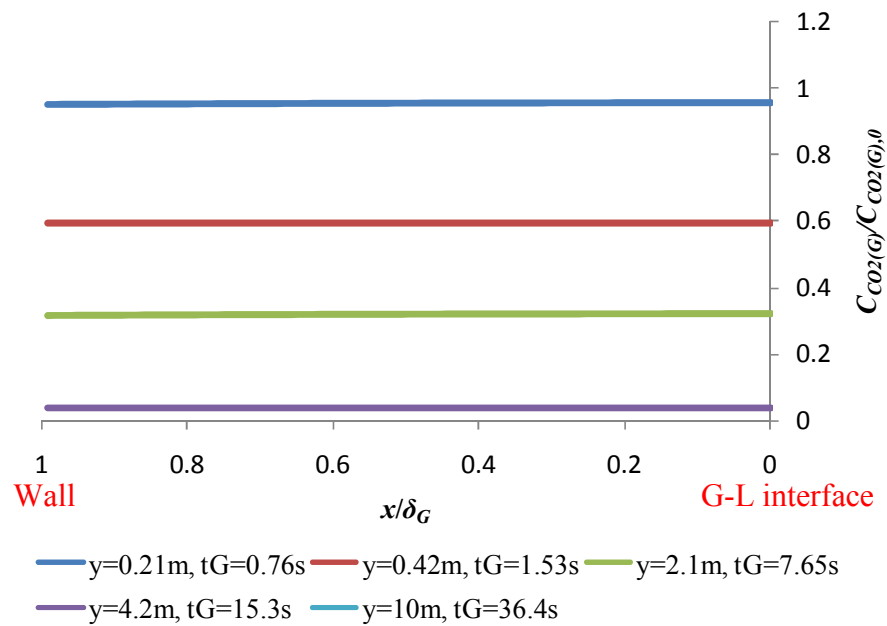


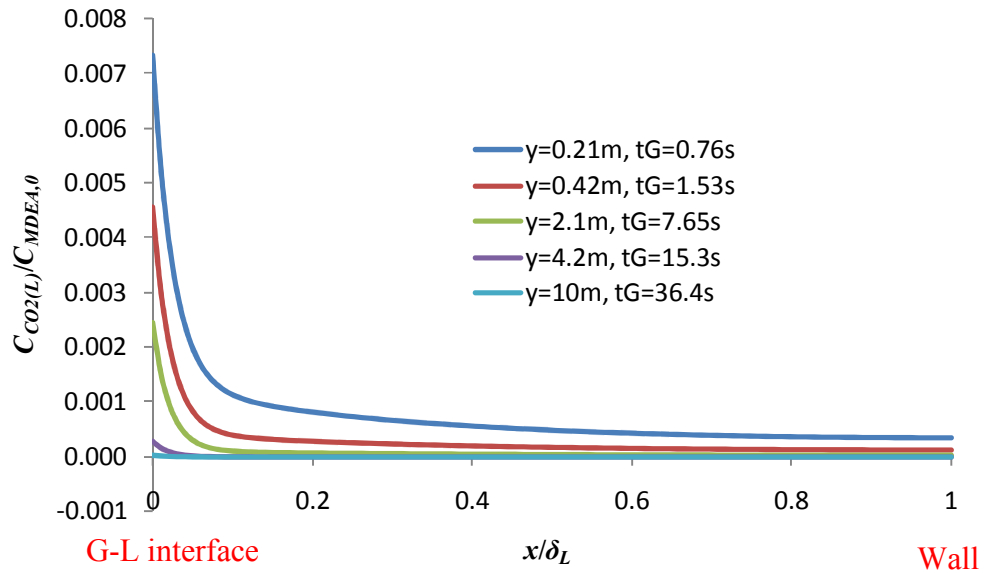
Figure 9.7 CO₂ conversion at different gas residence time in both co- and counter-currently operated falling film reactor. $\delta_G = 1\text{mm}$, $\delta_L = 218\mu\text{m}$, $k_l = 18.1\text{m}^3/(\text{kmol s})$, $C_{MDEA,0} = 4.578\text{kmol/m}^3$, $Q_L = 0.194\text{m}^3/\text{s}$, $Q_G = 3.954\text{m}^3/\text{s}$.

A gas chamber depth of 1mm is initially studied. When film thickness and plate thickness are not taken into account, the number of plates is determined to be 3600 according to Figure 9.4. The reactor then will provide a specific surface area of 1000m²/m³. The height of the reactor depends on the gas phase residence time to achieve the conversion specification. As seen in Figure 9.7, conversions in the reactor operated countercurrently always exceed those in one operated cocurrently. The countercurrent reactor achieves 99.9% conversion after $t_G = 36.4\text{s}$ (a reactor height of

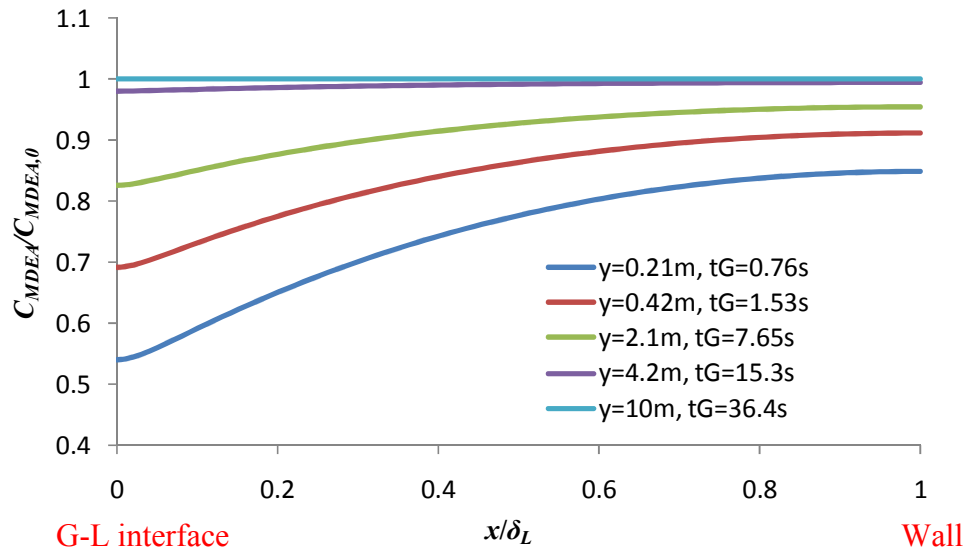
10m) while the cocurrent one, however, reaches equilibrium conversion of 93.2% after $t_G = 72.8s$ (a reactor height of 20m). From the transversal concentration profiles in the countercurrent reactor (Figure 9.8), there is no concentration gradient in the gas phase (Figure 9.8a) and the liquid phase reactant MDEA is consumed much quicker at the initial part of the reactor when CO_2 concentration is relatively high (Figure 9.8c). As CO_2 moves along the reactor, the concentration gradient for MDEA decreases and approaches the bulk value after about 15s ($h = 4.2m$) as a result of decreasing CO_2 concentration in the liquid (Figure 9.8b). Figure 9.8c shows that there is enough amount of MDEA in the system as at least 50% of MDEA still remains even at the fastest reaction rate at the beginning.



(a)



(b)



(c)

Figure 9.8 Transversal concentration profiles in countercurrent falling film reactor at different reactor height. (a) $C_{CO_2(G)}$; (b) $C_{CO_2(L)}$; (c) C_{MDEA} . $\delta_G = 1\text{mm}$, $\delta_L = 218\mu\text{m}$, $h = 10\text{m}$, $k_l = 18.1\text{m}^3/(\text{kmol s})$, $C_{MDEA,0} = 4.578\text{kmol/m}^3$, $Q_L = 0.194\text{m}^3/\text{s}$, $Q_G = 3.954\text{m}^3/\text{s}$.

Therefore, to achieve the specified CO_2 conversion ($X\% > 99.78\%$) in 53.5wt% MDEA under the operating conditions given in Table 9.2 and an initial reaction rate is $2.86\text{ kmol}/(\text{m}^3\text{ s})$ ($k_l = 18.1\text{m}^3/(\text{kmol s})$, $C_{MDEA,0} = 4.578\text{mol/l}$), the falling film reactor should be operated countercurrently and measure $4\text{m(w)} \times 3.6\text{l} \times 10\text{m(h)}$. When the gas chamber depth is designed to be 1mm , 3600 plates are requires to be operated in parallel. The rest of the falling film reactor study will focus on the sensitivity of the reactor performance on various parameters like gas and film thickness, reaction rate and MDEA

concentration. To save computational cost, a countercurrently operated unit with a 1mm gas chamber and 1m plate height is considered as the base case (Table 9.7). The Fourier number of the system (Eq. 9.24) is much larger than 1, indicating that CO₂ has more than enough time to travel to the gas-liquid interface before it leaves the reactor. The sensitivity study based on the base case aims to compare reactor performance, thus whether the conversion specification will be met or not will not be taken into account.

$$Fo = \frac{t_G}{\tau_D} = \frac{l}{v_G} \frac{D_{CO_2}^G}{\delta_G^2} = \frac{1}{0.275} \frac{(1.63E^{-5})}{(0.001)^2} = 59.27 \quad \text{Eq. 9.24}$$

9.3.3.2 Effect of liquid film thickness

Table 9.7 Sensitivity study cases and their parameters for the countercurrent falling film reactor. $k_L = 18.1 \text{ m}^3/(\text{kmol s})$.

No.	δ_G [m]	h [m]	v_G [m/s]	t_G [s]	Q_L [m ³ /s]	$\delta_L \times 10^6$ [m]	v_L [m/s]	t_L [s]	$X\%$ [-]	Ψ [-]
bas	0.001	1.00	0.26	3.64	0.19	218	0.062	16.2	55.78	680.5
e										
1	0.001	2.18	0.6	3.64	0.19	100	0.14	16.2	55.22	673.7
2	0.001	0.55	0.15	3.64	0.19	400	0.034	16.2	55.85	681.4
3	0.001	0.64	0.18	3.64	0.1	175	0.04	16.2	55.80	1322
4	0.001	1.62	0.45	3.64	0.4	278	0.1	16.2	55.85	330.7
5	0.003	1.0	0.28	3.64	0.19	315	0.13	7.78	48.82	595.6
6	0.005	1.0	0.28	3.64	0.19	373	0.18	5.54	46.00	561.2
7	0.01	1.0	0.28	3.64	0.19	470	0.29	3.49	39.17	477.9

Two approaches are applied in this section to investigate the effect of film thickness. Firstly, without changing the liquid flowrate, two assumed cases 1 and 2 with film thickness of 100μm and 400μm respectively are chosen to compare the reactor performance with that of a predicted 218μm of base case. Secondly, liquid flowrate are adjusted to be 0.1 and 0.4m³/s respectively (case 3 and 4) and film thickness changes accordingly. In both approaches, the reactor height h and gas phase velocity v_G are adjusted to ensure that all cases are compared with the same liquid and gas phase residence time (Table 9.7). A utilization factor (Eq. 9.25), representing the amount of CO₂ absorbed per unit volume of solution in the reactor, is used to compare the reactor performance.

$$\psi = \frac{F_{CO_2}^{in} - F_{CO_2}^{out}}{Q_L^{in}} = \frac{F_{CO_2}^{in} X}{F_{MDEA}^{in}/C_{MDEA}^{in}} = \frac{F_{CO_2}^{in}}{F_{MDEA}^{in}} C_{MDEA}^{in} X \quad \text{Eq. 9.25}$$

No significant difference in X and ψ is observed in cases 1 and 2 compared with the base case (Table 9.7). The fact that CO_2 is consumed or reach equilibrium within 60% of the liquid film (Figure 9.8b) explains the small effect of film thickness on X when 400 μ m film is used. In the case of 100 μ m film, which is less than 60% of 218 μ m, concentration build up along the radial direction is noticed (Figure 9.9). However, the deviation from the base case conversion is trivial (1% based on data in Table 9.7). Because of the same reason, little effect of liquid flowrate on X is observed (Table 9.7, case 3 and 4). However, increasing liquid flowrate brings significant decline in utilization factor, demonstrating that most of amine does not play a role. The above observations indicate that the small effect of film thickness on reactor performance eases out the concern coming either from the incorrect film thickness prediction or from the uneven film spread on the plate surface. On the other hand, the MDEA solvent flowrate can be decreased by 78% with an associated film thickness that is 60% of the base case (Eq. 9.22) in the current reaction system without influencing the reactor performance. However, how this depends on correct kinetics and equilibrium conditions warrants further investigation.

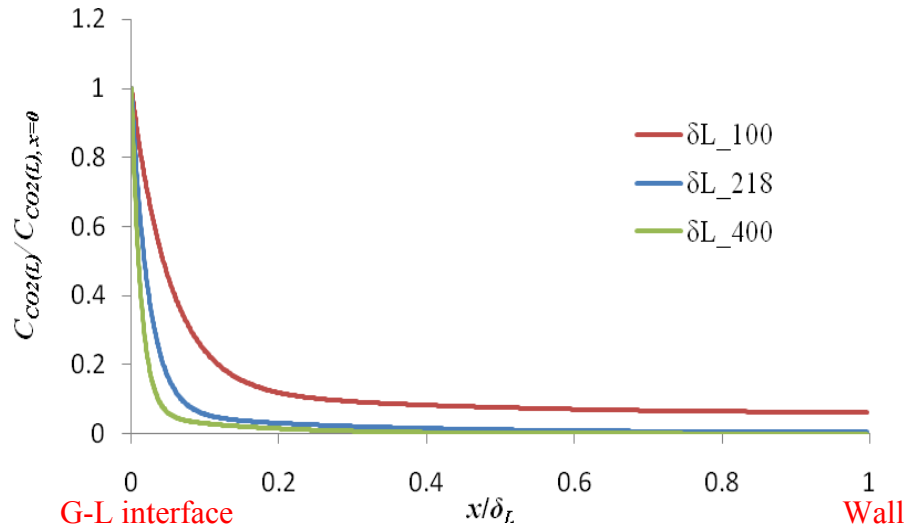


Figure 9.9 Transverse CO_2 profiles at reactor outlet for various film thicknesses. $\delta_G = 1\text{mm}$, $h = 1\text{m}$, $k_l = 18.1\text{ m}^3/(\text{kmol s})$, $C_{MDEA,0} = 4.578\text{kmol/m}^3$, $Q_L = 0.194\text{m}^3/\text{s}$, $Q_G = 3.954\text{m}^3/\text{s}$.

9.3.3.3 Effect of gas film thickness

To see how gas chamber size affects the reaction, a smaller number of plates – 1200 ($a = 333\text{m}^2/\text{m}^3$), 720 ($a = 200\text{m}^2/\text{m}^3$), and 360 ($a = 100\text{m}^2/\text{m}^3$) - are used, which form gas

chamber sizes of 3mm, 5mm, and 10mm respectively (case 5, 8 and 7 in Table 9.7). As the overall gas phase cross sectional area (lxw) remains the same, v_G and t_G do not change. A modification in liquid film thickness and residence time is necessary. The results in Figure 9.10 show that increasing the gas chamber depth lead to reduced CO₂ conversion and liquid utilization. Smaller specific area and less liquid residence time mostly explain these given that liquid film thickness has little effect on the reactor performance as seen in Section 9.3.3.2.

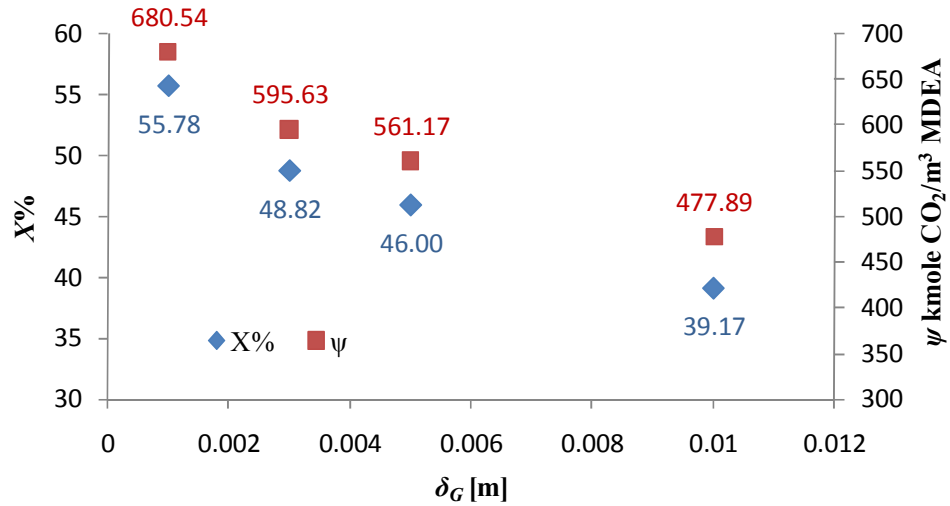


Figure 9.10 Effect of gas chamber size on CO₂ conversion in falling film reactor. $h = 1\text{m}$, $k_l = 18.1\text{m}^3/(\text{kmol s})$, $C_{MDEA,0} = 4.578\text{kmol/m}^3$, $Q_L = 0.194\text{m}^3/\text{s}$, $Q_G = 3.954\text{m}^3/\text{s}$.

9.3.3.4 Effect of MDEA concentration

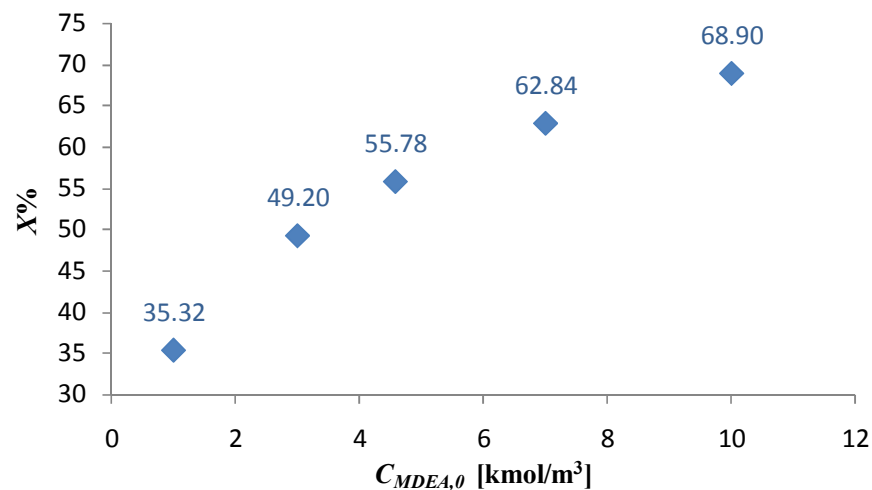


Figure 9.11. Effect of MDEA concentration on CO₂ conversion. $\delta_G = 1\text{mm}$, $\delta_L = 218\mu\text{m}$, $h = 1\text{m}$, $k_l = 18.1\text{m}^3/(\text{kmol s})$, $Q_L = 0.194\text{m}^3/\text{s}$, $Q_G = 3.954\text{m}^3/\text{s}$, $P = 67.46\text{atm}$, $T = 320.4\text{K}$.

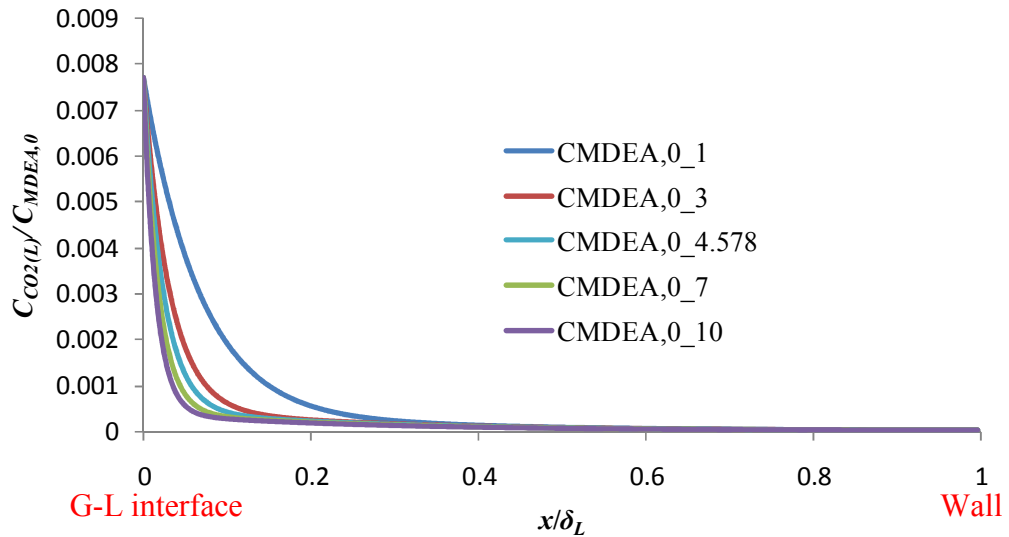


Figure 9.12 Transverse dimensionless CO_2 profiles at liquid phase outlet for various inlet MDEA concentrations. $\delta_G = 1\text{mm}$, $\delta_L = 218\mu\text{m}$, $h = 1\text{m}$, $k_I = 18\text{m}^3/(\text{kmol s})$, $Q_L = 0.194\text{m}^3/\text{s}$, $Q_G = 3.954\text{m}^3/\text{s}$, $P = 67.46\text{atm}$, $T = 320.4\text{K}$.

Based on the base case, the effect of MDEA concentration on the reactor performance is investigated. It is shown in Figure 9.11 that higher MDEA concentration is beneficial to the reaction by providing higher conversion at the outlet. On one hand higher MDEA concentration leads to higher reaction rate (Section 9.3.3.1); on the other hand it increases the ionic strength of the liquid phase which also increases the reaction rate (Rinker et al., 1995) although this has not been considered in the current study (Eq. 9.3). As shown in Figure 9.12, the higher the MDEA concentration, the sooner the CO_2 is depleted in the liquid film. At an inlet MDEA concentration of 1M and 10M, the CO_2 is consumed below 1% of the interfacial concentration within 63% and 45% of film thickness respectively.

9.3.3.5 Effect of reaction rate constant

The reaction rate between MDEA (tertiary amine) with CO_2 is much slower compared with primary and secondary amines and it is common in industry to use a blend of them to achieve better reactor performance. Liao and Li (2002) studied the kinetics of CO_2 absorption in a blend of MEA and MDEA and reported substantial increase in CO_2 absorption rate. For example, adding a small amount of MEA (0.5mol/l) to 1.5mol/l MDEA aqueous solution, a ten-fold enhancement in CO_2 absorption rate was observed because the kinetics had coupled the fast reaction between CO_2 and MEA.

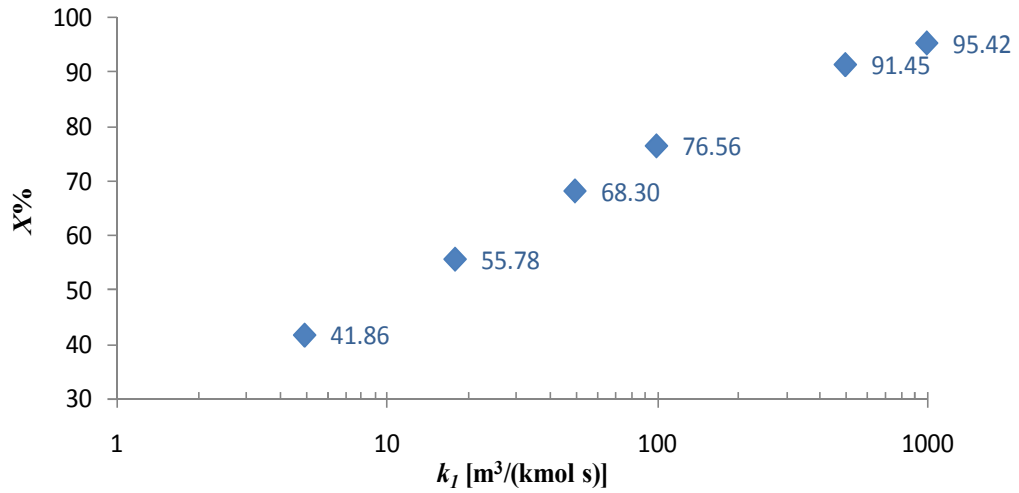


Figure 9.13 Effect of reaction rate constant on CO₂ conversion. $\delta_G = 1\text{mm}$, $\delta_L = 218\mu\text{m}$, $h = 1\text{m}$, $C_{MDEA} = 4.578\text{kmol}/\text{m}^3$, $Q_L = 0.194\text{m}^3/\text{s}$, $Q_G = 3.954\text{m}^3/\text{s}$.

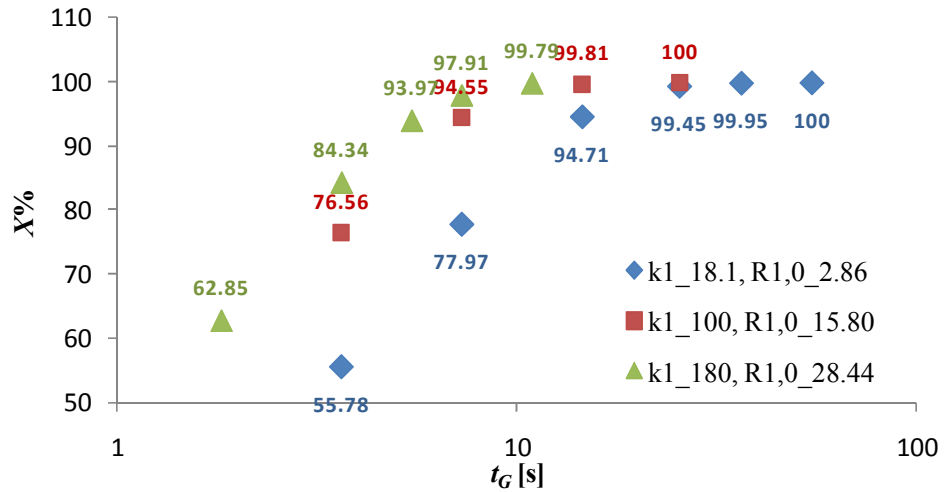


Figure 9.14 CO₂ conversion as a function of gas phase residence time for various reaction rate constant. $\delta_G = 1\text{mm}$, $\delta_L = 218\mu\text{m}$, $C_{MDEA,0} = 4.578\text{kmol}/\text{m}^3$, $Q_L = 0.194\text{m}^3/\text{s}$, $Q_G = 3.954\text{m}^3/\text{s}$.

In this study, the sensitivity of the reaction conversion on reaction rate is studied by adjusting k_I without modifying the reaction kinetics. As seen in Figure 9.13, faster reaction rate constant improves CO₂ conversion significantly. Within 3.64s ($h = 1\text{m}$), CO₂ conversion reaches 95.42% for a 55-fold increase in base case k_I value (from 18.1 to 1000 $\text{m}^3/(\text{kmol s})$). As a result, the reactor height can be shortened when amines blend is used. Figure 9.14 shows that in order to achieve the CO₂ conversion specification ($< 50\text{ppm}$, i.e. $X\% > 99.78\%$), a residence time of 33.1s ($h = 9.1\text{m}$), 14.56s ($h = 4\text{m}$) and 10.92s ($h = 3\text{m}$) is required for $k_I = 18.1, 100, \text{ and } 180\text{m}^3/(\text{kmol s})$ respectively. A 5.5

and 10 times increase in the reaction rate constant shortens the reactor length by 56% and 67% respectively.

9.3.4 Results and discussions – With elevated reaction rate

In this section, a ten-fold reaction rate constant is used, i.e. $k_I = 180\text{m}^3/(\text{kmol s})$, considering that amines blend is more commonly used in industry. In addition, the reaction rate achieved ($28.44\text{kmol}/(\text{m}^3\text{s})$) is comparable to that when NaOH is used as the absorbing liquid ($24.19\text{kmol}/(\text{m}^3\text{s})$ for 0.1M NaOH). The enhanced reaction rate makes mass transfer potentially the rate limiting step, and thus the use of microstructured reactors can be more beneficial (see Section 2.6). The equilibrium coefficient K_I remains the same for the reaction system. The new kinetics also applies to the other two reactor types: Taylor flow reactor and annular flow reactor. The characteristic dimension in the Taylor and annular flow reactor is considered to be 1mm, which corresponds to a 0.5mm characteristic dimension in the falling film reactor when films are forming from both sides of the plate, i.e. two films are facing each other to give 1mm total distance between two adjacent plates). Sensitivity studies on the reactor performance are carried out for each type of reactor, especially for the effect of solvent flowrate.

9.3.4.1 Base case characterization

In the reaction structure with liquid film forming on both sides of the plate, there are 7200 films formed on the 3600 plates, offering a 0.5mm dimension for a unit of gas chamber and its film. This structure is used as a base case.

Table 9.8 Base case parameters for countercurrent falling film reactor at elevated reaction rate. $k_I = 180\text{m}^3/(\text{kmol s})$.

d [m]	n [-]	Q_G [m^3/s]	Q_L [m^3/s]	$\delta_L \times 10^6$ [m]	v_G [m/s]	v_L [m/s]	a [m^2/m^3]	X_e [-]
0.001	3600	3.95	0.19	173	0.42	0.039	2000	0.93

The simulation conditions for the base case are as in Table 9.8. When calculating the film thickness using Eq. 9.21, plate number n should be substituted by the number of films, which is 7200. The gas core size and its velocity are adjusted accordingly, i.e. $\delta_G = 3.6/2n \cdot \delta_L$ and $v_G = Q_G/(2nw\delta_G)$.

The reaction conversions are shown in Figure 9.15 for reactors with different heights. Under cocurrent operation, X_e is achieved in reactors higher than 3.2m ($t_G = 7.6\text{s}$).

Under countercurrent operation, conversion target is achieved in reactors with a minimum height of 1.4m ($t_G = 3.3s$) (obtaining $0.95X_e$ within 0.75m for the 1.4m high reactor).

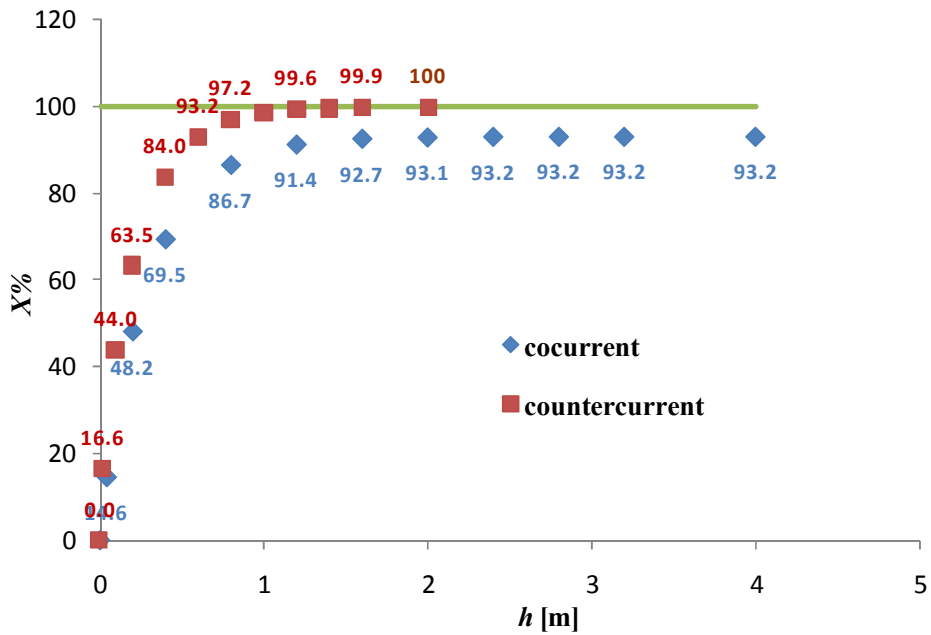
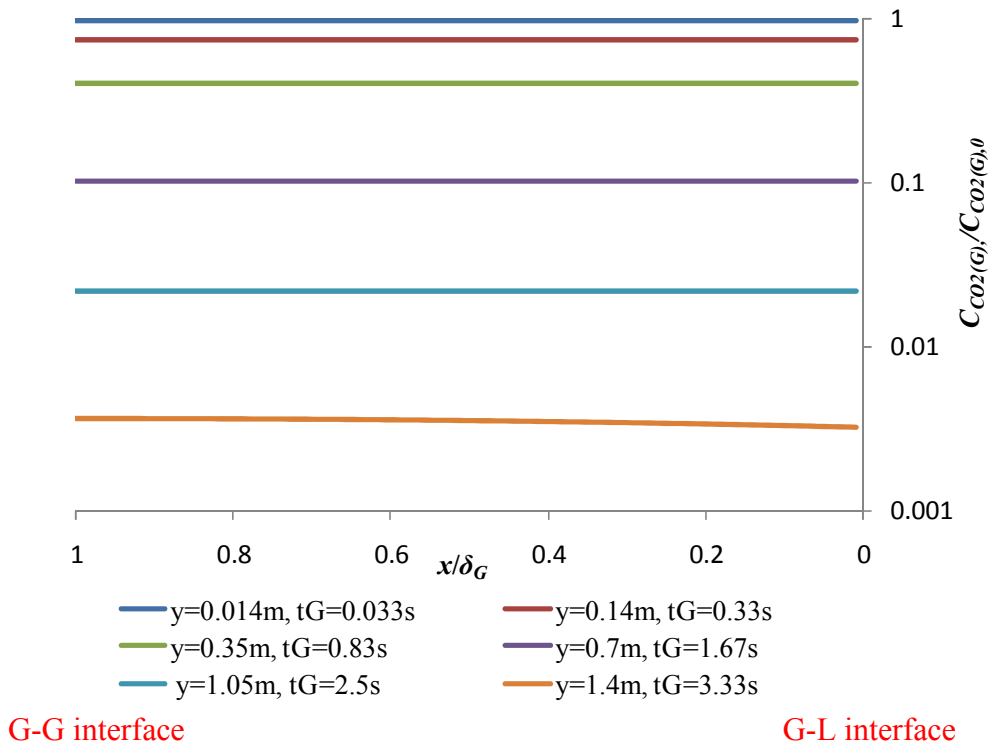


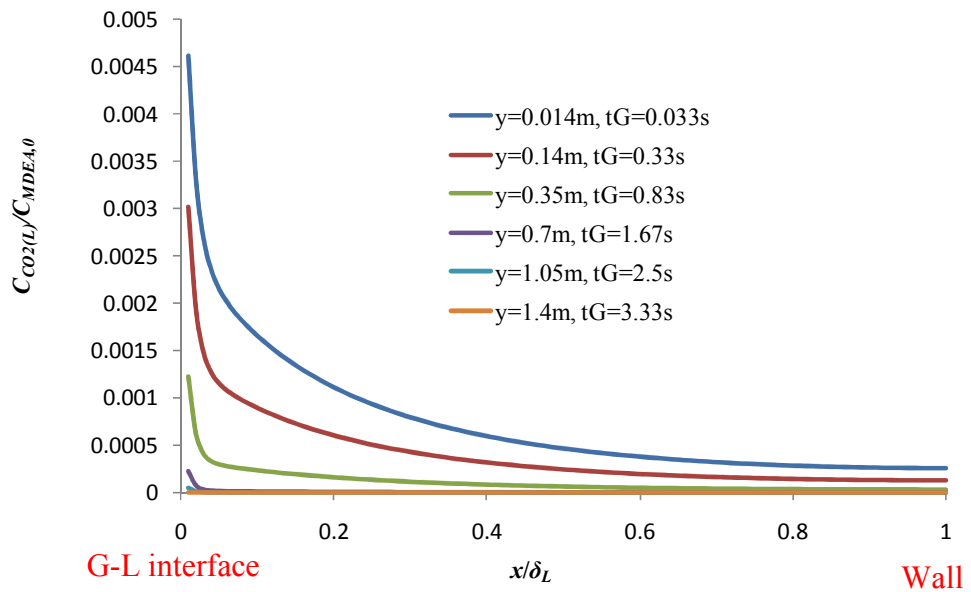
Figure 9.15 Base case conversions in the falling film reactor for both co- and counter-current operations. $d = 1\text{mm}$, $\delta_L = 173\mu\text{m}$, $C_{MDEA,0} = 4.578\text{kmol}/\text{m}^3$, $k_l = 180\text{m}^3/(\text{kmol s})$, $Q_L = 0.194\text{m}^3/\text{s}$, $Q_G = 3.954\text{m}^3/\text{s}$.



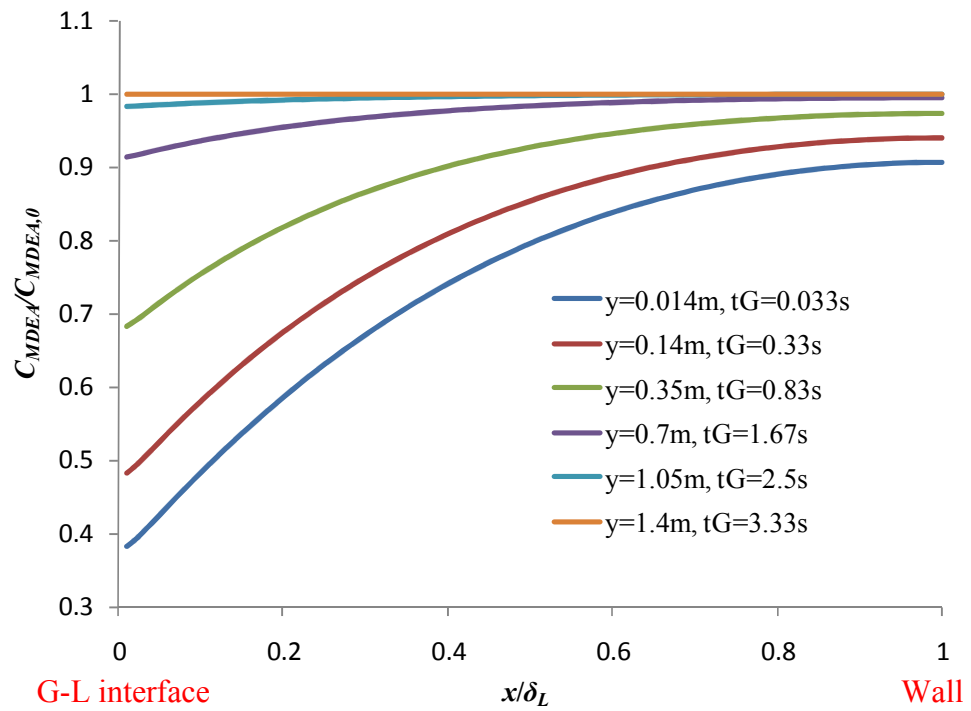
G-G interface

G-L interface

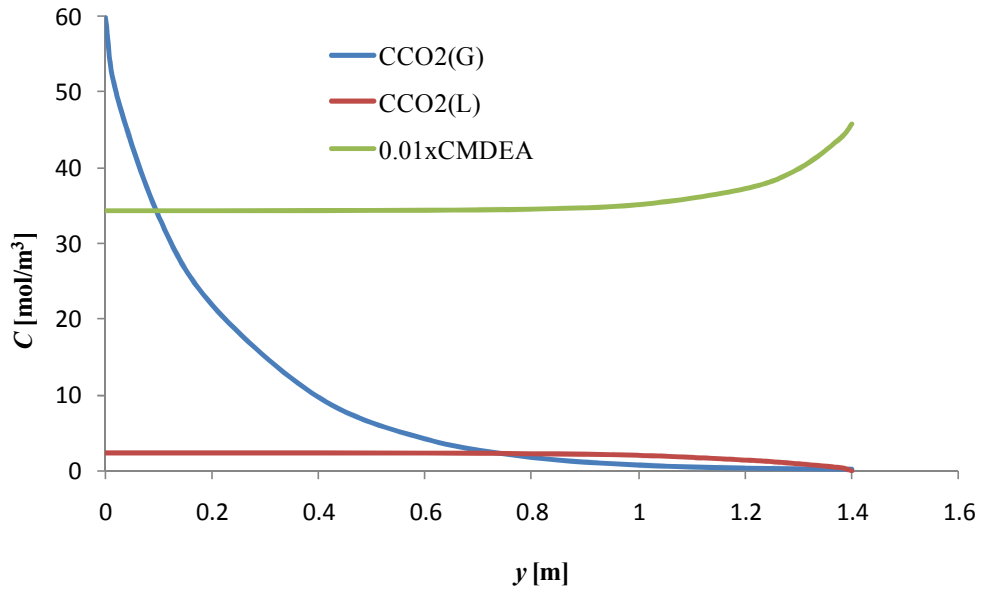
(a)



(b)



(c)



(d)

Figure 9.16 Plot of transversal and axial concentration profiles in the base case of the falling film reactor for countercurrent operation. (a) transversal $C_{CO_2(G)}$; (b) transversal $C_{CO_2(L)}$; (c) transversal C_{MDEA} ; (d) axial $C_{CO_2(G)}$, $C_{CO_2(L)}$, and C_{MDEA} . $d = 1\text{mm}$, $h = 1.4\text{m}$, $C_{MDEA,0} = 4.578\text{kmol/m}^3$, $k_1 = 180\text{m}^3/(\text{kmol s})$, $Q_L = 0.194\text{m}^3/\text{s}$, $Q_G = 3.954\text{m}^3/\text{s}$.

The concentration profiles in the reactor are plotted in Figure 9.16. The axial concentration at a reactor height is obtained by integrating the grid concentration over the cross section. Little transversal CO_2 concentration difference is observed in the gas phase (Figure 9.16a), demonstrating an absence of mass transfer resistance in the gas film. Much larger concentration gradient in the liquid phase is observed in Figure 9.16b compared with that shown in Figure 9.8b where the reaction rate is 10 times slower. As MDEA is a relatively weak amine, CO_2 can survive to the end of the film within 10% of reactor length where there is high CO_2 and low MDEA supply due to countercurrent operation. In Figure 9.16c, large MDEA concentration gradient appears close to the reactor inlet and its capacity to intake CO_2 remains high.

9.3.4.2 Effect of liquid viscosity

Sensitivity studies for the falling film reactor have been carried out in Section 9.3.3. One extra case on the effect of liquid film thickness is investigated in this section by changing the liquid viscosity. This will also change the gas and liquid superficial velocities in the respective domain. Simulation conditions are shown in Table 9.9 with liquid viscosity being enhanced by five-fold.

Comparing the reactor performance in Figure 9.17, higher liquid viscosity leads to slightly lower conversion at the same reactor height. This is because of the shorter gas phase residence time in a narrower gas core when the liquid is more viscous and produces thicker film (Eq. 9.21).

Table 9.9 Parameters for countercurrent falling film reactor at enhanced liquid viscosity and elevated reaction rate. $k_I = 180\text{m}^3/(\text{kmol s})$.

d [m]	n [-]	Q_G [m ³ /s]	Q_L [m ³ /s]	μ_L [Pa s]	$\delta_L \times 10^6$ [m]	v_G [m/s]	v_L [m/s]	a [m ² /m ³]
0.001	3600	3.95	0.19	0.013	296	0.67	0.023	2000

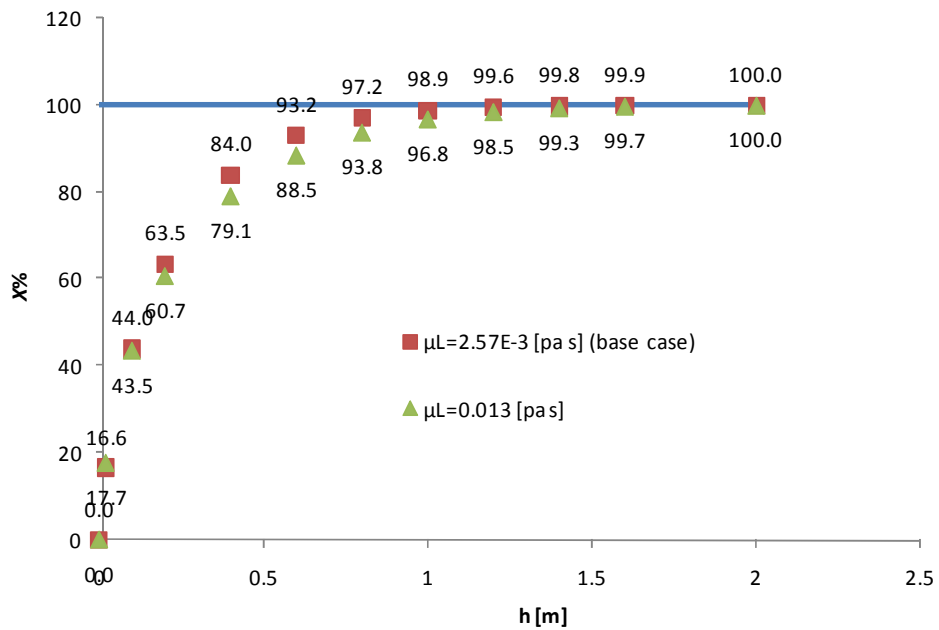


Figure 9.17 Conversions in countercurrent falling film reactors operated under different liquid viscosity. $d = 1\text{mm}$, $C_{MDEA,0} = 4.578\text{kmol}/\text{m}^3$, $k_I = 180\text{m}^3/(\text{kmol s})$, $Q_L = 0.194\text{m}^3/\text{s}$, $Q_G = 3.954\text{m}^3/\text{s}$.

9.4 Taylor flow reactor

In this section, the applicability of Taylor flow microreactor as CO₂ absorber is investigated. The study starts from a discussion on the model framework, followed by sensitivity studies on convection, bubble length, slug length (gas/liquid flow ratio), channel dimension and contacting interfacial area.

9.4.1 Model formulation

Taylor flow reactor here is assumed to be consisted of bundles of circular microchannels, similar to the topology of a monolith reactor (Figure 9.18). Other assumptions are:

- Uniform flow distribution is achieved among microchannels
- Uniform bubble size, i.e. uniform mass transfer performance
- Isothermal reaction
- Negligible effect of mass convection in gas phase, i.e. no velocity field exist
- Negligible physical property changes in gas phase and mass change in liquid phase as a result of CO₂ absorption due to its low volume fraction (2.28%)
- All reactor cross section is effective, i.e. no solid and interstices among channels

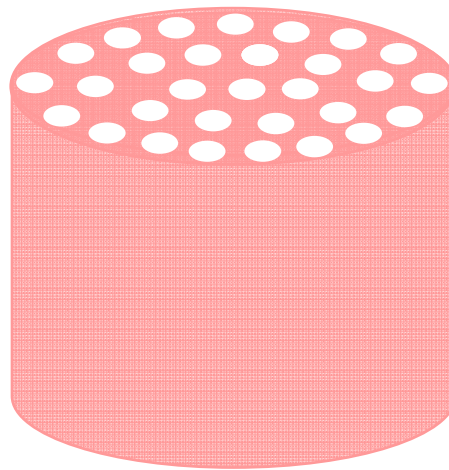


Figure 9.18 3D view of a Taylor flow microreactor, consisting of bundles of circular microchannels.

In Section 7.5, the Taylor flow unit cell topology consisted of a bubble with a cylindrical body and two spherical caps, a liquid slug and a liquid film surrounding the bubble cylindrical body. The film thickness was predicted by Eq. 2.18 (Section 2.5.4). Under the current high gas to liquid flowrate ratio ($Q_G/Q_L = 20.4$), however, there will not be enough liquid to fill the liquid slug and the liquid film if the above unit cell topology and film thickness are to be used. Therefore, a different unit cell topology is adopted to allow the formation of a liquid slug and a liquid film surrounding the bubble body by assuming that a uniform liquid layer surrounds the whole bubble as shown in Figure 9.19. The thickness of this layer is then calculated from Eq. 9.26 based on liquid mass conservation. A bubble length of $10d_C$ is applied as obtained from Figure 9.3, where the gas to liquid flowrate ratio is similar.

$$\frac{V_G}{V_{UC}} = \frac{(d_C - 2\delta)^2 L_B}{d_C^2 (L_B + 2\delta)} = \frac{Q_G}{(Q_G + Q_L)} \quad \text{Eq. 9.26}$$

$$X = 1 - \frac{\sum_{j,\text{domain}} \text{vol}_j \text{CO}_{2(G),t}}{\text{CO}_{2(G),0}} \quad \text{Eq. 9.27}$$

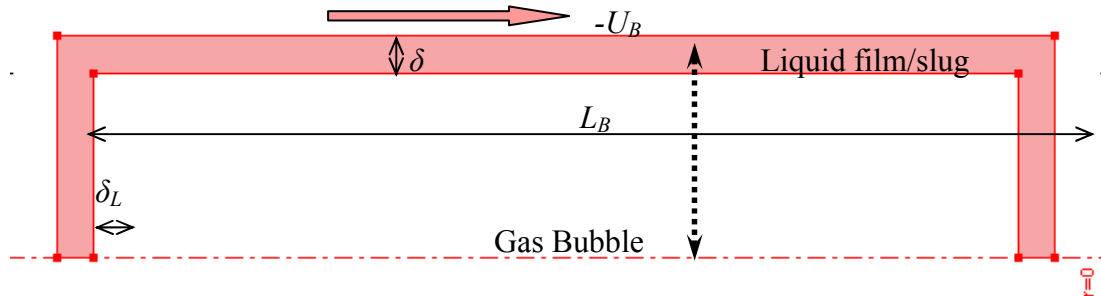


Figure 9.19 2D solution domain for Taylor flow microreactors. The scale has been modified to provide clearer visualization. The dotted line shows the location that concentration profiles are plotted in later study.

The numerical model has been presented in Section 7.5. The solution domain is shown in Figure 9.19 with the white rectangle and pink surrounding area representing the bubble and the liquid film/slug respectively. Governing equations, initial conditions and boundary conditions for each domain are presented in Table 9.10 and Table 9.11 respectively. Different from the approach used in the falling film reactor, where residence time is varied by adjusting the reactor height, it is now an independent parameter in Taylor flow reactor modelling. That is to say, simulations are transient and the change in residence time reflects the change of reactor height. In addition, the outlet of Taylor flow reactors do not exist in the simulations since the periodic boundary conditions are used (Section 7.5). As a result, Eq. 9.23, that is used to evaluate the reaction conversion in falling film reactors, has to be modified to be applicable for Taylor flow reactors. In Eq. 9.27, reaction conversion is calculated by replacing the exit CO_2 concentration with an averaged CO_2 concentration in the gas domain.

Table 9.10 2D model details in liquid domain for Taylor flow reactors.

Variables	u, v, p, C_j with $i = \text{CO}_2(\text{L}), \text{MDEA}, \text{MDEA}^+, \text{HCO}_3^-$	
Governing equations	$\nabla \cdot \mathbf{u} = 0$ $\rho_L \frac{\partial \mathbf{u}}{\partial t} + \nabla \cdot (\rho_L \mathbf{u}\mathbf{u} - \mu_L (\nabla \mathbf{u} + (\nabla \mathbf{u})^T)) = -\nabla p$ $\frac{\partial}{\partial t} C_i + \nabla \cdot (\mathbf{u} C_i - D_i \nabla C_i) = R_i$	
Reaction term	$R_i = \begin{cases} -k_1 C_{\text{CO}_2(\text{L})} C_{\text{MDEA}} + \frac{k_1}{K_1} C_{\text{MDEA}^+} C_{\text{HCO}_3^-} & \text{for } i = \text{CO}_2(\text{L}), \text{MDEA} \\ k_1 C_{\text{CO}_2(\text{L})} C_{\text{MDEA}} - \frac{k_1}{K_1} C_{\text{MDEA}^+} C_{\text{HCO}_3^-} & \text{for } i = \text{MDEA}^+, \text{HCO}_3^- \end{cases}$	
Intial conditions	$C_{\text{CO}_2(\text{L})} = 0 \text{ mol/l}, C_{\text{MDEA}} = C_{\text{MDEA}^+} = C_{\text{HCO}_3^-} = 0 \text{ mol/l}$	
Boundary conditions	Slug ends	$u_{in} = u_{out}, v_{in} = v_{out}, p_{in} = p_{out}, C_{i,in} = C_{i,out}$
	Wall	$u = 0, v = -U_b$ $\frac{\partial C_i}{\partial r} = 0$
	Gas-liquid interface	$C_{\text{CO}_2(\text{L})} = \text{He}RT C_{\text{CO}_2(\text{G})}$ $\frac{\partial C_i}{\partial x} = 0$ with $i \neq \text{CO}_2(\text{L})$

Table 9.11 2D model details in gas domain for Taylor flow reactors.

Variables	$C_{\text{CO}_2(\text{G})}$	
Governing equations	$\frac{\partial}{\partial t} C_G + \nabla \cdot (-D_G \nabla C_G) = R_G$	
Reaction term	$R_G = 0$	
Intial conditions	$C_{\text{CO}_2(\text{G})} = 0.0598 \text{ mol/l}$	
Boundary conditions	Gas-liquid interface	$C_{\text{CO}_2(\text{L})} = \text{He}RT C_{\text{CO}_2(\text{G})}$

9.4.2 Results and discussions

9.4.2.1 Base case characterization

Microchannel size of 1mm is used for Taylor flow reactor to correspond to the total 1mm distance between two plates in the film reactor (Section 9.3.4.1). Table 9.12 summarizes the parameters used for the base case.

Table 9.12 Base case parameters for Taylor flow reactor at elevated reaction rate. $d = 1\text{mm}$, $C_{MDEA,0} = 4.578\text{kmol/m}^3$, $k_I = 180\text{m}^3/(\text{kmol s})$.

d_C [m]	L_B/d_C	L_{UC}/d_C	δ/d_C	U_B [m/s]	Q_G/Q_L	a [m^2/m^3]	X_e
0.001	10	10.0226	0.0113	0.286	20.35	4091.4	0.933

Figure 9.20 shows how conversion X changes with reactor height h . Due to the cocurrent operation, the equilibrium conversion X_e is achieved at $t_G = 3.2\text{s}$, about 42% of the time required for a falling film reactor ($t_G = 7.6\text{s}$). From Chapter 8, the specific area is the determinant for mass transfer when there is fast reaction. In current Taylor flow reactor, the specific area is $4091.4\text{m}^2/\text{m}^3$, more than doubled that of the falling film reactor ($2000\text{m}^2/\text{m}^3$ for the base case with $k_I = 180\text{m}^3/(\text{kmol s})$).

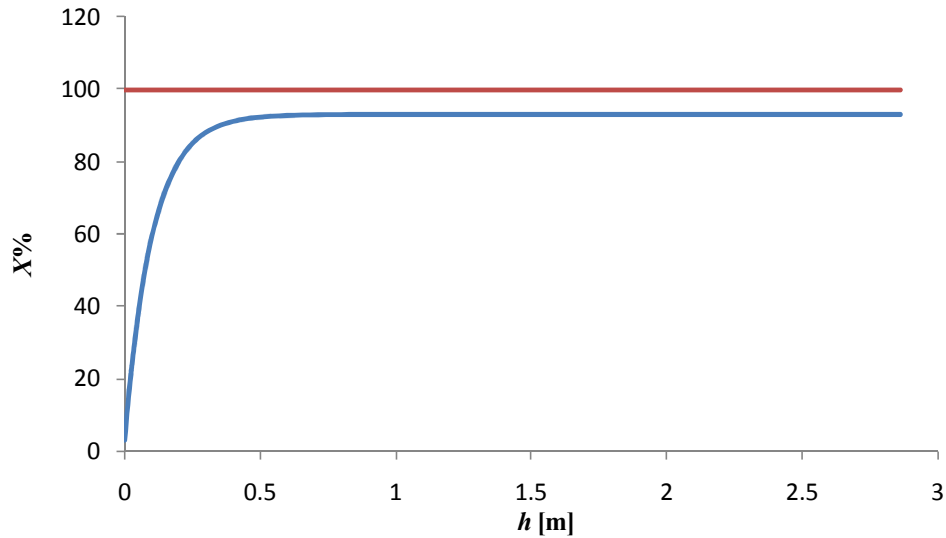
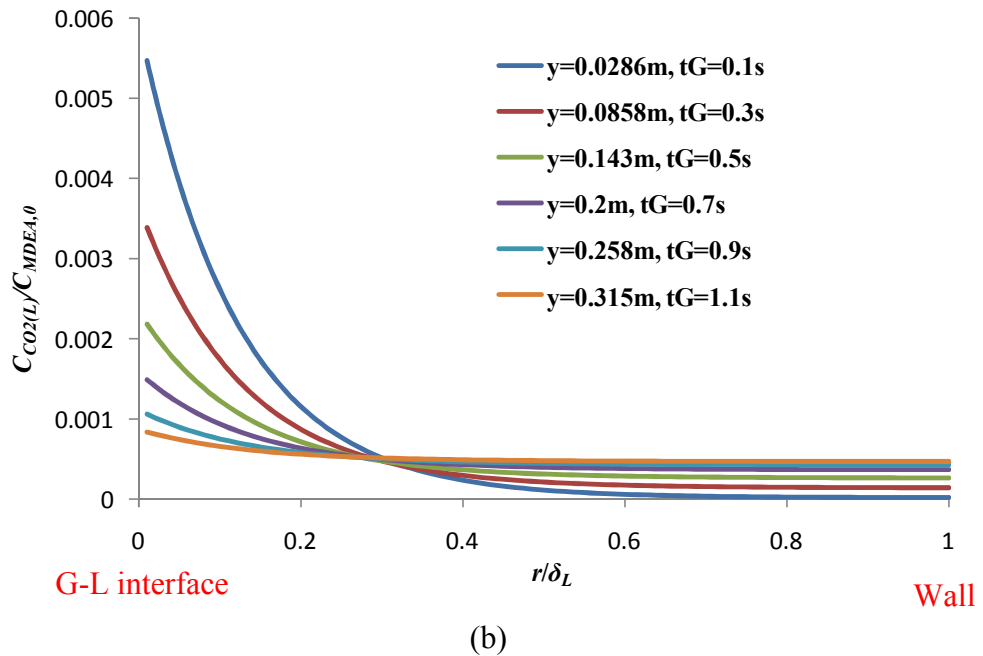
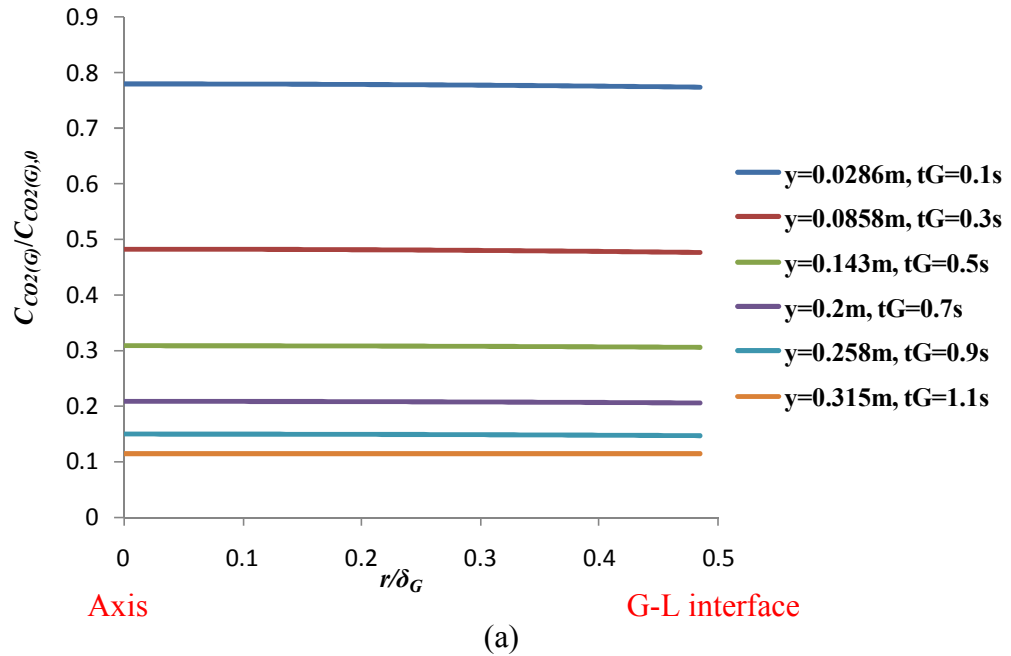


Figure 9.20 Reaction conversion changes with reactor height for the base case of Taylor flow reactor. $d = 1\text{mm}$, $C_{MDEA,0} = 4.578\text{kmol/m}^3$, $k_I = 180\text{m}^3/(\text{kmol s})$.

The concentration profiles along the middle cross section of the unit cell (dotted arrow in Figure 9.19) for both CO_2 and MDEA, are plotted in Figure 9.21. The upper time bound of 1.1s is selected because 95% equilibrium conversion is achieved by the time. No obvious CO_2 concentration gradient is detected in gas phase even at the beginning of

the reaction (Figure 9.21a), showing the absence of mass transfer resistance. In the liquid film, significant CO₂ concentration gradient exists when the reaction begins and it evens out gradually with time and is almost negligible after 95% of X_e is reached (Figure 9.21b). The change of MDEA concentration follows the same behaviour in the liquid film as seen in Figure 9.21c.



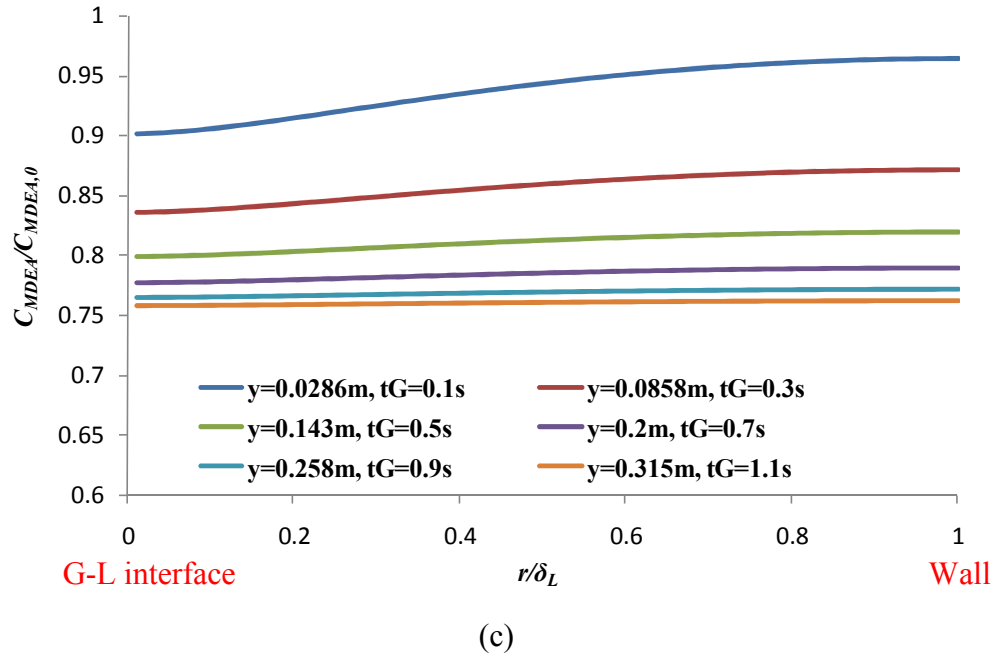


Figure 9.21 Transversal concentration profiles along the middle cross section of the unit cell for the base case of Taylor flow reactor. (a) $C_{CO_2(G)}$; (b) $C_{CO_2(L)}$; (c) C_{MDEA} . $d = 1\text{mm}$, $C_{MDEA,0} = 4.578\text{kmol/m}^3$, $k_1 = 180\text{m}^3/(\text{kmol s})$.

9.4.2.2 Multistage absorption

To reach the system specification in CO_2 conversion, multistage absorption arranged in a virtually countercurrent way is usually adopted for co-flow operations, as seen in Figure 9.22. The initial fuel gas is designed to be in contact with the liquid outflow from absorber S2 in absorber S1. The unabsorbed CO_2 is then directed to absorber S2, where it meets the lean amine solution. Due to the very small amount of CO_2 presented in the gas phase, the flowrate reduction due to the first stage absorption is neglected, i.e. $Q_{G1,in} = Q_{G1,out} = Q_{G2,in}$. However, CO_2 inlet concentration is modified according to the performance in the absorber S1. Optimisation is required to determine the optimum inlet CO_2 concentration for S1 so as to minimise the residence time difference between the two reactors, however, this is not investigated in this thesis. One scenario is examined here by specifying that 90% conversion has been achieved in absorber S1 before the gas mixture flows into S2. 1.7s is needed for a 90% conversion in stage one and after another 1.5s in stage two, 99.8% CO_2 is converted, meeting the system specification (Figure 9.23).

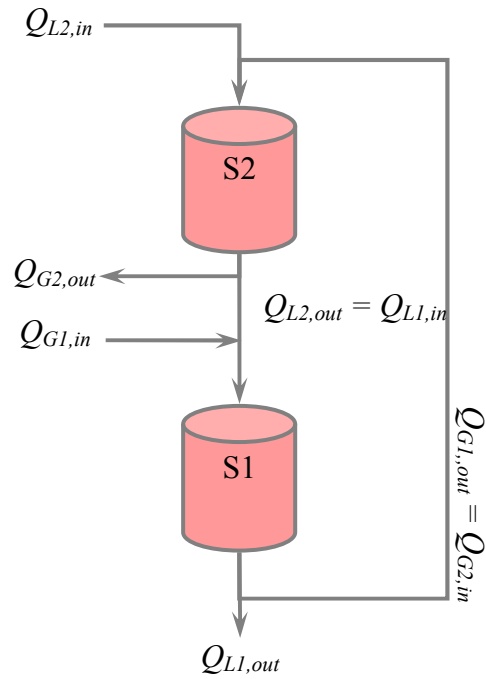


Figure 9.22 Schematic of two stage absorption with reactors arranged in a virtually countercurrent way.

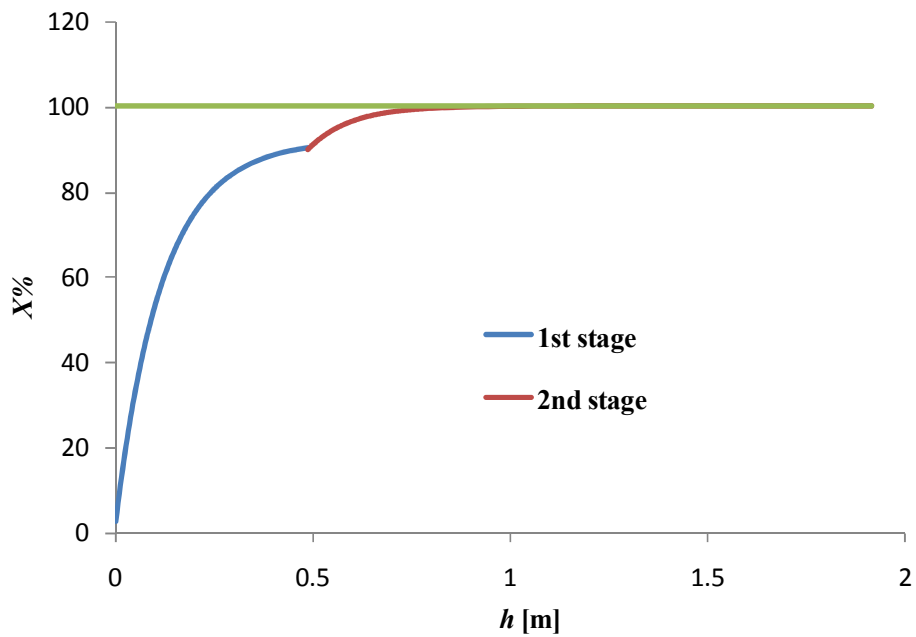


Figure 9.23 Conversion changes with reactor height for a two-stage CO_2 absorption in Taylor flow reactors.

9.4.2.3 Effect of bubble length

In the base case, the dimensionless bubble length L_B/d_C takes a value of 10 from measurements in Figure 9.3. As bubble size is also a function of inlet conditions other than gas and liquid flowrate (Section 5.3), a sensitivity study on L_B/d_C is carried out.

Together with the base case, conditions for another three scenarios have been listed in Table 9.13. It shows that the smaller the bubble length, the larger the specific interfacial area. From the results in Figure 9.24, less time is needed for the reactor to reach 95% of X_e when smaller bubble length is used (larger a , see Table 9.13). The time is linearly related to the specific area demonstrates the dominant effect of the specific area in mass transfer with reaction, which has also be observed in Chapter 8.

Table 9.13 Simulation parameters for cases with different L_B/d_C in Taylor flow reactors.

$$d = 1\text{mm}, C_{MDEA,0} = 4.578\text{kmol/m}^3, k_l = 180\text{m}^3/(\text{kmol s}), Q_G = 3.954\text{m}^3/\text{s}.$$

L_B/d_C	L_{UC}/d_C	δ/d_C	Q_G/Q_L	a [m^2/m^3]	X_e	$t_{0.95X_e}$ [s]
2	2.02	0.0095	20.42	4840.4	0.932	0.92
5	5.022	0.011	20.34	4278.0	0.932	1.04
10 (base)	10.02	0.011	20.4	4091.4	0.932	1.08
15	15.02	0.012	20.31	4029.1	0.932	1.11

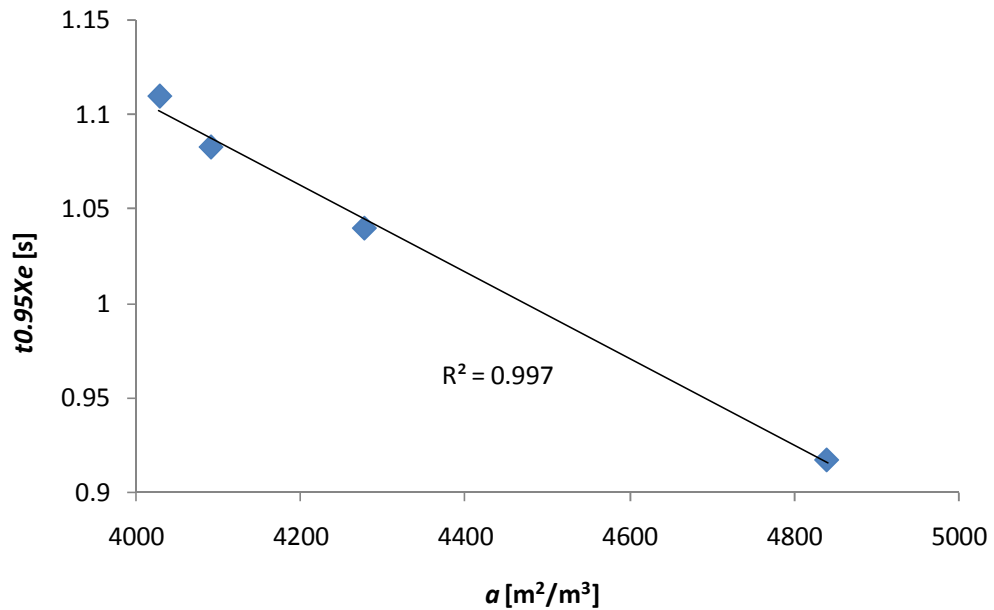


Figure 9.24 Time to achieve 95% X_e as a function of the specific area for various bubble lengths in Taylor flow reactors.

9.4.2.4 Effect of liquid flowrate

For different amount of solvent supplied without changing the gas flowrate, the bubble and slug sizes change (Section 5.3.2.1). Table 9.14 shows the simulation parameters for another two Q_G/Q_L scenaria besides the base case. Bubble topology is determined to be cylindrical with flat ends as the base case (Section 9.4.2.1) while the film thickness and

bubble length are predicted by Eq. 9.26 and Eq. 2.9 (see discussion in Section 2.5.2) for small Q_G/Q_L scenarios.

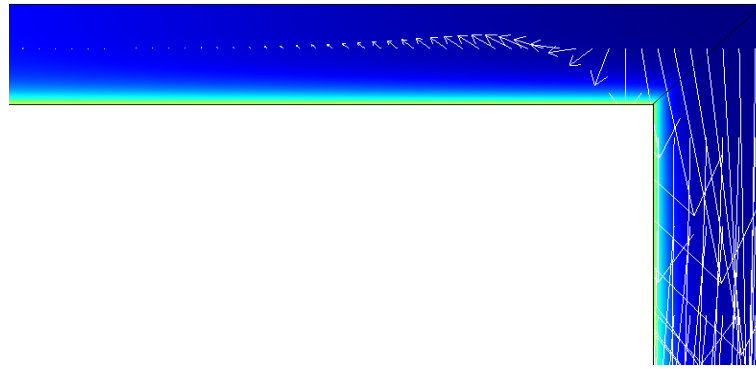
Table 9.14 Simulation parameters for different Q_G/Q_L scenaria in Taylor flow reactors.

$$d = 1\text{mm}, C_{MDEA,0} = 4.578\text{kmol/m}^3, k_I = 180\text{m}^3/(\text{kmol s}), Q_G = 3.954\text{m}^3/\text{s}.$$

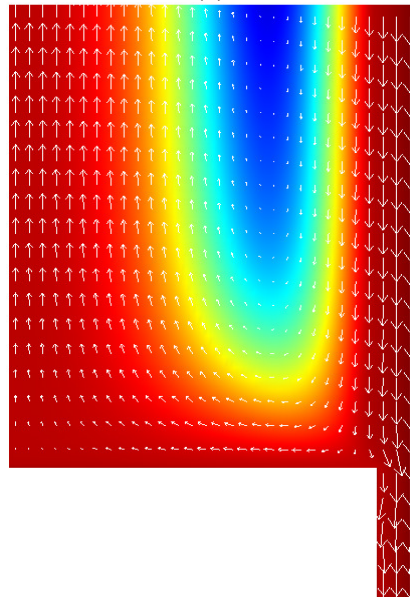
Q_G/Q_L	L_B/d_C	U_B [m/s]	δ/d_C	L_{UC}/d_C	a [m^2/m^3]	X_e	$t_{0.95X_e}$ [s]
1	2	0.545	0.049	3.254	2717.6	0.999	0.82
4	5	0.327	0.038	5.34	3780.44	0.999	1.02
20 (base)	11	0.286	0.0113	20.4	4091.5	0.933	1.08

When liquid flowrate is low, as in the base case, there is no recirculation in the very small liquid slug as seen in Figure 9.25a. As a result, conversions achieved are similar when convection in the liquid domain is considered or omitted (Navier-Stokes equation is solved or neglected) as seen in Figure 9.26a. For higher liquid flowrate ($Q_G/Q_L = 1$), the liquid slug size is larger and liquid recirculation develops (Figure 9.25b). Convection is observed to accelerate the mass transfer, even though slightly, i.e. reducing the time needed to reach 95% X_e from 0.94s to 0.82s (Figure 9.26b). The small contribution of recirculation in mass transfer with reaction has been discussed in Chapter 8.

In Section 9.4.2.3, shorter time is found to be required to achieve 0.95 X_e when the specific area is large. However, opposite results are observed in Table 9.14. This is because higher equilibrium conversion can be achieved in smaller Q_G/Q_L (Table 9.14), which accelerates the rate to reach equilibrium despite of the smaller specific area. In addition, the significantly increased amount of MDEA ($C_{MDEA} \times Q_L$) and better circulation (Figure 9.26) also contributes to the initial higher conversions in small Q_G/Q_L cases, as seen in Figure 9.27. Although increasing liquid flowrate means more solvent has to be used, the improved X_e can help to achieve the reaction specification ($X\% > 99.8\%$) in one-stage absorption using Taylor flow reactors. From Eq. 9.6 to Eq. 9.10, $X_e\% > 99.8\%$ can be achieved if $Q_G/Q_L > 4$, which means a five-fold volume increase in MDEA solvent.

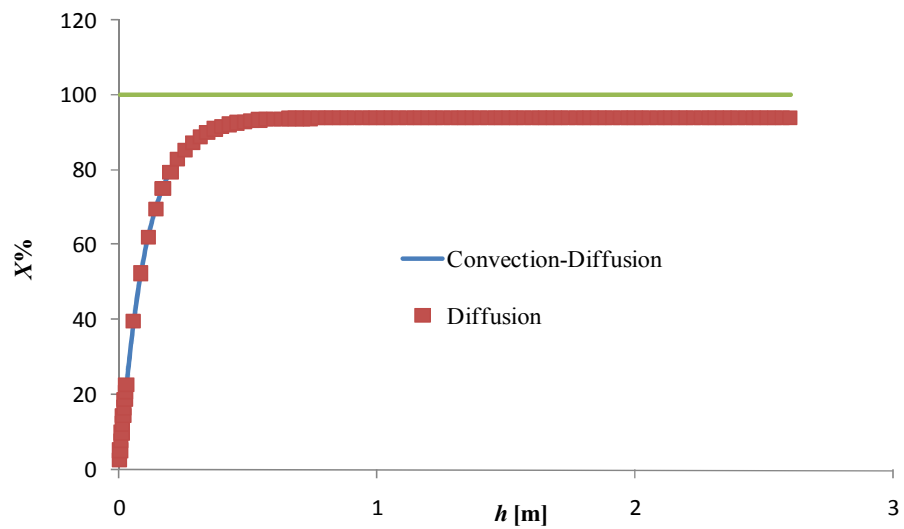


(a)



(b)

Figure 9.25 Concentration profile of CO₂ in liquid phase and velocity plot. (a) base case with colour scale ranges from 2.349 (blue) to 2.386 (red); (b) $Q_G/Q_L = 1$ with colour scale ranges from 4.613e-3 (blue) to 5.78e-3 (red).



(a)

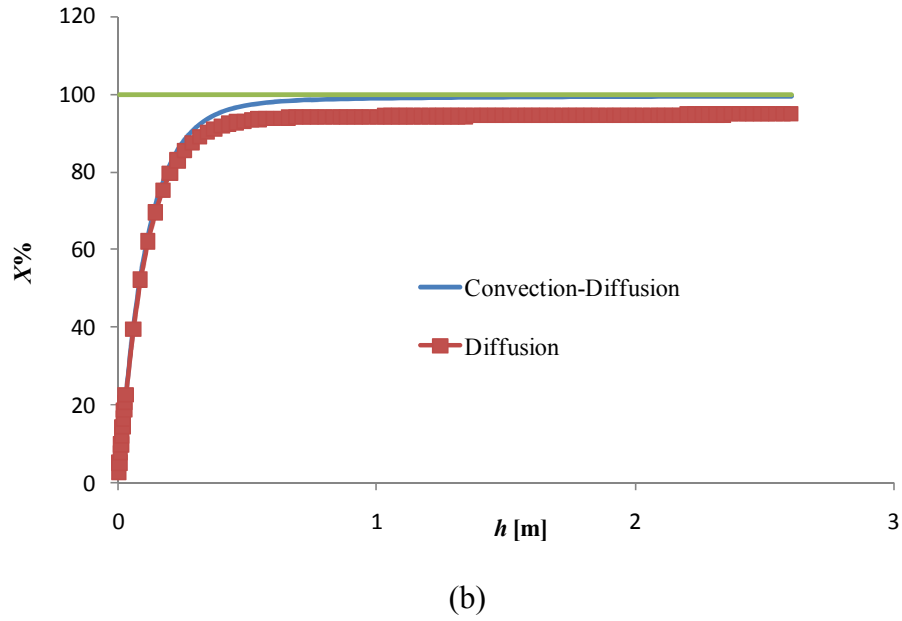


Figure 9.26 Conversion changes with reactor height when liquid convection is or is not solved. (a) base case; (b) $Q_G/Q_L = 1$.

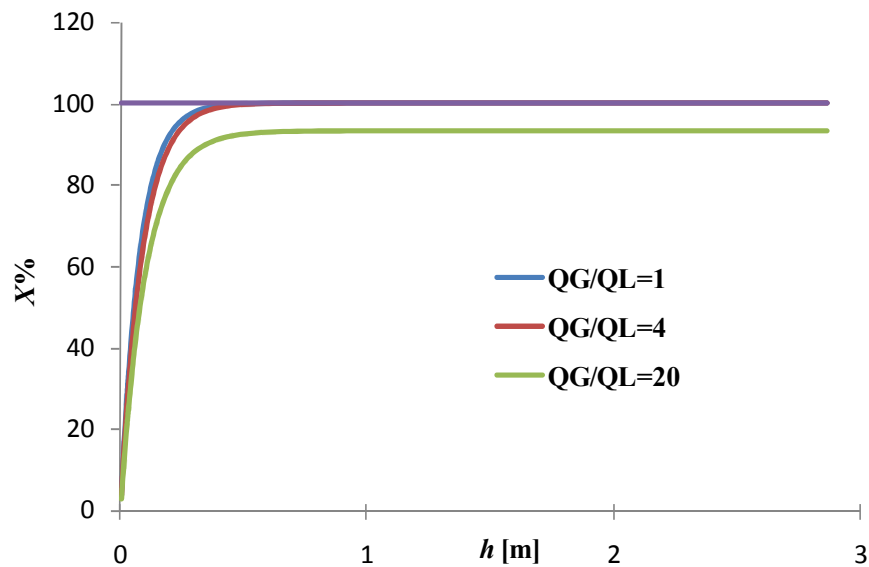


Figure 9.27 Conversion changes with reactor height for various Q_G/Q_L in Taylor flow reactor. $d = 1\text{mm}$, $C_{MDEA,0} = 4.578\text{kmol}/\text{m}^3$, $k_l = 180\text{m}^3/(\text{kmol s})$.

9.4.2.5 Effect of channel size

Figure 9.28 shows CO_2 conversions in the 1mm and 3mm microchannels. To reach 95% of X_e , a significantly longer residence time ($t_G = 3.6\text{s}$) is required in the 3mm channels than that in the 1mm channel (1.08s). This is equivalent to a 70% reduction in reactor length. In larger channels, the specific area is small that explains the above observation.

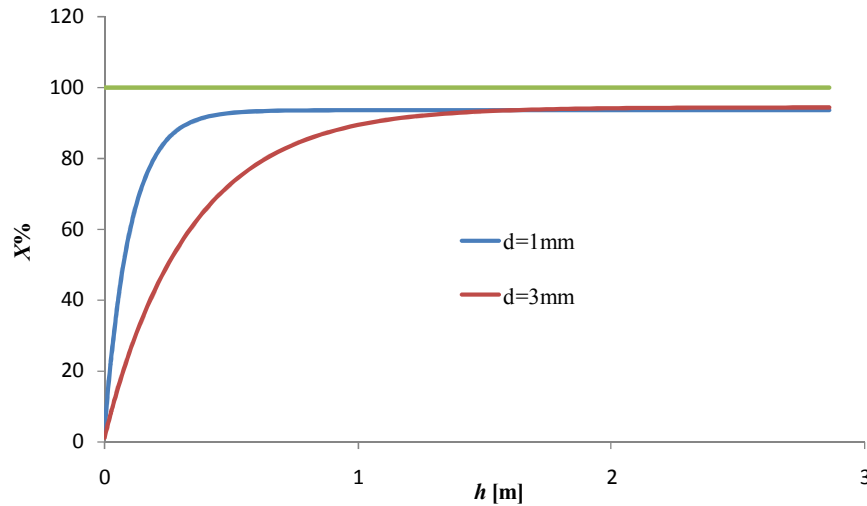


Figure 9.28 Conversion changes with reactor height for Taylor flow reactor of different channel size. $C_{MDEA,0} = 4.578 \text{ kmol/m}^3$, $k_l = 180 \text{ m}^3/(\text{kmol s})$.

9.5 Annular flow reactor

9.5.1 Model formulation

With increasing gas and liquid superficial velocities, Taylor-annular flow is developed where liquid surrounds the middle gas core with occasional appearance of liquid slugs (Figure 2.4a). In this part, a simplified Taylor-annular flow without liquid slugs, which is equivalent to annular flow (Figure 2.6), is investigated. The reactor geometry is similar to that of Taylor flow reactor. The reactor effective cross sectional area (no solid and interstices among channels) is decreased by a factor of 10 to boost flow velocities and enter the annular flow regime. To model such a system, the following extra assumptions are made besides what has been stated in Section 9.4.1:

- No entrainment of liquid in gas phase
- Film thickness is uniform along the length of the reactor, i.e. no waves and ripples
- The stress on the gas-liquid interface will not be taken into account.

The solution domain is 2D axisymmetric with gas and liquid operated cocurrently with the same velocity (Figure 9.29). The governing equations and boundary conditions are similar to those for a Taylor flow reactor (see Table 9.10 and Table 9.11). The liquid film thickness uses the correlation for Taylor flow (Eq. 2.18). This is an approximation that ideally needs to be re-evaluated theoretically and experimentally. The gas and liquid velocities are determined from their flowrates and occupied areas in the channel.

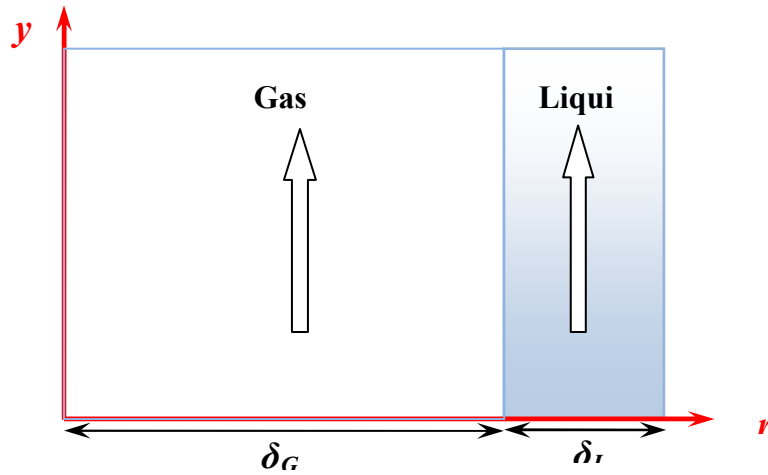


Figure 9.29 Simulation domains for an annular flow reactor. The scale has been adjusted for better visualization.

9.5.2 Results and discussions

9.5.2.1 Base case characterization

Annular flow formed in 1mm microchannel is treated as the base case with simulation parameters given in Table 9.15. From the conversion results shown in Figure 9.30, after 3.8m ($t_G = 1.21s$) and 9.6m ($t_G = 3.05s$) of reactor height, 95% X_e and X_e is reached respectively. Less time is needed than in Taylor flow (3.2s) even though the specific interfacial area is less.

Table 9.15 Simulation parameters in annular flow reactor. $d = 1mm$, $C_{MDEA,0} = 4.578kmol/m^3$, $k_l = 180m^3/(kmol s)$, $Q_G = 3.954m^3/s$, $Q_L = 0.19m^3/s$.

Scenario	d_C [mm]	δ_L/d_C	v_L [m/s]	v_G [m/s]	a [m^2/m^3]	X_e
Base	1	0.035	0.990	3.148	3720	0.932
1	1	0.015	2.262	2.894	3880	0.932
2	1	0.06	0.593	3.516	3520	0.932
3	1	0.1	0.371	4.255	3200	0.932
4	2	0.035	0.99	3.148	1860	0.932
5	3	0.033	1.038	3.126	1245	0.932

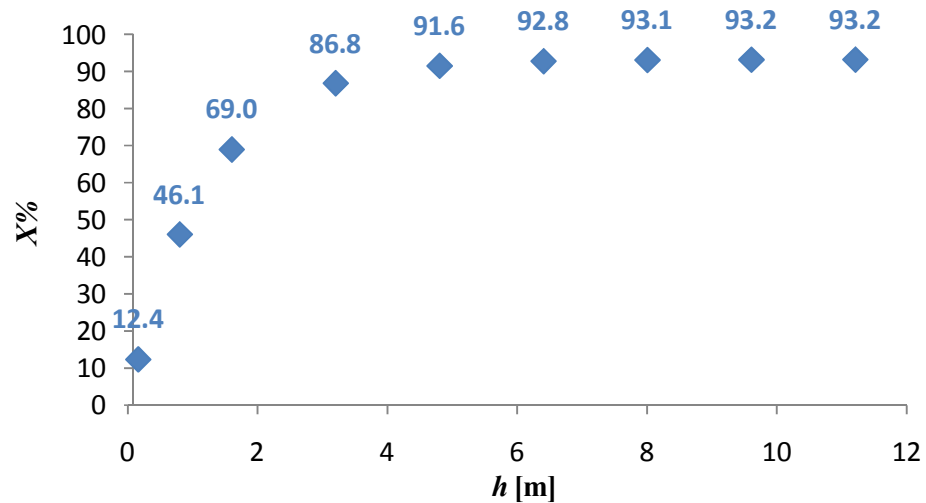
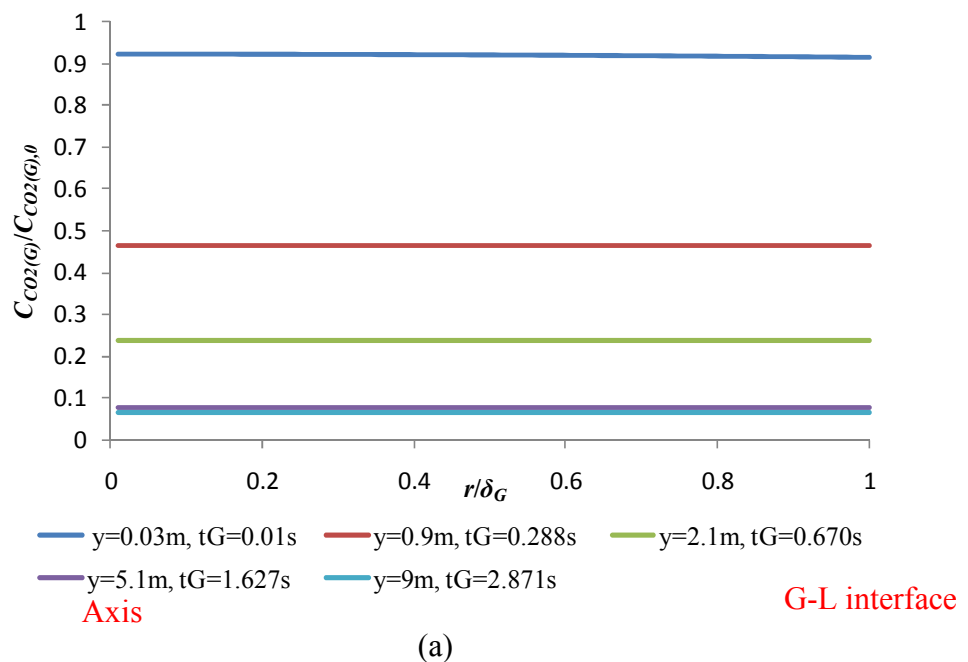
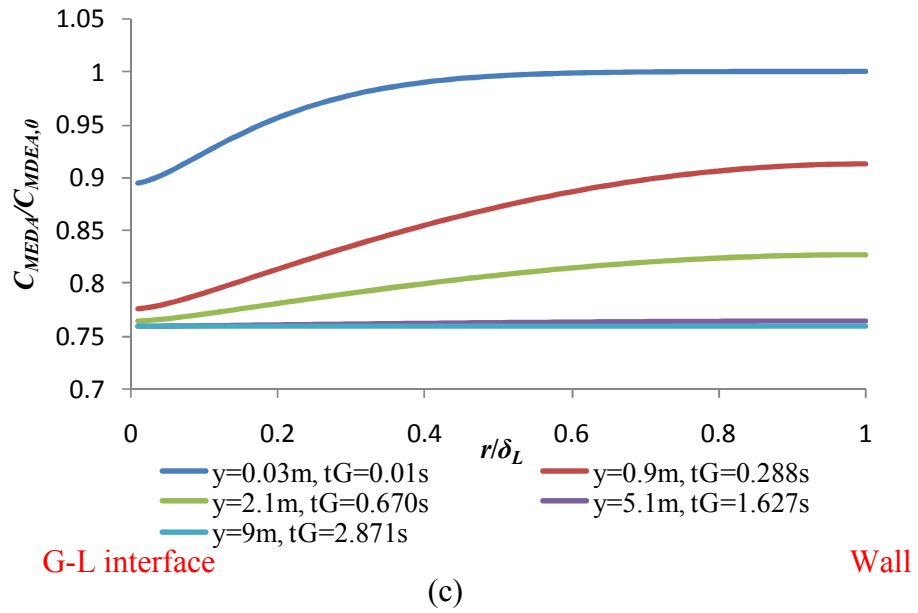
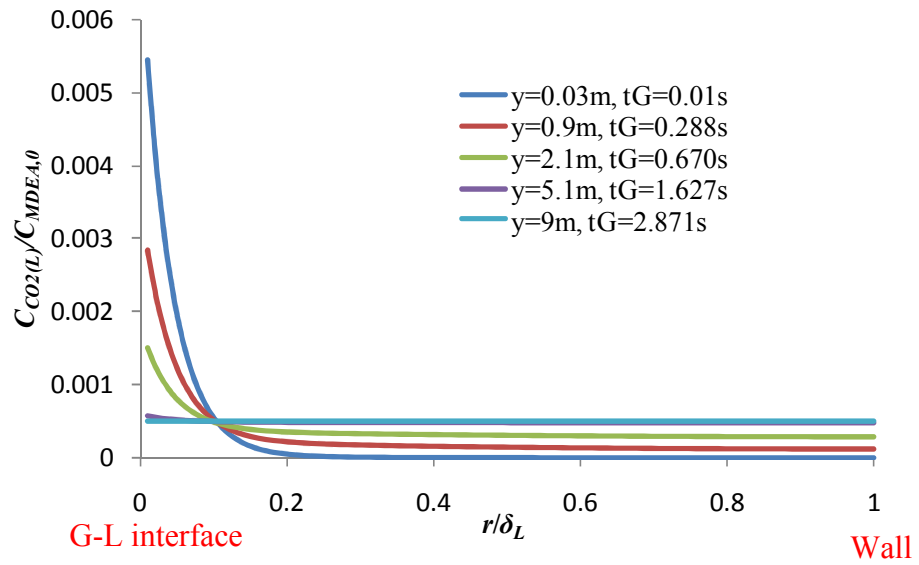


Figure 9.30 Base case conversion changes with annular flow reactor height. $d = 1\text{mm}$, $C_{MDEA,0} = 4.578\text{kmol/m}^3$, $k_I = 180\text{m}^3/(\text{kmol s})$, $Q_G = 3.954\text{m}^3/\text{s}$, $Q_L = 0.19\text{m}^3/\text{s}$.

The transversal and radial concentration of both reactants in gas and liquid phase are shown in Figure 9.31. Similar to falling film and Taylor flow reactor, the CO_2 concentration in gas phase presents little transversal gradient and decreases along the reactor length. When the reaction starts (at the entrance of the reactor), there is steep concentration gradient in liquid phase for both CO_2 and MDEA, similar to cocurrently operated Taylor flow. The gradients flatten along the reactor and no transversal difference could be identified after 9m reactor length (Figure 9.31a, b).





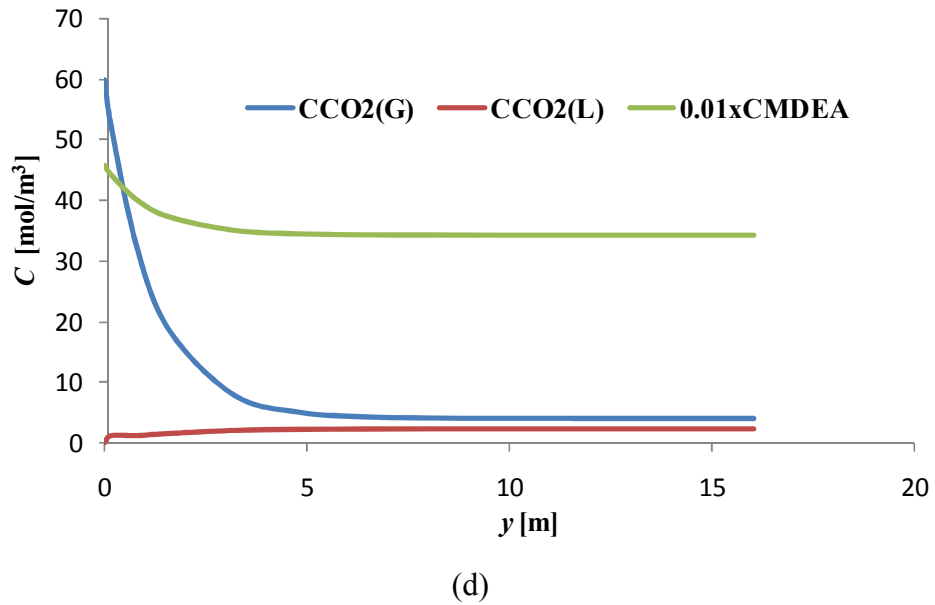


Figure 9.31 Transversal and axial reactants concentration for the base case in annular flow reactor. (a) $C_{CO_2(G)}$; (b) $C_{CO_2(L)}$; (c) C_{MDEA} ; (d) $C_{CO_2(G)}$, $C_{CO_2(L)}$, and C_{MDEA} . $d = 1\text{ mm}$, $C_{MDEA,0} = 4.578\text{ kmol /m}^3$, $k_I = 180\text{ m}^3/(\text{kmol s})$.

9.5.2.2 Multistage absorption

Similar to the study of Taylor flow reactor, a multistage absorption in annular flow reactor is investigated. A 90% conversion is assumed to have been achieved in S1 (Figure 9.22), which takes 6.4m reactor length ($t_G = 2.03\text{ s}$) from the simulation results (Figure 9.32). Another 4.8m reactor ($t_G = 1.52\text{ s}$) is needed for the second absorber S2 to meet system conversion specification of 99.8%.

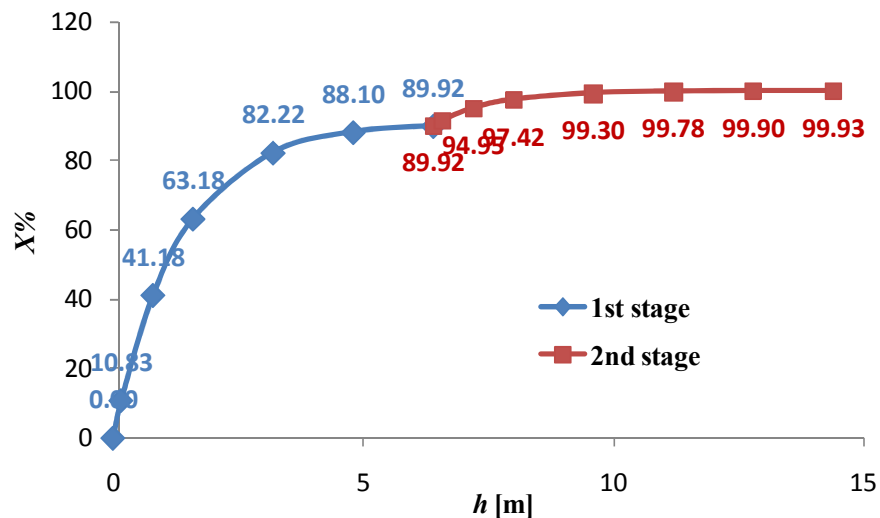
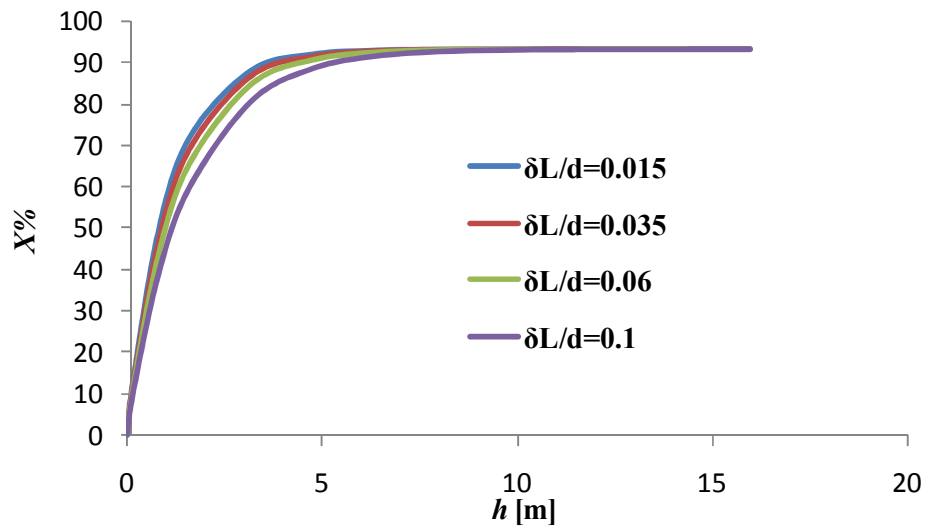


Figure 9.32 Conversion changes with reactor height for a two-stage absorption process in annular flow reactor. with $d = 1\text{ mm}$, $C_{MDEA,0} = 4.578\text{ kmol /m}^3$, $k_I = 180\text{ m}^3/(\text{kmol s})$.

9.5.2.3 Effect of film thickness

Film thickness is estimated using the correlation for Taylor flow (Eq. 2.18) since that for annular flow in microchannels is seldom available up to our knowledge. In this section, the film thickness is varied to study its effect on absorption (scenario 1 to 3 in Table 9.15). The change of film thickness by adjusting liquid flowrate will be excluded because the changed Q_G/Q_L value will lead to different equilibrium conversion under cocurrent operation. As shown in Figure 9.33a, in channels with thicker films, conversion is smaller at the same reactor height. This is due to shorter gas phase residence time, and lower specific interfacial area (Table 9.13). A 3.4m reactor is needed to reach 95% X_e when the film is 15 μm thick and this extends to 4.8m when the film thickness increases to 100 μm . Transversal CO_2 concentration in liquid film at the reactor entrance ($h = 0.2\text{m}$) is plotted in Figure 9.33b. Thicker film does not contribute to the reaction as the gas reactant can transport to less than 20% of the film thickness when it is 100 μm thick compared with a 60% penetration when it is 15 μm .



(a)

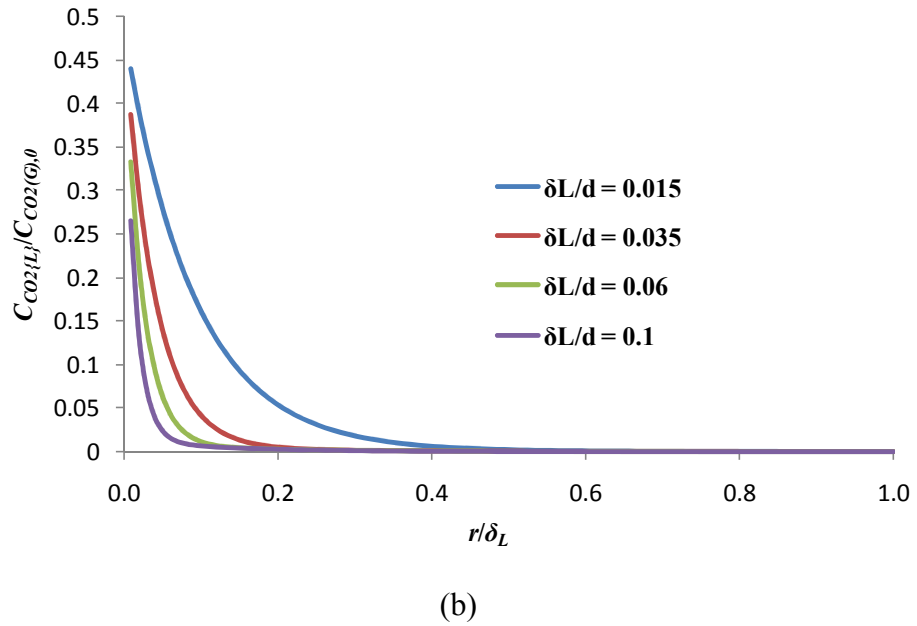


Figure 9.33 Conversions in annular flow reactor with various film thicknesses. $d = 1\text{mm}$, $C_{MDEA,0} = 4.578\text{kmol/m}^3$, $k_l = 180\text{m}^3/(\text{kmol s})$, $Q_L = 0.194\text{m}^3/\text{s}$, $Q_G = 3.954\text{m}^3/\text{s}$. (a) Conversion changes with reactor height; (b) transversal CO_2 concentration in liquid phase at a reactor height of 0.2m.

9.5.2.4 Effect of channel size

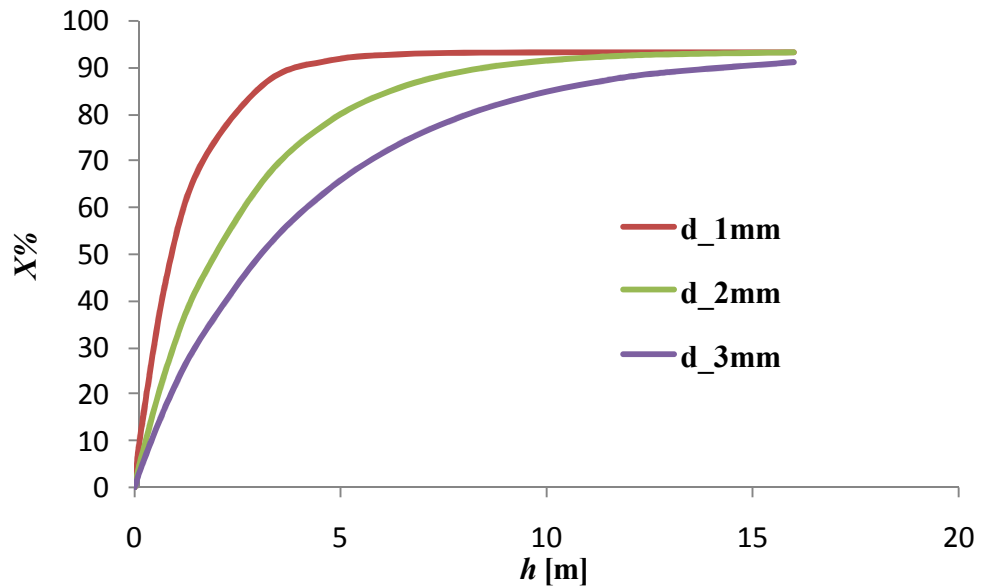


Figure 9.34 Conversion changes with reactor height for the annular flow reactor with various channel dimensions. $C_{MDEA,0} = 4.578\text{kmol/m}^3$, $k_l = 180\text{m}^3/(\text{kmol s})$, $Q_L = 0.194\text{m}^3/\text{s}$, $Q_G = 3.954\text{m}^3/\text{s}$.

As the overall reactor effective area remains the same, less number of channels will be required when the channel characteristic dimension increases. Two other channel sizes

of 2mm and 3mm are compared with the base case with simulation parameters listed as scenario 4 and 5 in Table 9.15. The results plotted in Figure 9.34. As the specific area is significantly reduced in large channels, the conversion achieved at the same reactor height is thus lowered (Figure 9.34). No gas phase resistance is identified even in the 3mm channel.

9.6 Reactor performance comparison

The performance of the three types of reactors is compared in Table 9.16 based on their base case. The unit volume required to meet CO₂ conversion (< 50ppm) target is plotted as a function of the specific area in Figure 9.35, which shows a nearly linear dependence of unit volume on the specific area. The small deviation of annular flow reactor could be a result of approximations used in annular flow film thickness estimation.

From Table 9.16, Taylor flow reactor has the highest specific interfacial area and the smallest overall reactor volume (13.33m³) to reach the CO₂ conversion target. However, many challenges remain with the reactor type as described below:

- Huge numbers of channels will be needed under the structure reported in Table 9.16, which will significantly increase the manufacturing cost and make flow equal distribution more challenging.
- Very small liquid slugs characterize the flow for the current Q_G/Q_L , which potentially destabilize the flow by bubble coalescence.
- The multistage absorption requires gas-liquid separation after each stage.

The last two challenges are due to the operating conditions used in this particular case, i.e. very high gas to liquid ratio ($Q_G/Q_L > 20$). If higher liquid flowrate is used, e.g. $Q_G/Q_L < 4$, the target conversion can be achieved in one absorber and in that case Taylor flow reactor will be preferred.

Annular flow reactor performs next but to Taylor flow reactor by requiring a reactor volume of 16.55m³. Although it shares with Taylor flow reactor the challenge of multistage operation and gas-liquid separation, it offers the following advantages compared with Taylor:

- A tenfold decrease in the number of channels required.
- Waves, ripples and entrained liquid droplet in gas have the potential to increase the specific interfacial area/ mass transfer coefficient.

Falling film reactor needs the largest reactor volume among the three, 62% more than that of Taylor flow reactor. The advantages of falling film reactor are its countercurrent operation, easy gas-liquid separation and the relatively simpler manufacturing process.

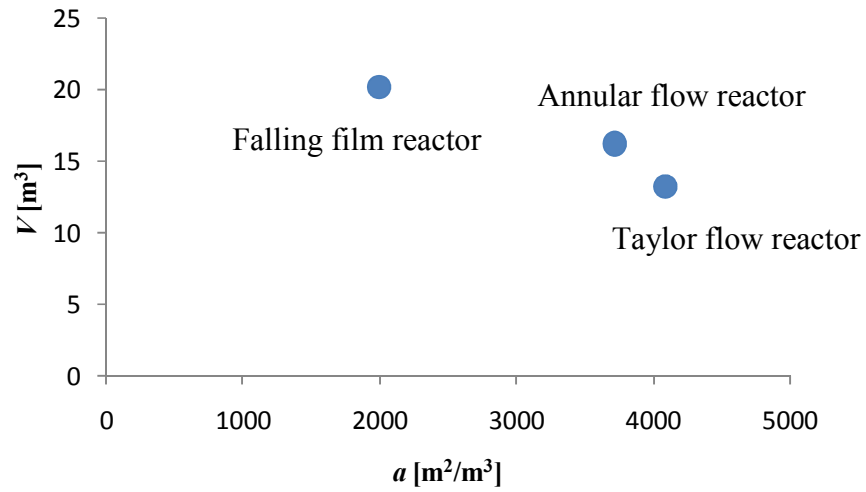


Figure 9.35 A plot of reactor volume changes with specific interfacial area. The data are from the base case for each reactor type. $d = 1\text{mm}$, $C_{MDEA,0} = 4.578\text{kmol}/\text{m}^3$, $k_I = 180\text{m}^3/(\text{kmol s})$, $Q_L = 0.194\text{m}^3/\text{s}$, $Q_G = 3.954\text{m}^3/\text{s}$.

9. Microreactor Application Study on Fuel Gas Absorption by Amine Solution

Table 9.16 Performance comparisons for the base case scenario for the three types of reactors. $d = 1\text{mm}$, $C_{MDEA,0} = 4.578\text{kmol/m}^3$, $k_I = 180\text{m}^3/(\text{kmol s})$, $Q_L = 0.194\text{m}^3/\text{s}$, $Q_G = 3.954\text{m}^3/\text{s}$.

Parameters	Falling film reactor	Taylor flow reactor	Annular flow reactor
Interfacial area $a \text{ m}^2/\text{m}^3$	2000	4091	3720
Reactor cross section area for flow $A \text{ m}^2$	14.4	14.52	1.452
Gas superficial velocity $v_G \text{ m/s}$	0.42	0.286	3.148
Liquid superficial velocity $v_L \text{ m/s}$	0.039	0.286	0.99
Cocurrent operation to achieve $Xe\%$	$V = 46\text{m}^3$, $t_G = 7.6\text{s}$	$V = 13.29\text{m}^3$, $t_G = 3.2\text{s}$	$V = 13.94 \text{ m}^3$, $t_G = 3.05\text{s}$
Countercurrent operation to achieve conversion specification of 99.8%	$V = 20.2\text{m}^3$, $t_G = 3.3\text{s}$	1 st stage: $V = 7.1\text{m}^3$, $t_G = 1.7\text{s}$ 2 nd stage: $V = 6.23\text{m}^3$, $t_G = 1.5\text{s}$	1 st stage: $V = 9.29 \text{ m}^3$, $t_G = 2.03\text{s}$ 2 nd stage: $V = 6.97 \text{ m}^3$, $t_G = 1.59\text{s}$
Reactor structures	3600 plates of 4m wide, separated from each other at 1mm. Film is formed on both sides.	18.49 million channels of 1mm diameter	1.85 million channels of 1mm diameter

9.7 Conclusions

In this chapter, the applicability of microreactors was investigated for an industrial process of CO₂ absorption into MDEA solvents. The operating conditions were from the same process that was operated in a conventional packed column. The system was able to be operated under Taylor, Taylor-annular and churn flow. Therefore, three types of reactors – falling film, Taylor flow and annular flow reactor - were studied. Cocurrent, countercurrent or virtual countercurrent operations were investigated for each type of reactor and some sensitivity studies were carried out.

9.7.1 Falling film reactor

- Falling film reactor can be operated both co- and countercurrently. In the former case, the equilibrium conversion X_e was achieved by $t_G = 7.6s$ in the base case scenario.
- Under countercurrent operation, it needed a reactor volume of 20.2m³ ($t_G = 3.3s$) to achieve the conversion specification of 99.8% (CO₂ < 50ppm at the reactor outlet).
- The reactor required 3600 plates of 4m width and there was 1mm separation between two adjacent plates.
- The reaction conversion was not found to be dependent on film thickness significantly when the gas and liquid residence time were kept constant. However, reducing the liquid film thickness by reducing the solvent supply enhanced solvent utilization significantly.
- The reaction conversion in countercurrent reactors was found to increase with reducing gas chamber size, increasing MDEA concentration and increasing reaction rate constant k_l .

9.7.2 Taylor flow reactor

- Taylor flow reactor can only be operated cocurrently. Equilibrium conversion was achieved by 3.2s in the base case scenario, a 58% save in time compared with falling film reactor.
- Multistage absorption with two absorbers arranged in a virtually countercurrent way was adopted to achieve 99.8% conversion specification, which required a total reactor volume of 13.3m³ (total $t_G = 3.2s$).
- 18.49 million channels of 1mm diameter and 0.92m height are needed for the reactor structure.

- Without changing the operating flowrates, smaller bubbles were found to contribute to higher conversion by providing larger specific area.
- The very small slugs resulting from the current operating conditions inhibit the liquid recirculation characteristic to Taylor flow.
- Higher conversion was observed at the same reactor height when more solvent was used because of higher X_e , larger amount of MDEA and improved liquid recirculation in the liquid slug.
- When larger channel is used, conversion is significantly reduced at the same reactor height due to the greatly reduced specific area.

9.7.3 Annular flow reactor

- Annular flow reactor can only be operated cocurrently. Equilibrium conversion was achieved by 3.05s for the base case scenario.
- Multistage absorption with two absorbers arranged in a virtually countercurrent way was adopted to achieve 99.8% conversion specification, which required a total reactor volume of 16.3m³ (total $t_G = 3.6$ s).
- 1.85 million channels of 1mm diameter and 11.3m height are required for the reactor. The effective cross sectional area is only 10% of the other two types (1.452m²) to obtain the high velocities to support annular flow.
- The effect of film thickness on reaction conversion is not significant.
- Larger channels can reduce the number of channels required to achieve the same reactor cross section but at the sacrifice of lowered gas conversion for the same reactor height.
- The annular flow was modelled as smooth film surrounding the gas core. There are uncertainties in the estimation of film thickness. And the factual specific area is expected to be larger than calculated as the films in annular flow usually present waves and ripples.

The comparison of the performance of the three reactors showed that every type of reactor had its advantages and disadvantages. The film reactor can be more easily realized due to the relatively easy manufacture and operation. However, the best performance was achieved by the Taylor flow microreactor due to the largest specific area and smallest reactor volume compared to the other reactor types. The two-stage operation suggested in Taylor flow would make the scale up of this reactor type difficult. This can be avoided if more liquid is used (see

discussion in Section 9.4.2.4) or the bubble and sizes are altered by using different inlet configuration (see discussion in Chapter 5-8).

Chapter 10
Conclusions and Recommendations for
Future Study

The advent of microengineering technology and the increasing demands on flow control, process intensification and new reactors for reactions that are unattainable in conventional reactors have been driving the development of microchemical systems, which are expected to achieve significant economic and environmental benefits. The industrial application of these system requires that the flow heat and mass transfer and reaction behaviour in them are well characterised and can be predicted. This thesis contributes to the development and application particularly of two-phase gas-liquid microreactors operating in Taylor flow by correlating the performance of the device to the design parameters and proposing simulation tools for the study.

10.1 Thesis summary

In the first part of the thesis the parameters affecting the gas-liquid flow patterns and the conditions necessary for having Taylor flow in microchannels were identified. In Chapter 3, the parameters influencing flow pattern transitions for adiabatic gas-liquid flow in microchannels were discussed. Channel size, phase superficial velocities, liquid phase surface tension, wall wettability and inlet conditions were found to affect the flow pattern formed while channel cross sectional geometry affected the patterns but to a lesser degree. Liquid viscosity and flow orientation with respect to gravity also seemed to play some role but the results were not conclusive. A universal flow regime map does not seem to exist and this was attributed to a lack of consistency in the inlets used in the various studies as well as to the effects of wall properties, such as wettability, contamination and roughness which were not usually varied systematically in the experimental studies or reported. From the different flow regime maps suggested, those using $U_{GS} - U_{LS}$ as coordinates represented better the transitions between patterns.

Chapter 4 dealt with the effects of inlet conditions on flow patterns and their transitions during gas-liquid flow in microchannels. Inlet conditions such as gas inlet size, inlet configuration and channel size were investigated experimentally. The flow patterns observed were bubbly, Taylor, churn, Taylor-annular and annular flow. It was found that increasing the size of the gas inlet increased the size of the bubbles formed and delayed the transition from Taylor to bubbly flow to higher superficial liquid velocities while it shifted the transition to Taylor-annular and churn flows to lower superficial gas velocities. Increasing the test channel size for the conditions tested, shifted the transition from Taylor to bubbly flow to lower superficial liquid velocities and the transition to Taylor-annular or churn flow to lower superficial gas velocities.

The inlet configuration also affected the bubble size but to a lesser degree than the inlet size.

In the following chapters microchannel reactors operating under Taylor flow were studied in more detail. In Chapter 5, a CFD model was formulated to investigate the Taylor flow formation mechanism and the resulting bubble sizes. The simulation was run in CFX using the interface tracking method of Volume of Fluid. A co-flow inlet configuration in a 1mm ID capillary with two gas nozzle sizes of 0.11mm and 0.34mm ID respectively was used. Air and three liquids-water, octane and “semi-octane”-were used as test fluids. Bubble formation followed a multi-stage mechanism while the bubble shape during formation deviated from the spherical one assumed in the literature. Bubble sizes were found to increase with increasing gas and decreasing liquid velocities and increasing nozzle size and nozzle wall thickness. From the fluid properties, surface tension was found to have a strong effect on bubble size but not density or viscosity. An increase in contact angle also increased bubble size. From the available literature correlations those that included phase fraction or ratios of superficial phase velocities were found to better predict the observed bubble sizes.

In Chapter 6 the effect of inlet conditions and design on the characteristics of Taylor flow were investigated experimentally. Three inlet configurations T-, Y- and M-junction and varying gas inlet and main channel sizes with hydraulic diameters 0.345mm, 0.577mm and 0.816mm were used. Bubble lengths were found to increase with increasing gas flowrate, gas inlet size, liquid surface tension and decreasing liquid flowrate. Little effect of liquid inlet size and channel orientation was observed. A single liquid inlet was found to produce narrower bubble length distribution compared to flow focusing inlets for in-house fabricated microchannels. From the different inlet configurations, the M-junction resulted in the largest bubbles and the Y-junction in the smallest ones particularly at low liquid flowrates. The experimental bubble sizes were tested against a number of literature correlations but the agreement was not very good. Two new correlations were developed for the T- and the Y-junctions to calculate the unit cell frequency from which the bubble length can be found. Bubble lengths predicted from these correlations were in good agreement with experimental ones obtained from video recordings. The correlations were used in the chapters later on to predict bubble size.

Continuing to the inlet design, the main channel and outlet design for Taylor flow microreactor was addressed in Chapter 7, where mass transfer and reaction under Taylor

flow were examined through a fast reaction system of CO₂ absorption into NaOH solution. Experimental and numerical investigations were carried out in single-channel microreactors of different diameter and geometry. The numerical model was formulated in the commercial software Comsol Multiphysics 3.3a using finite elements. Both the liquid and gas phases (a Taylor bubble unit cell) were solved so that the CO₂ concentration at the gas-liquid interface could be updated and was not considered constant as in the literature works. An acid quenching stream at the end of the main channel was found out to be necessary to terminate the reaction before the flow entered the gas-liquid separator. By reducing the channel dimension, mass transfer was improved due to the decreased diffusion path and increased specific interfacial area. In order to improve mass transfer, different reactor channel geometries were considered. A meandering channel geometry did not improve mass transfer as would be expected. However, a bifurcating channel geometry improved conversion because in the bifurcation new fresh interfaces are formed that enhance interfacial mass transfer and the slug size is reduced thus improving mixing. This was extremely important at high gas volume fractions when small bubble size was not possible. The simulation results agreed well with the experiments, suggesting that can be reliably used in further investigations.

Parametric studies on the reactor performance with and without a chemical reaction were carried out in Chapter 8 using the numerical model formulated in Chapter 7. Parameters investigated included bubble velocity, bubble geometry and capillary size. The reactor performance was assessed using the CO₂ absorption fraction $X\%$ and the liquid utilization index Ψ . It was found that CO₂ absorption fraction was significantly improved when reaction was present. The absorption fraction also increased with increasing bubble velocity, slug length and film thickness, while it decreased with increasing bubble length and unit cell length. Decreasing the channel size improved the absorption fraction when reaction was present but decreased it when there was no reaction. The effects of bubble velocity and slug length were relatively small while generally the effects on absorption fraction of the above parameters were more significant in the physical absorption cases. Similar to the absorption fraction, the liquid utilization index was found to be higher in the reaction cases, and increased with increasing bubble velocity and bubble length, and with decreasing slug length, film thickness, unit cell length and channel dimension. The effect of bubble length, slug length and film thickness was significant. When the reaction was absent, Ψ increased

with increasing bubble velocity, bubble length and channel dimension and decreasing slug length and unit cell length. And the effect of film thickness did not have a trend. Overall, the determinants in chemical and physical absorptions were the effective specific area and the mixing quality in the liquid slug respectively. The volumetric mass transfer coefficient at $0.3\text{-}1.5\text{s}^{-1}$ and the specific area at $1000\text{-}10000\text{m}^2/\text{m}^3$ achieved by this pattern were found to agree with literature values. With reaction present, CO_2 absorption was found to be enhanced at least three times, up to eighteen times.

In the last chapter the applicability of microstructured reactors was examined through an industrial system of fuel gas absorption in amine solutions. For the given operating conditions, the reactor could operate in Taylor, Taylor-annular and churn flow, which all involve formation of liquid films. Therefore, three types of reactors, namely falling film, Taylor flow and annular flow, were studied in detail. Reactor height (gas phase residence time) for both co- and countercurrent operations were evaluated. In Taylor and annular flow reactors that could not operate in countercurrent flow, a virtually countercurrent operation was implemented by using two-stage absorption.

Reactor performance comparison:

- The falling film reactor had the largest reactor volume (20.2m^3 for 1mm characteristic dimension) among the three. Its advantages were the countercurrent operation and the relatively simple manufacturing process. In addition, the amine usage could be potentially reduced in the falling film reactor.
- The Taylor flow reactor had the highest specific interfacial area and the smallest overall reactor volume (13.33m^3 for 1mm characteristic dimension) to reach the conversion specification. However, the absorption had to be completed using a multistage absorber due to the cocurrent operation at the very high gas to liquid volume ratio and a large number of channels (18.49million) were needed. In addition, the flow was potentially unstable due to bubble coalescence for the current very small liquid slugs while downstream gas-liquid separation was required for multistage operation.
- The annular flow reactor performed similarly to Taylor flow reactor with a total reactor volume of 16.55m^3 (for 1mm characteristic dimension). In the annular flow reactor the number of channels was reduced by tenfold compared to the Taylor flow one and it could be further reduced if higher specific area was obtained. This could be achieved by using featured channels. Also, the specific

area could be potentially increased by waves, ripples and entrained liquid droplets. However, it shared with Taylor flow the disadvantages of cocurrent operation and the need of gas-liquid separation for multistage absorption.

Although the falling film microreactor is comparatively easier to realize for this reaction system, Taylor flow microreactor offers the best reactor performance.

10.2 Recommendation for microreactor design

The selection of a microreactor for an operation greatly depends on the reaction system and the operating conditions. For example, for a kinetically controlled reaction, microreactors that improve mass transfer, such as Taylor flow, may not offer any benefits. Even when a mass transfer controlled reaction system is studied, as in Chapter 9, Taylor flow microreactor may not be a good candidate if multistage operation has to be used. Of course, apart from mass transfer intensification there may be other reasons to consider microreactors, such as small inventory, inherent safety etc.

The following opinions are made when only Taylor flow microreactor is to be studied for a suitable reaction system and under suitable operating conditions.

For processes without chemical reaction between a gas and a liquid phase, e.g. physical absorption between gas and liquid phase or chemical reaction in liquid phase only (where the gas phase is introduced to form Taylor bubbles and separate the liquid in slugs), the recirculation inside the liquid slug is important, especially the first recirculation, for the reactor performance (Chapter 8). Smaller unit cells are more beneficial as more “unit reactors” are working in parallel for a given reactor. Within each unit cell, the longer the slug length, the better the mass transfer as more contributions will come from the first circulation. The Taylor bubble size also has to be large enough to ensure that, when needed, there is sufficient gas component.

For processes involving gas-liquid two-phase reactions, specific interfacial area is important for the reactor performance (Chapter 8). Similarly, more unit cells are beneficial. In each unit cell, slug size should be minimized to improve the unit cell specific area provided that enough liquid reactant is available in the unit cell.

Bubble and slug lengths can be modified significantly by changing the gas to liquid flowrate ratio (Chapter 5 and 6). Any changes in the flowrates should, however, be within the reaction requirements for gas to liquid ratio (Chapter 8) and of course result in Taylor flow (Chapter 2 and 3). When the gas to liquid flowrate ratio is fixed, bubble and slug sizes can be adjusted by changing the gas inlet size (Chapter 5 and 6). Surface

tension is another way to modify bubble and slug lengths, by adding surface active additives in the liquid phase. In this case the effects of the additives on the reaction system and the physical properties of the liquid should be evaluated.

Although wettability and inlet configuration were found to play a small role on average bubble and slug lengths, they affected the size distribution which can lead in variations in the reactor performance, and need to be addressed during reactor design. When additional microreactor functionalities are involved, such as gas-liquid separation, heat transfer, on-line measurements, their impact on hydrodynamic and mass transfer would also need to be evaluated.

10.3 Recommendations for future study

Multiphase chemical reactions are a broad subject and in this thesis only the simplest system – non-catalytic reaction between gas and liquid phases – is investigated. There are abundant systems that are interesting such as gas-liquid homogeneously catalyzed reactions (e.g. chlorination of aromatics using a Lewis acid such as FeCl_3 as catalyst), gas-liquid heterogeneously catalyzed reactions (e.g. hydrogenations using noble metals as catalyst), liquid-liquid non-catalytic reactions (e.g. polymerizations of styrene in cyclohexane) and liquid-liquid catalytic reactions (e.g. canola oil reacts with methanol with sodium hydroxide as the catalyst). On one hand, work can be carried out for process intensification purposes to bring economic and environmental profit, such as to reduce reactor volume, save reactant and energy consumption, and improve conversion and selectivity. On the other hand, for multiphase reactions with unknown kinetics, microstructured devices can be used to explore the kinetics and reactor design parameters.

The results of this thesis are a good starting point for future investigations. For the same non-catalytic gas-liquid reaction system, the following suggestions are made. Firstly, a more efficient gas-liquid separator is needed so that the reaction can be terminated immediately and the quenching stream can be excluded. The idea of using a negative differential pressure as suggested in Section 2.6.2.3 offers a promising solution. Apart from terminating the contact between the two phases promptly, this idea can potentially reduce pressure fluctuations in the system by preventing the gas-liquid interface exiting the microchannel. For this type of outlet design more precise fabrication technology is needed than the one currently used. Secondly, further investigations in bubble break in bifurcating channels or any other main channel design that can largely increase the effective surface to volume ratio, which was found to be able to significantly enhance

the mass transfer in this thesis. Thirdly, the design of integrated heat management system that can improve the control of reaction temperature. The next stage of future work would be the microchannel reactor scale out design. This is mainly concerned with the design of the inlet manifold. A multi-layer microreactor concept, i.e. inlet, main channel and outlet are designated to different channel layers, seems interesting, which can guarantee the simultaneous contact of the two phases among different channels and make a common gas-liquid separator at the end possible. Of course, the common problem of fluids maldistribution in any scale-out design has to be resolved.

Investigations on functional elements, e.g. actuators, sensors, dispensers, mixers, filters and heat exchangers, will be needed to expand the applicability of microstructured devices and allow improved system control and operation.

In parallel with channel geometry, interface chemistry provides a useful tool to better manipulate the flow in microstructured devices. Channel surface treatment can adjust the hydrophilicity and hydrophobicity of the channel, and thus influence the flow pattern and its stability through contact angle (Chapters 3 and 4). Another interesting topic is to change the surface tension on the gas-liquid interface by using surfactants. Large surface tension could make some operations problematic, e.g. increase pressure fluctuations as the interface emerges at the inlet and bubbles form, make bubble split in bifurcating channels more difficult, and large bubble size at high gas to liquid flow ratio. Adding surfactants to reduce the surface tension can help to alleviate the above problems. However, the effect of surfactant addition needs to be clarified, e.g. Marangoni effects, whether the surfactant affects the reaction, while separation at the end will be more difficult.

In terms of flow hydrodynamics, velocity profiles and film thickness in microstructured devices play an important role on reactions, but are largely unexplored particularly in non-circular channels or channels with non-symmetric cross section that are common in microdevices. With the better availability of flow analysis devices, e.g. confocal micro-PIV, investigations in that area can bring important results that will help to better characterise the two-phase microreactors.

On the simulation side, the model can be expanded to include heat transfer phenomena, which are involved in most of the chemical reactions. When temperature effect is taken into account, there will be variations in fluid physical properties, gas volume and concentration gradients. How to integrate these changes are challenging but interesting work. The expanded model will be more applicable for multiphase reaction studies. For

10. Conclusions and Recommendations for Future Study

example, the desorption process can be simulated for the case study of fuel gas absorption in amines (Chapter 9).

Bibliography

- Akbar, M.K., Ghiaasiaan, S.M., 2006. Simulation of Taylor flow in capillaries based on the volume-of-fluid technique. *Ind. Eng. Chem. Res.* 45, 5396-5403.
- Akbar, M.K., Plummer, D.A., Ghiaasiaan, S.M., 2003. On gas-liquid two-phase flow regimes in microchannels. *Int. J. Multiphase Flow* 29, 855-865.
- Al-Rawashdeh, M., Hessel, V., Löb, P., Mevissen, K., Schönfelda, F., 2008. Pseudo 3-D simulation of a falling film microreactor based on realistic channel and film profiles. *Chem. Eng. Sci.* 63, 5149-5159.
- Amador, C., Salman, W., Sanganapiyapan, S., Gavriilidis, A., Angeli, P., 2004. Effect of gas-inlet conditions on the mechanism of Taylor flow formation. 5th Int. Conf. Multiphase Flow, Yokohama, Japan, paper No. 515.
- Aroonwilas, A., Veawab, A., Tontiwachwuthikul, P., 1999. Behaviour of the mass transfer coefficient of structured packings in CO₂ absorbers with chemical reaction. *Ind. Eng. Chem. Res.* 38, 2044-2050.
- Astarita, G., 1967. Mass transfer with chemical reaction. Elsevier: New York.
- Aussilous, P., Quéré, D., 2000. Quick deposition of a fluid on the wall of a tube. *Phys. Fluids* 12, 2367-2371.
- Barajas, A.M., Panton, R.L., 1993. The effects of contact angle on two-phase flow in capillary tubes. *Int. J. Multiphase Flow* 19, 337-346.
- Barnea, D., Luninski, Y., Taitel, Y., 1983. Flow pattern in horizontal and vertical two phase flow in small diameter pipes. *Can. J. Chem. Eng.* 61, 617-620.
- Becht, S., Franke, R., Geißelmann, A., Hahn, H., 2009. An industrial view of process intensification. *Chem. Eng. Process* 48, 329-332.
- Berčić, G., Pintar, A., 1997. The role of gas bubbles and liquid slug lengths on mass transport in the Taylor flow through capillaries. *Chem. Eng. Sci.* 52, 3709-3719.
- Bhunia, A., Pais, S.C., Kamotani, Y., Kim, I.H., 1998. Bubble formation in a coflow configuration in normal and reduced gravity. *AIChE J.* 44, 1495-1509.

Bibliography

- Bird, B.R., Stewart, W.E., Lightfoot, E.N., 2002. *Transport Phenomena*, John Wiley: New York.
- Blauwholf, P.M.M., Versteeg, G.F., van Swaaij, W.P.M., 1984. A study on the reaction between CO₂ and alkanolamines in aqueous solutions. *Chem. Eng. Sci.* 39, 207–225.
- Bousman, W.S., McQuille, J.B., Witte, L.C., 1996. Gas-liquid flow patterns in microgravity: Effects of tube diameter, liquid viscosity, and surface tension. *Int. J. Multiphase Flow* 22, 1035-1053.
- Brauner, N., Moalem-Maron, D., 1992. Identification of the range of “small diameter” conduits, regarding two-phase flow pattern transitions. *Int. Commun. Heat Mass Transfer* 19, 29-39.
- Bretherton, F.P., 1961. The motion of long bubbles in tubes. *J. Fluid Mech.* 10, 166-188.
- Brophy, J., 2005. The microchannel revolution. *Focus on Catalysts* 2, 1.
- Byakova, A.V., Gnyloskurenko, S.V., Nakamura, T., Raychenko, O.I., 2003. Influence of wetting conditions on bubble formation at orifice in an inviscid liquid: Mechanism of bubble evolution. *Colloids Surf. A* 229, 19-32.
- Chambers, R.D., Holling, D., Sandford, G., Batsanov, A.S., Howard, J.A.K., 2004. Elemental fluorine part 15. Selective direct fluorination of quinoline derivatives. *J. Fluorine Chem.* 125, 661-671.
- Chen, L., Tian, Y.S., Karayiannis, T.G., 2006. The effect of tube diameter on vertical two-phase regimes in small tubes. *Int. J. Heat Mass Transfer* 49, 4220-4230.
- Chen, W.L., Twu, M.C., Pan, C., 2002. Gas-liquid two-phase flow in micro-channels. *Int. J. Multiphase Flow* 28, 1235-1247.
- Chung, P.M.Y, Kawaji, M., 2004. The effect of channel diameter on adiabatic two-phase flow characteristics in microchannels. *Int. J. Multiphase Flow* 30, 735-761.
- Coleman, J.W., Garimella, S., 1999. Characterization of two-phase flow patterns in small diameter round and rectangular tubes. *Int. J. Heat Mass Transfer* 42, 2869-2881.

Bibliography

- Collier, J.G., Thome, J.R., 1994. Convective boiling and condensation. 3rd edn. Oxford: Clarendon Press.
- Collins, R., 1978. The motion of large bubbles rising through liquid flowing in a tube. *J. Fluid Mech.* 89, 497-514.
- Commenge, J.M., Falk, L., Corriou, J.P., Matlosz, M., 2005. Analysis of microstructured reactor characteristics for process miniaturization and intensification. *Chem. Eng. Technol.* 28, 446-458.
- Comyns, A.E., 2007. Microstructured reactors: part 2. Focus on catalysts 9, 1.
- Cox, B.G., 1964. An experimental investigation of the streamlines in viscous fluid expelled from a tube. *J. Fluid Mech.* 1964, 193-200.
- Cubaud, T., Ho, C.M., 2004. Transport of bubbles in square microchannels. *Phys. Fluids* 16, 4575-4585.
- Cubaud, T., Tatineni, M., Zhong, X., Ho, C.M., 2005. Bubble dispenser in microfluidic devices. *Phys. Rev. E* 72, 037302.
- Cubaud, T., Ulmanella, U., Ho, C.M., 2006. Two-phase flow in microchannels with surface modifications. *Fluid Dyn. Res.* 38, 772-786.
- Dabir, B., Riazi, M.R., Davoudirad, H.R., 1996. Modelling of falling film reactors. *Chem. Eng. Sci.* 51, 2553-2558.
- Damianides, C.A., 1987. Horizontal two-phase flow of air-water mixtures in small diameter tubes and compact heat exchangers, Ph.D. thesis, University of Illinois at Urbana-Champaign.
- Damianides, C.A., Westwater, J.W., 1988. Two-phase flow patterns in a compact heat exchanger and in small tubes. *Proc. UK National Heat Transfer Cont.*, 2nd, 1257-1268.
- Dankwerts, P.V., 1970. Gas-liquid reactions. McGraw-Hill: New York.
- de Mas, N., Günther, A., Schmidt, M.A., Jensen, L.F., 2003a. Microfabricated multiphase reactors for the selective direct fluorination of aromatics. *Ind. Eng. Chem. Res.* 42, 698-710.

- de Mas, N., Günther, A., Schmidt, M.A., Jensen, L.F., 2003b. Scalable microfabricated multiphase reactors for direct fluorination reactions. The 12th Int. Conf. on Solid State Sensors, Actuators and Microsystems, Boston, June 8-12.
- Donaldson, T.L., Nguyen, Y.N., 1980. Carbon dioxide reaction kinetics and transport in aqueous amine membranes. *Ind. Eng. Chem. Fundam.* 19, 260-266.
- Fabre, J., Liné, A., 1992. Modelling of two-phase slug flow. *Annu. Rev. Fluid Mech.* 24, 21-46.
- Fairbrother, F., Stubbs, A.E., 1935. Studies in electro-endosmosis -VII, the “bubble tube” method of measurement. *J. Chem. Soc.* 1, 527–529.
- Farrauto, R.J., Bartholomew, C.H., 1997. *Fundamentals of industrial catalytic processes.* Blackie Academic & Professional: London.
- Feron, P.H.M., Jansen, A.E., 2002. *Purif. Tech.* 27, 231.
- Freguia, S., Rochelle, G.T., 2003. Modelling of CO₂ capture by aqueous monoethanolamine. *AIChE J.* 49, 1676-1686.
- Fukano, T., Kariyasaki, A., 1993. Characteristics of gas-liquid two-phase flow in a capillary. *Nucl. Eng. Des.* 141, 59-68.
- Fukano, T., Kariyasaki, A., Kagawa, M., 1989. Flow patterns and pressure drop in isothermal gas-liquid cocurrent flow in a horizontal capillary tube. *ANS Proc. National Heat Transfer Conference: Technical Sessions*, 153-161.
- Furukawa, T., Fukano, T., 2001. Effects of liquid viscosity on flow patterns in vertical upward gas-liquid two-phase flow. *Int. J. Multiphase Flow* 27, 1109-1126.
- Galbiati, L., Andreini, P., 1992. Flow pattern transition for vertical downward two-phase flow in capillary tubes. Inlet mixing effects. *Int. Commun. Heat Mass Transfer* 19, 791-799.
- Galbiati, L., Andreini, P., 1994. Flow pattern transition for horizontal air-water flow in capillary tubes. A microgravity equivalent system simulation. *Int. Commun. Heat Mass Transfer* 21, 461-468.

- Garstecki, P., Fuerstman, M.J., Stone, H.A., Whitesides, G.M., 2006. Formation of droplets and bubbles in a microfluidic T-junction – scaling and mechanism of break-up. *Lab Chip* 6, 437-446.
- Ghiaasiaan, S.M., Abdel-Khalik, S.I., 2001. Two-phase flow in microchannels. *Adv. Heat Transfer* 34, 145-254.
- Giavedoni, M.D., Saita, F.A., 1997. The axisymmetric and plane case of a gas phase steadily displacing a Newtonian liquid – a simultaneous solution to the governing equations. *Phys. Fluids* 9, 2420–2428.
- Giavedoni, M.D., Saita, F.A., 1999. The rear meniscus of a long bubble steadily displacing a Newtonian liquid in a capillary tube. *Phys. Fluids* 11, 786–794.
- Gnyloskurenko, S.V., Byakova, A.V., Raychenko, O.I., Nakamura, T., 2003. Influence of wetting conditions on bubble formation at orifice in an inviscid liquid. Transformation of bubble shape and size. *Colloids Surf. A* 218, 73-87.
- Gregor, C., Stojan, P., Lztok, T., 2001. Coupling of the interface tracking and the two-fluid models for the simulations of incompressible two-phase flow. *J. Comput. Phys.* 171, 776–804.
- Günther, A., Jhunjunwala, M., Schmidt, M.A., Jensen, K.F., 2003. Liquid mixing using inert gas and integrated gas-liquid separator. 7th Int. Conf. on Miniaturized Chemical and Biochemical Analysis Systems, October 5-9, Squaw Valley, California USA, 9743611.
- Günther, A., Jhunjunwala, M., Thalmann, M., Schmidt, M.A., Jensen, K. F., 2005. Micromixing of miscible liquids in segmented gas-liquid flow. *Langmuir* 21, 1547-1555.
- Haimour, N., Bidarian, A., Sandall, O.C., 1987. Kinetics of the reaction between carbon dioxide and methyldiethanolamine. *Chem. Eng. Sci.* 42, 1393-1398.
- Halpern, D., Jensen, O.E., Grotberg, J.B., 1998. A theoretical study of surfactant and liquid delivery into the lung. *J. Appl. Physiol.* 85, 333-352.
- Hardt, S., Doffing, F., Pennemann, H., 2002. Simulation of hydrodynamic dispersion in gas-liquid micro reactors. *Proceedings, 5th Int. Conf. on Modeling and Simulation, San Juan, Puerto Rico, 22-25 April, Computational Publications: Boston, 54-57.*

Hassan, I., Vaillancourt, M., Pehlivan, K., 2005. Two-phase flow regime transitions in microchannels: a comparative experimental study. *Microscale Therm. Eng.* 9, 165-182.

Haverkamp, V., Hessel, V., Löwe, H., Menges, G., Warnier, M.J.F., Rebrow, E.V., de Croon, M.H.J.M., Schouten, J.C., Liauw, M.A., 2006. Hydrodynamics and mixer-induced bubble formation in micro bubble columns with single and multiple-channels. *Chem. Eng. Technol.* 29, 1015-1026.

Hazel, A.L., Heil, M., 2002. The steady propagation of a semi-infinite bubble into a tube of elliptical or rectangular cross-section. *J. Fluid Mech.* 470, 91–114.

Heiszwolf, J.J., Engelvaart, L.B., van der Eijnden, M.G., Kreutzer, M.T., Kapteijn, F., Moulijn, J.A., 2001. Hydrodynamic aspects of the monolith loop reactor. *Chem. Eng. Sci.* 56, 805–812.

Hessel, V., Angeli, P., Gavriilidis, A., Löwe, H., 2005. Gas-liquid and gas-liquid-solid microstructured reactors: contacting principles and applications. *Ind. Eng. Chem. Res.* 44, 9750-9769.

Hessel, V., Ehrfeld, W., Herweck, T., Haverkamp, V., Löwe, H., Schiewe, J., Wille, Ch., 2000. Gas/liquid microreactors: hydrodynamics and mass transfer. Proceedings, IMRET 4, Atlanta, GA, March 5-9, AIChE: New York, 174-186.

Irandoost, S., Andersson, B., 1989. Liquid film in Taylor flow through a capillary. *Ind. Eng. Chem. Res.* 28, 1684-1688.

Irandoost, S., Ertle, S., Andersson, B., 1992. Gas liquid mass transfer of Taylor flow through a capillary. *Can. J. Chem. Eng.* 70, 115.

Jähnisch, K., Baerns, M., Hessel, V., Ehrfeld, W., Haverkamp, V., Löwe, H., Wille, C., Guber, A., 2000. Direct fluorination of toluene using elemental fluorine in gas-liquid microreactors. *J. Fluorine Chem.* 105, 117-128.

Jähnisch, K., Hessel, V., Löwe, H., Baerns, M., 2004. Chemistry in Microstructured reactors. *Angew. Chem. Int.* 43, 406-446.

Jayawardena, S.S., Balakotaiah, V., Witte, L.C., 1997. Flow pattern transition maps for microgravity two-phase flows. *AIChE J.* 43, 6137-1640.

Jensen, K.F., 2001. Microreaction engineering – is small better? *Chem. Eng. Sci.* 56, 293-303.

Jensen, M.J., 2002. Bubbles in microchannels. Mikroelektronik centret – MIC Technical University of Denmark-Master Project, c960853.

Jiang, F., Drese, K. S., Hardt, S., Küpper, M., Schönfeld, F., 2004. Helical flows and chaotic mixing in curved micro channels. *AIChE J.* 50, 2297-2305.

Karimi, G., Kawaji, M., 1998. An experimental study of freely falling films in a vertical tube. *Chem. Eng. Sci.* 53, 3501-3512.

Kawahara, A., Chung, P.M.-Y., Kawaji, M., 2002. Investigation of two-phase flow pattern, void fraction and pressure drop in a microchannel. *Int. J. Multiphase Flow* 28, 1411-1435.

Khan, S.A., Günther, A., Schmidt, M.A., Jensen, K.F., 2004. Microfluidic Synthesis of Colloidal Silica. *Langmuir* 20, 8604-8611.

Kim, I., Kamotani, Y., Ostrach, S., 1994. Modelling bubble and drop formation in flowing liquids in microgravity. *AIChE J.* 40, 19-28.

Kolb, W.B., Cerro, R.L., 1991. Coating the inside of a capillary of square cross-section. *Chem. Eng. Sci.* 46, 2181–2195.

Kreutzer, M.T., 2003. Hydrodynamics of Taylor flow in capillaries and monolith reactors. Delft University Press, Delft.

Kreutzer, M.T., Kapteijn, F., Moulijn, J.A., Kleijn, C.R., Heiszwolf, J.J., 2005a. Inertial and interfacial effects on pressure drop of Taylor flow in capillaries. *AIChE J.* 51, 2428-2440.

Kreutzer, M.T., Kapteijn, F., Moulijn, J.A., 2005b. Multiphase monolith reactors: Chemical reaction engineering of segmented flow in microchannels. *Chem. Eng. Sci.* 60, 5895-5916.

Kreutzer, M.T., Bakker, J.J.W., Kapteijn, F., Moulijn, J.A., 2005c. Scaling-up multiphase monolith reactors: linking residence time distribution and feed maldistribution. *Ind. Eng. Chem. Res.* 44, 4898-4913.

- Kumar, R., Kuloor, N.R., 1967. Chem. Technol. 19, 733.
- Kumar, V., Vashisth, S., Hoarau, Y., Nigam, K.D.P., 2007. Slug flow in curved microreactors: hydrodynamic study. Chem. Eng. Sci. 62, 7494-7504.
- Laborie, S., Cabassud, C., Durand-Bourlier, L., Laine, J.M., 1999. Characterization of gas-liquid two-phase flow inside capillaries. Chem. Eng. Sci. 54, 5723-5735.
- Lee, C.Y., Lee, S.Y., 2006. Influence of interfacial tension on transition of two-phase flow pattern in mini-channels. 6th Int. Conf. Multiphase Flow, S7_Wed_A_31.
- Lee, C.Y., Lee, S.Y., 2008. Influence of surface wettability on transition of two-phase flow pattern in round mini-channels. Int. J. Multiphase Flow 34, 706-711.
- Lettel, R.J., van Swaaij, W.P.M., Versteeg, G.F., 1990. Kinetics of carbon dioxide with tertiary amines in aqueous solution. AIChE J. 36, 1633-1640.
- Liao, C.H., Li, M.H., 2002. Kinetics of absorption of carbon dioxide into aqueous solutions of monoethanolamine + N-methyldiethanolamine. Chem. Eng. Sci. 57, 4569-4582.
- Lida, K., Chastek, T.Q., Beers, K.L., Cavicchi, K.A., Chunc, J., Fasolkaa, M.J., 2008. Living anionic polymerization using a microfluidic reactor. Lab Chip 9, 339-345.
- Link, D., Anna, S.L., Weitz, D., Stone, H.A., 2004. Geometric mediated breakup of drops in microfluidic devices. Phys. Rev. Lett. 92, 054503.
- Liu, H., Vando, C.O., Krishna, R., 2005. Hydrodynamics of Taylor flow in vertical capillaries: flow regimes, bubble rise velocity, liquid slug length, and pressure drop. Ind. Eng. Chem. Res. 44, 4884-4897.
- Löb, P., Löwe, H., Hessel, V., 2004. Fluorinations, chlorinations and brominations of organo compounds in microstructured reactors. J. Fluorine Chem. 125, 1677-1694.
- Losey, M.W., Jackman, R.J., Firebaugh, S.L., 2002. Design and fabrication of microfluidic devices for multiphase mixing and reaction. J. Microelectromechanical Sys. 11, 709-717.

Bibliography

- Mandhane, J.M., Gregory, G.A., Aziz, K., 1974. A flow pattern map for gas-liquid flow in horizontal pipes. *Int. J. Multiphase Flow* 1, 537-553.
- Mantle, M.D., Sederman, A.J., Gladden, L.F., 2002. Dynamic MRI visualization of two-phase flow in a ceramic monolith. *AIChE J.* 48, 909-912.
- Martinez, M.J., Udell, K., 1989. Boundary integral analysis of the creeping flow of long bubbles in capillaries. *Trans. ASME, J. Appl. Mech.* 56, 211-217.
- Mishima, K., Hibiki, T., 1996. Some characteristics of air-water two-phase flow in small diameter vertical tubes. *Int. J. Multiphase Flow* 22, 703-712.
- Mishima, K., Hibiki, T., Nishihara, H., 1993. Some characteristics of gas-liquid flow in narrow rectangular ducts. *Int. J. Multiphase Flow* 19, 115-124.
- Mishima, K., Ishii, M., 1984. Flow regime transition criteria for upward two-phase flow in vertical tubes. *Int. J. Heat Mass Transfer* 27, 723-737.
- Müller, A., Cominos, V., Horn, B., Ziogas, A., Jähnisch, K., Grosser, V., Hillmann, V., Jam, K.A., Bazzanella, A., Rinke, G., Kraut, M., 2005. Fluidic bus system for chemical micro process engineering in the laboratory and for small-scale production. *Chem. Eng. J.* 107, 205-214.
- Nahral, H.K., Kamotani, Y., 2000. Bubble formation from wall orifice in liquid cross-flow under low gravity. *Chem. Eng. Sci.* 55, 4653-4665.
- Nicklin, D.J., 1962. Two phase flow in vertical tubes. *T. I. Chem. Eng.* 40, 61-68.
- Pehlivan, K., 2003. Experimental study on two-phase flow regimes and pressure drop in mini- and micro-channels, Masters thesis, Concordia University, Montreal, Quebec, Canada.
- Oyenekan, B.A., Rochelle, G.T., 2006. *Ind.Eng. Chem. Res.* 45, 2457-2464.
- Pinsent, B.R.W., Pearson, L., Roughton, F.J.W., 1956. The kinetics of combination of carbon dioxide with hydroxide ions. *Trans. Faraday Soc.* 52, 1512-1520.
- Pohorecki, R., Moniuk, W., 1988. Kinetics of reaction between carbon dioxide and hydroxyl ions in aqueous electrolyte solutions. *Chem. Eng. Sci.* 43, 1677-1684.

- Pohorecki, R., Sobieszuk, P., Kula, K., Moniuk, W., Zieliński, M., Cygański, P., Gawiński, P., 2008. Hydrodynamic regimes of gas-liquid flow in a microreactor channel. *Chem. Eng. J.* 135S, S185-S190.
- Qian, D., Lawal, A., 2006. Numerical study on gas and liquid slugs for Taylor flow in a T-junction microchannel. *Chem. Eng. Sci.* 61, 7609-7625.
- Ramshaw, C., 1995. The incentive for process intensification. *Proceedings, 1st Int. Conf. Proc. Intensif. for Chem. Ind.*, 18, BHR Group, London, p. 1.
- Rezkallah, K.S., 1996. Weber number based flow-pattern maps for liquid-gas flows at microgravity. *Int. J. Multiphase Flow* 22, 1265-1270.
- Rinker, E.B., Ashour, S.S., Sandall, O.C., 1995. Kinetics and modelling of carbon dioxide absorption into aqueous solutions of N-methyldiethanolamine. *Chem. Eng. Sci.* 50, 755-768.
- Rinker, E.B., Oelschlager, D.W., Colussi, A.T., Henry, K.R., Sandall, O.C., 1994. Viscosity, density and surface tension of binary mixtures of water and N-methyldiethanolamine and water and diethanolamine and tertiary mixtures of these amines with water over the temperature range 20-100°C. *J. Chem. Eng Data* 39, 392-395.
- Salman, W., Angeli, P., 2005. Characterization and modelling of Taylor flow in small circular channels for the purpose of sequential screening. Ph.D. thesis, University College London, London.
- Salman, W., Gavriilidis, A., Angeli, P., 2004. A model for predicting axial mixing during gas-liquid Taylor flow in microchannels at low Bodenstein numbers. *Chem. Eng. J.* 101, 391-396.
- Salman, W., Gavriilidis, A., Angeli, P., 2006. On the formation of Taylor bubbles in small tubes. *Chem. Eng. Sci.* 61, 6653 – 6666.
- Salman, W., Gavriilidis, A., Angeli, P., 2007. Axial mass transfer in Taylor flow through circular microchannels. *AIChE J.* 53, 1413-1428.
- Schumpe, A., 1993. The estimation of gas solubilities in salt solutions. *Chem. Eng. Sci.* 48, 153-158.

- Serizawa, A., Feng, Z., Kawara, Z., 2002. Two-phase flow in microchannels. *Exp. Therm Fluid Sci.* 26, 703-714.
- Song, H., Tice, D.J., Ismagilov, R.F., 2003. A microfluidic system for controlling reaction networks in time. *Angew. Chem.* 115, 792-796.
- Stankiewicz, A.I., Moulijn, J.A., 2000. Process intensification: transforming chemical engineering. *Chem. Eng. Prog.* 96, 22-34.
- Suo, M., Griffith, P., 1964. Two-phase flow in capillary tubes. *J. Basic Eng.* 86, 576-582.
- Taha, T., Cui, Z.F., 2006a. CFD modelling of slug flow inside square capillaries. *Chem. Eng. Sci.* 61, 665-675.
- Taha, T., Cui, Z.F., 2006b. CFD modelling of slug flow in vertical tubes. *Chem. Eng. Sci.* 61, 676-687.
- Taitel, Y., Barnea, D., Dukler, A.E., 1980. Modelling flow pattern transitions for steady upward gas-liquid flow in vertical tubes. *AIChE J.* 26, 345-354.
- Taitel, Y., Dukler, A.E., 1976. A model for predicting flow regime transitions in horizontal and near horizontal gas-liquid flow. *AIChE J.* 22, 47-55.
- Tamimi, A., Rinker, E.B., Sandall, O.C., 1994a. Diffusion coefficients for H₂S, CO₂ and N₂O in water over the temperature range 293-368K. *J. Chem. Eng. Data* 39, 330-332.
- Tamimi, A., Rinker, E.B., Sandall, O.C., 1994b. Diffusivity of N₂O in aqueous solutions of methyldiethanolamine and diethanolamine from 293K to 368K. *J. Chem. Eng. Data* 39, 396-398.
- Tan, J., Li S.W., Wang, K., Luo, G.S., 2009. Gas-liquid flow in T-junction microfluidic devices with a new perpendicular rupturing flow route. *Chem. Eng. J.* 146, 428-433.
- Taylor, G.I., 1961. Deposition of a viscous fluid on the wall of a tube. *J. Fluid Mech.* 10, 161.
- Teh, S.Y., Lin, R., Hung, L.H., Lee, A.P., 2008. Droplet microfluidics. *Lab Chip* 8, 198-220.

Bibliography

- Thulasidas, T.C., Abraham, M.A., Cerro, R.L., 1995. Bubble-train flow in capillaries of circular and square cross section. *Chem. Eng. Sci.* 50, 183-199.
- Thulasidas, T.C., Abraham, M.A., Cerro, R.L., 1997. Flow patterns in liquid slugs during bubble-train flow inside capillaries. *Chem. Eng. Sci.* 52, 2947-2962.
- Tobiesen, F.A., Svendsen, H.F., 2006. *Ind.Eng. Chem. Res.* 45, 2489-2496.
- Tomcej, R., Otto, F., 1989. Absorption of CO₂ and N₂O into aqueous solutions of methyldiethanolamine. *AIChE J.* 35, 861-864.
- Triplett, K.A., Ghiaasiaan, S.M., Abdel-Khalik, S.I., Sadowski, D.L., 1999. Gas-liquid two-phase flow in microchannels Part I: two-phase flow patterns. *Int. J. Multiphase Flow* 25, 377-394.
- Tseng, Y.T., Tseng, F.G., Chen, Y.F., Chieng C.C., 2004. Fundamental studies on micro-droplet movement by Marangoni and capillary effects. *Sensors Actuators A* 114, 292-301.
- Tsoligkas, A.N., Simmons, M.J.H., Wood, J., 2007. Influence of orientation upon the hydrodynamics of gas-liquid flow for square channels in monolith supports. *Chem. Eng. Sci.* 62, 4365-4378.
- van Baten, J.M., Krishna, R., 2004. CFD simulations of mass transfer from Taylor bubbles rising in circular capillaries. *Chem. Eng. Sci.* 59, 2535-2545.
- van Baten, J.M., Krishna, R., 2005. CFD simulations of wall mass transfer for Taylor flow in circular capillaries. *Chem. Eng. Sci.* 60, 1117-1126.
- van Steijn, V., Kreutzer, M.T., Kleijn, C.R., 2008. Velocity fluctuations of segmented flow in microchannels. *Chem. Eng. J.* 135S, S159-S165.
- Vandu, C.O., Ellenberger, J., Krishna, R., 2005a. Hydrodynamics and mass transfer in an upflow monolith loop reactor. *Chem. Eng. Process.* 44, 363-374.
- Vandu, C.O., Liu, H., Krishna, R., 2005b. Mass transfer from Taylor bubbles rising in single capillaries. *Chem. Eng. Process.* 60, 6430-6437.

- Vankayala, B.K., Löb, P., Hessel, V., Menges, G., Hofmann, C., Metzke, D., Krtschil, U., Kost, H.J., 2007. Scale-up of process intensifying falling film microreactors to pilot production scale. *Int. J. Chem. React. Eng.* 5, A91.
- Wada, Y., Schmidt, M.A., Jensen, K.F., 2006. Flow distribution and ozonolysis in gas-liquid multichannel microreactors. *Ind. Eng. Chem. Res.* 45, 8036-8042.
- Waelchli, S., von Rohr, P.R., 2006. Two-phase flow characteristics in gas-liquid microreactors. *Int. J. Multiphase Flow* 32, 791-806.
- Wallis, G.B., 1969. One-dimensional two-phase flow. McGraw Hill, New York.
- Walters, J.K., Davidson, J.F., 1963. The initial motion of a gas bubble formed in an inviscid liquid, Part 2. The three-dimensional bubble and the toroidal bubble. *Fluid Mech.* 17, 321-336.
- Weber, M.W., Shandas, R., 2007. Computational fluid dynamics analysis of microbubble formation in microfluidic flow-focusing devices. *Microfluid Nanofluid* 3, 195-206.
- Wenn, D.A., Shaw, J.E.A., Mackenzie, B., 2003. A mesh microcontactor for 2-phase reactions. *Lab Chip* 3, 180-186.
- Wilke, C.R., 1950. A viscosity equation for gas mixtures. *J. Chem. Phys.* 18, 517-519.
- Xiong, R., Bai, M., Chung, J.N., 2007. Formation of bubbles in a simple co-flowing micro-channel. *J. Micromech. Microeng.* 17, 1002-1011.
- Xu, J., 1999. Experimental study on gas-liquid two-phase flow regimes in rectangular channels with mini caps. *Int. J. Heat Fluid Flow* 20, 422-428.
- Yang, C.Y, Shieh, C.C, 2001. Flow pattern of air-water and two-phase R-134a in small circular tubes. *Int. J. Multiphase Flow* 27, 1163-1177.
- Yen, B.K.H., Günther, A., Schmidt, M.A., Jensen, K.F., Bawendi, M.G., 2005. A microfabricated gas-liquid segmented flow reactor for high-temperature synthesis: the case of CdSe quantum dots. *Angew. Chem. Int. Ed.* 44, 5447-5451.

Bibliography

- Yue, J., Chen, G., Yuan, Q., Luo, L., Gonthier, Y., 2007. Hydrodynamics and mass transfer characteristics in gas-liquid flow through a rectangular microchannel. *Chem. Eng. Sci.* 62, 2096-2108.
- Yue, J., Luo, L., Gonthier, Y., Chen, G., Yuan, Q., 2008. An experimental investigation of gas-liquid two-phase flow in single microchannel contactors. *Chem. Eng. Sci.* 63, 4189-4202.
- Zanfir, M., Gavriilidis, A., Wille. Ch., Hessel, V., 2005. Carbon dioxide absorption in a falling film microstructured reactor: experiments and modeling. *Ind. Eng. Chem. Res.* 44, 1742-1751.
- Zhang, H., Chen, G., Yue, J., Yuan, Q., 2009. Hydrodynamics and mass transfer of gas-liquid flow in a falling film microreactor. *AIChE J.* 55, 1110-1120.
- Zhao, J.F., Hu W.R., 2000. Slug to annular flow transition of microgravity two-phase flow. *Int. J. Multiphase Flow* 26, 1295-1304.
- Zhao, T.S., Bi, Q.C., 2001. Co-current air-water two-phase flow patterns in vertical triangular microchannels. *Int. J. Multiphase Flow* 27, 765-782.
- Zhao, L., Rezkallah K.S., 1993. Gas-liquid flow patterns at microgravity conditions. *Int. J. Multiphase Flow* 19, 751-763.

Appendix

Nomenclature

A	Cross sectional area, m^2
d	Diameter, m
C^*	Concentration, mol/l
D	Diffusivity, m^2/s
f	Frequency, 1/s
L	Length, m
n	Number of mole, mol
Q	Volumetric flowrate, m^3/s
r	Radius, m
U	Velocity, m/s
V	Volume, m^3
X	CO ₂ absorption fraction, -
y	CO ₂ volume fraction in the gas mixture, -

Greek Symbols

μ	Dynamic viscosity, Pa·s
σ	Surface tension, N/m
δ	Film thickness, m
ε	Volume fraction, -
δ	Film thickness, m

Dimensionless numbers

Ca	Capillary number, $Ca = \frac{\mu_L U_B}{\sigma}$
------	---

Subscripts

B	Bubble
C	Channel or capillary
Cap	Bubble caps
CO_2	Related to carbon dioxide
$film$	Film region
G	Gas
in	Inlet

<i>L</i>	Liquid
<i>Out</i>	Outlet
<i>S</i>	Slug
<i>UC</i>	Unit cell

APPENDIX A CALCULATING BUBBLE/SLUG LENGTH FROM BUBBLE
 FREQUENCY

Unit cell geometry is presented in Figure A-1, with unit cell length, bubble length and film thickness characterizing the flow.

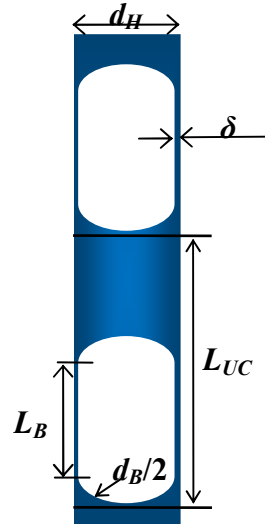


Figure A-1 Schematic plot of unit cell geometry.

Unit cell length is calculated from unit cell frequency using Eq. A-1 (Liu et al., 2005). Bubble frequency can also be used.

$$L_{UC} = \frac{U_B}{f_{UC}} \quad \text{Eq. A-1}$$

Bubble velocity can be calculated from Eq. A-2 (Liu et al., 2005), valid for capillary number ranging from 0.0002 to 0.39. U_{TP} is defined as in Eq. A-3. Unit cell frequency can be either recorded during experiment or calculated using correlations derived in Chapter 6 (Eq. 6.1 and Eq. 6.2).

$$U_B = \frac{l}{1 - 0.61Ca^{0.33}} U_{TP} \quad \text{Eq. A-2}$$

$$U_{TP} = \frac{Q_G + Q_L}{A_C} \quad \text{Eq. A-3}$$

Long bubble length (including two bubble caps lengths) is then obtained from Eq. A-4.

$$L_{B'} = L_B + d_B = L_{UC} \epsilon_B \quad \text{Eq. A-4}$$

To get the bubble cap diameter d_B , ($d_H - 2\delta$), film thickness has to be obtained, and that from Aussillous and Quéré, (2000) is used, as in Eq. A-5.

$$\delta = \frac{0.66Ca^{2/3}}{\left(1 + 3.33Ca^{2/3}\right)} d_H \quad \text{Eq. A-5}$$

Bubble volume fraction is calculated as shown in Eq. A-6.

$$\varepsilon_B = \frac{Q_G}{Q_G + Q_L} \quad \text{Eq. A-6}$$

From Eq. A-1 to Eq. A-6, unit cell length and bubble/slug length are obtained from the unit cell frequency. In most cases, the specific area of the unit cell is of interest and can be calculated using Eq. A-7, where A_{bubble} and A_{cap} are the interfacial area of the bubble and the caps respectively.

$$\alpha = \frac{A_{bubble} + A_{cap}}{V_{UC}} = \frac{\pi d_B L_B + \pi d_B^2}{\frac{\pi}{4} d_H^2 L_{UC}} = \frac{4\left((d_H - 2\delta)L_B + (d_H - 2\delta)^2\right)}{d_H^2 L_{UC}} \quad \text{Eq. A-7}$$

APPENDIX B COMPARISON OF METHODS TO UPDATE THE GAS-LIQUID INTERFACIAL CONCENTRATION

In the numerical study of Taylor flow mass transfer, [Van Baten and Krishna \(2005\)](#) formulated a single domain model (solve for liquid phase only) and used a constant tracer concentration at the gas-liquid interface. When reaction occurs in the liquid phase, as in the current investigation, the same boundary condition leads to $> 100\%$ CO_2 conversion as shown in Figure B-1. Given the assumption that the gas phase volume is independent of the reaction in the numerical model, a constant CO_2 interfacial concentration is equivalent to unlimited CO_2 supply.

To improve, an updated CO_2 interfacial concentration can be applied. By monitoring the number of moles of NaOH being consumed within a short time period, the amount of CO_2 being transferred is calculated and the CO_2 interfacial concentration as a result can be updated. In Figure B-1, by using the updated CO_2 interfacial concentration the CO_2 conversion is found to be physically incorrect to approach 100%. However, different updating frequency results in very different CO_2 conversions. A low frequency, i.e. time step of 0.01s, boosts a steeper increase in CO_2 conversion at the beginning of the reaction because the interfacial concentration of CO_2 is being over-estimated. Higher frequency, i.e. time step is 0.001s for the first 0.2s and 0.005s afterwards, shows better results but a significant more time is used.

If gas phase is solved simultaneously, the CO_2 interfacial concentration can be updated dynamically. As seen in Figure B-1, the CO_2 conversion is predicted more accurately.

The above comparison shows that a two-phase model is necessary for the mass transfer study involving fast reactions.

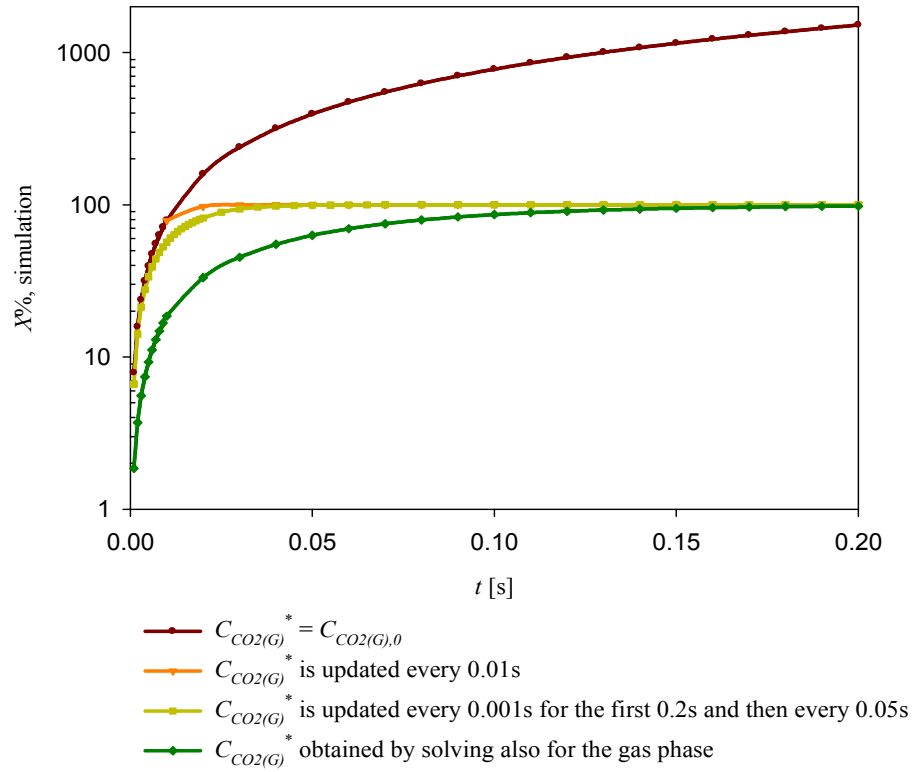


Figure B-1 CO₂ conversion for different techniques used to account for the change in CO₂ interfacial concentration.

APPENDIX C SENSITIVITY STUDY ON SIMULATION TIME STEPS

Four different time step length ranging from 0.005s to 0.1s are used for the simulation. Results (Figure C-1) show no difference between time steps of 0.01s and 0.005s, while deviations appear when the time steps are larger than 0.05s. It is obvious that the larger the time step, the greater the deviation of CO₂ conversion. Therefore, a time step of 0.01s is used in numerical models in Chapter 7, 8 and 9.

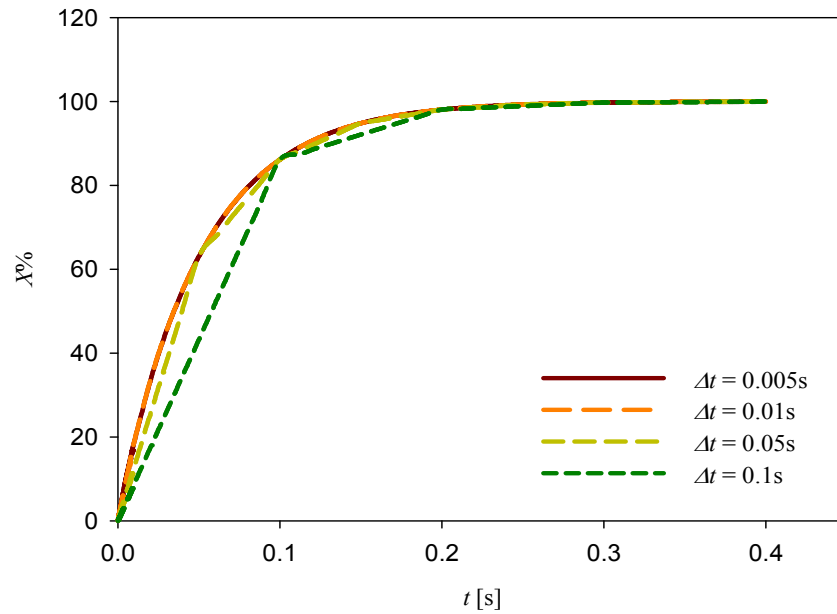
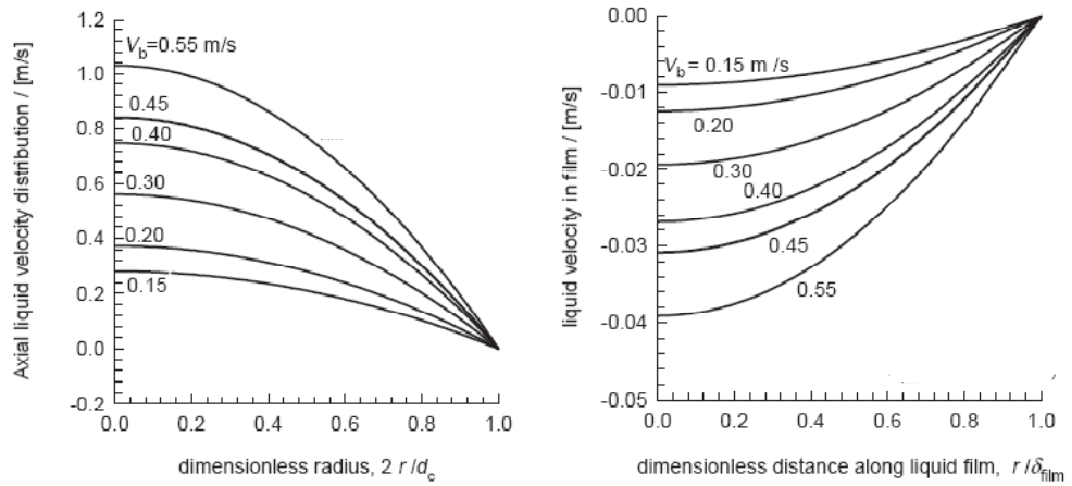


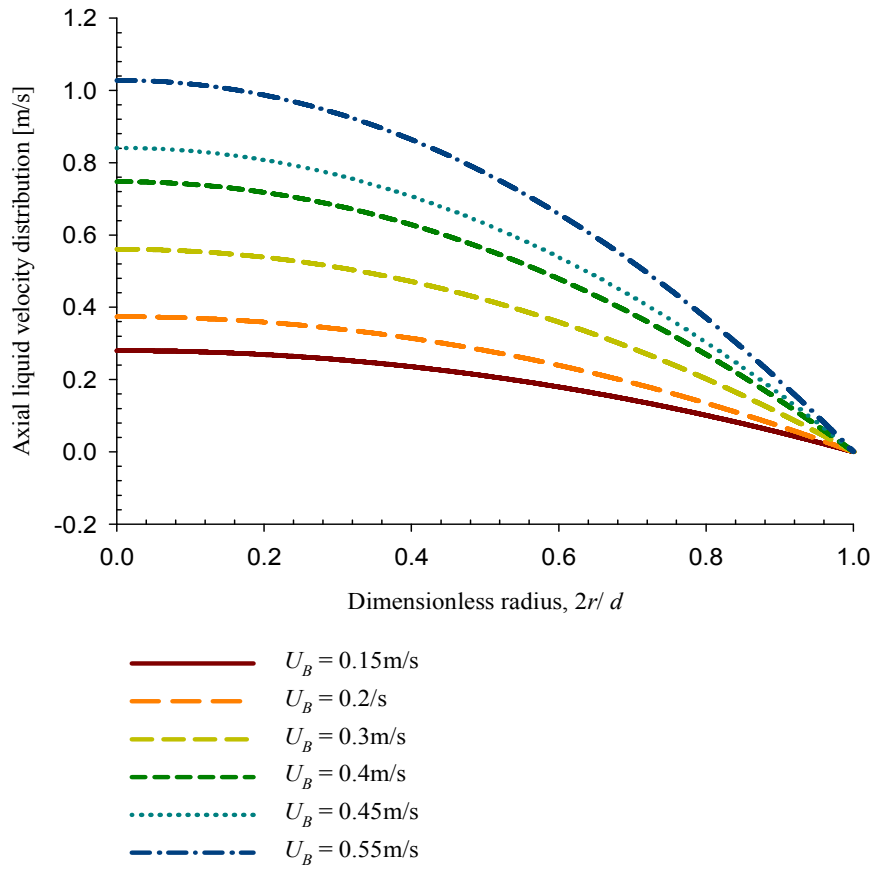
Figure C-1 CO₂ conversion at different simulation time steps. $d = 0.25\text{mm}$, $L_S = 0.26\text{mm}$, $L_B = 0.25\text{mm}$, $L_{UC} = 1\text{mm}$, $\delta = 5\mu\text{m}$.

APPENDIX D NUMERICAL MODEL VERIFICATION

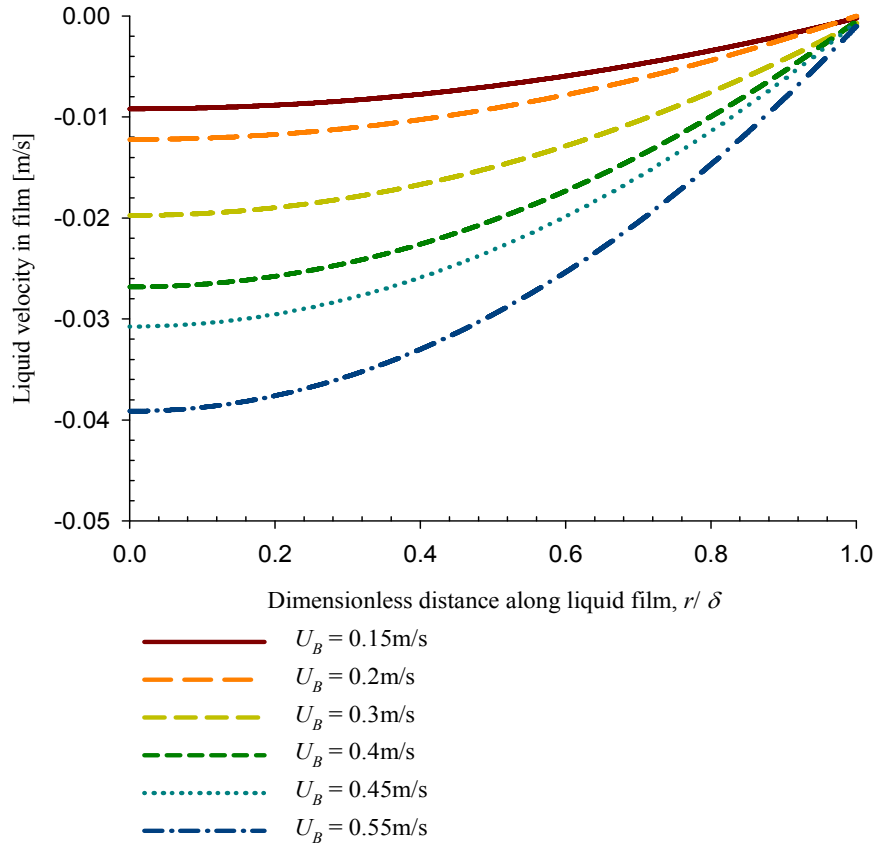
The numerical model developed in Section 7.5 is verified using results from [van Baten and Krishna \(2004\)](#). Only the hydrodynamic results (velocity field in the liquid phase) are compared considering that firstly, the current model will be compared with experimental data and secondly, the dimension solved in [van Baten and Krishna \(2004\)](#), e.g. $d = 3\text{mm}$ and $L_{UC} = 40\text{mm}$, is very time-consuming under our computational environment.

The comparison in Figure D-1 shows excellent agreement in term of velocity field in the liquid phase between the two models.





(b)



(c)

Figure D-1 Comparison of velocity field in the liquid phase between the numerical model formulated in Section 7.5 and that of [van Baten and Krishna \(2004\)](#). $d = 3\text{mm}$, $\delta = 48\mu\text{m}$, $D = 1 \times 10^{-9}\text{m}^2/\text{s}$, $L_{UC} = 0.04\text{m}$, $L_S = 5.321\text{mm}$. (a) results from [van Baten and Krishna \(2004\)](#); (b), (c) results from the numerical model in Section 7.5.

APPENDIX E CALCULATION OF REACTION CONVERSION FOR CO₂
ABSORPTION EXPERIMENTS

The labelled 20vol%/80vol% CO₂/N₂ mixture was initially sent to Gas Chromatograph to measure the CO₂ volume fraction before the reaction, $y_{CO_2, in}$. The CO₂ volume fraction at the outlet under various operating conditions was recorded. Reaction conversion $X\%$ was calculated as shown in Eq. E-1 to Eq. E-4, and an example calculation was given.

Bubble volume changes as CO₂ is consumed, so the conversion is calculated by the mole of CO₂ change, as in Eq. E-1:

$$X\% = \left(1 - \frac{n_{CO_2, out}}{n_{CO_2, in}} \right) \% \quad \text{Eq. E-1}$$

Assuming the pressure inside the bubble is constant, so the mole ratio can be substituted by volume ratio (Eq. E-2) according to the Ideal Gas Law:

$$\frac{n_{CO_2, out}}{n_{CO_2, in}} = \frac{V_{CO_2, out}}{V_{CO_2, in}} = \frac{V_{out} y_{CO_2, out}}{V_{in} y_{CO_2, in}} \quad \text{Eq. E-2}$$

As the volume of N₂ remains the same during the reaction, Eq. E-3 is obtained:

$$V_{in} (1 - y_{CO_2, in}) = V_{out} (1 - y_{CO_2, out}) \quad \text{Eq. E-3}$$

Substituting Eq. E-1 and Eq. E-3 into Eq. E-2, the reaction conversion is obtained in Eq. E-4;

$$X\% = \left(1 - \frac{(1 - y_{CO_2, in}) y_{CO_2, out}}{(1 - y_{CO_2, out}) y_{CO_2, in}} \right) \% = \frac{(y_{CO_2, in} - y_{CO_2, out})}{(1 - y_{CO_2, out}) y_{CO_2, in}} \% \quad \text{Eq. E-4}$$

Accordingly, an example reaction conversion is given as below:

Eq. 6.2 was used to calculate the unit cell frequency using the experimental operating conditions. Flow geometric parameters, e.g. L_B , L_{UC} , were obtained and used as simulations input, as presented in 0.

For a Series I straight channel reactor (Table 7.5), $Q_G = 0.585\text{ml/min}$, $y_{CO_2, in}\% = 2.175\%$ and $y_{CO_2, out}\% = 2.628\%$:

$$X\% = \frac{(y_{CO_2, in} - y_{CO_2, out})}{(1 - y_{CO_2, out}) y_{CO_2, in}} \% = \frac{(0.2175 - 0.04022)}{(1 - 0.04022) 0.2175} \% = 84.9\%$$

APPENDIX F TAYLOR BUBBLE SPLITTING IN BIFURCATING CHANNELS

Taylor bubble splitting in bifurcating channels is investigated. A typical Taylor bubble splitting process is shown in Figure F-1, where differences in bubble length in the upper and the lower daughter channels are observed. The average bubble lengths in the upper and the lower daughter channel are measured (Aequitas) and the ratio of these two lengths is calculated. For each flow condition, about 10 length ratios are obtained and shown in Figure F-2, in which the average length ratio is also presented (dashed or solid lines). It appears that

- The splitting in air-water system is less reproducible than air-octane system as the data is more scattered as seen in Figure F-2. This is due to the poorer wettability of water for acrylic than octane.
- The ratio of the bubble length in the air-octane system is closer to “1”, representing that the bifurcation is more even than in the air-water system. This is probably because the lower surface tension in the air-octane system makes it easier to break the gas-liquid interface and reform the new one.

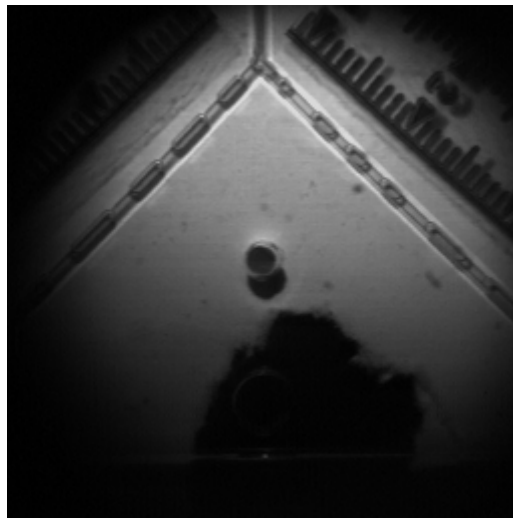


Figure F-1 A snapshot of Taylor bubble splitting in a bifurcating channel. $Q_G = 0.585\text{ml/min}$, $Q_L = 0.6\text{ml/min}$, air-water system, $d_H = 0.577\text{mm}$.

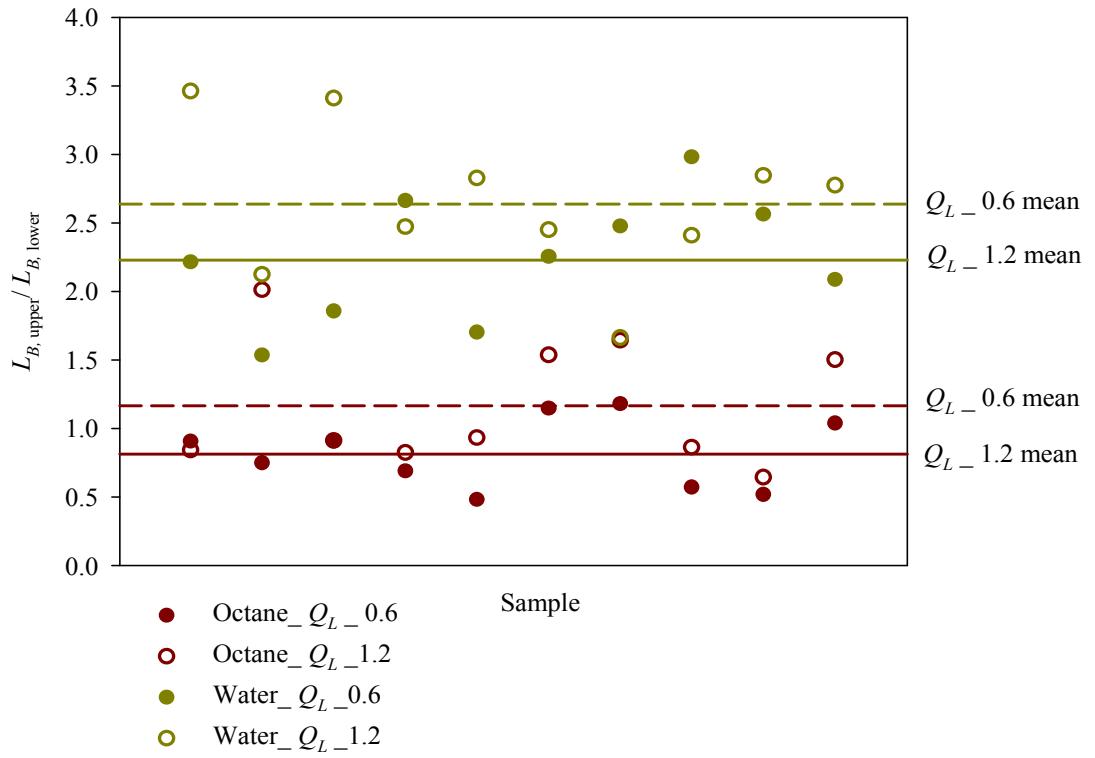


Figure F-2 The ratio of bubble length in the upper and lower daughter channels for both air-water and air-octane systems. $Q_G = 1.121 \text{ ml/min}$, $d_H = 0.577 \text{ mm}$.

APPENDIX G NUMERICAL MODEL CODE FOR TAYLOR FLOW FORMATION

The code for the numerical model in Chapter 5 is provided, which is run in CFX4.

```
>>CFX4
  >>SET LIMITS
    TOTAL INTEGER WORK SPACE 30000000
    TOTAL CHARACTER WORK SPACE 40000
    TOTAL REAL WORK SPACE 100000000
  >>OPTIONS
    TWO DIMENSIONS
    RECTANGULAR GRID
    CYLINDRICAL COORDINATES
    AXIS INCLUDED
    AXISYMMETRIC MODIFICATION
    LAMINAR FLOW
    ISOTHERMAL FLOW
    INCOMPRESSIBLE FLOW
    TRANSIENT FLOW
    NUMBER OF PHASES 2
  >>PHASE NAMES
    PHASE1 'LIQUID'
    PHASE2 'GAS'
>>MODEL TOPOLOGY
  >>CREATE BLOCK
    BLOCK NAME 'TUBE'
    BLOCK DIMENSIONS 2000 50 1
  >>CREATE BLOCK
    BLOCK NAME 'NOZZLE'
    BLOCK DIMENSIONS 40 11 1
  >>CREATE PATCH
    PATCH NAME 'LIQUID OUTLET'
    BLOCK NAME 'TUBE'
    PATCH TYPE 'PRESSURE BOUNDARY'
    HIGH I
  >>CREATE PATCH
    PATCH NAME 'TUBEWALL'
    BLOCK NAME 'TUBE'
    PATCH TYPE 'WALL'
    HIGH J
  >>CREATE PATCH
    PATCH NAME 'SYMMETRY1'
    BLOCK NAME 'TUBE'
    PATCH TYPE 'SYMMETRY PLANE'
    LOW J
  >>CREATE PATCH
    PATCH NAME 'NOZZLEWALL'
    BLOCK NAME 'TUBE'
    PATCH TYPE 'WALL'
    PATCH LOCATION 1 1 12 21 1 1
    LOW I
  >>CREATE PATCH
    PATCH NAME 'NOZZLEOUT'
    BLOCK NAME 'TUBE'
    PATCH TYPE 'INTER BLOCK BOUNDARY'
    PATCH LOCATION 1 1 1 11 1 1
    LOW I
  >>CREATE PATCH
    PATCH NAME 'LIQUIDINLET'
    BLOCK NAME 'TUBE'
    PATCH TYPE 'INLET'
```

Appendix G Numerical Model Code for Taylor Flow Formation

```
PATCH LOCATION 1 1 22 50 1 1
LOW I
>>CREATE PATCH
  PATCH NAME 'SYMMETRY2'
  BLOCK NAME 'NOZZLE'
  PATCH TYPE 'SYMMETRY PLANE'
  LOW J
>>CREATE PATCH
  PATCH NAME 'NOZZLEWALL'
  BLOCK NAME 'NOZZLE'
  PATCH TYPE 'WALL'
  HIGH J
>>CREATE PATCH
  PATCH NAME 'GASINLET'
  BLOCK NAME 'NOZZLE'
  PATCH TYPE 'INLET'
  LOW I
>>CREATE PATCH
  PATCH NAME 'NOZZLEOUT2'
  BLOCK NAME 'NOZZLE'
  PATCH TYPE 'INTER BLOCK BOUNDARY'
  HIGH I
>>GLUE PATCHES
  FIRST PATCH NAME 'NOZZLEOUT'
  SECOND PATCH NAME 'NOZZLEOUT2'
  ORIENTATION CHANGE 'HIGH I' 'HIGH J' 'HIGH K'
>>MODEL DATA
  >>AMBIENT VARIABLES
    PHASE NAME 'LIQUID'
    U VELOCITY 0.0000E+00
    V VELOCITY 0.0000E+00
    PRESSURE 1.0000E+00
    VOLUME FRACTION 0.0000E+00
  >>AMBIENT VARIABLES
    PHASE NAME 'GAS'
    U VELOCITY 0.0000E+00
    V VELOCITY 0.0000E+00
    PRESSURE 1.0000E+00
    VOLUME FRACTION 1.0000E+00
  >>DIFFERENCING SCHEME
    ALL EQUATIONS 'HYBRID'
  >>SET INITIAL GUESS
    >>SET CONSTANT GUESS
      PHASE NAME 'GAS'
      U VELOCITY 41.32231
      V VELOCITY 0.0
      PRESSURE 0.0
      VOLUME FRACTION 0.0
    >>SET CONSTANT GUESS
      PHASE NAME 'LIQUID'
      U VELOCITY 2.428363
      V VELOCITY 0.0
      PRESSURE 0.0
      VOLUME FRACTION 1.0
  >>RHIE CHOW SWITCH
    IMPROVED
    QUADRATIC EXTRAPOLATION
    MULTIPHASE DAMPING
    STANDARD RESISTANCE TREATMENT
  >>TITLE
    PROBLEM TITLE 'INLET INFO'
  >>VARIABLE TYPE
    ALL EQUATIONS 'SIGN DEFINITE'
```

Appendix G Numerical Model Code for Taylor Flow Formation

```
>>WALL TREATMENTS
  PHASE NAME 'LIQUID'
  WALL PROFILE 'QUADRATIC'
  NO SLIP
>>WALL TREATMENTS
  PHASE NAME 'GAS'
  WALL PROFILE 'QUADRATIC'
  NO SLIP
>>PHYSICAL PROPERTIES
  >>FLUID PARAMETERS
    PHASE NAME 'LIQUID'
    VISCOSITY 1
    DENSITY 49.9
  >>FLUID PARAMETERS
    PHASE NAME 'GAS'
    VISCOSITY 1.7000E-02
    DENSITY 0.0595
  >>MULTIPHASE PARAMETERS
    >>MULTIPHASE MODELS
      >>MOMENTUM
        HOMOGENEOUS
        SINCE
        SURFACE SHARPENING ALGORITHM
        SURFACE SHARPENING LEVEL 1
        SURFACE TENSION MODEL
        SURFACE TENSION COEFFICIENT 722.6
        WALL CONTACT ANGLE IN DEGREES 0
      >>HOMOGENEOUS
        SINCE
        SURFACE SHARPENING ALGORITHM
        SURFACE SHARPENING LEVEL 1
        SURFACE TENSION MODEL
        SURFACE TENSION COEFFICIENT 722.6
        WALL CONTACT ANGLE IN DEGREES 0
    >>TRANSIENT PARAMETERS
      >>FIXED TIME STEPPING
        TIME STEPS 5000* 1.00E-4
        INITIAL TIME 0.0000E+00
        BACKWARD DIFFERENCE
        QUADRATIC TIME DIFFERENCING
>>SOLVER DATA
  >>PROGRAM CONTROL
    MAXIMUM NUMBER OF ITERATIONS 20
    MASS SOURCE TOLERANCE 1.0000E-05
  >>EQUATION SOLVERS
    ALL PHASES
    U VELOCITY 'AMG'
    V VELOCITY 'AMG'
    PRESSURE 'AMG'
    VOLUME FRACTION 'AMG'
  >>PRESSURE CORRECTION
    SIMPLEC
  >>REDUCTION FACTORS
    ALL PHASES
    U VELOCITY 2.5000E-02
    V VELOCITY 2.5000E-02
    PRESSURE 1.0000E-02
    VOLUME FRACTION 1.0000E-02
  >>SWEEPS INFORMATION
    >>MINIMUM NUMBER
      ALL PHASES
      U VELOCITY 1
      V VELOCITY 1
```

Appendix G Numerical Model Code for Taylor Flow Formation

```
        PRESSURE 1
        VOLUME FRACTION 1
>>CREATE GRID
  >>SIMPLE GRID
    BLOCK NAME 'TUBE'
    DX 2000*0.01
    DY 11*0.01 10*0.01 29*0.01
    DZ 1* 1.000000E+00
    X START 1.0000E+00
    Y START 0.0000E+00
    Z START 0.0000E+00
  >>SIMPLE GRID
    BLOCK NAME 'NOZZLE'
    DX 40*0.01
    DY 11*0.01
    DZ 1* 1.000000E+00
    X START 0.60000E+00
    Y START 0.0000E+00
    Z START 0.0000E+00
>>MODEL BOUNDARY CONDITIONS
  >>INLET BOUNDARIES
    PHASE NAME 'GAS'
    PATCH NAME 'GASINLET'
    NORMAL VELOCITY 41.32231
    VOLUME FRACTION 1.0000E+00
  >>INLET BOUNDARIES
    PHASE NAME 'LIQUID'
    PATCH NAME 'GASINLET'
    NORMAL VELOCITY 41.32231
    VOLUME FRACTION 0.0000E+00
  >>INLET BOUNDARIES
    PHASE NAME 'GAS'
    PATCH NAME 'LIQUIDINLET'
    NORMAL VELOCITY 2.428363
    VOLUME FRACTION 0.0000E+00
  >>INLET BOUNDARIES
    PHASE NAME 'LIQUID'
    PATCH NAME 'LIQUIDINLET'
    NORMAL VELOCITY 2.428363
    VOLUME FRACTION 1.0000E+00
  >>PRESSURE BOUNDARIES
    PHASE NAME 'GAS'
    PATCH NAME 'LIQUID OUTLET'
    PRESSURE 0.0000E+00
    STATIC PRESSURE SPECIFIED
    VOLUME FRACTION 0.0000E+00
  >>PRESSURE BOUNDARIES
    PHASE NAME 'LIQUID'
    PATCH NAME 'LIQUID OUTLET'
    PRESSURE 0.0000E+00
    STATIC PRESSURE SPECIFIED
    VOLUME FRACTION 1.0000E+00
>>OUTPUT OPTIONS
  >>FRONTEND PRINTING
    NO FRONTEND PRINTING
    NO TOPOLOGY STRUCTURE
  >>DUMP FILE FORMAT
    UNFORMATTED
  >>DUMP FILE OPTIONS
    ALL PHASES
    TIME INTERVAL 0.100
    ALL REAL DATA
    GEOMETRY DATA
```

Appendix G Numerical Model Code for Taylor Flow Formation

```
VOLUME FRACTION  
>>STOP
```

APPENDIX H NUMERICAL MODEL REPORT FOR TAYLOR FLOW MASS TRANSFER

The report for the numerical model formulated in Chapter 7 and also used in Chapter 8 and 9 is provided here. The simulation environment is Comsol Multiphysics 3.3a. The contents are also available from this link:

<G:\Nan\Comsol\model\Taylor flow reactor.html>

1. Table of Contents

Title - COMSOL Model Report
Table of Contents
Model Properties
Constants
Geometry
Geom1
Integration Coupling Variables
Periodic Conditions
Solver Settings
Postprocessing
Variables

2. Model Properties

Property	Value
Model name	
Author	
Company	
Department	
Reference	
URL	
Saved date	May 9, 2008 3:52:00 PM
Creation date	Apr 10, 2008 4:30:27 PM
COMSOL version	COMSOL 3.3.0.511

Application modes and modules used in this model:

Geom1 (Axial symmetry (2D))

Convection and Diffusion (Chemical Engineering Module)

Diffusion (Chemical Engineering Module)

Incompressible Navier-Stokes (Chemical Engineering Module)

3. Constants

Name	Expression	Value	Description
Dg	1.63e-5		
vb	0.4084		
R	0.082e-3		
T	313.15		
P0	67.456		atm
cg0	$P0 \cdot 0.022763 / R / T$		
M	1e5		
cr0	4575.864		
He	$1 / (44.605 / 1000)$		
Dl	1.3992e-9		
rho1	1018.5		
mul	0.00257		
d	0.001		
Ca	$mul \cdot vb / 0.0454$		
delta	$0.66 \cdot Ca^{(2/3)} / (1 + 3.33 \cdot Ca^{(2/3)}) \cdot d$		
k1	$(2.91e7 \cdot \exp(-4579/T1)) / 100$		
Dr	$4.682e-14 \cdot mul^{(-0.569842)} \cdot T$		
T1	320.4		
rhog	50.53677		
mug	1.32e-5		
K1	156.8		
cl0	0		

4. Geometry

Number of geometries: 1

4.1. Geom1

4.1.1. Point mode

4.1.2. Boundary mode

4.1.3. Subdomain mode

5. Geom1

Space dimensions: Axial symmetry (2D)

Independent variables: r, phi, z

5.1. Mesh

5.1.1. Mesh Statistics

Number of degrees of freedom	311448
Number of mesh points	16731
Number of elements	16500
Triangular	0
Quadrilateral	16500
Number of boundary elements	860
Number of vertex elements	12
Minimum element quality	0.01
Element area ratio	0.001

5.2. Application Mode: Convection and Diffusion (chcd)

Application mode type: Convection and Diffusion (Chemical Engineering Module)

Application mode name: chcd

5.2.1. Application Mode Properties

Property	Value
Default element type	Lagrange - Quadratic
Analysis type	Transient
Equation form	Non-conservative
Equilibrium assumption	Off
Frame	Frame (ref)
Weak constraints	Off

5.2.2. Variables

Dependent variables: cl, cr, cp1, cp2

Shape functions: shlag(2,'cl'), shlag(2,'cr'), shlag(2,'cp1'), shlag(2,'cp2')

Interior boundaries not active

5.2.3. Boundary Settings

Boundary	1, 3, 7, 9	2, 11
Type	Axial symmetry	Convective flux
Inward flux (N)	mol/(m ² ·s)	{0;0;0;0}

Boundary	6, 8, 12	15-17
Type	Flux	Insulation/Symmetry
Inward flux (N)	{M*(He*R*TI*cg-cl);0;0;0}	{0;0;0;0}

5.2.4. Subdomain Settings

Subdomain		1-2, 4-6
Diffusion coefficient (D)	m ² /s	{Dl;Dr;Dl;Dl}
Reaction rate (R)	mol/(m ³ ·s)	{-k1*cl*cr+k1/K1*cp1*cp2;-k1*cl*cr+k1/K1*cp1*cp2;-(-k1*cl*cr+k1/K1*cp1*cp2);-(-k1*cl*cr+k1/K1*cp1*cp2)}
r-velocity (u)	m/s	{u;u;u;u}
z-velocity (v)	m/s	{v;v;v;v}
Streamline diffusion switch (sdon)		{1;1;1;1}

Subdomain initial value		1-2, 4-6
Concentration, cl (cl)	mol/m ³	cl0
Concentration, cr (cr)	mol/m ³	cr0

5.3. Application Mode: Diffusion (chdi)

Application mode type: Diffusion (Chemical Engineering Module)

Application mode name: chdi

5.3.1. Application Mode Properties

Property	Value
Default element type	Lagrange - Quadratic
Analysis type	Transient
Equilibrium assumption	Off
Frame	Frame (ref)
Weak constraints	Off

5.3.2. Variables

Dependent variables: cg

Shape functions: shlag(2,'cg')

Interior boundaries not active

5.3.3. Boundary Settings

Boundary	5	6, 8, 12
Type	Axial symmetry	Flux
Inward flux (N)	mol/(m ² ·s)	0 M*(cl-He*R*tl*cg)

5.3.4. Subdomain Settings

Subdomain	3
Diffusion coefficient (D)	m ² /s Dg

Subdomain initial value	3
Concentration, cg (cg)	mol/m ³ cg0

5.4. Application Mode: Incompressible Navier-Stokes (chns)

Application mode type: Incompressible Navier-Stokes (Chemical Engineering Module)

Application mode name: chns

5.4.1. Application Mode Properties

Property	Value
Default element type	Lagrange - P ₂ P ₁
Analysis type	Stationary
Stress tensor	Total
Corner smoothing	Off
Non-isothermal flow	Off
Turbulence model	None
Realizability	Off
Non-Newtonian flow	Off
Brinkman on by default	Off
Two-phase flow	Single-phase flow
Swirl velocity	Off
Frame	Frame (ref)
Weak constraints	Off

5.4.2. Variables

Dependent variables: u, v, w, p, logk, logd, logw, phi, nrw, nzw

Shape functions: shlag(2,'u'), shlag(2,'v'), shlag(1,'p')

Interior boundaries not active

5.4.3. Point Settings

Point	1-8, 10-12	9
pnton Pa	0	1
style	{0,{0,0,255}}	{0,{0,0,255}}

5.4.4. Boundary Settings

Boundary	1, 3, 7, 9	2, 11
Type	Axial symmetry	Neutral
z-velocity (v0) m/s	0	0

Boundary	6, 8, 12	15-17
----------	----------	-------

Type	Slip/Symmetry	Velocity
z-velocity (v0)	0	-vb

5.4.5. Subdomain Settings

Subdomain		1-2, 4-6
Integration order (gporder)		4 4 2
Constraint order (cporder)		2 2 1
Density (rho)	kg/m ³	rhol
Dynamic viscosity (eta)	Pa·s	mul
Streamline diffusion switch (sdon)	m ²	1

6. Integration Coupling Variables

6.1. Geom1

6.1.1. Source Subdomain: 3

Name	Value
Variable name	Ng
Expression	2*pi*r*cg
Order	4
Global	Yes

7. Periodic Conditions

7.1. Geom1

7.1.1. Source Boundary: 2

Name	Value
Expression	u
Transformation type	Linear
Destination Boundary	11 (Geom1)
Source vertices	1, 9
Destination vertices	6, 11
Name	pconstru

7.1.2. Source Boundary: 2

Name	Value
Expression	v
Transformation type	Linear
Destination Boundary	11 (Geom1)

Source vertices	1, 9
Destination vertices	6, 11
Name	pconstrv

7.1.3. Source Boundary: 2

Name	Value
Expression	p
Transformation type	Linear
Destination Boundary	11 (Geom1)
Source vertices	1, 9
Destination vertices	6, 11
Name	pconstrp

7.1.4. Source Boundary: 2

Name	Value
Expression	cl
Transformation type	Linear
Destination Boundary	11 (Geom1)
Source vertices	1, 9
Destination vertices	6, 11
Name	pconstrcl

7.1.5. Source Boundary: 2

Name	Value
Expression	cr
Transformation type	Linear
Destination Boundary	11 (Geom1)
Source vertices	1, 9
Destination vertices	6, 11
Name	pconstrcr

7.1.6. Source Boundary: 2

Name	Value
Expression	cp1
Transformation type	Linear
Destination Boundary	11 (Geom1)
Source vertices	1, 9
Destination vertices	6, 11
Name	pconstrep1

7.1.7. Source Boundary: 2

Name	Value
Expression	cp2
Transformation type	Linear
Destination Boundary	11 (Geom1)
Source vertices	1, 9
Destination vertices	6, 11
Name	pconstrep2

8. Solver Settings

Solve using a script: off

Analysis type	Transient
Auto select solver	On
Solver	Time dependent
Solution form	Automatic
Symmetric	auto
Adaption	Off

8.1. Direct (UMFPACK)

Solver type: Linear system solver

Parameter	Value
Pivot threshold	0.1
Memory allocation factor	0.7

8.2. Time Stepping

Parameter	Value
Times	0:0.01:5
Relative tolerance	0.01
Absolute tolerance	0.0010
Times to store in output	Specified times
Time steps taken by solver	Free
Manual tuning of step size	Off
Initial time step	0.0010
Maximum time step	1.0
Maximum BDF order	5
Singular mass matrix	Maybe

Consistent initialization of DAE systems	Backward Euler
Error estimation strategy	Include algebraic
Allow complex numbers	Off

8.3. Advanced

Parameter	Value
Constraint handling method	Elimination
Null-space function	Sparse
Assembly block size	5000
Use Hermitian transpose of constraint matrix and in symmetry detection	Off
Use complex functions with real input	Off
Stop if error due to undefined operation	On
Type of scaling	Automatic
Manual scaling	
Row equilibration	On
Manual control of reassembly	Off
Load constant	On
Constraint constant	On
Mass constant	On
Damping (mass) constant	On
Jacobian constant	On
Constraint Jacobian constant	On

9. Postprocessing

10. Variables

10.1. Boundary

10.1.1. Boundary 1-4, 7, 9-11, 13-17

Name	Description	Expression
ndflux_cl_chcd	Normal diffusive flux, cl	$nr_ched * dflux_cl_r_ched + nz_ched * dflux_cl_z_ched$
ncflux_cl_chcd	Normal convective flux, cl	$nr_ched * cflux_cl_r_ched + nz_ched * cflux_cl_z_ched$
ntflux_cl_chcd	Normal total flux, cl	$nr_ched * tflux_cl_r_ched + nz_ched * tflux_cl_z_ched$
ndflux_cr_chcd	Normal diffusive flux, cr	$nr_ched * dflux_cr_r_ched + nz_ched * dflux_cr_z_ched$
ncflux_cr_chcd	Normal convective flux, cr	$nr_ched * cflux_cr_r_ched + nz_ched * cflux_cr_z_ched$
ntflux_cr_chcd	Normal total flux, cr	$nr_ched * tflux_cr_r_ched + nz_ched * tflux_cr_z_ched$
ndflux_cp1_chcd	Normal diffusive flux, cp1	$nr_ched * dflux_cp1_r_ched + nz_ched * dflux_cp1_z_ched$
ncflux_cp1_chcd	Normal convective flux, cp1	$nr_ched * cflux_cp1_r_ched + nz_ched * cflux_cp1_z_ched$
ntflux_cp1_chcd	Normal total flux, cp1	$nr_ched * tflux_cp1_r_ched + nz_ched * tflux_cp1_z_ched$
ndflux_cp2_chcd	Normal diffusive flux, cp2	$nr_ched * dflux_cp2_r_ched + nz_ched * dflux_cp2_z_ched$
ncflux_cp2_chcd	Normal convective flux, cp2	$nr_ched * cflux_cp2_r_ched + nz_ched * cflux_cp2_z_ched$
ntflux_cp2_chcd	Normal total flux, cp2	$nr_ched * tflux_cp2_r_ched + nz_ched * tflux_cp2_z_ched$
ndflux_cg_chdi	Normal diffusive flux, cg	
K_r_chns	Viscous force per area, r component	$2 * nr_chns * eta_chns * ur + nz_chns * eta_chns * (uz + vr)$
T_r_chns	Total force per area, r component	$-nr_chns * p + 2 * nr_chns * eta_chns * ur + nz_chns * eta_chns * (uz + vr)$
K_z_chns	Viscous force per area, z component	$nr_chns * eta_chns * (vr + uz) + 2 * nz_chns * eta_chns * vz$
T_z_chns	Total force per area, z component	$-nz_chns * p + nr_chns * eta_chns * (vr + uz) + 2 * nz_chns * eta_chns * vz$

10.1.2. Boundary 5

Name	Description	Expression
ndflux_cl_chcd	Normal diffusive flux, cl	
ncflux_cl_chcd	Normal convective flux, cl	
ntflux_cl_chcd	Normal total flux, cl	
ndflux_cr_chcd	Normal diffusive flux, cr	
ncflux_cr_chcd	Normal convective flux, cr	
ntflux_cr_chcd	Normal total flux, cr	
ndflux_cp1_chcd	Normal diffusive flux, cp1	
ncflux_cp1_chcd	Normal convective flux, cp1	
ntflux_cp1_chcd	Normal total flux, cp1	
ndflux_cp2_chcd	Normal diffusive flux, cp2	
ncflux_cp2_chcd	Normal convective flux, cp2	
ntflux_cp2_chcd	Normal total flux, cp2	
ndflux_cg_chdi	Normal diffusive flux, cg	$nr_chdi * dflux_cg_r_chdi + nz_chdi * dflux_cg_z_chdi$
K_r_chns	Viscous force per area, r component	
T_r_chns	Total force per area, r component	
K_z_chns	Viscous force per area, z component	
T_z_chns	Total force per area, z component	

10.1.3. Boundary 6, 8, 12

Name	Description	Expression
ndflux_cl_chcd	Normal diffusive flux, cl	$nr_ched * dflux_cl_r_ched + nz_ched * dflux_cl_z_ched$
ncflux_cl_chcd	Normal convective flux, cl	$nr_ched * cflux_cl_r_ched + nz_ched * cflux_cl_z_ched$
ntflux_cl_chcd	Normal total flux, cl	$nr_ched * tflux_cl_r_ched + nz_ched * tflux_cl_z_ched$
ndflux_cr_chcd	Normal diffusive flux, cr	$nr_ched * dflux_cr_r_ched + nz_ched * dflux_cr_z_ched$
ncflux_cr_chcd	Normal convective flux, cr	$nr_ched * cflux_cr_r_ched + nz_ched * cflux_cr_z_ched$
ntflux_cr_chcd	Normal total flux, cr	$nr_ched * tflux_cr_r_ched + nz_ched * tflux_cr_z_ched$
ndflux_cp1_chcd	Normal diffusive flux, cp1	$nr_ched * dflux_cp1_r_ched + nz_ched * dflux_cp1_z_ched$
ncflux_cp1_chcd	Normal convective flux, cp1	$nr_ched * cflux_cp1_r_ched + nz_ched * cflux_cp1_z_ched$
ntflux_cp1_chcd	Normal total flux, cp1	$nr_ched * tflux_cp1_r_ched + nz_ched * tflux_cp1_z_ched$
ndflux_cp2_chcd	Normal diffusive flux, cp2	$nr_ched * dflux_cp2_r_ched + nz_ched * dflux_cp2_z_ched$
ncflux_cp2_chcd	Normal convective flux, cp2	$nr_ched * cflux_cp2_r_ched + nz_ched * cflux_cp2_z_ched$
ntflux_cp2_chcd	Normal total flux, cp2	$nr_ched * tflux_cp2_r_ched + nz_ched * tflux_cp2_z_ched$
ndflux_cg_chdi	Normal diffusive flux, cg	$nr_chdi * dflux_cg_r_chdi + nz_chdi * dflux_cg_z_chdi$
K_r_chns	Viscous force per area, r component	$2 * nr_chns * eta_chns * ur + nz_chns * eta_chns * (uz + vr)$
T_r_chns	Total force per area, r component	$-nr_chns * p + 2 * nr_chns * eta_chns * ur + nz_chns * eta_chns * (uz + vr)$
K_z_chns	Viscous force per area, z component	$nr_chns * eta_chns * (vr + uz) + 2 * nz_chns * eta_chns * vz$
T_z_chns	Total force per area, z component	$-nz_chns * p + nr_chns * eta_chns * (vr + uz) + 2 * nz_chns * eta_chns * vz$

10.2. Subdomain

10.2.1. Subdomain 1-2, 4-6

Name	Description	Expression
grad_cl_r_chcd	Concentration gradient, cl, r component	clr
dflux_cl_r_chcd	Diffusive flux, cl, r component	-Drr_cl_chcd * clr-Drz_cl_chcd * clz
cflux_cl_r_chcd	Convective flux, cl, r component	cl * u_cl_chcd
tflux_cl_r_chcd	Total flux, cl, r component	dflux_cl_r_chcd+cflux_cl_r_chcd
grad_cl_z_chcd	Concentration gradient, cl, z component	clz
dflux_cl_z_chcd	Diffusive flux, cl, z component	-Dzr_cl_chcd * clr-Dzz_cl_chcd * clz
cflux_cl_z_chcd	Convective flux, cl, z component	cl * v_cl_chcd
tflux_cl_z_chcd	Total flux, cl, z component	dflux_cl_z_chcd+cflux_cl_z_chcd
beta_cl_r_chcd	Convective field, cl, r component	r * u_cl_chcd
beta_cl_z_chcd	Convective field, cl, z component	r * v_cl_chcd
grad_cl_chcd	Concentration gradient, cl	sqrt(grad_cl_r_chcd^2+grad_cl_z_chcd^2)
dflux_cl_chcd	Diffusive flux, cl	sqrt(dflux_cl_r_chcd^2+dflux_cl_z_chcd^2)
cflux_cl_chcd	Convective flux, cl	sqrt(cflux_cl_r_chcd^2+cflux_cl_z_chcd^2)
tflux_cl_chcd	Total flux, cl	sqrt(tflux_cl_r_chcd^2+tflux_cl_z_chcd^2)
cellPe_cl_chcd	Cell Peclet number, cl	h * sqrt(beta_cl_r_chcd^2+beta_cl_z_chcd^2)/Dm_cl_chcd
Dm_cl_chcd	Mean diffusion coefficient, cl	r * (Drr_cl_chcd * u_cl_chcd^2+Drz_cl_chcd * u_cl_chcd * v_cl_chcd+Dzr_cl_chcd * v_cl_chcd * u_cl_chcd+Dzz_cl_chcd * v_cl_chcd^2)/(u_cl_chcd^2+v_cl_chcd^2+eps)
res_cl_chcd	Equation residual for cl	r * (-Drr_cl_chcd * clrr-

Name	Description	Expression
		$Drz_{cl_ched} * clrz + clr * u_{cl_ched} - Dzr_{cl_ched} * clzr - Dzz_{cl_ched} * clzz + clz * v_{cl_ched} - R_{cl_ched}$
res_sc_cl_chcd	Shock capturing residual for cl	$r * (clr * u_{cl_ched} + clz * v_{cl_ched} - R_{cl_ched})$
da_cl_ched	Total time scale factor, cl	$r * Dts_{cl_ched}$
grad_cr_r_chcd	Concentration gradient, cr, r component	crr
dflux_cr_r_chcd	Diffusive flux, cr, r component	$-Drr_{cr_ched} * crr - Drz_{cr_ched} * crz$
cflux_cr_r_chcd	Convective flux, cr, r component	$cr * u_{cr_ched}$
tflux_cr_r_chcd	Total flux, cr, r component	$dflux_{cr_r_ched} + cflux_{cr_r_ched}$
grad_cr_z_chcd	Concentration gradient, cr, z component	crz
dflux_cr_z_chcd	Diffusive flux, cr, z component	$-Dzr_{cr_ched} * crr - Dzz_{cr_ched} * crz$
cflux_cr_z_chcd	Convective flux, cr, z component	$cr * v_{cr_ched}$
tflux_cr_z_chcd	Total flux, cr, z component	$dflux_{cr_z_ched} + cflux_{cr_z_ched}$
beta_cr_r_chcd	Convective field, cr, r component	$r * u_{cr_ched}$
beta_cr_z_chcd	Convective field, cr, z component	$r * v_{cr_ched}$
grad_cr_ched	Concentration gradient, cr	$\sqrt{grad_{cr_r_ched}^2 + grad_{cr_z_ched}^2}$
dflux_cr_ched	Diffusive flux, cr	$\sqrt{dflux_{cr_r_ched}^2 + dflux_{cr_z_ched}^2}$
cflux_cr_ched	Convective flux, cr	$\sqrt{cflux_{cr_r_ched}^2 + cflux_{cr_z_ched}^2}$
tflux_cr_ched	Total flux, cr	$\sqrt{tflux_{cr_r_ched}^2 + tflux_{cr_z_ched}^2}$
cellPe_cr_chcd	Cell Peclet number, cr	$h * \sqrt{beta_{cr_r_ched}^2 + beta_{cr_z_ched}^2} / Dm_{cr_ched}$
Dm_cr_ched	Mean diffusion coefficient, cr	$r * (Drr_{cr_ched} * u_{cr_ched}^2 + Drz_{cr_ched} * u_{cr_ched} * v_{cr_ched} + Dzr_{cr_ched} * v_{cr_ched}^2)$

Name	Description	Expression
		$v_{cr_chcd} * u_{cr_chcd} + D_{zz_cr_chcd} * v_{cr_chcd}^2 / (u_{cr_chcd}^2 + v_{cr_chcd}^2 + \epsilon)$
res_cr_chcd	Equation residual for cr	$r * (-D_{rr_cr_chcd} * c_{rrr} - D_{rz_cr_chcd} * c_{rrz} + c_{rr} * u_{cr_chcd} - D_{zr_cr_chcd} * c_{rzz} + c_{rz} * v_{cr_chcd} - R_{cr_chcd})$
res_sc_cr_chcd	Shock capturing residual for cr	$r * (c_{rr} * u_{cr_chcd} + c_{rz} * v_{cr_chcd} - R_{cr_chcd})$
da_cr_chcd	Total time scale factor, cr	$r * D_{ts_cr_chcd}$
grad_cp1_r_chcd	Concentration gradient, cp1, r component	cp1r
dflux_cp1_r_chcd	Diffusive flux, cp1, r component	$-D_{rr_cp1_chcd} * cp1r - D_{rz_cp1_chcd} * cp1z$
cflux_cp1_r_chcd	Convective flux, cp1, r component	$cp1 * u_{cp1_chcd}$
tflux_cp1_r_chcd	Total flux, cp1, r component	$dflux_cp1_r_chcd + cflux_cp1_r_chcd$
grad_cp1_z_chcd	Concentration gradient, cp1, z component	cp1z
dflux_cp1_z_chcd	Diffusive flux, cp1, z component	$-D_{zr_cp1_chcd} * cp1r - D_{zz_cp1_chcd} * cp1z$
cflux_cp1_z_chcd	Convective flux, cp1, z component	$cp1 * v_{cp1_chcd}$
tflux_cp1_z_chcd	Total flux, cp1, z component	$dflux_cp1_z_chcd + cflux_cp1_z_chcd$
beta_cp1_r_chcd	Convective field, cp1, r component	$r * u_{cp1_chcd}$
beta_cp1_z_chcd	Convective field, cp1, z component	$r * v_{cp1_chcd}$
grad_cp1_chcd	Concentration gradient, cp1	$\sqrt{grad_cp1_r_chcd^2 + grad_cp1_z_chcd^2}$
dflux_cp1_chcd	Diffusive flux, cp1	$\sqrt{dflux_cp1_r_chcd^2 + dflux_cp1_z_chcd^2}$
cflux_cp1_chcd	Convective flux, cp1	$\sqrt{cflux_cp1_r_chcd^2 + cflux_cp1_z_chcd^2}$
tflux_cp1_chcd	Total flux, cp1	$\sqrt{tflux_cp1_r_chcd^2 + tflux_cp1_z_chcd^2}$
cellPe_cp1_chcd	Cell Peclet number, cp1	$h * \sqrt{beta_cp1_r_chcd^2 + beta_cp1_z_chcd^2}$

Name	Description	Expression
		$z_chcd^2)/Dm_cp1_chcd$
Dm_cp1_chcd	Mean diffusion coefficient, cp1	$r * (Drr_cp1_chcd * u_cp1_chcd^2 + Drz_cp1_chcd * u_cp1_chcd * v_cp1_chcd + Dzz_cp1_chcd * u_cp1_chcd + Dzz_cp1_chcd * v_cp1_chcd^2) / (u_cp1_chcd^2 + v_cp1_chcd^2 + eps)$
res_cp1_chcd	Equation residual for cp1	$r * (-Drr_cp1_chcd * cp1r - Drz_cp1_chcd * cp1r * u_cp1_chcd - Dzz_cp1_chcd * cp1z + cp1z * v_cp1_chcd - R_cp1_chcd)$
res_sc_cp1_chcd	Shock capturing residual for cp1	$r * (cp1r * u_cp1_chcd + cp1z * v_cp1_chcd - R_cp1_chcd)$
da_cp1_chcd	Total time scale factor, cp1	$r * Dts_cp1_chcd$
grad_cp2_r_chcd	Concentration gradient, cp2, r component	cp2r
dflux_cp2_r_chcd	Diffusive flux, cp2, r component	$-Drr_cp2_chcd * cp2r - Drz_cp2_chcd * cp2z$
cflux_cp2_r_chcd	Convective flux, cp2, r component	$cp2 * u_cp2_chcd$
tflux_cp2_r_chcd	Total flux, cp2, r component	$dflux_cp2_r_chcd + cflux_cp2_r_chcd$
grad_cp2_z_chcd	Concentration gradient, cp2, z component	cp2z
dflux_cp2_z_chcd	Diffusive flux, cp2, z component	$-Dzz_cp2_chcd * cp2z - Dzz_cp2_chcd * cp2z$
cflux_cp2_z_chcd	Convective flux, cp2, z component	$cp2 * v_cp2_chcd$
tflux_cp2_z_chcd	Total flux, cp2, z component	$dflux_cp2_z_chcd + cflux_cp2_z_chcd$
beta_cp2_r_chcd	Convective field, cp2, r component	$r * u_cp2_chcd$
beta_cp2_z_chcd	Convective field, cp2, z component	$r * v_cp2_chcd$
grad_cp2_chcd	Concentration gradient, cp2	$sqrt(grad_cp2_r_chcd^2 + grad_cp2_z_chcd^2)$
dflux_cp2_chcd	Diffusive flux, cp2	$sqrt(dflux_cp2_r_chcd^2 + dflux_cp2_z_chcd^2)$
cflux_cp2_chcd	Convective flux, cp2	$sqrt(cflux_cp2_r_chcd^2 + cflux_cp2_z_chcd^2)$

Name	Description	Expression
cd		$2 \cdot z_chcd^2$
tflux_cp2_chcd	Total flux, cp2	$\sqrt{(tflux_cp2_r_chcd^2 + tflux_cp2_z_chcd^2)}$
cellPe_cp2_chcd	Cell Peclet number, cp2	$h \cdot \sqrt{(\beta_{cp2_r_chcd}^2 + \beta_{cp2_z_chcd}^2)} / Dm_cp2_chcd$
Dm_cp2_chcd	Mean diffusion coefficient, cp2	$r \cdot (Drr_cp2_chcd \cdot u_cp2_chcd^2 + Drz_cp2_chcd \cdot u_cp2_chcd \cdot v_cp2_chcd + Dzz_cp2_chcd \cdot v_cp2_chcd^2) / (u_cp2_chcd^2 + v_cp2_chcd^2 + \epsilon)$
res_cp2_chcd	Equation residual for cp2	$r \cdot (-Drr_cp2_chcd \cdot cp2r - Drz_cp2_chcd \cdot cp2r \cdot u_cp2_chcd - Dzz_cp2_chcd \cdot cp2z \cdot v_cp2_chcd - R_cp2_chcd)$
res_sc_cp2_chcd	Shock capturing residual for cp2	$r \cdot (cp2r \cdot u_cp2_chcd + cp2z \cdot v_cp2_chcd - R_cp2_chcd)$
da_cp2_chcd	Total time scale factor, cp2	$r \cdot Dts_cp2_chcd$
grad_cg_r_chdi	Concentration gradient, cg, r component	
dflux_cg_r_chdi	Diffusive flux, cg, r component	
grad_cg_z_chdi	Concentration gradient, cg, z component	
dflux_cg_z_chdi	Diffusive flux, cg, z component	
grad_cg_chdi	Concentration gradient, cg	
dflux_cg_chdi	Diffusive flux, cg	
U_chns	Velocity field	$\sqrt{u^2 + v^2}$
V_chns	Vorticity	$uz - vr$
divU_chns	Divergence of velocity field	$ur + vz + u/r$
cellRe_chns	Cell Reynolds number	$\rho_chns \cdot U_chns \cdot h / \eta_chns$
res_u_chns	Equation residual for u	$r \cdot (\rho_chns \cdot (u \cdot ur + v \cdot uz) + pr - F_r_chns) + 2 \cdot \eta_chns \cdot (u/r - ur) - \eta_chns \cdot (2 \cdot r \cdot urr + r \cdot (uzz + vrz))$
res_tst_u_chn	Variational equation residual	$r \cdot (nojac(\rho_chns) \cdot (nojac(u) \cdot$

Name	Description	Expression
s	for u	$ur+nojac(v) * uz)+pr)+2 * nojac(eta_chns) * (u/r-ur)-nojac(eta_chns) * (2 * r * urr+r * (uzz+vrz))$
res_sc_u_chns	Shock capturing residual for u	$r * (rho_chns * (u * ur+v * uz)+pr-F_r_chns)+2 * eta_chns * (u/r-ur)$
res_v_chns	Equation residual for v	$r * (rho_chns * (u * vr+v * vz)+pz-F_z_chns)-eta_chns * (r * (vrr+uzr)+2 * r * vzz+uz+vr)$
res_tst_v_chns	Variational equation residual for v	$r * (nojac(rho_chns) * (nojac(u) * vr+nojac(v) * vz)+pz)-nojac(eta_chns) * (r * (vrr+uzr)+2 * r * vzz+uz+vr)$
res_sc_v_chns	Shock capturing residual for v	$r * (rho_chns * (u * vr+v * vz)+pz-F_z_chns)$
beta_r_chns	Convective field, r component	$r * rho_chns * u$
beta_z_chns	Convective field, z component	$r * rho_chns * v$
Dm_chns	Mean diffusion coefficient	$r * eta_chns$
da_chns	Total time scale factor	$r * rho_chns$

10.2.2. Subdomain 3

Name	Description	Expression
grad_cl_r_chcd	Concentration gradient, cl, r component	
dflux_cl_r_chcd	Diffusive flux, cl, r component	
cflux_cl_r_chcd	Convective flux, cl, r component	
tflux_cl_r_chcd	Total flux, cl, r component	
grad_cl_z_chcd	Concentration gradient, cl, z component	
dflux_cl_z_chcd	Diffusive flux, cl, z component	
cflux_cl_z_chcd	Convective flux, cl, z component	
tflux_cl_z_chcd	Total flux, cl, z component	
beta_cl_r_chcd	Convective field, cl, r component	
beta_cl_z_chcd	Convective field, cl, z component	
grad_cl_chcd	Concentration gradient, cl	
dflux_cl_chcd	Diffusive flux, cl	
cflux_cl_chcd	Convective flux, cl	
tflux_cl_chcd	Total flux, cl	
cellPe_cl_chcd	Cell Peclet number, cl	
Dm_cl_chcd	Mean diffusion coefficient, cl	
res_cl_chcd	Equation residual for cl	
res_sc_cl_chcd	Shock capturing residual for cl	
da_cl_chcd	Total time scale factor, cl	

Name	Description	Expression
grad_cr_r_chcd	Concentration gradient, cr, r component	
dflux_cr_r_chcd	Diffusive flux, cr, r component	
cflux_cr_r_chcd	Convective flux, cr, r component	
tflux_cr_r_chcd	Total flux, cr, r component	
grad_cr_z_chcd	Concentration gradient, cr, z component	
dflux_cr_z_chcd	Diffusive flux, cr, z component	
cflux_cr_z_chcd	Convective flux, cr, z component	
tflux_cr_z_chcd	Total flux, cr, z component	
beta_cr_r_chcd	Convective field, cr, r component	
beta_cr_z_chcd	Convective field, cr, z component	
grad_cr_chcd	Concentration gradient, cr	
dflux_cr_chcd	Diffusive flux, cr	
cflux_cr_chcd	Convective flux, cr	
tflux_cr_chcd	Total flux, cr	
cellPe_cr_chcd	Cell Peclet number, cr	
Dm_cr_chcd	Mean diffusion coefficient, cr	
res_cr_chcd	Equation residual for cr	
res_sc_cr_chcd	Shock capturing residual for cr	
da_cr_chcd	Total time scale factor, cr	
grad_cp1_r_chcd	Concentration gradient, cp1, r component	
dflux_cp1_r_chcd	Diffusive flux, cp1, r component	
cflux_cp1_r_chcd	Convective flux, cp1, r component	
tflux_cp1_r_chcd	Total flux, cp1, r component	
grad_cp1_z_chcd	Concentration gradient, cp1, z component	
dflux_cp1_z_chcd	Diffusive flux, cp1, z component	
cflux_cp1_z_chcd	Convective flux, cp1, z component	
tflux_cp1_z_chcd	Total flux, cp1, z component	
beta_cp1_r_chcd	Convective field, cp1, r component	
beta_cp1_z_chcd	Convective field, cp1, z component	
grad_cp1_chcd	Concentration gradient, cp1	
dflux_cp1_chcd	Diffusive flux, cp1	
cflux_cp1_chcd	Convective flux, cp1	

Name	Description	Expression
tflux_cp1_chcd	Total flux, cp1	
cellPe_cp1_chcd	Cell Peclet number, cp1	
Dm_cp1_chcd	Mean diffusion coefficient, cp1	
res_cp1_chcd	Equation residual for cp1	
res_sc_cp1_chcd	Shock capturing residual for cp1	
da_cp1_chcd	Total time scale factor, cp1	
grad_cp2_r_chcd	Concentration gradient, cp2, r component	
dflux_cp2_r_chcd	Diffusive flux, cp2, r component	
cflux_cp2_r_chcd	Convective flux, cp2, r component	
tflux_cp2_r_chcd	Total flux, cp2, r component	
grad_cp2_z_chcd	Concentration gradient, cp2, z component	
dflux_cp2_z_chcd	Diffusive flux, cp2, z component	
cflux_cp2_z_chcd	Convective flux, cp2, z component	
tflux_cp2_z_chcd	Total flux, cp2, z component	
beta_cp2_r_chcd	Convective field, cp2, r component	
beta_cp2_z_chcd	Convective field, cp2, z component	
grad_cp2_chcd	Concentration gradient, cp2	
dflux_cp2_chcd	Diffusive flux, cp2	
cflux_cp2_chcd	Convective flux, cp2	
tflux_cp2_chcd	Total flux, cp2	
cellPe_cp2_chcd	Cell Peclet number, cp2	
Dm_cp2_chcd	Mean diffusion coefficient, cp2	
res_cp2_chcd	Equation residual for cp2	
res_sc_cp2_chcd	Shock capturing residual for cp2	
da_cp2_chcd	Total time scale factor, cp2	
grad_cg_r_chdi	Concentration gradient, cg, r component	cgr
dflux_cg_r_chdi	Diffusive flux, cg, r component	-Drr_cg_chdi * cgr-Drz_cg_chdi *
grad_cg_z_chdi	Concentration gradient, cg, z component	cgz

Name	Description	Expression
dflux_cg_z_chdi	Diffusive flux, cg, z component	$-Dzr_cg_chdi * cgr - Dzz_cg_chdi * cgz$
grad_cg_chdi	Concentration gradient, cg	$\sqrt{grad_cg_r_chd i^2 + grad_cg_z_chd i^2}$
dflux_cg_chdi	Diffusive flux, cg	$\sqrt{dflux_cg_r_ch di^2 + dflux_cg_z_c hdi^2}$
U_chns	Velocity field	
V_chns	Vorticity	
divU_chns	Divergence of velocity field	
cellRe_chns	Cell Reynolds number	
res_u_chns	Equation residual for u	
res_tst_u_chns	Variational equation residual for u	
res_sc_u_chns	Shock capturing residual for u	
res_v_chns	Equation residual for v	
res_tst_v_chns	Variational equation residual for v	
res_sc_v_chns	Shock capturing residual for v	
beta_r_chns	Convective field, r component	
beta_z_chns	Convective field, z component	
Dm_chns	Mean diffusion coefficient	
da_chns	Total time scale factor	

Refereed Research Papers from This Thesis

Journal Papers

Shao, N., Gavriilidis, A., Angeli, P. Effect of inlet conditions on gas-liquid flow regimes in microchannels. In preparation.

Shao, N., Gavriilidis, A., Angeli, P. Process intensification in Taylor flow microreactor - a case study on CO₂ absorption. In preparation.

Shao, N., Gavriilidis, A., Angeli, P., 2009. Effect of inlet conditions on Taylor bubble length in microchannels. *International Journal of Heat Transfer*, MNF 2009 Special Issue. Invited.

Shao, N., Gavriilidis, A., Angeli, P., 2009. Mass transfer during Taylor flow in microchannels with and without chemical reaction. *Chemical Engineering Journal*, IMRET 10 Special Issue. Submitted.

Shao, N., Gavriilidis, A., Angeli, P., 2009. Flow regimes for adiabatic gas-liquid flow in microchannels. *International Journal of Multiphase Flow* 64, 2749-2761.

Shao N., Salman W., Gavriilidis A., Angeli P., 2008. CFD simulations of the effect of inlet conditions on Taylor flow formation. *International Journal of Heat and Fluid Flow* 29, 1603-1611.

Conference Papers

Shao, N., Gavriilidis, A., Angeli, P., 2009. Effect of inlet conditions on Taylor bubble length in Microchannels. 2nd Micro and Nano Flows Conference, 1-2 September, London, UK.

Shao, N., Gavriilidis, A., Angeli, P., 2009. Effect of inlet conditions on gas-liquid flow regimes in microchannels. 1st International Conference on Microfluidics, 10-12 December, Bologna, Italy.

Shao N., Gavriilidis A., Angeli P., 2008. Intensified CO₂ capture using microstructured reactors. IChemE day meeting, 18 April, London, UK.

Shao N., Gavriilidis A., Angeli P., 2008. Mass transfer during Taylor flow in microchannels with and without chemical reaction. 10th International Conference on Microreaction Technology, 7-10 April, New Orleans, United States.

Xu, G., Shao, N., Papageorgiou, L.G., 2007. A mixed integer optimisation approach for data classification with multiple groups. 17th European Symposium on Computer Aided Process Engineering, 27-30 May, Bucharest, Romania.

Shao, N., Gavriilidis, A., Angeli, P., 2006. Overcoming mass transfer limitations in Taylor flow microreactors. 9th International Conference on Microreaction Technology, 6-8 September, Potsdam/Berlin, Germany.

Shao, N., Salmon, W., Gavriilidis, A., Angeli, P., 2005. CFD simulations of the effect of inlet conditions on Taylor flow formation. International Conference on Heat Transfer and Fluid Flow in Microscale, 25-30 September, Tuscany, Italy.